

THE ANTENNA LABORATORY

COPY	2	OF	3
HARD COPY	\$. 6.00		
MICROFICHE	\$. 1.50		

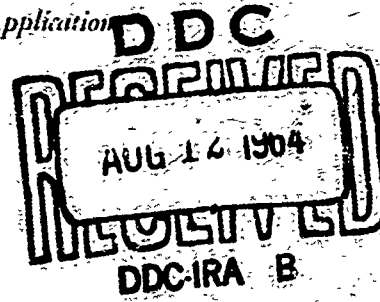
283p

RESEARCH ACTIVITIES in ---

Automatic Controls
Microwave Circuits
Terrain Investigations
Wave Propagation

Antennas
Astronautics
Radomes

Echo Area Studies
E M Field Theory
Systems Analysis
Submillimeter Application



Proceedings of the OSU-RTD Symposium
on
Electromagnetic Windows

2-4 June 1964

Vol. II

Department of ELECTRICAL ENGINEERING



THE OHIO STATE UNIVERSITY
RESEARCH FOUNDATION
Columbus, Ohio

AD 605 400

**Best
Available
Copy**

**CLEARINGHOUSE FOR FEDERAL SCIENTIFIC AND TECHNICAL INFORMATION CFSTI
DOCUMENT MANAGEMENT BRANCH 410.11**

LIMITATIONS IN REPRODUCTION QUALITY

ACCESSION # AD 605 402

- 1. WE REGRET THAT LEGIBILITY OF THIS DOCUMENT IS IN PART UNSATISFACTORY. REPRODUCTION HAS BEEN MADE FROM BEST AVAILABLE COPY.
- 2. A PORTION OF THE ORIGINAL DOCUMENT CONTAINS FINE DETAIL WHICH MAY MAKE READING OF PHOTOCOPY DIFFICULT.
- 3. THE ORIGINAL DOCUMENT CONTAINS COLOR, BUT DISTRIBUTION COPIES ARE AVAILABLE IN BLACK-AND-WHITE REPRODUCTION ONLY.
- 4. THE INITIAL DISTRIBUTION COPIES CONTAIN COLOR WHICH WILL BE SHOWN IN BLACK-AND-WHITE WHEN IT IS NECESSARY TO REPRINT.
- 5. LIMITED SUPPLY ON HAND: WHEN EXHAUSTED, DOCUMENT WILL BE AVAILABLE IN MICROFICHE ONLY.
- 6. LIMITED SUPPLY ON HAND: WHEN EXHAUSTED DOCUMENT WILL NOT BE AVAILABLE.
- 7. DOCUMENT IS AVAILABLE IN MICROFICHE ONLY.
- 8. DOCUMENT AVAILABLE ON LOAN FROM CFSTI (TT DOCUMENTS ONLY).
- 9.

PROCESSOR: *(Signature)*

+

Proceedings of the OSU-RTD Symposium
on
-- Electromagnetic Windows

2-4 June 1964

Vol. II
Session III-Electrical Design
Session IV-Structural Design for Large Radomes

The publication of this report does not constitute approval by either The Ohio State University or the United States Air Force of the findings contained herein. It is published only for the fruitful exchange and stimulation of ideas.

FOREWORD

The papers presented in this report were submitted for the Seventh Symposium on Electromagnetic Windows held at The Ohio State University, Columbus, Ohio, 2, 3, and 4 June 1964. They were compiled by Alan I. Slonim of The Ohio State University under Air Force Contract AF 33(615)-1081 administered by The Research and Technology Division, Air Force Systems Command, Wright-Patterson Air Force Base, Ohio with Richard A. Ireland serving as Task Engineer.

The proceedings are published in five volumes as follows:

Vol. I

- Session I - Objectives and New Techniques
- Session II - Materials for High Temperature Applications

Vol. II

- Session III - Electrical Design
- Session IV - Structural Design for Large Radomes

Vol. III

- Session V - Fabrication and Testing of Airborne Radomes
- Session VI - Hypersonic Environment

Vois. IV and V

Oral papers received too late for inclusion in Vols. I, II, and III.
Papers submitted for the proceedings only.

Vol. II
CONTENTS

SESSION III - ELECTRICAL DESIGN

- A. Slotted Metal Radome for High-Speed Flight,
C.H. Chiou, L.L. Oh, C.D. Lunden
- B. Antenna Radome-Gratings for Conical Scan Systems,
A.H. Schaufelberger
- C. Wide Band ECM Radomes on High Performance Aircraft,
J.F. Harder, W.P. Guarino
- D. The Scannable Ray-Fed Radome,
Stephen J. Gotkis
- E. An Application of Radome Broadbanding,
Peter Zuzole, Chandler Hom, Stanley Jurczak

SESSION IV - STRUCTURAL DESIGN FOR LARGE RADOMES

- A. Biaxial Stress Considerations of a Brittle Dielectric Material,
J.E. Burroughs and H.R. Thornton
- B. Design Techniques for Sectionalized Structurally Supported
Airborne Ceramic Radomes - A Progress Report,
Eino J. Luoma, Russell Stetson, Samuel J. Mason
- C. Feasibility of Monolithic Foam Radomes,
George C. Fretz
- D. Design and Performance of 60-Foot C-Band Rigid Radome,
CW-424/FPS-26,
C.S. Beal, J.R. Gruber, D.J. Driscoll
- E. Hardened Ground Radomes for System Survival,
G.J. Cook

SESSION III

SLOTTED METAL RADOME

for

HIGH-SPEED FLIGHT

C. H. Chiou, L. L. Oh, and C. D. Lunden
The Boeing Company
Airplane Division
Renton, Washington

I. INTRODUCTION

Radomes mounted on supersonic vehicles must operate at high temperatures and must be able to withstand severe aerodynamic stresses and rain erosion. These requirements have resulted in a trend toward the use of inorganic materials such as alumina, ceramics, glass, and glass-bonded mica. In the construction of radomes, such materials have been used successfully for some missile radomes, but their mechanical strength is apt to be marginal in certain supersonic applications. As a possible alternative, the properties of slotted metal sheets for radome structures have been investigated. The present study was conducted to determine the electrical properties of metal radomes with empty ($\epsilon = 1.0$) slots. Data are also given on the properties of a dielectric-covered slot.

II. MICROWAVE TRANSMISSION THROUGH SLOTTED METAL PLANE SHEET

In an analysis of the electrical properties of a radome, it is often sufficient to replace the curved radome wall locally by a plane wall of the same cross section. The scattered (reflected and transmitted) waves may then be determined from plane-sheet theory.

A metal sheet with periodically spaced slots exhibits band-pass characteristics in the microwave region. The frequency at which the electromagnetic wave is transmitted with minimum attenuation is determined by the dimension and periodicity of slots (Fig. 1).

If a TEM electromagnetic wave impinging on the slotted metal plane sheet has the electric vector parallel to the narrow side of the slots, the equivalent transmission line model shown in Fig. 2 can be used to represent this scattering system. In the transmission line model, the effect of an obstacle will be to cause part of the impinging energy to be reflected. Therefore, the reflection by the obstacle at a certain frequency can be represented, in the case of lossless obstacles, by a shunt susceptance, B . The expressions for equivalent susceptance of periodically slotted metal sheet can be found elsewhere.^{1,2} The transmission line model reflection coefficient, and transmission³ coefficient can then be calculated (Fig. 2).

Typical curves showing the theoretical transmission coefficient as a function of normalized frequency, ka , are shown in Fig. 3. In this figure, "k" is the wave number, and "a," "b," "c," and "d" are geometric dimension of slots as shown in Fig. 1. These curves clearly indicate the resonance characteristics. Total resonance -- complete cancellation of the reflection of the incident wave by the metal part of the sheet -- is obtained and should be distinguished from the individual slot resonance that may occur at a wavelength approximately equal to the slot circumference. Theoretical and measured transmission losses of slotted metal sheets whose geometrical dimensions are $a/b = 2$, $c/a = 1/2$, $d/b = 1/3$, and $a = 1.5$ inches are plotted in Fig. 4 for normal incidence. Discrepancies between these two curves may be caused by mechanical imperfection of the slots, the non-planar incident wave, and the existence of high-order modes. Transmission characteristics for oblique incidence were also measured for the above-mentioned sheets (Fig. 5). The effect of wave polarization is evident. For normal-polarized waves (E-vector normal to plane of incidence), attenuation increases with the angle of incidence. For parallel-polarized waves, the attenuation decreases as the angle increases. These results agree with the theoretical prediction. 2,3

The simple transmission line model shown in Fig. 2 is applicable to a system in which the medium around the metal sheet is uniform and infinite in extent. However, in practice, the slots must have dielectric inserts to obtain a smooth aerodynamic surface. Thus, the transmission line model must be modified to account for the dielectric, as shown in Fig. 6. Here, the normalized characteristic admittance of free space is Y_0 , and that of the dielectric is Y_1 . The electrical lengths of dielectric layers on each side are represented by ϕ_1 and ϕ_2 . The susceptance, B , is introduced by metal sheet in the same manner as before. The transmission coefficient of this model can be calculated by transmission line theory. 4,5

III. FENESTRATED METAL RADOMES

The slotted metal plane sheet technique was applied to the construction of a full-size nose radome for a Boeing 707 aircraft. The antenna used in the scanning experiments was an AVQ-10 weather radar antenna. As the AVQ-10 is an azimuthal-scanning, horizontally polarized antenna, the slots must be arranged in a meridian-line configuration so that the electric field of the signal is parallel to the narrow side of the slot at all usable scan angles (Fig. 7). The AVQ-10 weather radar was mounted inside the metal radome in a position exactly as it would be in a 707. The antenna is a 30-inch parabolic dish, operating at a center frequency of 5.4Gc. Radiation pattern measurements were taken with the parabolic antenna rotating on its azimuth axis. To simulate different scan angles, θ , the radome was tilted to the desired angle, but the position of the antenna was not changed.

For the construction of a smooth metallic copy of the 707 radome, a production radome was used as a mandrel. Masking-tape, cut to the size of the desired slots, was stuck on the outside surface of the radome and was spaced in a meridian-line configuration. Conducting silver paint was applied to the radome until microwave transmission through the painted radome became negligible (below 40 db). The tape was then removed, leaving an array of slots (Fig. 8). The same radome could be used for other slot dimensions by removing the silver paint, applying different tape sizes, and repainting.

The geometric dimensions used for the radome were $a/b = 2$, $c/a = 2/3$, and $d/b = 1$. The calculated free-space resonance was at $ka = 4.55$. A value of $a = 1.5$ inches was chosen to account for the 20-percent resonance frequency reduction caused by the dielectric. The radome was expected to operate at 4.6Gc.

Antenna patterns with and without the metal radome were taken at 4.0, 4.25, 4.5, 4.875, 5.0, 5.5 and 6.0 Gc (Fig. 9). The frequency of highest transmission efficiency between 4.5 and 4.875 Gc agreed with the calculated frequency of 4.6 Gc. Fig. 10 shows the antenna patterns taken at 4.875 Gc for 0° , 10° , 20° , 30° , 40° , 50° , 70° , and 90° scan-angles. The antenna pattern and the input VSWR were not appreciably modified by the radome; however, the transmission loss was about 1.3 db at 4.875 Gc for all scan-angles. Some of these losses were caused by attenuation in the dielectric.

IV. CONCLUSION

A promising technique has been developed for the construction of fenestrated metal radomes that are transparent to microwaves. Because of unavoidable reflections at an air-metal interface, even the most ingeniously filligreed metal radome will not become perfectly transparent. However, a predominantly metal radome built on these principles should be useful in supersonic aircraft and in applications where strength of metal and microwave transparency are required. It is estimated that such a slotted metal radome will retain 50 percent of the structural integrity of the solid metal sheet; however, the mechanical strength of the slotted metal was not investigated. If a high-strength-at-high-temperature alloy is used, metal thicknesses of $1/8$ to $1/4$ inch should be sufficient even at Mach 2 or Mach 3.

REFERENCES

1. R. Kieburtz and A. Ishimaru, "Scattering by a Periodically-Apertured Conducting Screen", IRE Trans. AP-9, pp. 506-519, November, 1961.
2. C. Chiou, Fenestrated Metal Radomes for Microwaves, Boeing Document D6-9034, June, 1962.
3. L. L. Oh, C. D. Lunden and C. Chiou, "Fenestrated Metal Radomes", Microwave Journal, Vol. 7, pp. 62-66, April, 1964.
4. L. Robinson, Electrical Properties of Metal-Loaded Radomes, Stanford Research Institute, WADD Tech. Report No. 60-84, February, 1960.
5. Montgomery, Dike, and Purcell, Principles of Microwave Circuits, McGraw-Hill

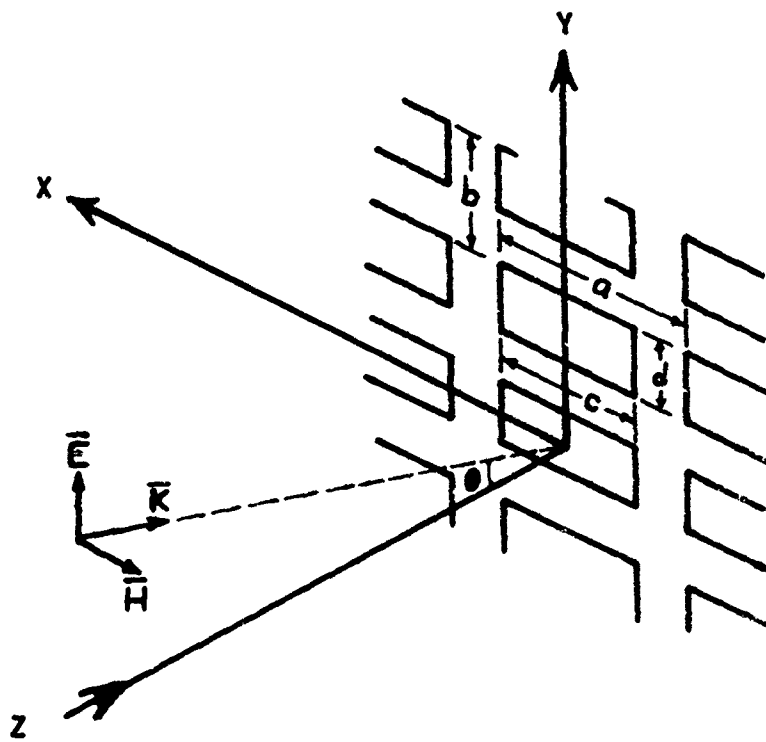
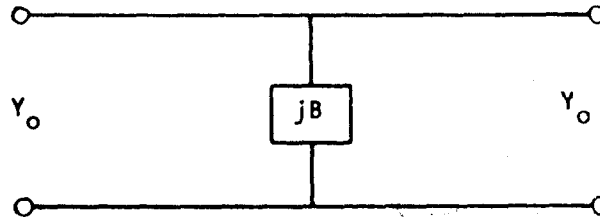


FIG. 1 - SLOTTED METAL SHEET



For Wave Polarized Parallel to the Plane of Incidence

$$B = \cos \theta \sum_{\substack{m=-\infty \\ n=-\infty}}^{\infty} \left[\frac{\frac{kb}{2\pi} \frac{d}{b} \sin \theta}{J_1 \left(\frac{kb}{2\pi} \frac{d}{b} \sin \theta \right)} \right]^2 \left[\frac{J_1 \left(\frac{m\pi c}{a} \right)}{\frac{m\pi c}{2a}} \right]^2 \left[\frac{J_1 \left(\frac{d}{b} \left(n - \frac{kb}{2\pi} \sin \theta \right) \right)}{\frac{d}{b} \left(n - \frac{kb}{2\pi} \sin \theta \right)} \right]^2$$

$$\left[\frac{kb}{\pi \sqrt{\left(m \frac{b}{a} \right)^2 + \left(n - \frac{kb}{2\pi} \sin \theta \right)^2}} \frac{\left(n - \frac{kb}{2\pi} \sin \theta \right)^2}{\left(\frac{kb}{2\pi} \right)^2 \left(m \frac{b}{a} \right)^2 + \left(n - \frac{kb}{2\pi} \sin \theta \right)^2} \right]$$

$$\left[\frac{4\pi \sqrt{\left(m \frac{b}{a} \right)^2 + \left(n - \frac{kb}{2\pi} \sin \theta \right)^2} - \left(\frac{kb}{2\pi} \right)^2}{kb} \frac{m^2}{m^2 + \left(\frac{a}{b} \right)^2 \left(n - \frac{kb}{2\pi} \sin \theta \right)^2} \right]$$

$$Y_0 = \sec \theta$$

For Wave Polarized Perpendicular to the Plane of Incidence

$$B = \sec \theta \sum_{\substack{m=-\infty \\ n=-\infty}}^{\infty} \left[\frac{\frac{ka}{2\pi} \frac{c}{2a} \sin \theta}{J_1 \left(\frac{ka}{2\pi} \frac{c}{2a} \sin \theta \right)} \right]^2 \left[\frac{J_1 \left(\frac{c\pi}{a} \left(m - \frac{ka}{2\pi} \sin \theta \right) \right)}{\frac{c\pi}{2a} \left(m - \frac{ka}{2\pi} \sin \theta \right)} \right]^2 \left[\frac{J_1 \left(\frac{n\pi d}{b} \right)}{\frac{n\pi d}{2b}} \right]^2$$

$$\left[\frac{ka}{\pi \sqrt{\left(m - \frac{ka}{2\pi} \sin \theta \right)^2 + \left(n \frac{a}{b} \right)^2}} \frac{n^2}{\left(\frac{ka}{2\pi} \right)^2 \left(\frac{b}{a} \right)^2 \left(m - \frac{ka}{2\pi} \sin \theta \right)^2 + n^2} \right]$$

$$\left[\frac{4\pi \sqrt{\left(m - \frac{ka}{2\pi} \sin \theta \right)^2 + \left(n \frac{a}{b} \right)^2} - \left(\frac{ka}{2\pi} \right)^2}{ka} \frac{\left(m - \frac{ka}{2\pi} \sin \theta \right)^2}{\left(m - \frac{ka}{2\pi} \sin \theta \right)^2 + \left(n \frac{a}{b} \right)^2} \right]$$

$$Y_0 = \cos \theta$$

Reflection and Transmission Coefficients are given by

$$r = \frac{-jB}{2Y_0 + jB} \quad t^2 = 1 - r^2$$

FIG. 2 - TRANSMISSION LINE MODEL FOR SLOTTED METAL SHEET IN FREE SPACE

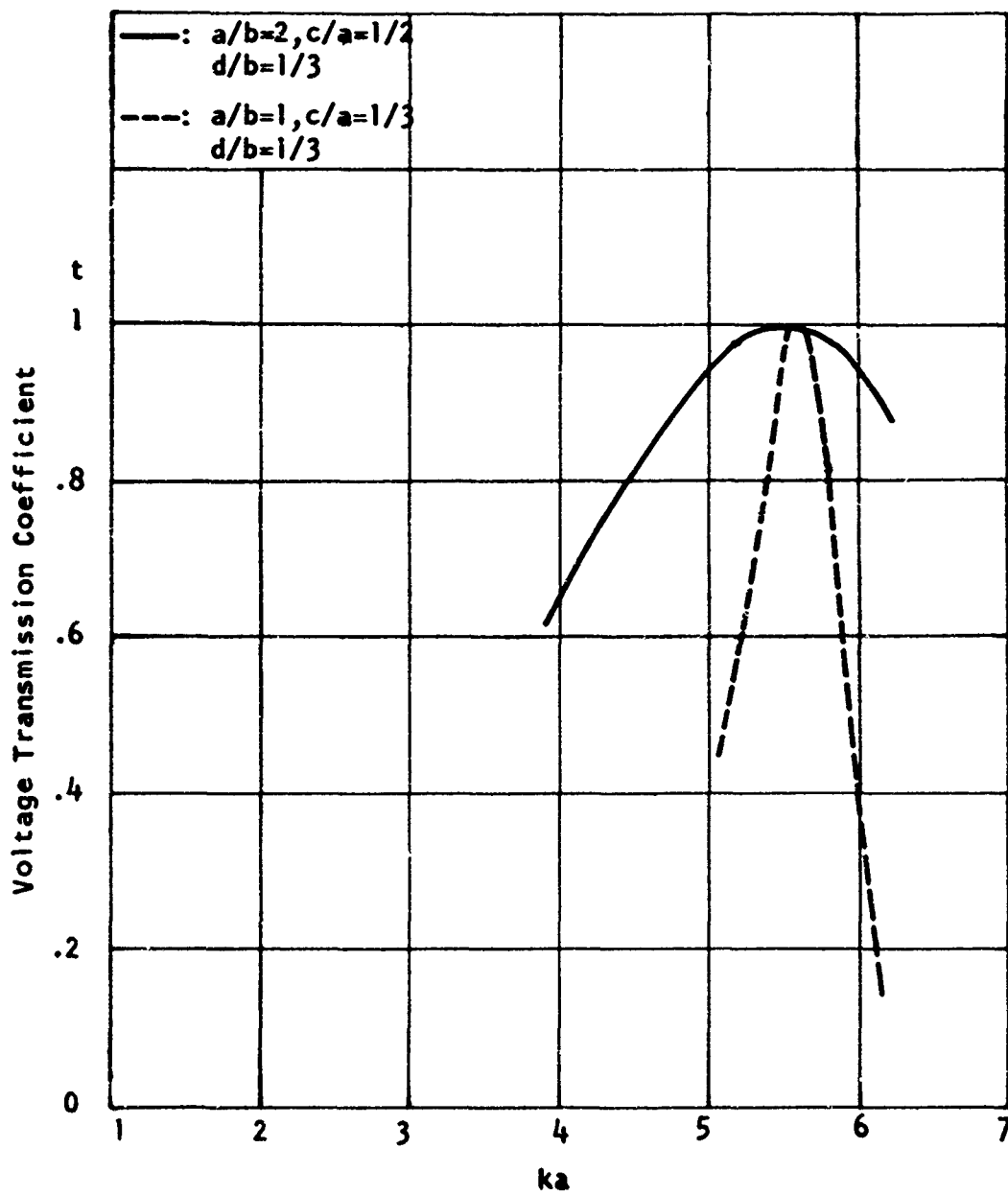


FIG. 3 - CALCULATED TRANSMISSION COEFFICIENT AS A FUNCTION OF KA.

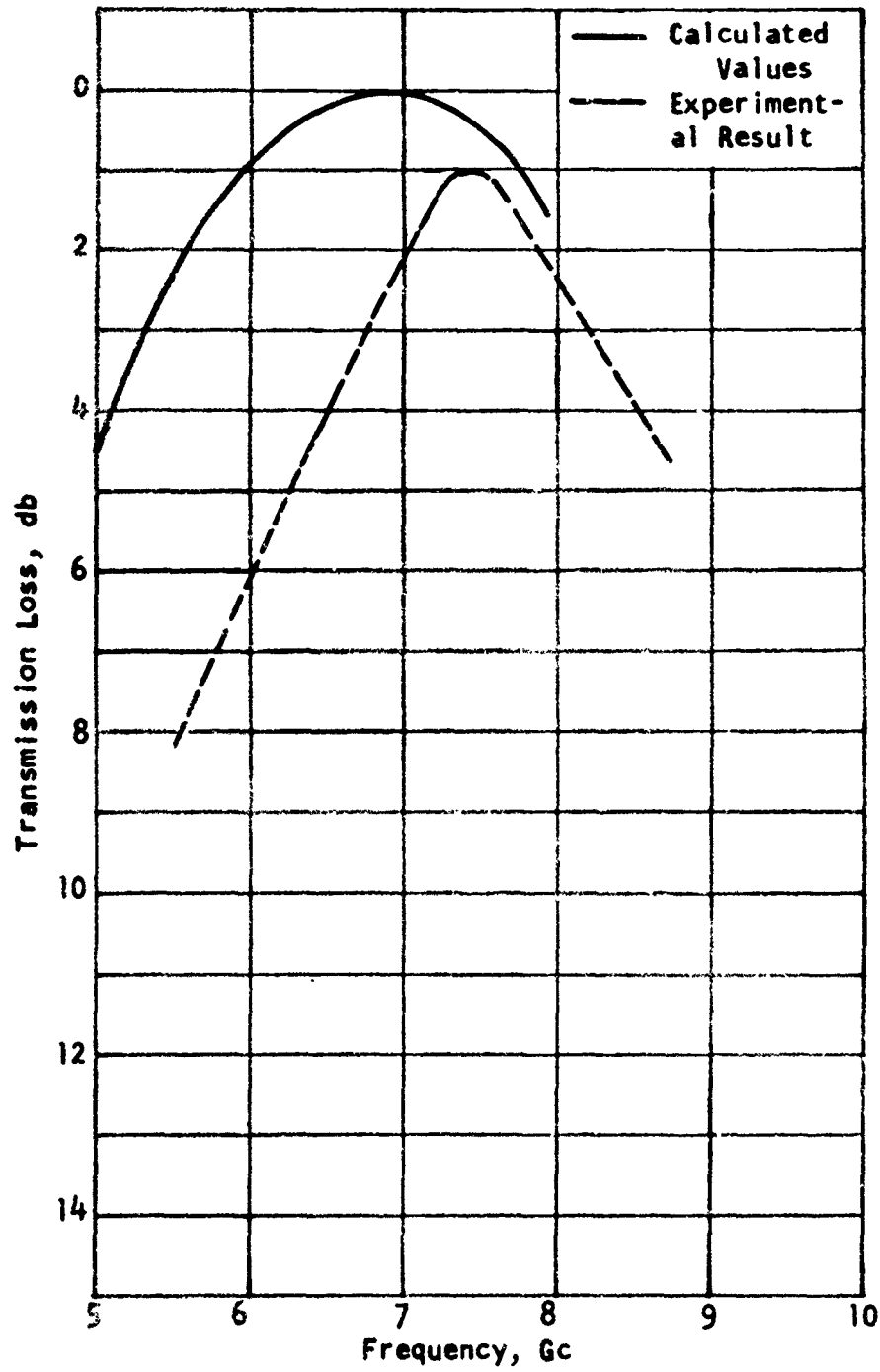


FIG. 4 - TRANSMISSION LOSS AS A FUNCTION OF FREQUENCY (NORMAL INCIDENCE)

$a/b = 2, c/a = 1/2, d/b = 1/3, a = 1-1/2$ inches

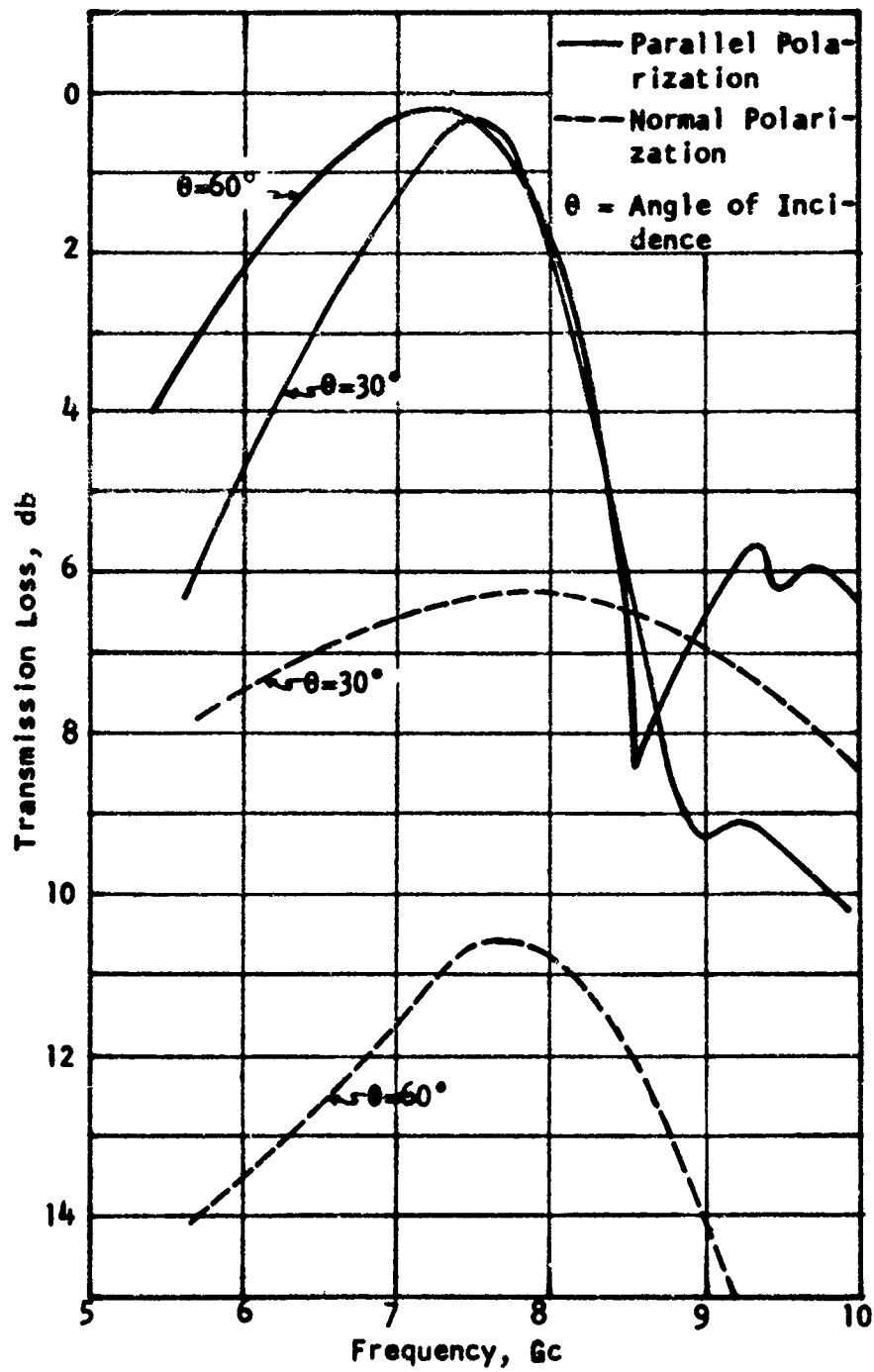
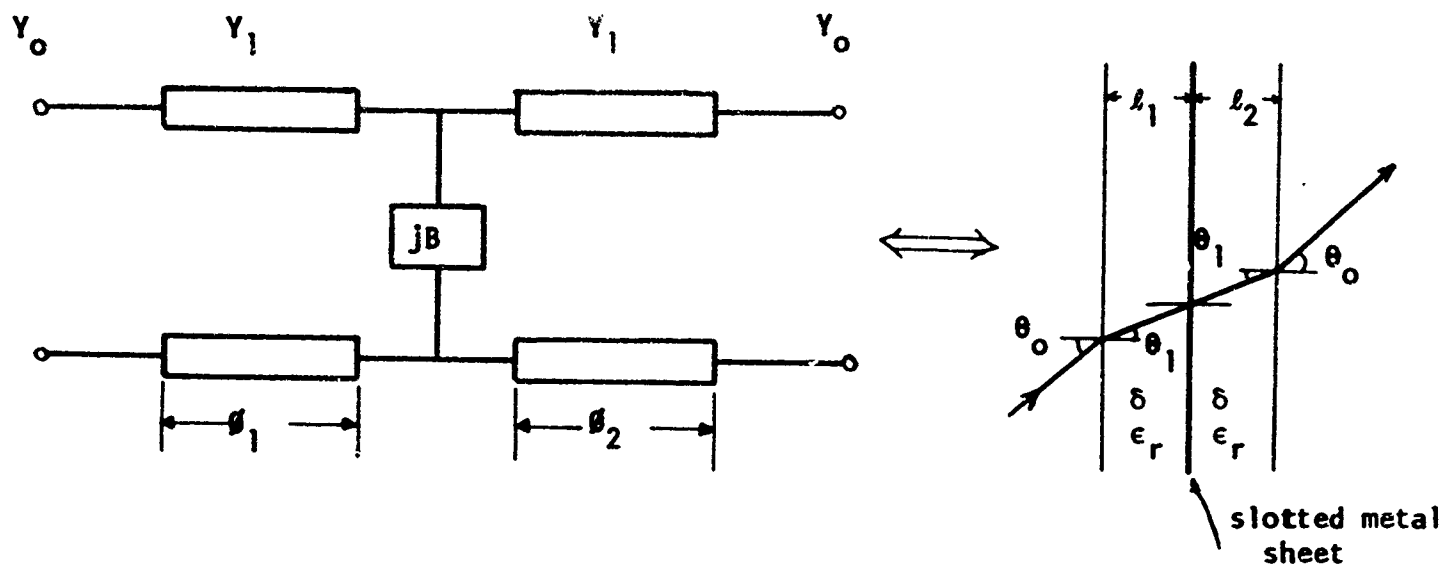


FIG. 5 - MEASURED TRANSMISSION LOSS AS A FUNCTION OF FREQUENCY (OBLIQUE INCIDENCE)

$a/b = 2$, $c/a = 1/2$, $d/b = 1/3$, $a = 1-1/2$ inches



ABCD matrix of the transmission line model of dielectric covered slotted metal sheet,

$$\begin{pmatrix} A & B \\ C & D \end{pmatrix} = \begin{pmatrix} \cosh \gamma l_1 & \frac{\sinh \gamma l_1}{Y_1} \\ Y_1 \sinh \gamma l_1 & \cosh \gamma l_1 \end{pmatrix} \cdot \begin{pmatrix} 1 & 0 \\ jB & 1 \end{pmatrix} \cdot \begin{pmatrix} \cosh \gamma l_2 & \frac{\sinh \gamma l_2}{Y_1} \\ Y_1 \sinh \gamma l_2 & \cosh \gamma l_2 \end{pmatrix}$$

For parallel-polarized waves

$$Y_0 = \sec \theta_0 \quad Y_1 = \sqrt{\epsilon_r} \sec \theta_1$$

For normal-polarized waves

$$Y_0 = \cos \theta_0 \quad Y_1 = \sqrt{\epsilon_r} \cos \theta_1$$

Where

$$\gamma l_i = \alpha l_i + j \beta_i$$

$$\beta_i = \frac{2\pi l_i \cos \theta_1}{\lambda_d}$$

$$\alpha = \frac{\pi \tan \delta}{\lambda_d \cos \theta_1}$$

$$\frac{\sin \theta_1}{\sin \theta_0} = \frac{1}{\sqrt{\epsilon_r}}$$

transmission coefficient is given by

$$t^2 = \frac{4}{|A + BY_0 + C/Y_0 + D|^2}$$

FIG. 6 - TRANSMISSION LINE MODEL OF DIELECTRIC - COVERED SLOTTED METAL SHEET.

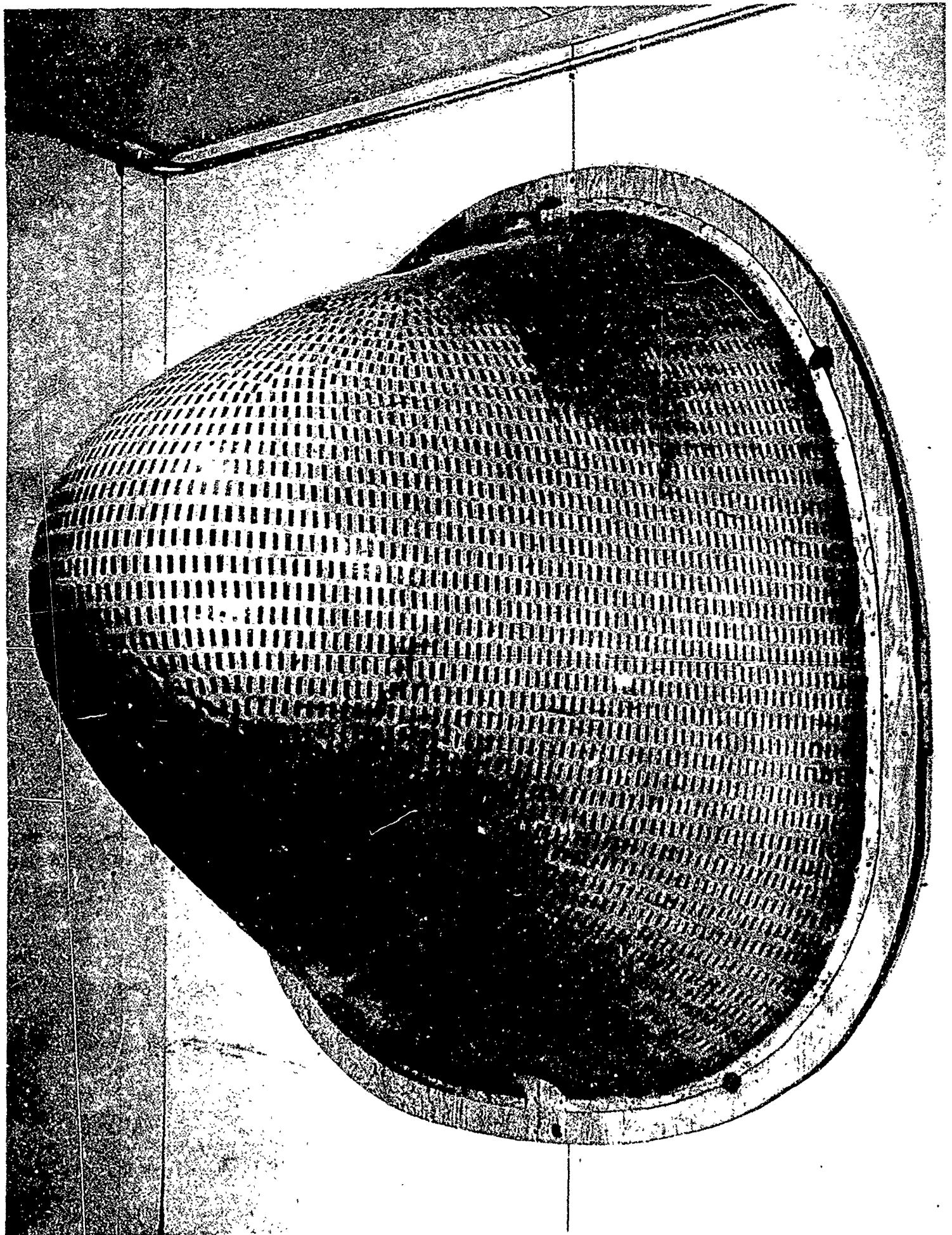


FIG. 8 - SILVER SLOTTED RADOME (707)

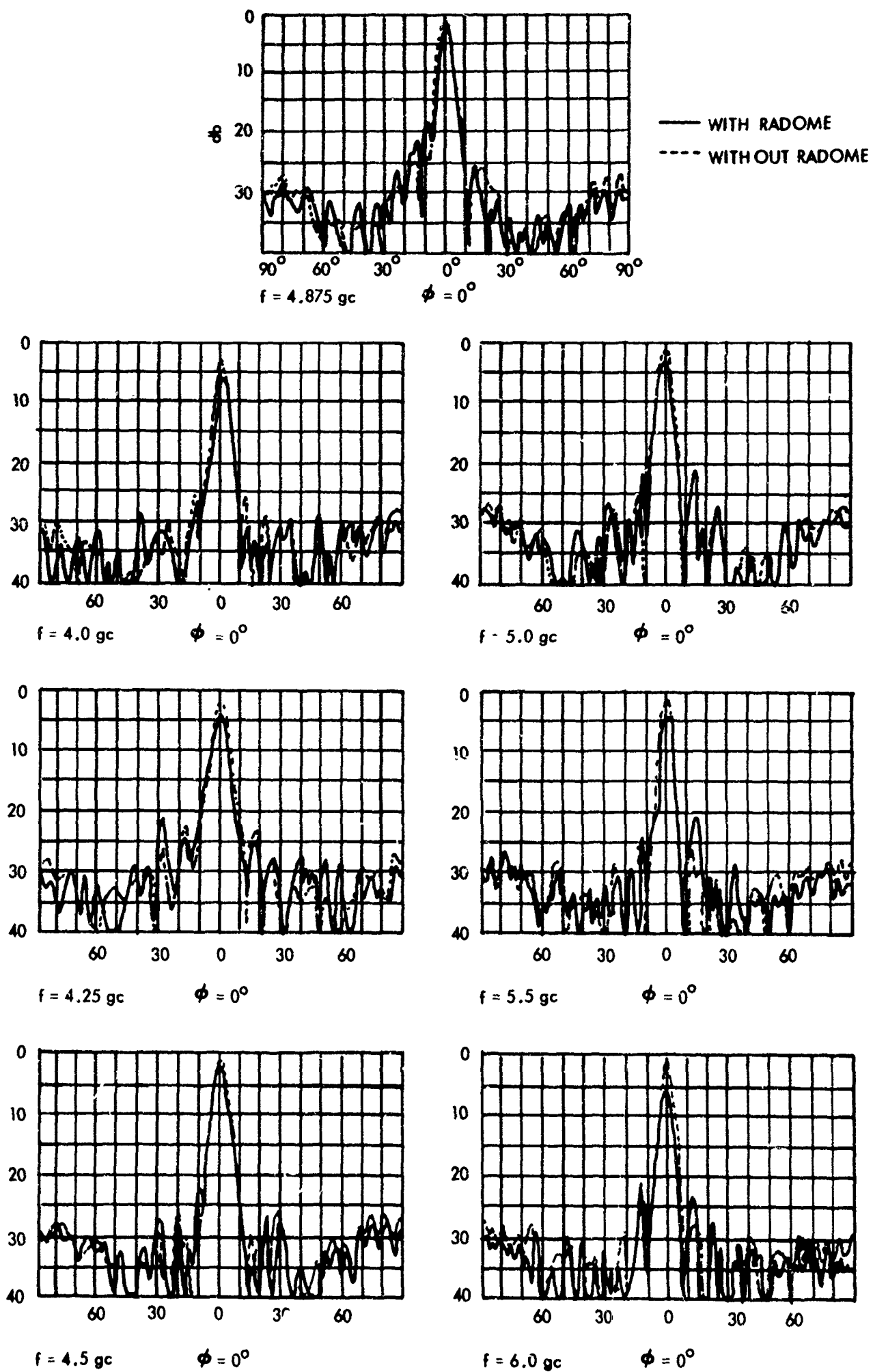


FIG. 9 - ANTENNA PATTERNS OF THE METAL RADOME TAKEN AT SEVERAL FREQUENCIES.

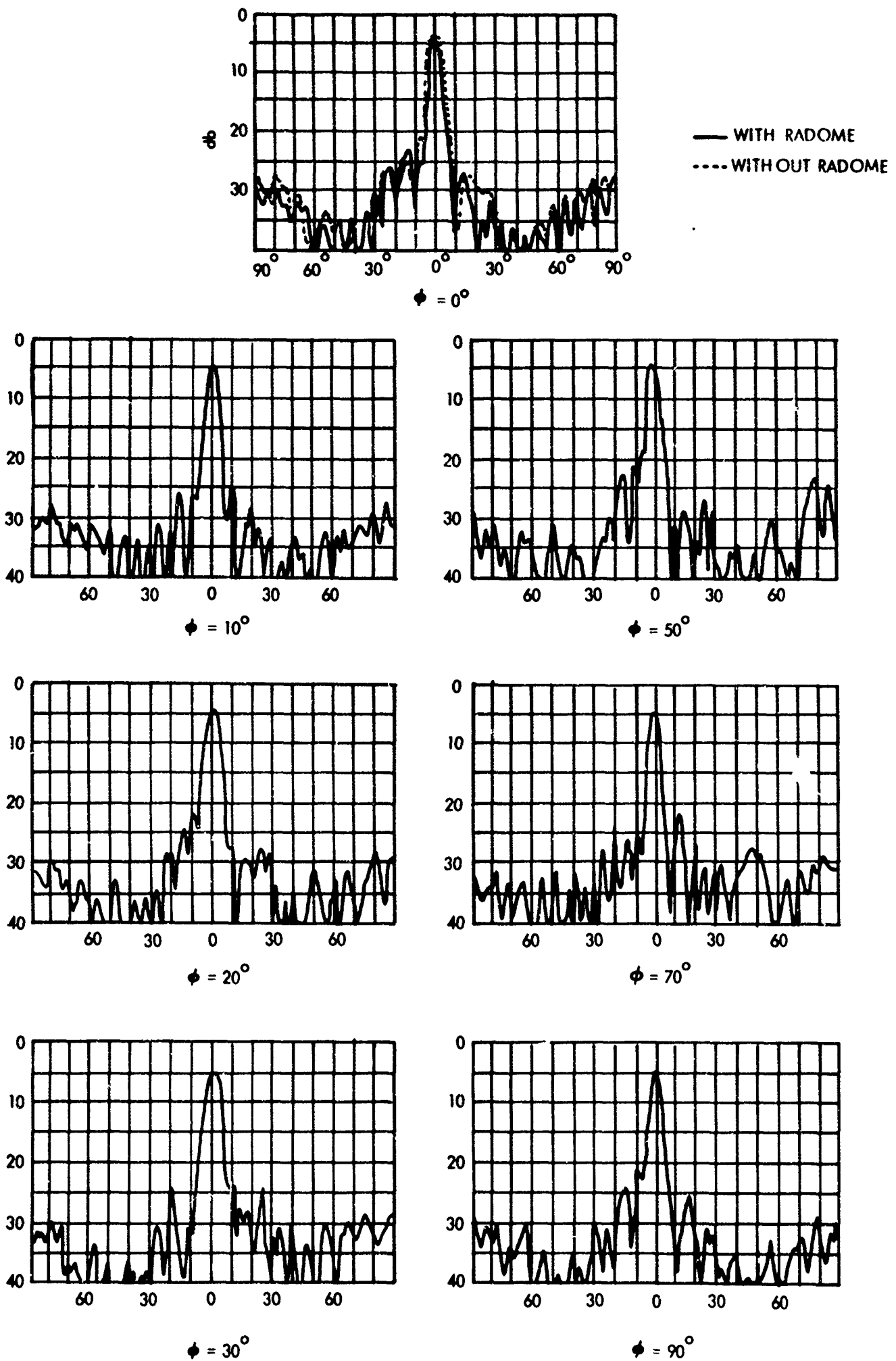


FIG. 10 - ANTENNA PATTERNS OF THE METAL RADOME AT 4.875 GC TAKEN AT DIFFERENT SCAN ANGLES, ϕ

ANTENNA RADOME-GRATINGS
for
CONICAL SCAN SYSTEMS

May 1964

Author: A. H. Schaufelberger
Engineering Staff Consultant

SPERRY MICROWAVE ELECTRONICS COMPANY
Division of Sperry Rand Corporation
Clearwater, Florida

SPERRY PIEDMONT COMPANY
Division of Sperry Rand Corporation
Charlottesville, Virginia

Contract Number SP 51327
SF 53712

Antenna Radome - Gratings for Conical Scan Systems

INTRODUCTION

The results reported in this paper were performed under a contract from Sperry Piedmont Company for a Navy program administered by the Applied Physics Lab of John Hopkins. Because of the unclassified nature of this symposium, certain details of the antennas used and the results obtained are omitted from this presentation.

The requirement for a polarization grating or filter originated with acquisition problems which had been encountered with vertically polarized conical-scan radars. In these antennas power modulation is employed to reduce low angle scatter return. The result of this type of modulation is the production of a depressed null axis which is not coincident with the axis of the paraboloid and results in the introduction of a significant amount of cross polarization on the depressed null axis. In working with a target which employs an antenna which is nominally circularly polarized, the modulation of the cross polarization component produced a shift in the indicated null position of approximately 10 mils from the true null or boresight. This null shift was a function of the departure of the polarization of the target antenna from the ideal circular condition and varied with target orientation and from one target to another.

Since redesign of the target antenna was not an acceptable solution, one alternative was the suppression of the cross polarized component in the radar system antenna. When APL sponsored tests with a breadboard grating showed a substantial decrease in boresight shift, a contract was awarded to Sperry Microwave for the design, development and subsequent production of polarization gratings capable of surviving and operating in a shipboard environment.

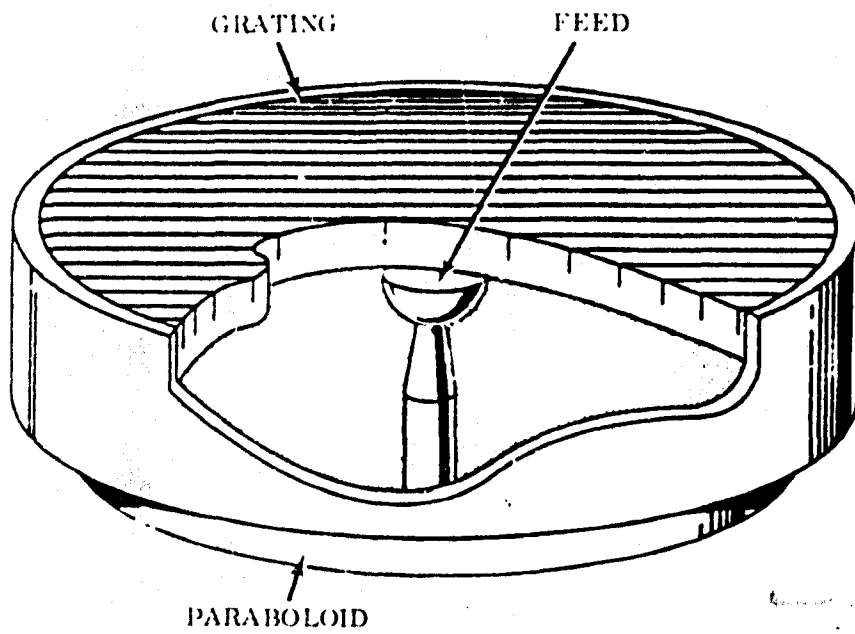
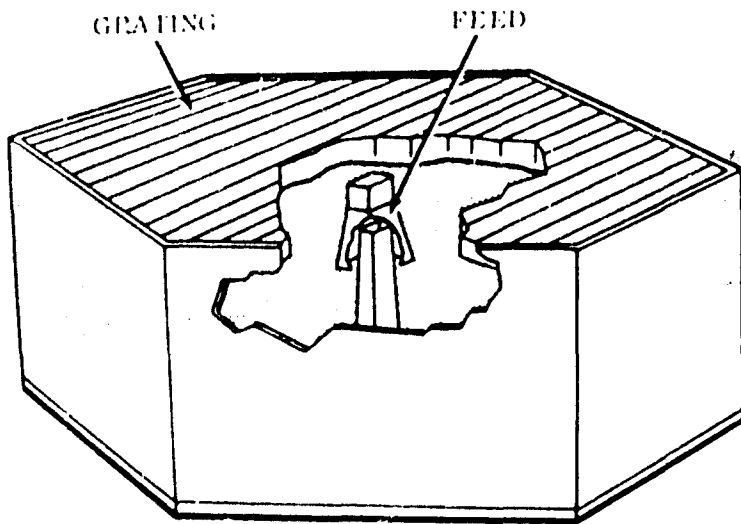


Figure 1 GRATING CONFIGURATIONS SCANNING ANTENNAS "A" & "B"

In this paper are described the radome-grating configurations which were developed to provide dual functions of environmental protection of the antenna and rejection of the orthogonally polarized component of the signal. Primary design goals, relative merits of different types of gratings and test results are discussed.

The gratings were designed for two different antenna configurations which were similar electrically but differed in reflector contour shape due to different approaches used to obtain the desired pattern characteristics. The grating configurations used are shown schematically in Slide No. 1. The top configuration for scanning antenna "A" has been dubbed the "sarcophagus" for obvious reasons. The bottom configuration is a cylindrical configuration for a standard paraboloid. These configurations will be discussed in more detail later in the talk.

The following requirements were used as design objectives in the development of the antenna gratings:

- 30 db rejection of the component of incident energy orthogonal to the desired polarization orientation.
- First sidelobe of antenna and grating combination to be at least 25 db below the main lobe.
- Modulation slopes of the antennas without grating to remain unchanged upon addition of grating.
- Requirement of 3 1/2 degrees of power modulation to remain unchanged upon addition of grating.
- Insertion loss not to exceed 1/2 db.
- VSWR to remain within original antenna specifications.
- Protection of the projecting feed if consistent with the other objectives

The tendency to use the projecting feed for a handhold when climbing around the antenna during maintenance made the last objective advisable.

TECHNICAL DISCUSSION

In investigating methods for the suppression in a linearly polarized system of energy polarized in a sense orthogonal to the desired polarization, several configurations were considered. Included in these were a grating integral with the antenna reflector. All of these configurations utilize the attenuation and/or reflecting properties of a parallel plate system in which the plate spacing is small enough to be in the cutoff condition for energy whose electric vector is oriented parallel to the plate. The attenuation, A , of such a system is given by the equation

$$A = 54.5 d/W_0 \left[1 - (W_c/W_0)^2 \right]^{\frac{1}{2}} \text{ db} \quad (1)$$

In this equation, d is the length of the parallel plates in the direction of propagation, W_0 is the free space wavelength, and $W_c = 2a$ is the cutoff wavelength where a is the plate spacing.

In evaluating the relative merits of the different configurations, the following factors were considered:

- Efficiency of Suppression
- Fabrication Complexity
- Development Time
- Over-all Cost

THE FEED GRATING

In this configuration, a grating is placed over the feed unit proper with the plates oriented normal to the desired sense of polarization. For the feed configuration used, this grating would be in two sections arranged on either side of the circular waveguide input to the unit feed. In order to achieve the desired 30 db of additional isolation for the undesired polarization, a plate spacing, a , of one-fourth wavelength is used in conjunction with a plate

length, d , of 0.32 wavelength. Substitution of these values in equation (1) gives a value of 30.2 for the resultant attenuation.

The advantages of the feed grating are its small size, ease of fabrication, and low costs. The main disadvantage is the need for rebalance of the dynamic system due to the additional mass at the end of the feed. In addition, the required rejection of polarization would be obtained only in the feed proper. Introduction of the undesired cross polarization component from irregularities in the reflector and the off-axis location of the feed point inherent in the scan system and scattering caused by the feed itself in the field of the antenna could not be compensated for by such a grating.

GRATING OVER ENTIRE APERTURE

The grating over the entire aperture could assume any of four configurations. The first is a plane grating over the aperture and in a plane containing the antenna periphery. In the center of the grating a circular hole is located to accommodate the waveguide feed structure. The second configuration is a plane grating located beyond the feed and supported by a cylindrical structure. A third possibility is a grating with a conical configuration attached at the antenna periphery and encompassing the feed structure. Finally, there is the grating with a hemispherical configuration attached at the antenna periphery and encompassing the feed. In all cases, the plates are oriented normal to the desired polarization and spaced approximately one-fourth wavelength.

Discussion of these configurations will be limited to the final three configurations.

PLANE GRATING BEYOND FEED UNIT

This configuration utilizes a plane grating supported by a cylindrical shell. The grating consists of a series of straight parallel aluminum plates

spaced approximately one-fourth wavelength apart and supported in a slotted styrofoam structure. The entire structure is covered with a thin epoxy-fiber glass laminate for mechanical protection and for strength forming a cylindrical structure approximately 2 inches thick.

As a support for this grating assembly a cylindrical shell is used. This shell consists of styrofoam cores sandwiched between two layers of epoxy-fiber glass laminate. The shell is bonded by epoxy to the grating structure and fastened mechanically to the periphery of the paraboloid.

The configurations which result from the combination of grating and support for scanning antennas "A" and "B" were shown in Slide No. 1.

CONICAL GRATING

The conical grating configuration shown in Slide 2 consists of a series of parallel plates spaced one-fourth wavelength and supported in a styrofoam structure reinforced with epoxy-fiber glass laminate. Since the plates are parallel to the axis of the cone, they will have a hyperbolic contour in the elevation plane. The feed is contained within the boundaries of the cone which is fastened at its base to the paraboloid.

The effective length, l_e , of a grating composed of parallel plates in a conical configuration is given by the equation

$$l_e = d - a \tan \theta \quad (2)$$

In this equation, d , is the length of the plates in the direction of propagation a is the spacing between the plates, and θ is the angle between the plane of the antenna aperture and the side of the cone.

From equation (2), it is evident that the required plate length d is given by the equation

$$d = l_e + a \tan \theta \quad (3)$$

Since the same effective plate length, $0.32W_0$, and spacing, $0.25W_0$ would be required for the conical grating as for the plane grating, the required plate length is then

$$d = l_0 + a \tan \theta = W_0 \left[0.32 + 0.25 \tan \theta \right] \quad (4)$$

In order to encompass the feed structure, the value of θ is approximately 33° , then

$$d = W_0 \left[0.32 + 0.25 \tan \theta \right] = 0.46 W_0 \quad (5)$$

HEMISPHERICAL GRATING

The hemispherical grating would be composed of a series of metal plates parallel to the axis of the paraboloid and to one another. These plates would have a circular contour and be supported in a styrofoam structure which would be reinforced with an epoxy-fiber glass laminate. As in the case of the conical grating, the base of the hemisphere would be fastened to the periphery of the paraboloid.

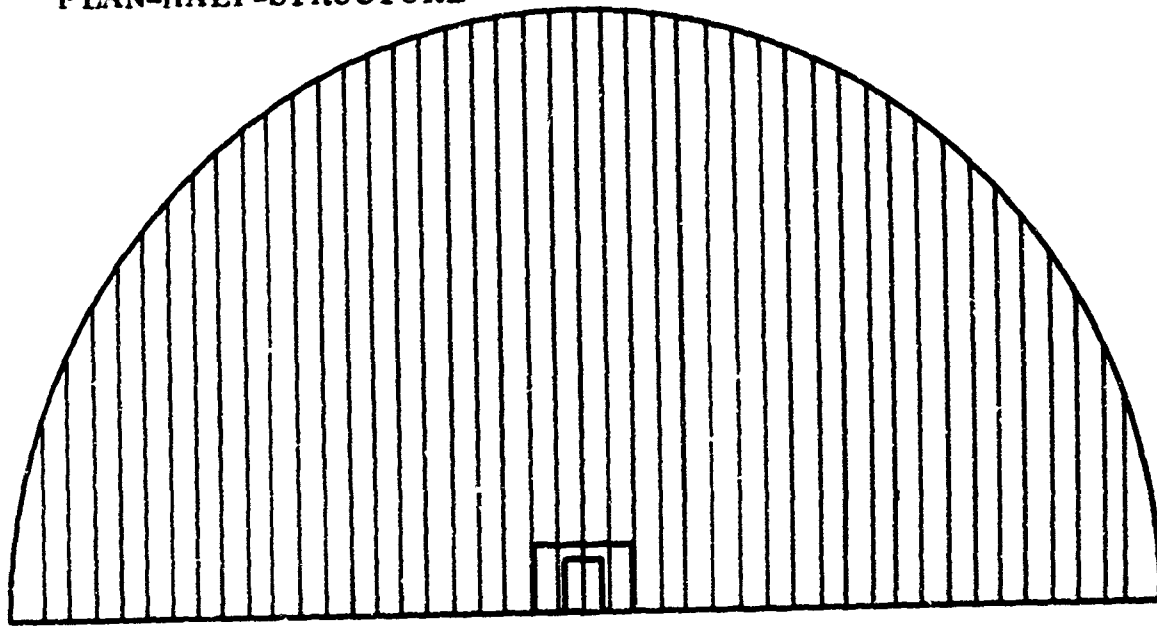
THE GRATING = REFLECTOR

The integral type of grating consists of a reflector composed of a system of parallel plates whose inner configuration is paraboloidal. The plates in this type of grating would be arranged parallel to the desired sense of polarization which would be essentially completely reflected. The undesired orthogonal polarization would be transmitted through the grating. In order to prevent reflection and retransmission of this component back through the grating, a highly efficient absorber would be located behind the grating reflector.

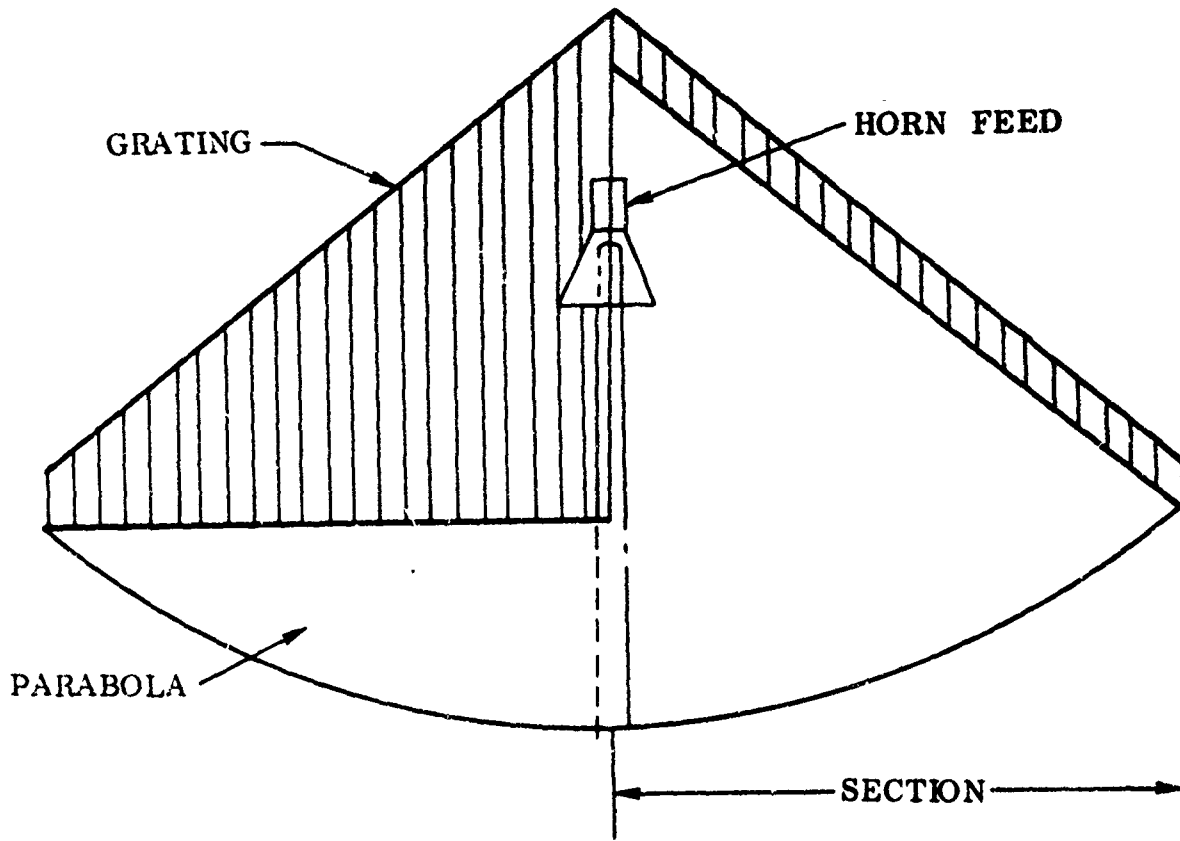
CHARACTERISTICS OF GRATINGS

In comparing the relative merits of the grating configurations discussed in previous sections, the chief factors involved were suppression efficiency,

PLAN-HALF-STRUCTURE



E VECTOR →



1133B

Figure 2 CONICAL GRATING ON PARABOLA

fabrication complexity, development time and overall cost.

The advantages of the plane grating over the aperture and in the plane of the aperture are the simplicity of structure and the relative ease of mounting. Cross polarization components originating in the paraboloid itself are virtually eliminated by this configuration. The disadvantages are primarily electrical. The cross polarization component originating in the feed is almost completely reflected by the grating and will appear in the far field as will the cross polarization component caused by scattering from the feed itself.

The plane grating over the aperture and outside the plane of the feed has the advantage that all cross polarization components regardless of origin must pass through and be attenuated by the grating. In addition, the configuration in itself is relatively simple to construct and provides protection for the feed. The disadvantage lies in the somewhat lower inherent strength of the required mounting structure as compared to the other structures considered.

The conical grating configuration has the same electrical advantages as the plane grating over the aperture and outside the plane of the feed horn. In addition, it is inherently a stronger and more rigid structure than the plane grating and would be more easily mounted. The primary disadvantage is the complexity of fabrication compared to the plane grating structure.

The hemispherical grating configuration has the same electrical advantages as the plane grating outside the feed horn plane and the conical grating. It is somewhat stronger than the conical grating and would be as easily mounted. The fabrication complexity is somewhat less than that of the conical grating because of the circular contour of the parallel plates as compared to hyperbolic contour of the plates in the conical grating. However, as compared to the plane grating, fabrication still presents rather difficult problems.

The advantages of the integral grating-reflector structure are the combination of the reflector and grating into one compact unit and the virtual elimination of the cross-polarization present in the antenna feed. The disadvantages are several. In the first place, cross-polarization resulting from scattering by the feed of energy reflected from the paraboloid would be unaffected by this grating. In addition, the cross-polarization component resulting from the offset position of the feed in scanning and the curvature of the reflector would likewise be unaffected. From a fabrication standpoint, the grating-reflector presents rather complex fabrication problems and would also necessitate the scrapping of the existing antenna structures.

SELECTED GRATING CONFIGURATIONS

At the beginning of the development program for the antenna grating, the most suitable configuration from both electrical and mechanical standpoints seemed to be the hemispherical structure. However, early in the program, the problems envisaged in the fabrication of this configuration did not lessen in difficulty after closer examination. It also became apparent that essentially the same problems would be encountered in successive fabrications so the production units would not be significantly easier to fabricate or less expensive than the prototype. The same conclusion was reached for the conical structure. At this point the simplicity involved in the design of a plane grating appeared even more attractive than it did originally since the use of cylindrical support structure provided adequate strength for the overall configuration. In view of these considerations, the plane grating beyond the aperture was selected for scanning antenna "A" with the final configuration appearing as shown in the upper figure of Slide 3. The initial results achieved with this configuration led to adopting the same type for antenna "B" particularly in view of the symmetry of the antenna itself. The final configuration for this system is shown in the lower figure in Slide 3.

In both gratings, a center to center plate spacing of $1/2''$ was employed with a plate thickness of $0.020''$ thus providing a nominal guide width of $0.480''$. A plate depth of $3/4''$ was employed in both gratings. Utilizing these figures in equation (1), a minimum attenuation of 37 db is obtained at the low frequency end of the band. The grating construction is shown in cross section in Slide 4.

TEST SET UP

The test set-up for the grating measurements was much more critical than for conventional antenna measurements due to the low level of the cross polarization component to be measured. A portion of the test set up was evolved during the first stages of testing as extraneous sources of radiation became apparent. One such source was the power source itself located at the foot of the transmitting tower. Shielding of this entire unit was required to prevent cross polarization pickup.

A second major source of interference at levels of measurement 45 db or more below the main lobe peak was ground reflection from the antenna sidelobe structure. This interference was eliminated by the use of metallic fences at several points along the ground on a plane containing the axes of transmitting and receiving antennas.

TEST PROGRAM

The test program consisted of the evaluation of the antenna pattern characteristics for both dominant and cross polarizations, measurement of modulation slopes and VSWR and measurement of boresight shift with various test antennas.

The evaluation of antenna patterns for the dominant polarization, measurement of modulation slopes and VSWR were of secondary importance to the evaluation of cross polarization characteristics and the boresight shift measurements.

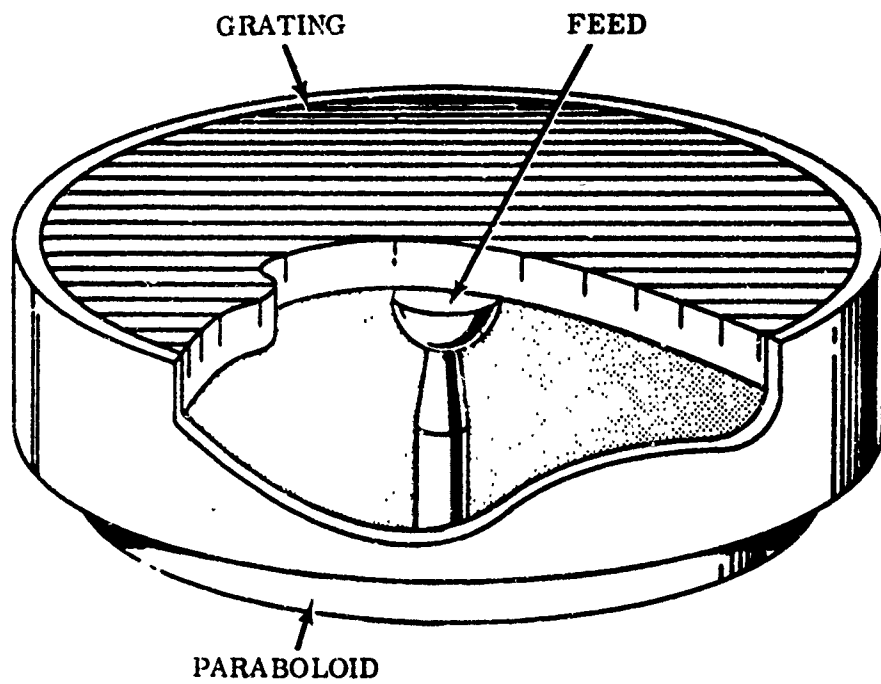
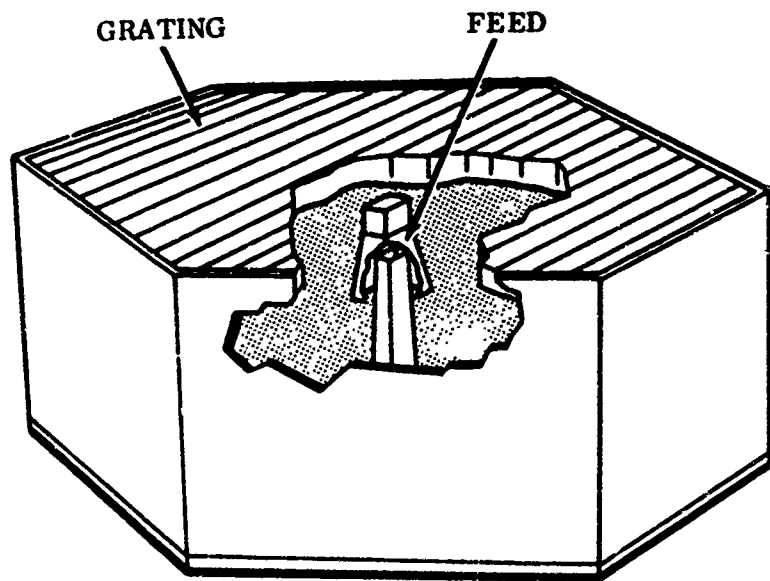


Figure 3 GRATING CONFIGURATIONS SCANNING ANTENNAS "A" & "B"

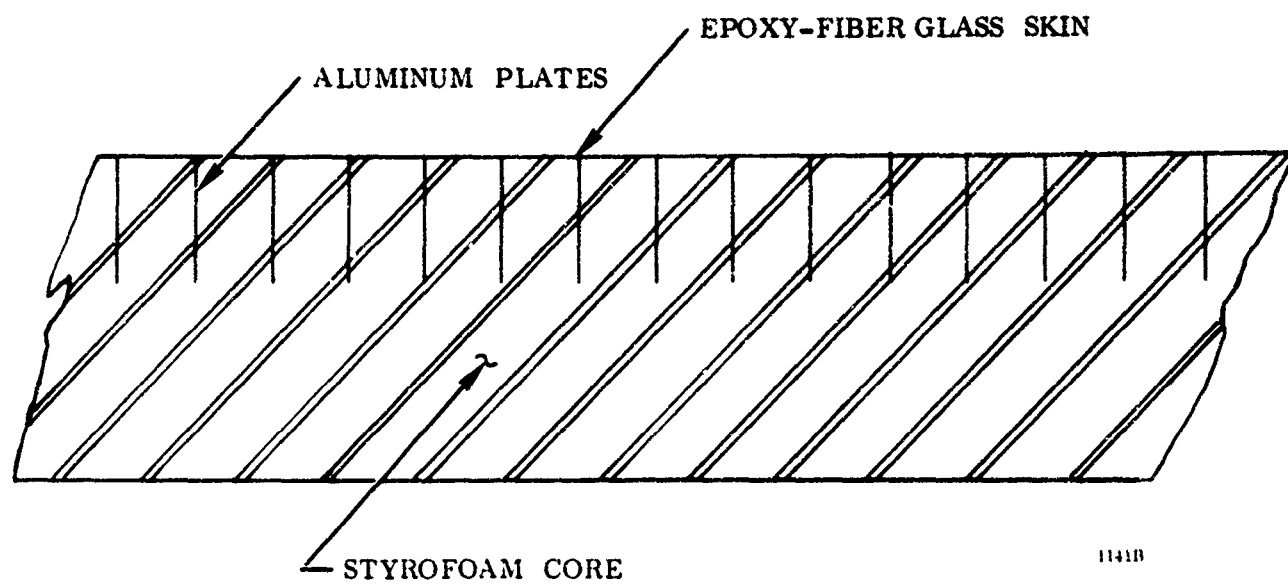


Figure 4 CONSTRUCTION DETAILS OF GRATINGS

These measurements were required, however, to assure that the basic antenna characteristics were not adversely affected by the addition of the grating. For this reason the measurements relating to these characteristics will not be discussed. For clarification of the terms involved in the discussion, a typical pattern set is shown in Slide 5.

The two solid curves are elevation patterns obtained for the feed in the up or 270° position and in the down or 90° position. These patterns form the normal vertical crossover pattern with the crossover point located on the antenna axis. A similar set of patterns is obtained in the horizontal plane. The dashed pattern represents the lower beam when power modulation is applied to produce a null depressed below the antenna axis. The term modulation slope refers to the difference in level between the upper and lower beams at any angle off either the normal crossover axis or the depressed null axis.

TEST RESULTS

Initial laboratory measurements of a prototype grating showed an attenuation of a proximately 38 db at the center frequency with the plates oriented parallel to the incident E vector. The first range measurements made showed the same attenuation when working with the dominant polarization. However, when working with the cross polarized component, the expected composite axial ratio of grating and antenna was not realized.

Typical plots of the cross polarization component in the vicinity of the depressed null axis with and without grating are shown in Slide 6. These plots were taken with the feed rotating in order to provide an average value of the cross polarization component through the scan cycle. The most notable improvement in polarization characteristics occurs off axis at the peaks of the cross polarization lobes. The relative y small improvement of 9 db in the cross polarization ratio on axis was later found to be due to a combination of leakage

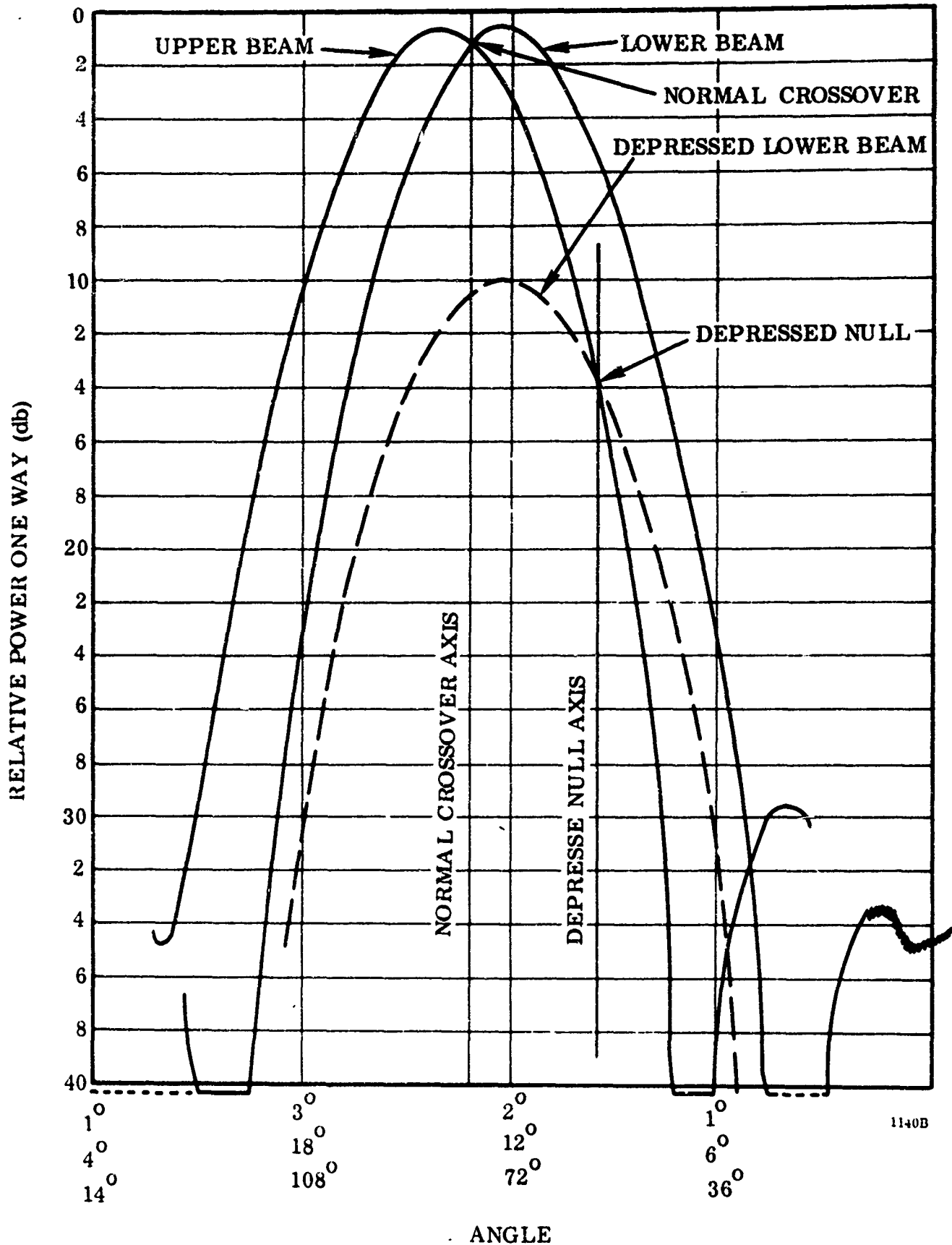


Figure 5 TYPICAL CROSSOVER PATTERNS

around the transmission grating and leakage in the waveguide output of the antenna under test. However, a much more important characteristic in evaluation of the grating performance was the amount of boresight shift with and without the grating. The results of the measurements made of this characteristic are shown in Slide 7. A waveguide horn antenna was used for the reference standard. Two different types of target antennas were compared to this standard. The first antenna was a pair of crossed dipoles in a typical installation mock-up. The second was a helical antenna also installed in a typical mock-up. The departure of the helical antenna characteristics from the ideal circularly polarized antenna is indicated by the change in boresight readings with antenna rotation when no grating was installed on the test antenna. The degree of effectiveness of the grating may be judged from the fact that no measurable boresight shift could be observed with the grating in place for either the crossed dipoles or for the helix in any orientation. These readings were obtained before the polarization leakage problem had been corrected. It is obvious, however, that no improvement in boresight shift reduction could be expected over that shown in this slide.

In summarizing, the fundamental objective of the program, virtual elimination of boresight shift was attained. In accomplishing this objective, the sidelobe level of the antenna-grating combination was increased slightly over the frequency band but remained below the design goal level. Grating insertion loss and VSWR were less than the design goals specified. In addition, protection of the vulnerable feed was provided by the radome-grating configuration.

Shipboard tests of the antenna-grating combinations developed on this program showed that target acquisition was much more readily accomplished with the modified units.

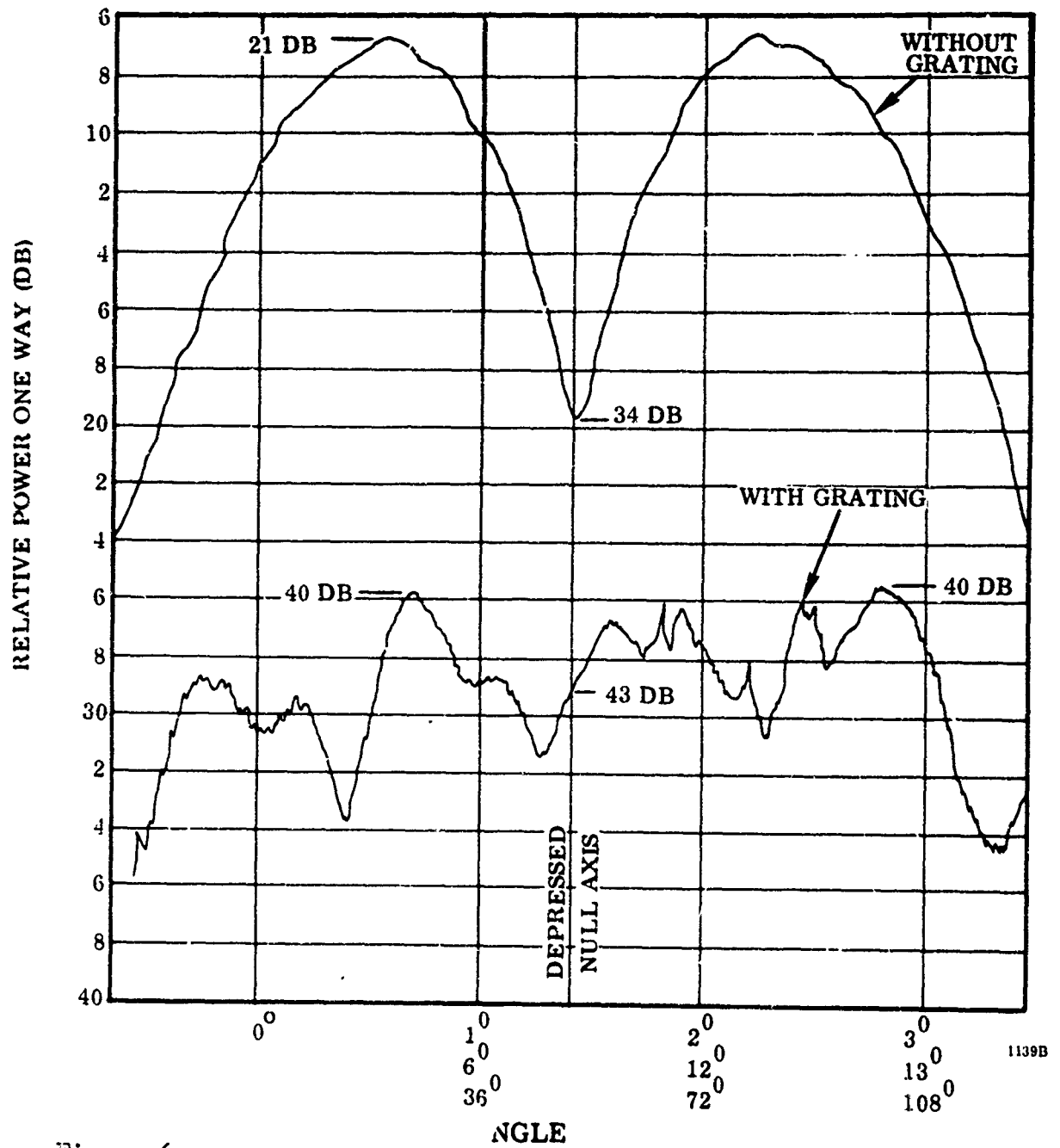


Figure 6 TYPICAL CROSS POLARIZATION PATTERNS

CONICAL SCANNING ANTENNA "A"
BORESIGHT SHIFT MEASUREMENTS
DYNAMIC-FEED NUTATING AT DEPRESSED NULL

WITH GRATING W. G. PROTOTYPE
WITHOUT GRATING W. O. G

TABLE - V		CAPTURE ANTENNA SETTING			
CENTER FREQ.		WITHOUT GRATING		WITH GRATING	
ANTENNA	ORIENTATION	AZIMUTH	ELEVATION	AZIMUTH	ELEVATION
WAVEGUIDE HORN	E PLANE VERTICAL	0°	0°	0°	0°
CROSSED DIPOLES	IN TARGET ASSEMBLY	0.3°CW	0.1°UP	0°	0°
HELIX	* 0°	0°	0°	0°	0°
	45°	0.6°CW	0.2°UP	0°	0°
	90°	0.3°CW	0.1°UP	0°	0°
	135°	0.1°CW	0°	0°	0°
	180°	0.25°CW	0°	0°	0°
	225°	0.3°CW	0°	0°	0°
	270°	0.5°CW	0.1°UP	0°	0°
HELIX	315°	0.4°CW	0°	0°	0°

* 0° Setting Corresponds to Vertical Orientation of the Input End of the Spiral

UP- Antenna Beam Elevated

C, W - Antenna Beam Rotated Clockwise

Figure 7

BORESIGHT SHIFT MEASUREMENTS

1144b

WIDE BAND ECM RADOMES ON HIGH PERFORMANCE AIRCRAFT

by

J. F. Harder/ W. P. Guarino
Grumman Aircraft Engineering Corp.
Bethpage, New York

INTRODUCTION

Grumman has recently completed a radome program for housing, sophisticated, wide-band system antennas on a modified production airplane. This paper traces the development of the complex radome program through the successive phases of concept, design, fabrication and test. The radomes designed and manufactured for this program are the result of an application of the theoretical, computer optimization techniques presented at the 1962 O. S. U. symposium. The severe confrontation of structural/ aerodynamic/ and electronic problems encountered on this program and highlighted in this paper serves to emphasize the need for parallel development of systems and materials for airborne applications.

CONCEPT: Modification Of A Production Airplane

A production airplane was modified for installation of a complement of sophisticated electronic equipment. The modifications to the airframe included lengthening the fuselage eight inches to obtain additional space for equipment compartments and a complete redesign of the wing and vertical fin structure to accept the mounting of large pod shaped radomes.

Three pods were required to house externally mounted, large form factor, antenna systems which were designed to have 360 degrees, azimuthal coverage. The radome pods were located under each wing and the third, on top of the vertical fin. Each of these pod radomes had to be designed to pass a broad spectrum of electromagnetic energy within severely restraining structural and aerodynamic requirements.

The shape and dimensions of the left and right wing pod radomes were made identical to assure aerodynamic stability; while the shape selected for the fin radome had to maintain the control stability and effectiveness of the rudder. The basic production airplane is shown in Figure (1). Figure (2) shows the airplane after all modifications have been completed and the pod radomes have been installed.

RADOME SHAPE: Aerodynamic Smoothness and Stability

The size and shapes of the radomes were greatly influenced by the antenna form factor, space required for accessory equipment and the streamlining required to assure compliance with the performance profile of the airplane. Preliminary layouts of the radomes were contoured closely around the swept volume of the system antennas. These preliminary shapes were compatible with the electrical design parameters required to achieve a high performance radome and were subsequently subjected to wind tunnel tests at the Cornell Aerodynamics Laboratory. The results

of these tests showed that these somewhat short, blunt shaped radomes would induce severe drag, buffeting and separation.

Successive modifications of the shapes were made and tried in the wind tunnel until a wing pod and fin pod were obtained which nullified the adverse aerodynamic effects previously encountered. Primarily, the shape change involved additional streamlining of the fore and aft sections of each pod. This streamlining of the wing pods was supplemented by the use of weapon carrier pylon for attaching to the airplane to minimize airflow perturbations over the wing. A comparison of the preliminary and finalized shapes of the fin and wing pad radomes are presented in Figures (3) and (4) respectively. The radomes for the wing installation are 12 feet long, tear drop shaped pods; the vertical fin radome is a contoured airfoil, 8 feet in length.

RADOME DESIGN STUDIES: Structural Limitations of the Sandwich Design

Preliminary electrical design studies indicated that an "A" sandwich design could be used for these radomes provided the skin and core thicknesses required for a satisfactory level of electrical performance were compatible with the strength requirements. If this condition could not be satisfied, a multilayer design would be necessary.

Typical thickness values for skins and cores were determined from flat panel transmission data. Representative flat panel samples of "A" sandwich and multilayer configurations were provided for structural analysis and static test for determining the physical properties. This information, together with flight load data derived from the "parent" aircraft program were thoroughly analyzed to determine the cross-sectional beam thickness dimension for the radomes.

The results of this stress analysis showed that thick skins and cores would be required for an "A" sandwich construction. These skin and core dimensions could be satisfactorily adjusted for an "A" sandwich configuration for only the left wing pod radome because of its comparatively lower frequency of operation. A multilayer electrical design was mandatory for both the vertical fin radome and the right wing pod radome.

A continuing stress analysis of the strength requirements showed that to maintain the structural beam stability with a multilayer construction a minimum total thickness of 0.700 inch would be needed for the wing pod and a minimum total thickness of 1.000 inch would be needed for the fin pod. Additionally, to assure adequate skin to core bond strength an epoxy film adhesive would be required between the inner-most and outer-most interfaces.

ELECTRICAL DESIGN: Multilayer Optimization Techniques

The radome design philosophy was based on the classical techniques for "A" sandwich and multilayer walls described in references (a), (b), (c), and (d). These techniques were supplemented with the computer optimization programs of reference (e) and permitted the selection of a final wall configuration which would provide satisfactory electrical performance within the boundaries established to maintain the structural integrity throughout the flight profile of the airplane.

As part of the electrical design a ray analysis was performed to determine the incidence and polarization angles of the impinging energy using geometric optics techniques described in the references. During this study, complete illumination of the radome surface was accomplished analytically by investigating a series of discrete antenna/radome orientations or "looks" traversing 360 degrees in azimuth.

Equations for each radome were readily defined since the shapes were established by conic lofting methods; therefore, this ray analysis and the subsequent transmission evaluation were performed completely by programming (f) a high speed digital computer.

Using the results of the incidence angle study as input data, the power transmission coefficients for each ray is computed as a function of the angle of incidence, the angle of polarization, the frequency, and the electrical parameters of the materials. The efficiency of the radome is determined by a weighted averaging of all computed transmission data.

These theoretical studies were continued for each radome using the structural dimensions as boundary conditions on the optimization programs. For the fin pod and right wing pod radomes, multilayer walls of five to fifteen layers, symmetrically and asymmetrically configured were analyzed, while several "A" sandwich walls were evaluated for the left wing pod radome to obtain a design that would comply with the electrical requirements. As an integral part of the design studies, the neoprene coating used for rain erosion protection was considered as a separate layer of 0.010 inch nominal thickness.

The results of this extensive design investigation showed that the following configurations offered a compatible solution to the structural and electronic requirements.

(a) The Left Wing Pod Radome - (Shown in Figure 5) A symmetrically configured three layer or "A" sandwich wall of solid laminate interfaces ("skins") interspaced by nylon phenolic honeycomb core. Total thickness of this radome is 0.700 inch.

(b) The Vertical Fin Radome - (Shown in Figure 6). A symmetrically configured seven layer sandwich of four solid laminate interfaces interspaced by three cores of nylon phenolic honeycomb, for a total thickness of 1.000 inch.

(c) The Right Wing Pod Radome - (Shown in Figure 7) A symmetrically configured eleven layer sandwich of six solid laminate interfaces interspaced by five cores of nylon phenolic honeycomb, for a total thickness of 0.700 inch.

Figures 8 and 9 present, for the "A" sandwich radome, the power transmission as a function of frequency for perpendicular and parallel polarization with angle of incidence as a parameter. Similar data are presented in Figures 10 through 13 for the multilayer fin pod and right wing pod radomes. To illustrate the results obtained from the transmission programs, Figures 14 and 15 are presented to show the total, weighted average transmission obtained from the computer optimization program for the right wing pod radome.

MANUFACTURING: Female Molds, Pre-Impregnated Glass Cloth, Nylon Phenolic Honeycomb

With the design firmed, processing and fabrication methods for making the radomes were established. The radomes were manufactured in female molds; the wing pod radomes were made in the mold shown in Figure 16 while the fin pod was made in the mold shown in Figure 17. An epoxy, preimpregnated glass cloth (g) was used for the "skins" with 3/16 inch cell size, preformed, nylon phenolic honeycomb material (h) used for the cores. A section of this preformed core installed in the nose section of the right wing pod radome is shown in Figure 18.

A film adhesive (i) was used to assure adequate peel strength at the inner-most and outer-most skin/core interfaces. Additionally, all inner layer, skin/core interfaces of the two multilayer radomes were roller coated with a liquid epoxy adhesive (j) to improve bond strengths.

The outer skin was prepared in the mold using the preimpregnated glass fabric. A "bag" was sealed in place over the "skins" preparatory to drawing vacuum pressure. The entire mold was then put in the autoclave for additional pressure during the cure cycle.

This step in the processing of the fin radome is shown in Figure 19; the "bag" is being sealed while the mold sits on the platen of the autoclave. The platen and the mold are rolled into the clave for the complete cure cycle. After cure this outer skin was scuff sanded and cleaned.

For the "A" sandwich radome only a two step molding process was required to complete the part. A layer of film adhesive was applied on the cured, outer skin and the core set in place. Over the exposed core, a light roller coat of the liquid adhesive was applied and the second or inner "skin" laid in place. After completing the lay up of the inner skin, the bag was sealed and a vacuum drawn. Final cure was under vacuum in the pressure environment of the autoclave.

For the critical multilayer radomes a more repetitious molding process was required. After scuff sanding and cleaning the first or outer layer, the film adhesive was applied and the first layer of core was set in place. A bag was sealed over the core and this first layer was cured only under vacuum pressure in an oven. The cured, first layer of core in the right pod radome is shown in Figure 20.

After cure, a roller coat of the liquid adhesive was applied over the exposed core. The second layer of skins were prepared and laid, wrinkle free, on the core. A coat of the liquid adhesive was applied on the cloth and the second layer of core was set in place. The part was then sealed with a bag, evacuated and placed in the autoclave to complete the cure cycle. These steps were repeated for the seccessive inner layers of skins and cores. The final step in the molding process was the lay up and cure of the inner skin.

Figures 21 and 22 are photographs of the right wing pod radome and fin pod radome after the processing has been completed. The discontinuity in the shape of the aft section of the fin radome is most evident in Figure 22.

Upon completion of the molding process, the radomes were trimmed at the attach edge for subsequent mating to the airframe. The nose section of each radome was sprayed with a coating of neoprene material for rain erosion protection. An acrylic paint system was used to finish each radome in a color scheme to match the airplane. Figure 23 shows the finished radomes installed on the airplane. Prior to this installation on the airplane, the radomes were subjected to electrical qualification tests.

ELECTRICAL TESTS: Transmission, Static and Dynamic Patterns -

In addition to the standard electrical qualification tests delineated in MIL-R-7705A (ASG) for broad-band, Type III, radomes, static and dynamic antenna patterns were recorded to demonstrate full compliance with system requirements.

The transmission test procedures outlined in the military specification requires the use of the system antenna and tuning the receiving plumbing to a VSWR of approximately 1.04. This close match on the system antenna assures recording accurate and valid radome transmission data. With wide band, receiving antennas a VSWR of 1.04 is usually not attainable. A VSWR characteristic of 5:1 is typical for these complex antenna systems. As a consequence of this high VSWR characteristic, measuring the transmission efficiency of a broad-band radome in accordance with the military specification procedures results in extremely erratic results. The data record is characterized by an oscillating curve of the apparent transmission of the radome. The magnitude of this oscillation often exceeds the reference power level. This phenomenon is the result of complex changes occurring to the VSWR of the antenna as a consequence of the interaction of the radome/antenna combination. Data recorded under these conditions are not representative of the actual microwave transmission efficiency of the radome wall.

To assure an accurate and valid evaluation of the transmission efficiency of these radomes, standard gain horns were substituted, where feasible, for the system antenna. The horn was located in the radome in a position identical to that of the system antenna. With a standard gain horn a VSWR match of 1.04 could be achieved, and transmission data truly indicative of the radome wall could be measured.

Figure 24 illustrates the typical oscillating characteristics recorded when measuring transmission on a broad-band radome using the system antenna. Figure 25 shows the measurement repeated but with a standard gain horn substituted for the system antenna. Figure 25 exhibits a close correlation with the performance level predicted in the design studies and shown in Figure 26. A compilation of these data for direct comparison are shown in Figure 27.

These data were measured with the vertical fin radome. The decrease in performance level through the aft 90 degree quadrant, ± 45 degrees from the vertical centerline, is a result of the discontinuity in the shape of the radome at this section and was predicted during the design studies.

In addition to transmission data, antenna pattern distortion tests were performed in accordance with the applicable military specification procedures. These test procedures describe a method of recording patterns under static conditions; that is, the pattern is recorded by rotating the system antenna and radome together at discrete orientations all relative to a fixed signal.

Under actual system conditions the antenna pattern is rotating in relation to a fixed radome and a fixed target. This dynamic condition was duplicated on the test range by a special two axis mount which orientated the radome in azimuth relative to a fixed signal source. The system antenna was then rotated independently of the fixed radome and fixed signal (target) source. Patterns were recorded at successive 15 degree increments of azimuthal off-sets of the radome from 0 degrees through 360 degrees.

The bearing error data for the radome were reduced and charted from these patterns. These curves of radome error data showed close correlation with similar data derived from actual flight tests assuring a complete and satisfactory integration of the radomes and the system.

FUTURE PROGRAMS - "Radant" Concept and Materials Development -

The diversity of radome design techniques described in the references provided the means for achieving a compatible solution to the confronting structural/ aerodynamic/ and electronic requirements encountered in this program. Future wide-band programs however, especially on higher performance type aircraft, will demand even closer coordination of the needs of all the engineering disciplines concerned.

On transonic aircraft, large form factor antennas for wide band use will have to be replaced by flush mounted systems. The concept of "Radant" housings, made with materials capable of sustaining high temperature environments will have to be augmented in keeping with the added complexities of future wide-band systems.

Security restrictions prevented a more detailed description in this paper of the system operation and configuration details of the radomes. The prime motive in presenting this paper is to indicate that the problem areas, satisfactorily resolved in this program, represent only the threshold of what will be encountered on future programs. The radome design techniques offer a certain range of flexibility to effect a satisfactory electrical performance; however additional emphasis must be placed on the development of new materials having good structural and electrical properties at elevated temperatures. If this development is not forthcoming the performance levels of future wide-band systems on high speed aircraft will be severely compromised.

LIST OF FIGURES

Figure No.	Title
(1)	Sketch of Production Airplane
(2)	Sketch of Modified Airplane
(3)	Preliminary Shape Layouts of Vertical Fin Radome
(4)	Preliminary Shape Layouts of Wing Pod Radomes
(5)	Isometric of Left Wing Pod Radome
(6)	Isometric of Fin Pod Radome
(7)	Isometric of Right Wing Pod Radome
(8)	Left Wing Pod Transmission vs Frequency- \perp Polarization
(9)	Left Wing Pod Transmission vs Frequency- \parallel Polarization
(10)	Vertical Fin Pod Transmission vs Frequency- \perp Polarization
(11)	Vertical Fin Pod Transmission vs Frequency- \parallel Polarization
(12)	Right Wing Pod Transmission vs Frequency- \perp Polarization
(13)	Right Wing Pod Transmission vs Frequency- \parallel Polarization
(14)	Right Wing Pod Total Transmission vs Frequency Vertical Polarization
(15)	Right Wing Pod Total Transmission vs Frequency Horizontal Polarization
(16)	Photo G195667 - Wing Pod Radome Mold
(17)	Photo G195688 - Fin Pod Radome Mold
(18)	Photo G195669 - Preformed Nose Section Core-Right Wing Pod Radome
(19)	Photo G195695 - Bagging Operation - Fin Pod Radome
(20)	Photo G195690 - First Layer of Core-Right Wing Pod Radome
(21)	Photo G195736 - Completed Right Wing Pod Radome
(22)	Photo G295222 - Completed Fin Pod Radome
(23)	Photo P195896 - Installation of Radomes on Airplane
(24)	Transmission Data Fin Radome Using System Antenna

LIST OF FIGURES (Cont.)

Figure No.	Title
(25)	Transmission Data Fin Radome Using Standard Gain Horn
(26)	Predicted Transmission Data at Test Frequency-Fin Radome
(27)	Transmission Comparison-System Antenna/Horn/Predicted.

LIST OF REFERENCES

- | Reference Letter | Title |
|------------------|------------------------------------------------------------------------------------------------------------------------------------------------------------------------------------------------------------------------------------|
| (a) | N. A. D. C. Report No. EL-5116- "Theory of Lossy High Incidence Radomes" |
| (b) | W. A. D. C. Technical Report 57-67- "Techniques for Airborne Radome Design" |
| (c) | D. H. McClure and S. S. Oleesky, "Microwave Radomes for Use With Extreme Bandwidths" - Proceedings of the OSU-WADC Radome Symposium Vol. II - Ohio State University - August 1956. |
| (d) | G. Tricoles, "A Simple Theory of broad-band Radome Design" - Proceedings of the OSU-WADC Radome Symposium - Vol. I, Ohio State University, June 1957 |
| (e) | M. C. Blyseth, - "Computer Design and Optimization of broad-band Structures With Arbitrary Dielectric Distributions," - Proceedings of the ASD-OSU Symposium On Electromagnetic Windows, Vol. I, Ohio State University, July 1962. |
| (f) | Grumman Aircraft Engineering Corp - R. F. Engineering Section - Transmission and Ray Analysis Programs by Z. Grins |
| (g) | U. S. Polymeric Corp. , Stamford, Conn. Polypreg E780 Epoxy Resin System Preimpregnated Glass Cloth. |
| (h) | Hexcel Corp. , Berkely, Calif. - 3/16 inch cell size, nylon phenolic, honeycomb core material. |
| (i) | Minnesota Mining & Mfg. Co. , Saint Paul, Minnesota - AF110 Film Adhesive. |
| (j) | Minnesota Mining & Mfg. Co. , Saint Paul, Minnesota - EC2186 Liquid Adhesive. |

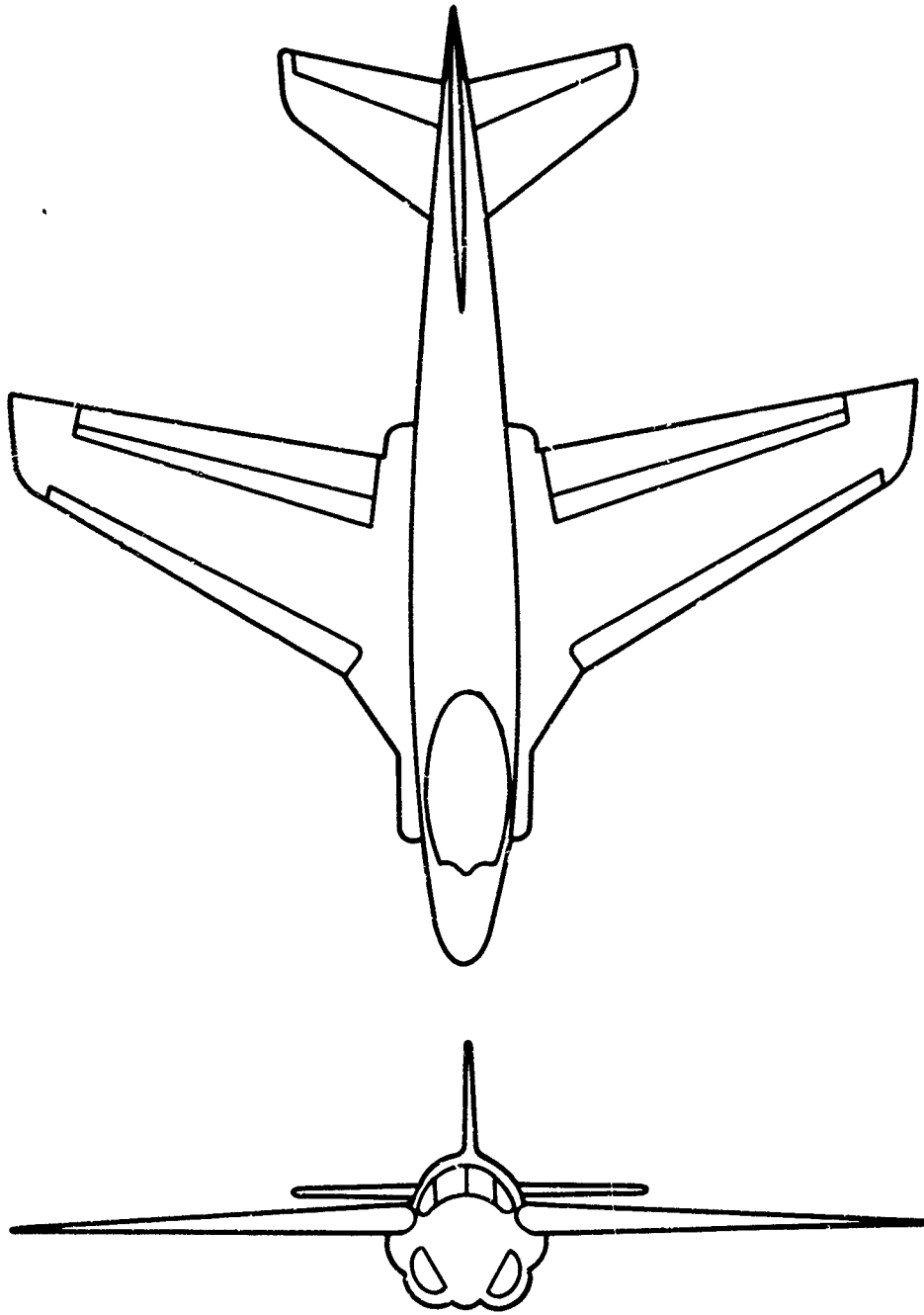


Figure 1. The "Parent" Production Airplane

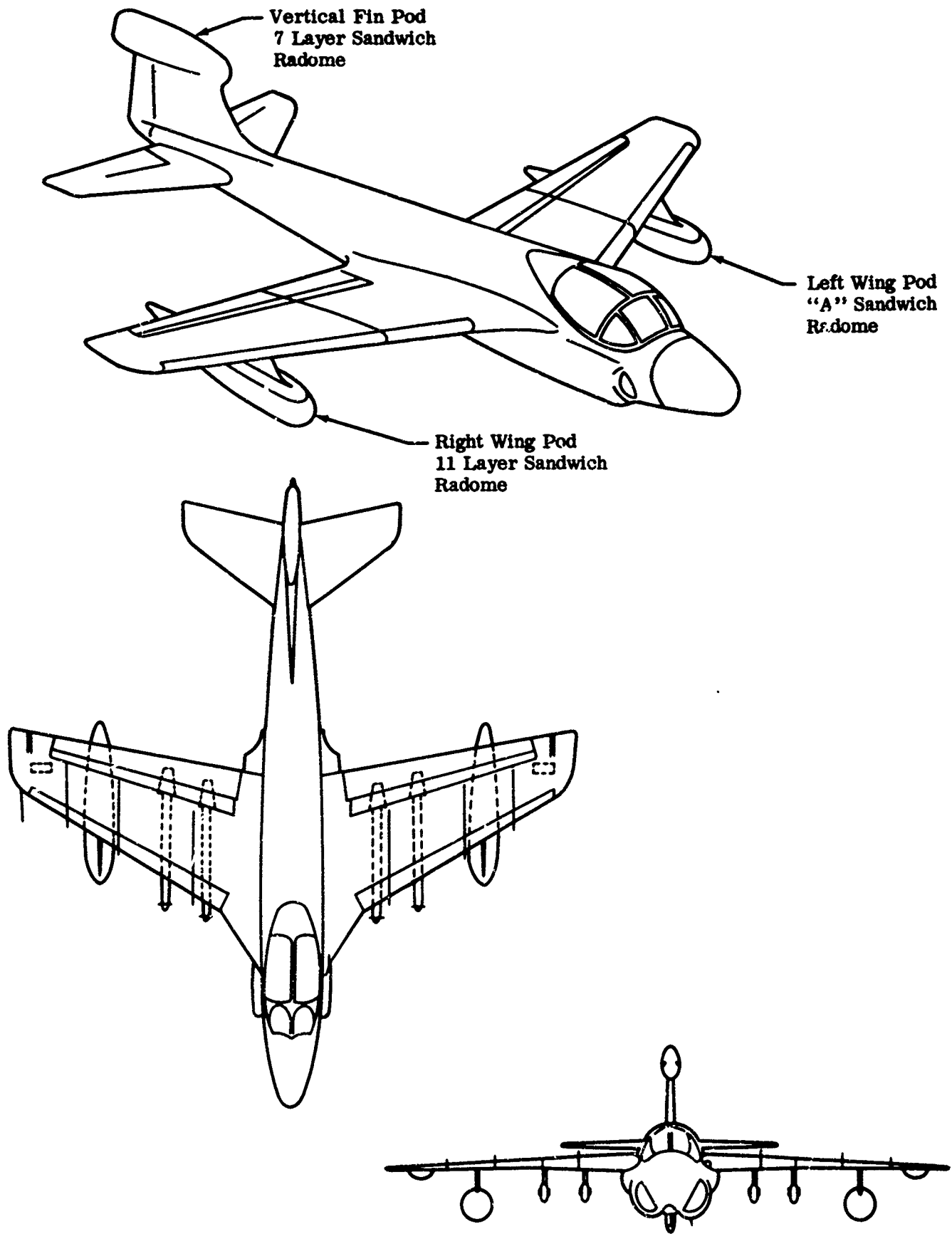


Figure 2. The Modified Airplane

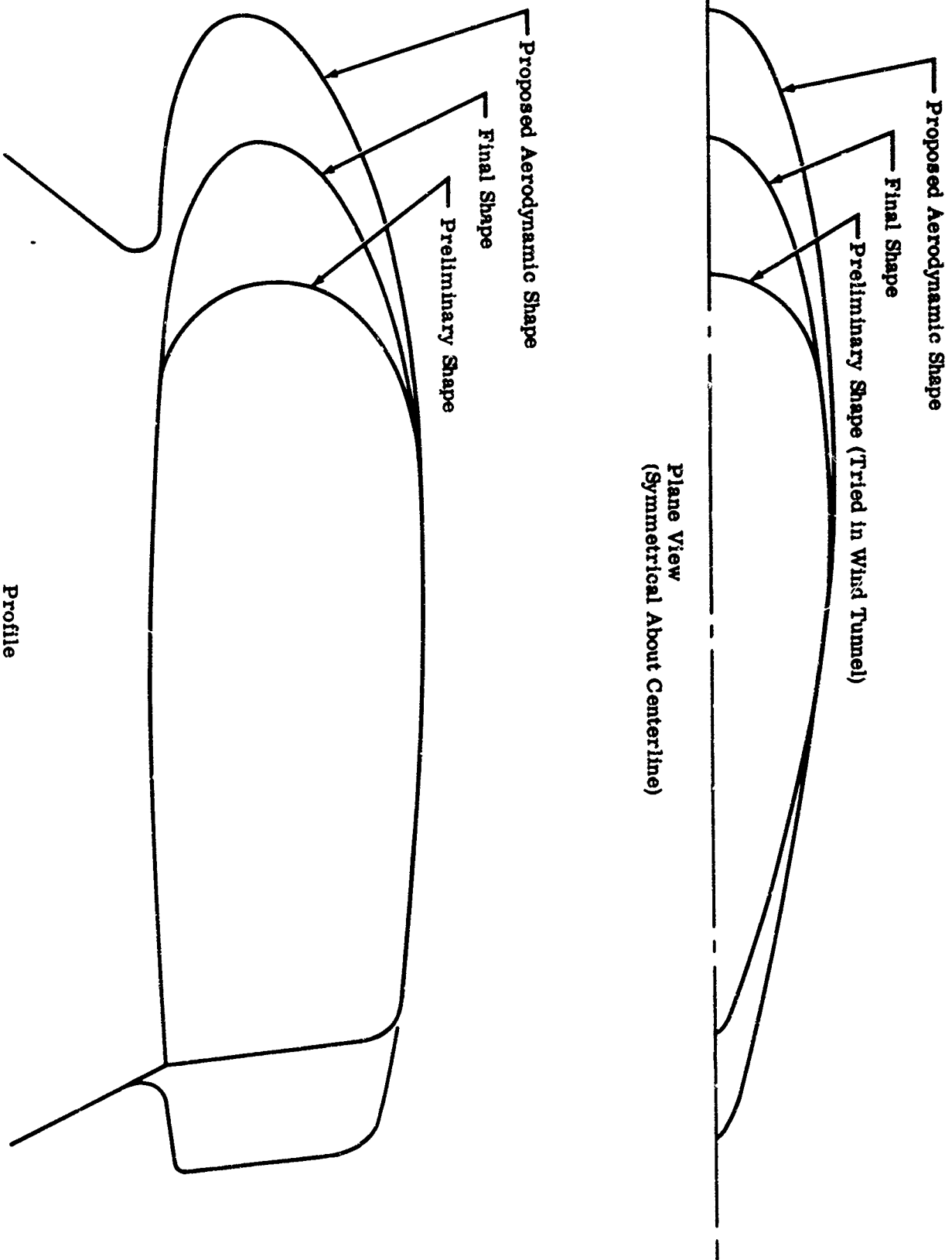


Figure 3. Preliminary Shapes of Γ in Radome

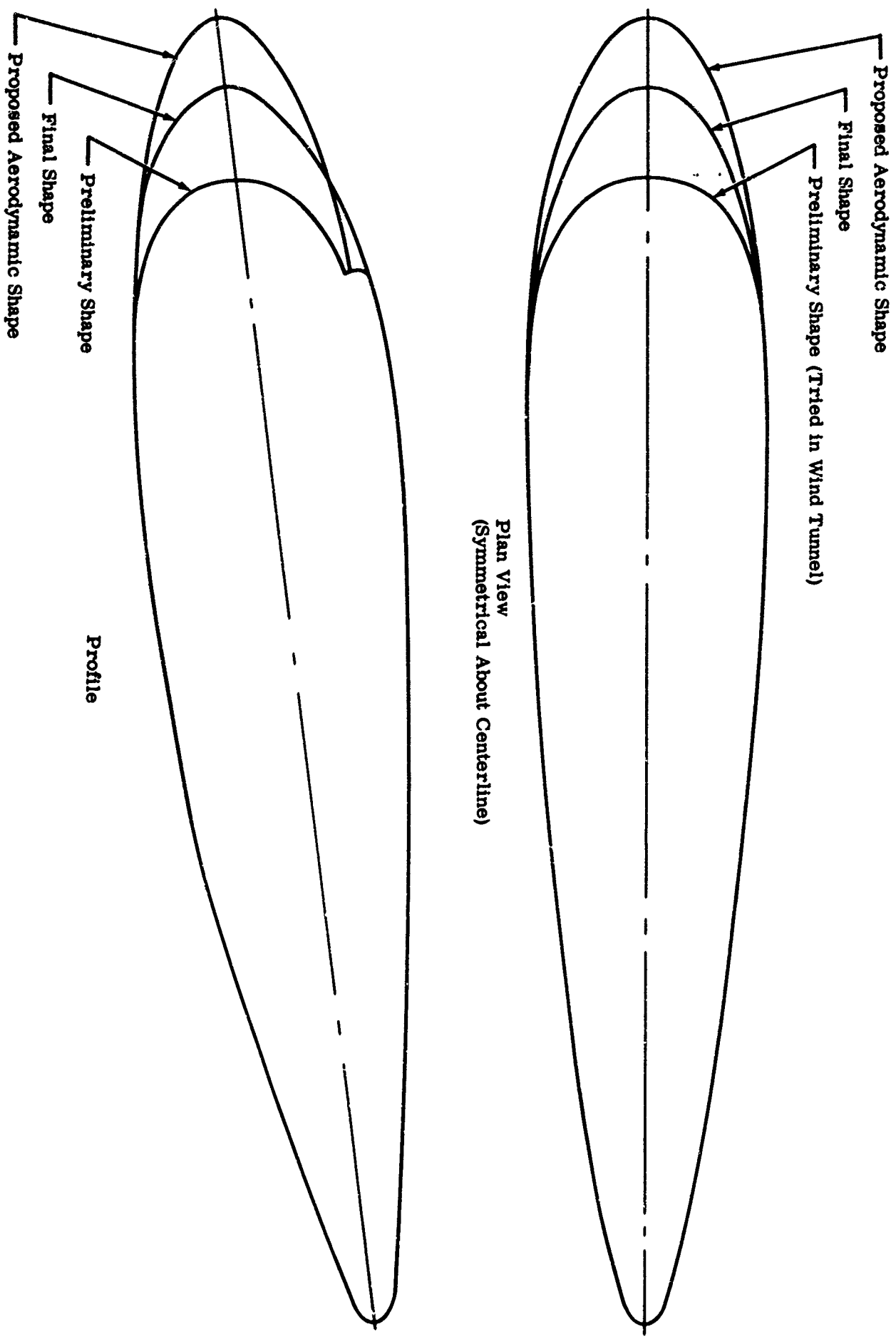
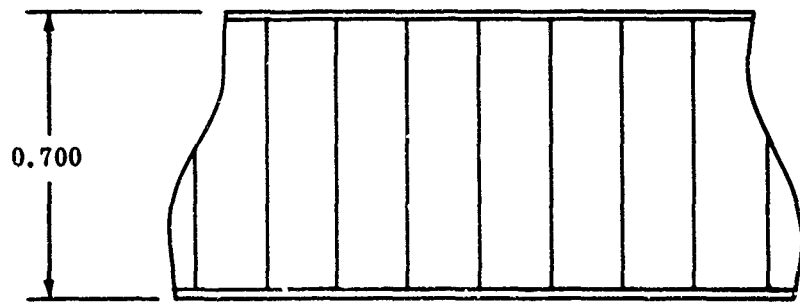
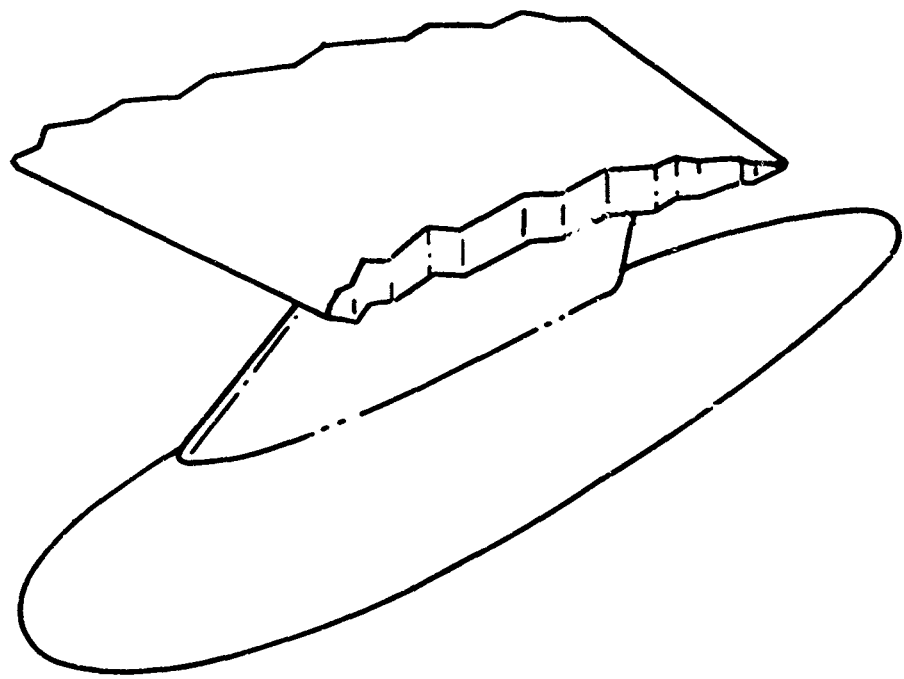
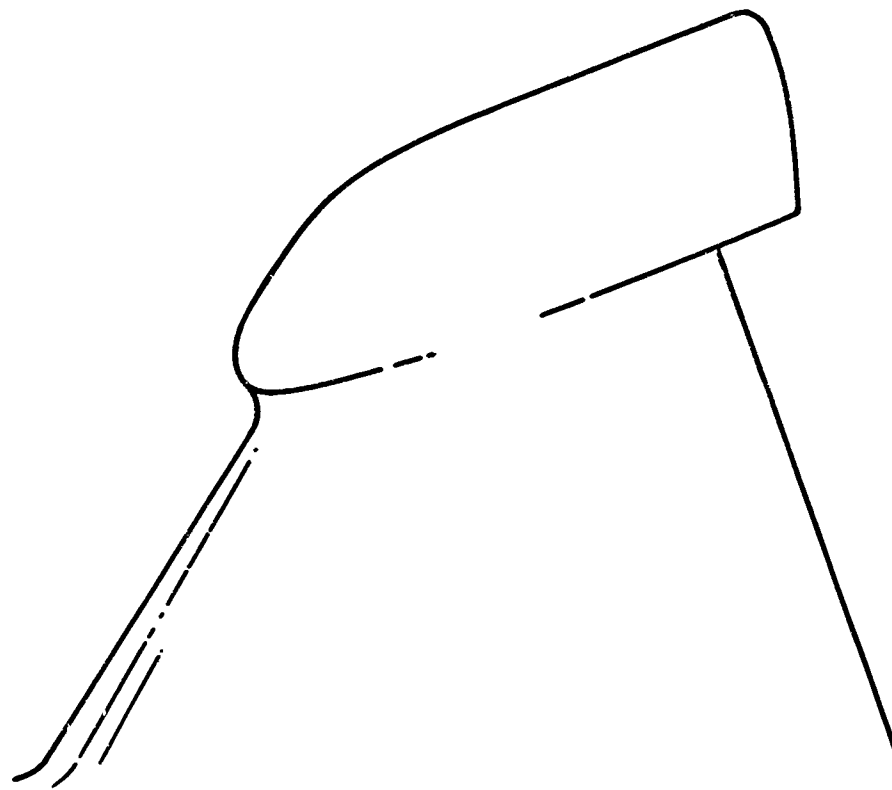


Figure 4. Preliminary Shapes of Wing Pod Radomes



Typical Wall Cross-Section
("A" Sandwich)

Figure 5. Left Wing Pod Radome



Typical Cross-Section
(7 Layer Sandwich)

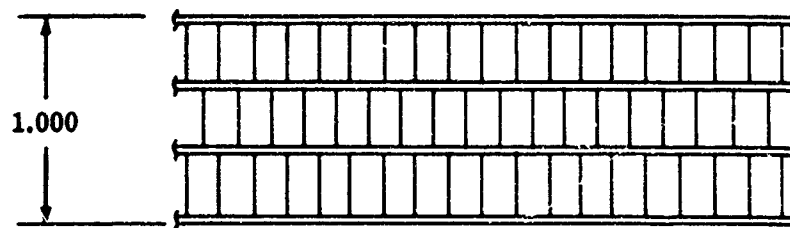
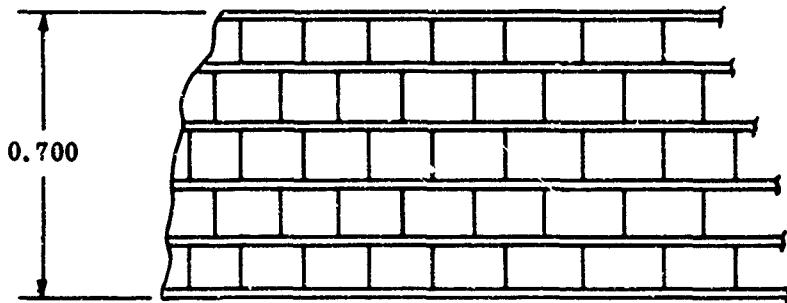
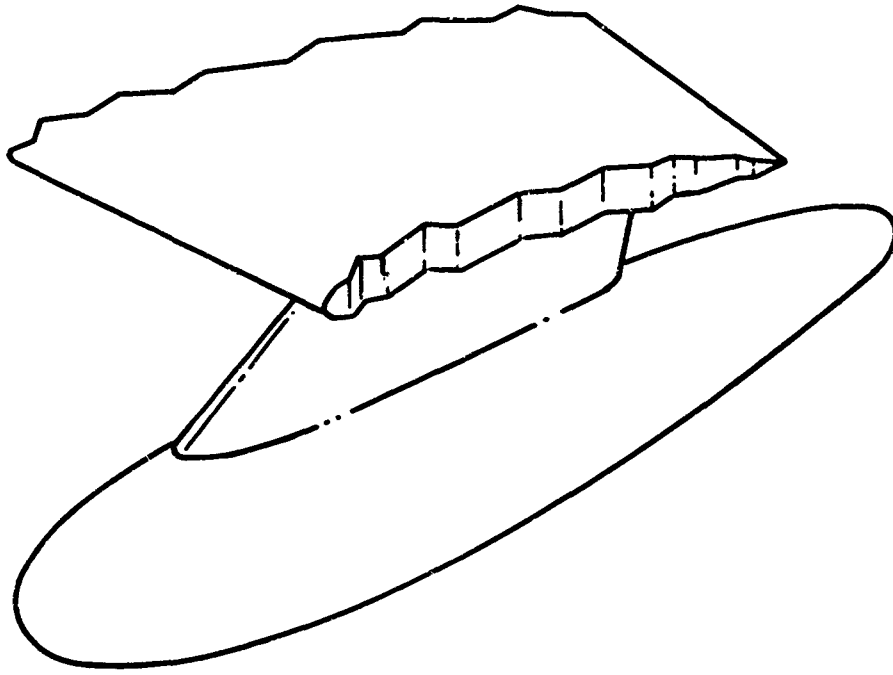


Figure 6. Vertical Fin Radome



Typical Wall Cross-Section
(11 Layer Sandwich)

Figure 7. Right Wing Pod Radome

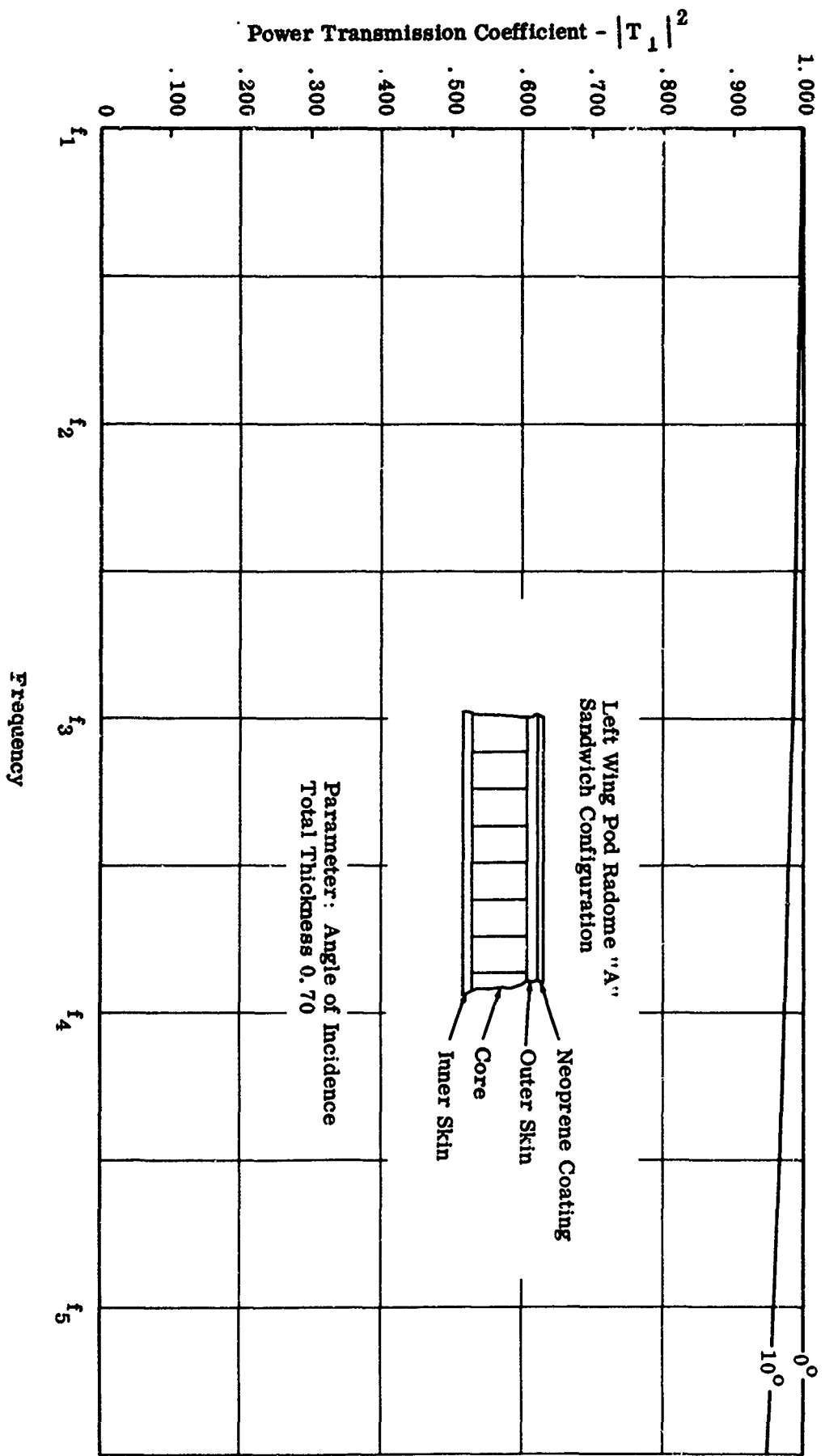


Figure 8. Power Transmission Coefficient vs Frequency
(For Perpendicular Polarization)

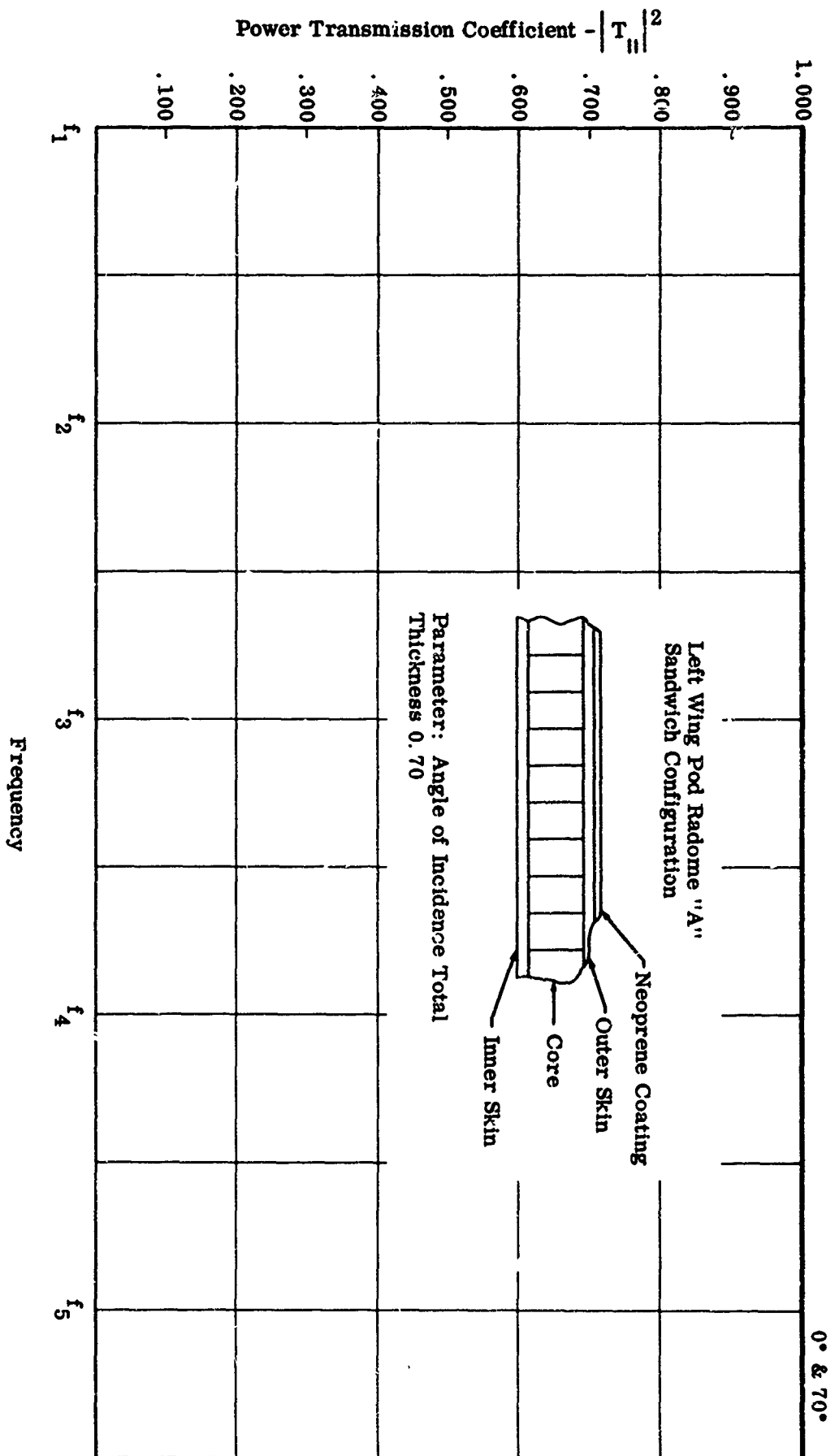


Figure 9. Power Transmission Coefficient vs Frequency
(For Parallel Polarization)

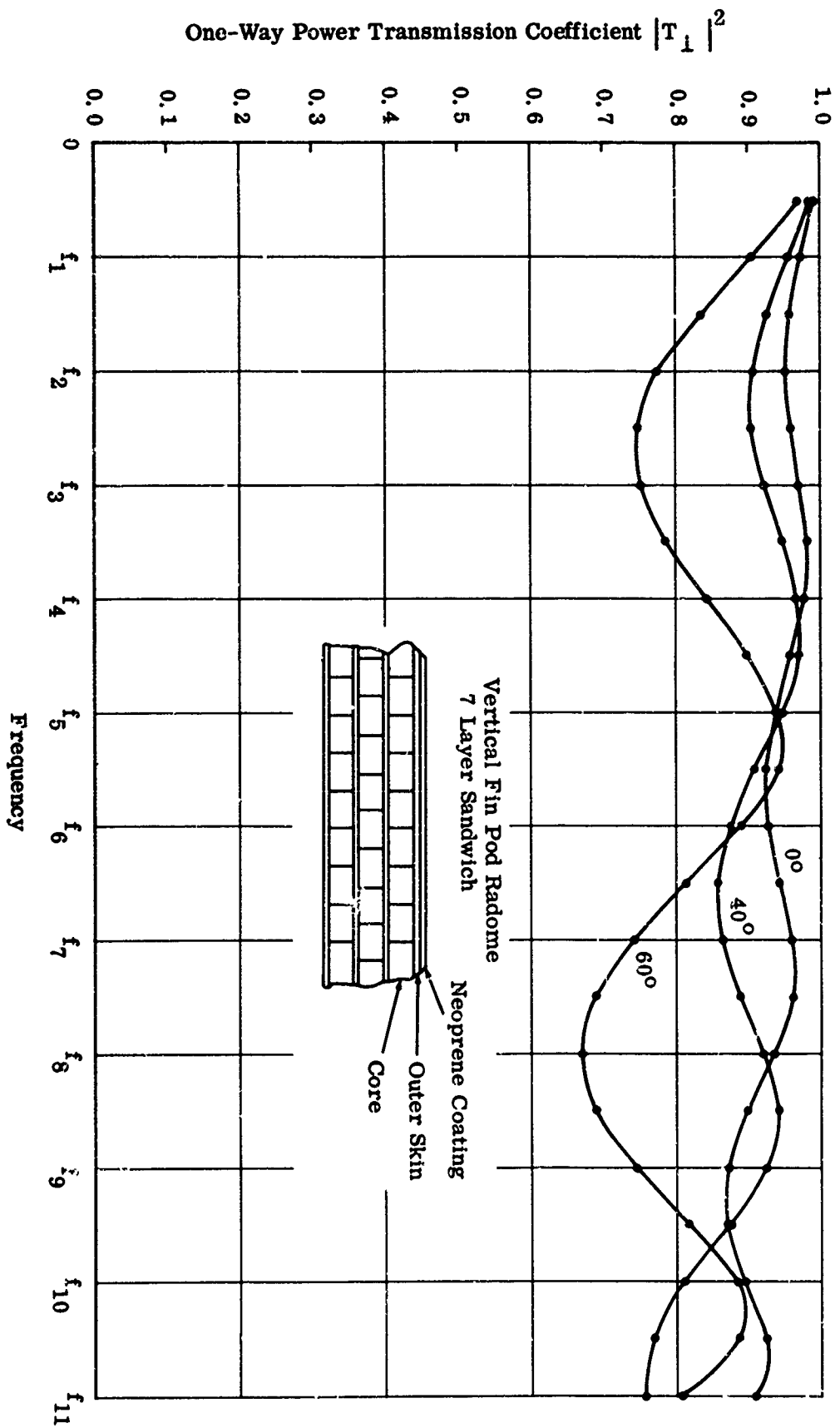


Figure 10. Power Transmission Coefficient vs Frequency
Perpendicular Polarization

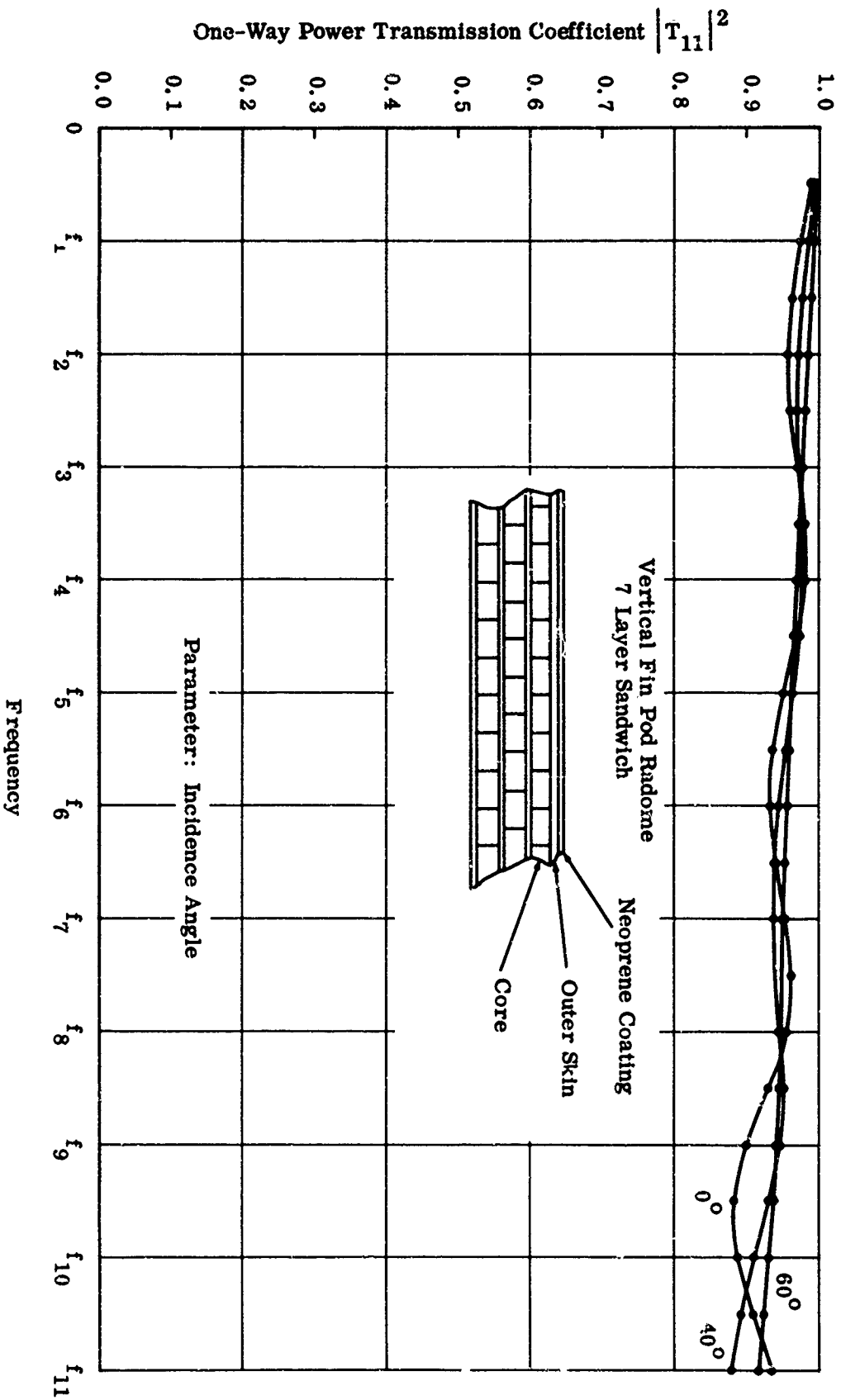
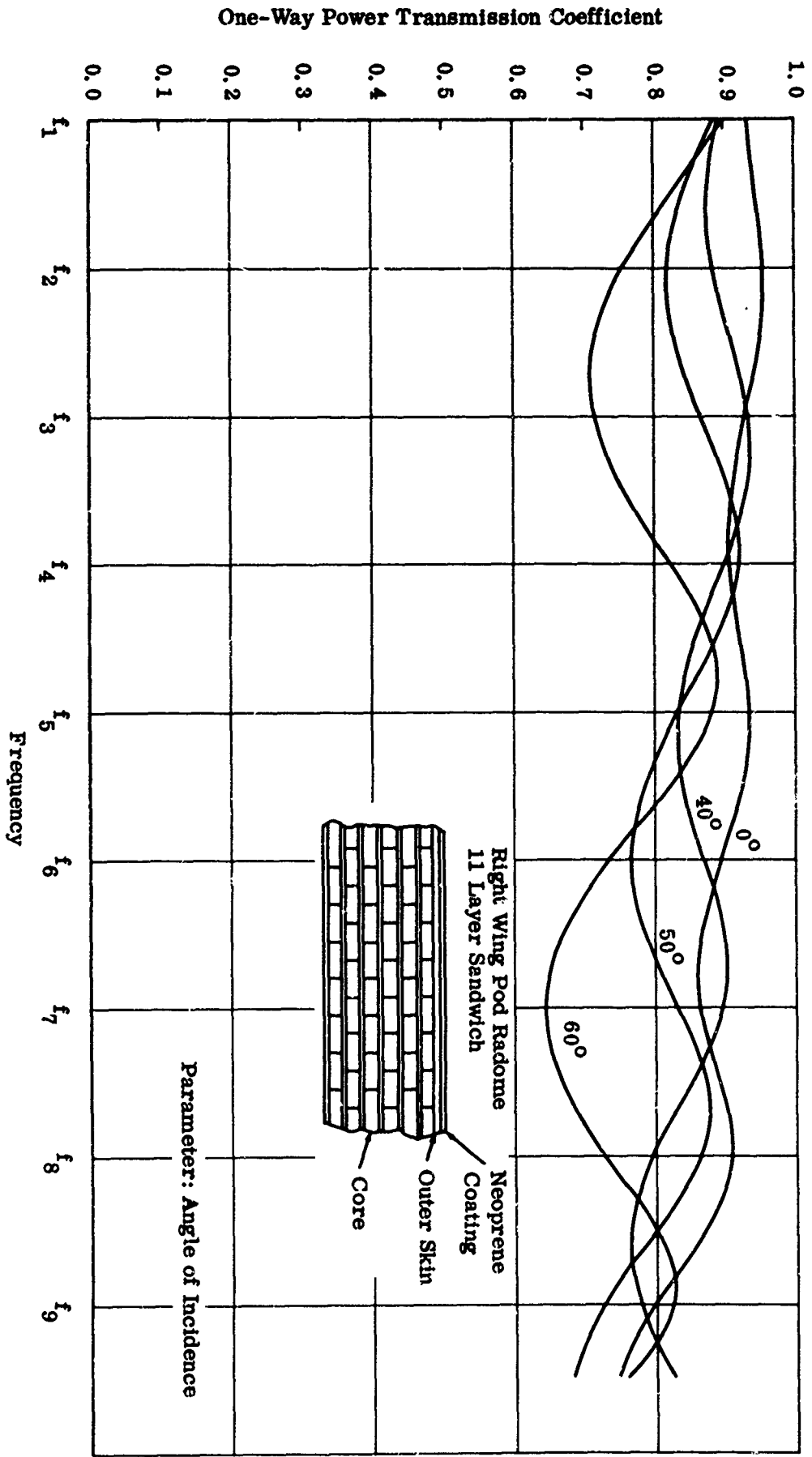
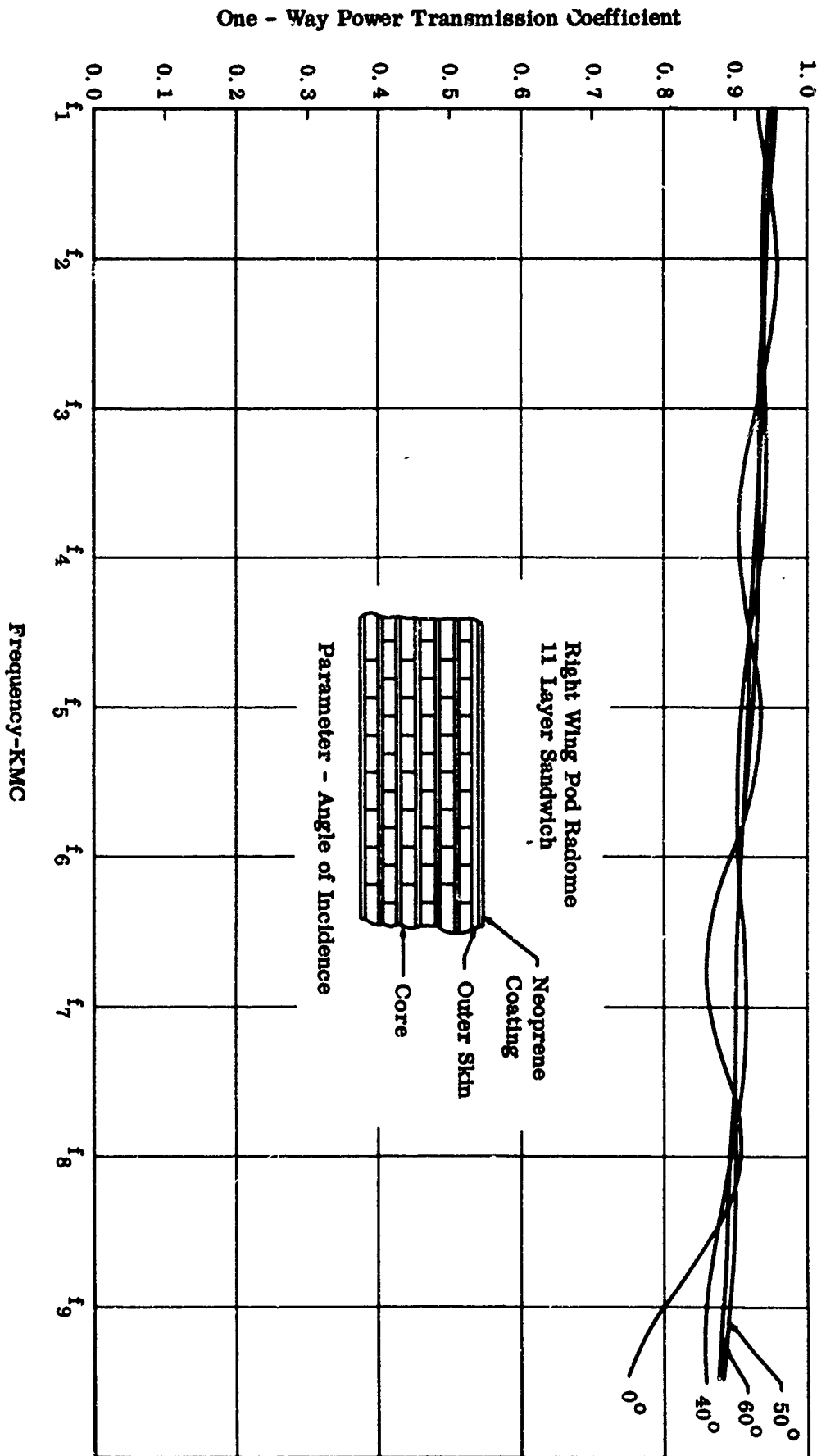


Figure 11. Power Transmission Coefficient vs Frequency
Parallel Polarization



**Figure 12. Power Transmission Coefficient vs Frequency
Perpendicular Polarization
Theoretical Data**



**Figure 13. Power Transmission Coefficient vs. Frequency
Parallel Polarization
Theoretical Data**

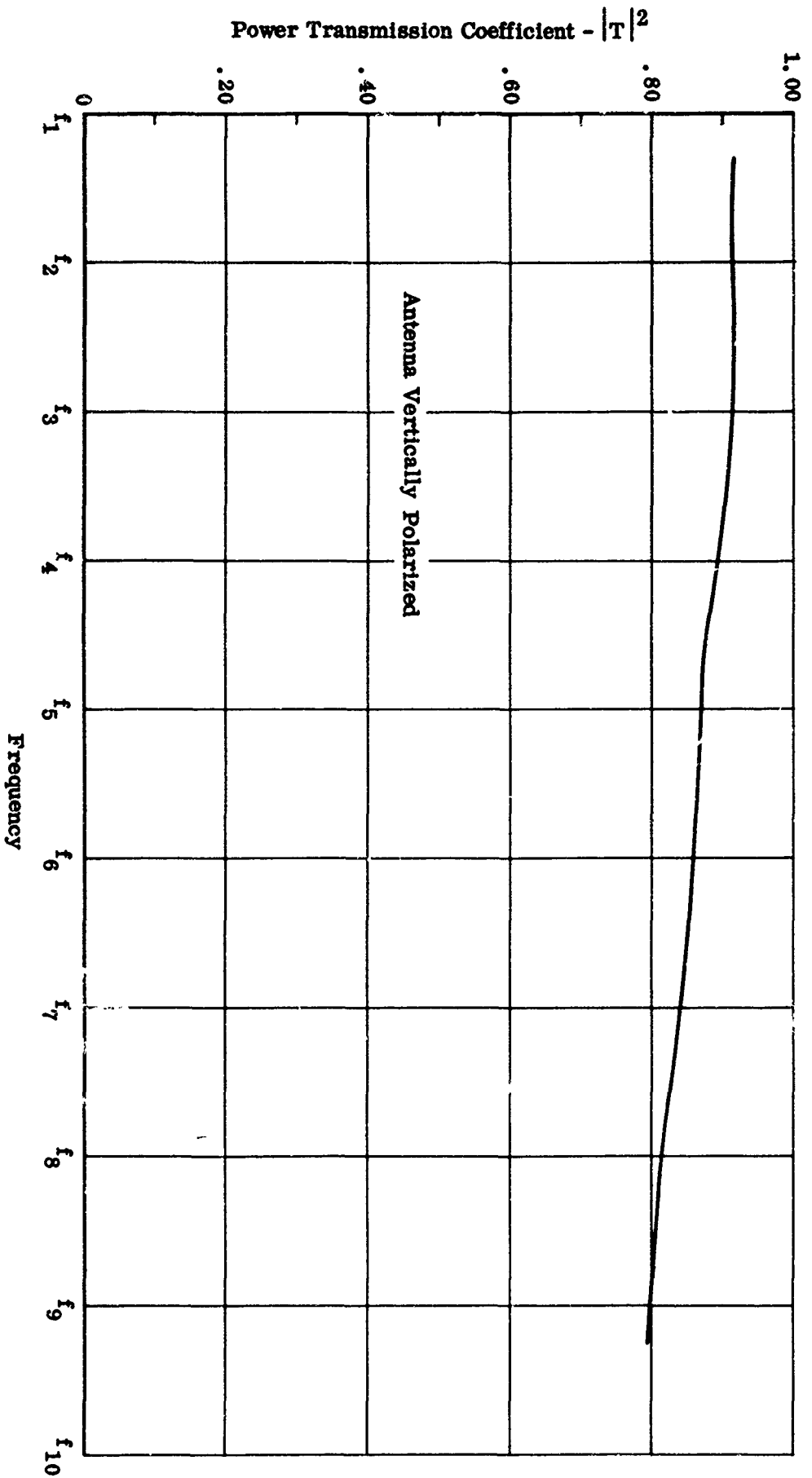


Figure 14. Total Weighted Average vs Transmission vs Frequency
Right Wing Pod Radome

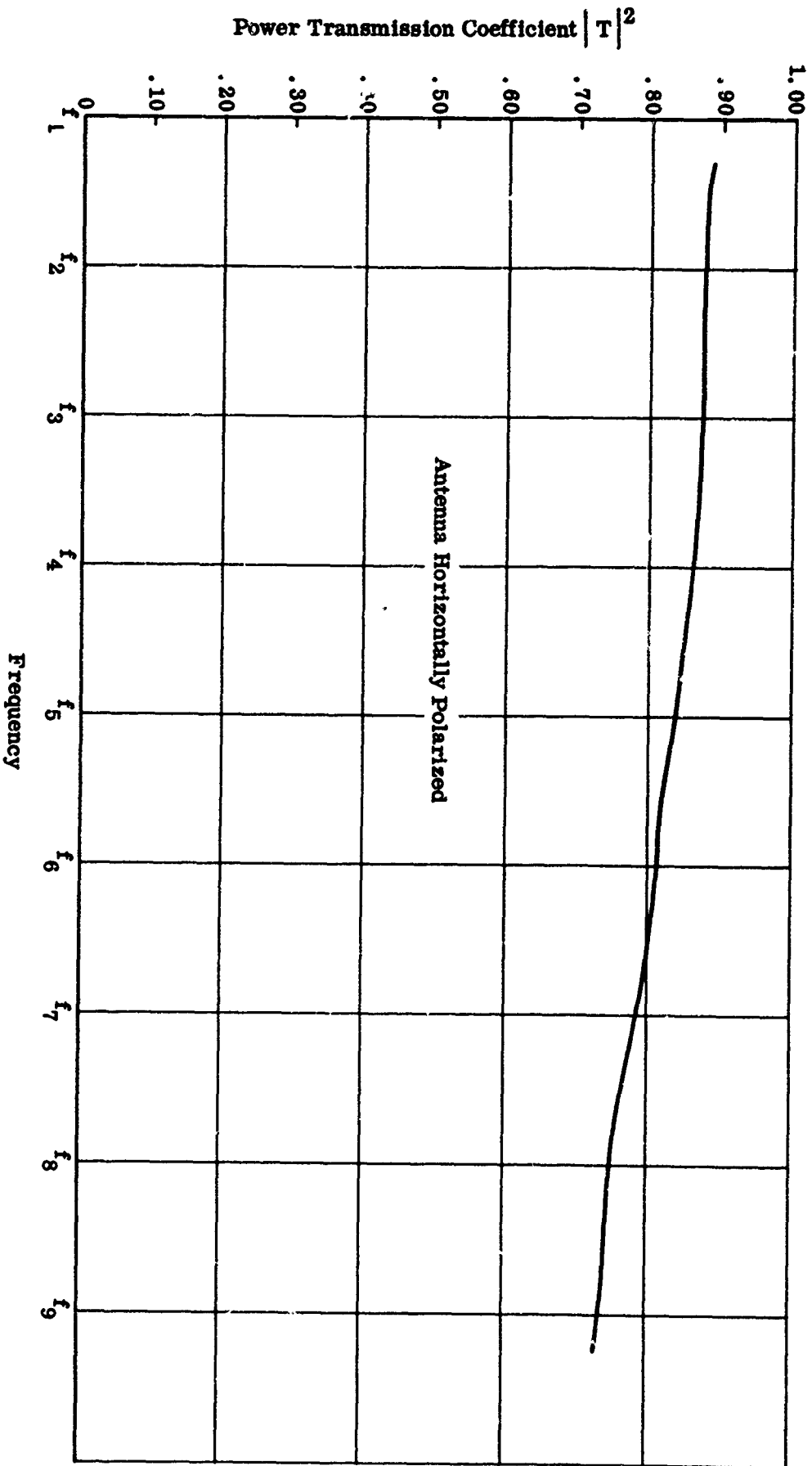


Figure 15. Total Weighted Average Transmission vs Frequency
Right Wing Pod Radome



Figure 16. Wing Pod Radome Mold

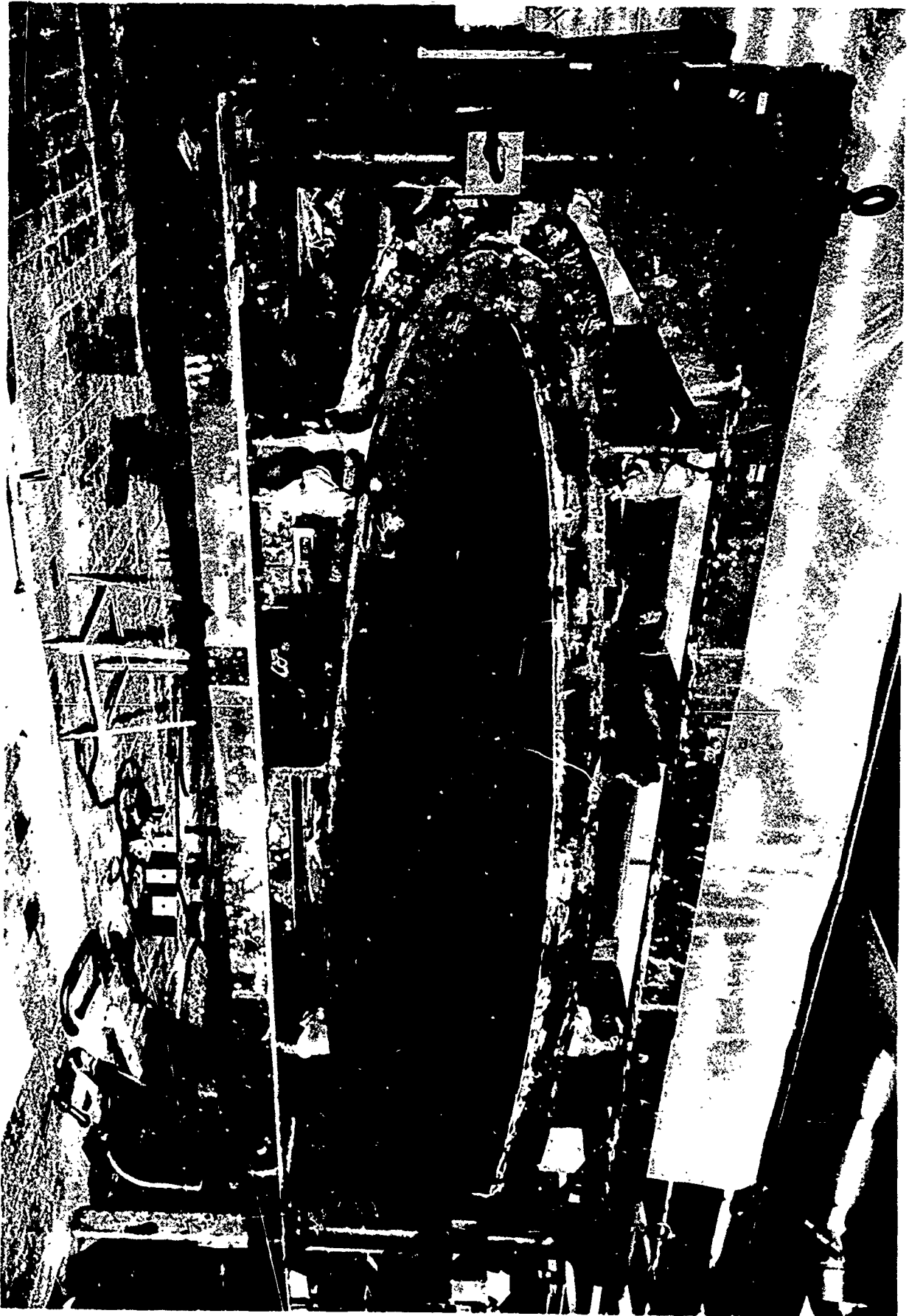


Figure 17. Fin Pod Mold Ready for Use

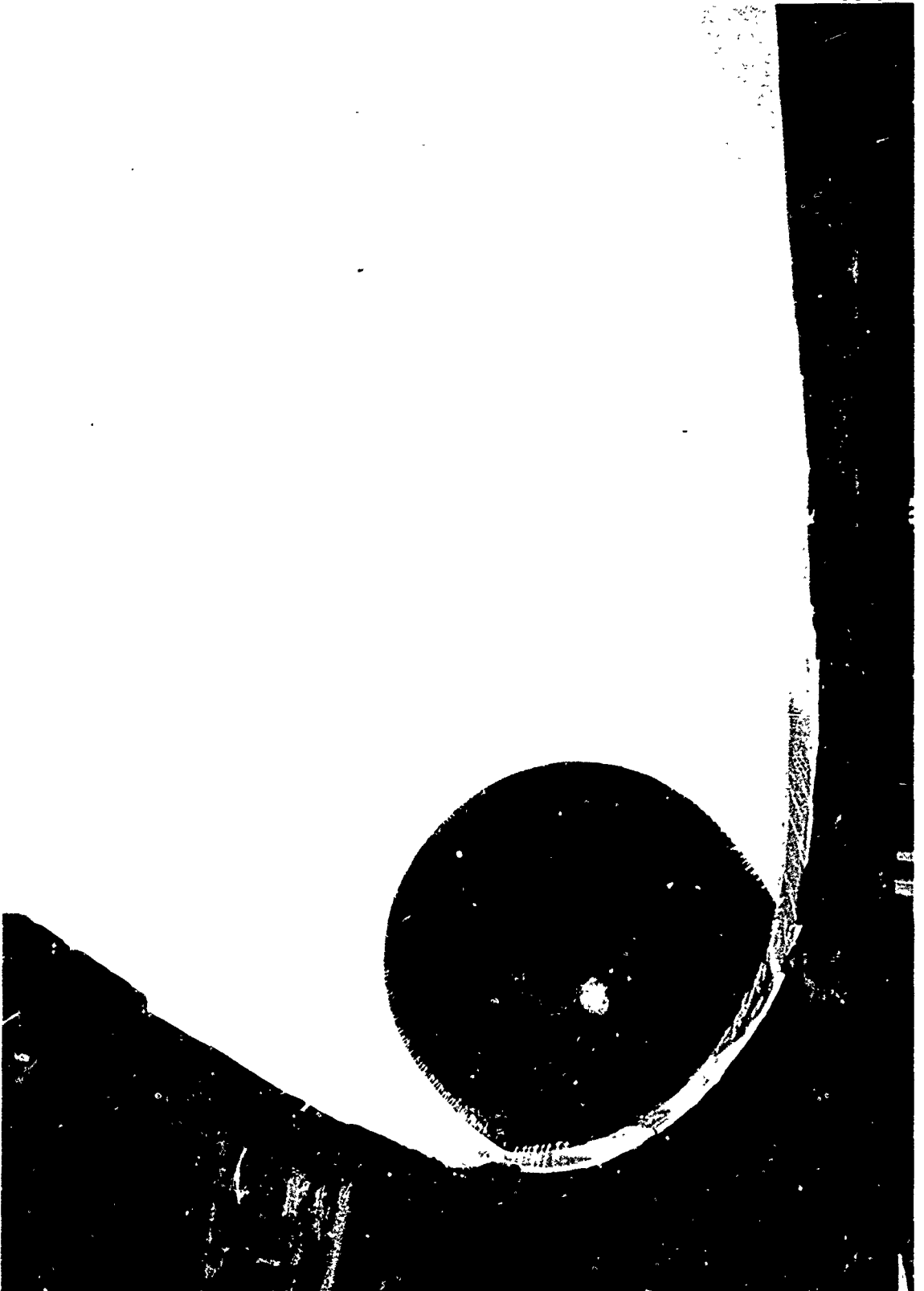


Figure 18. Nose Section - Preformed Core Right Wing Pod Radome

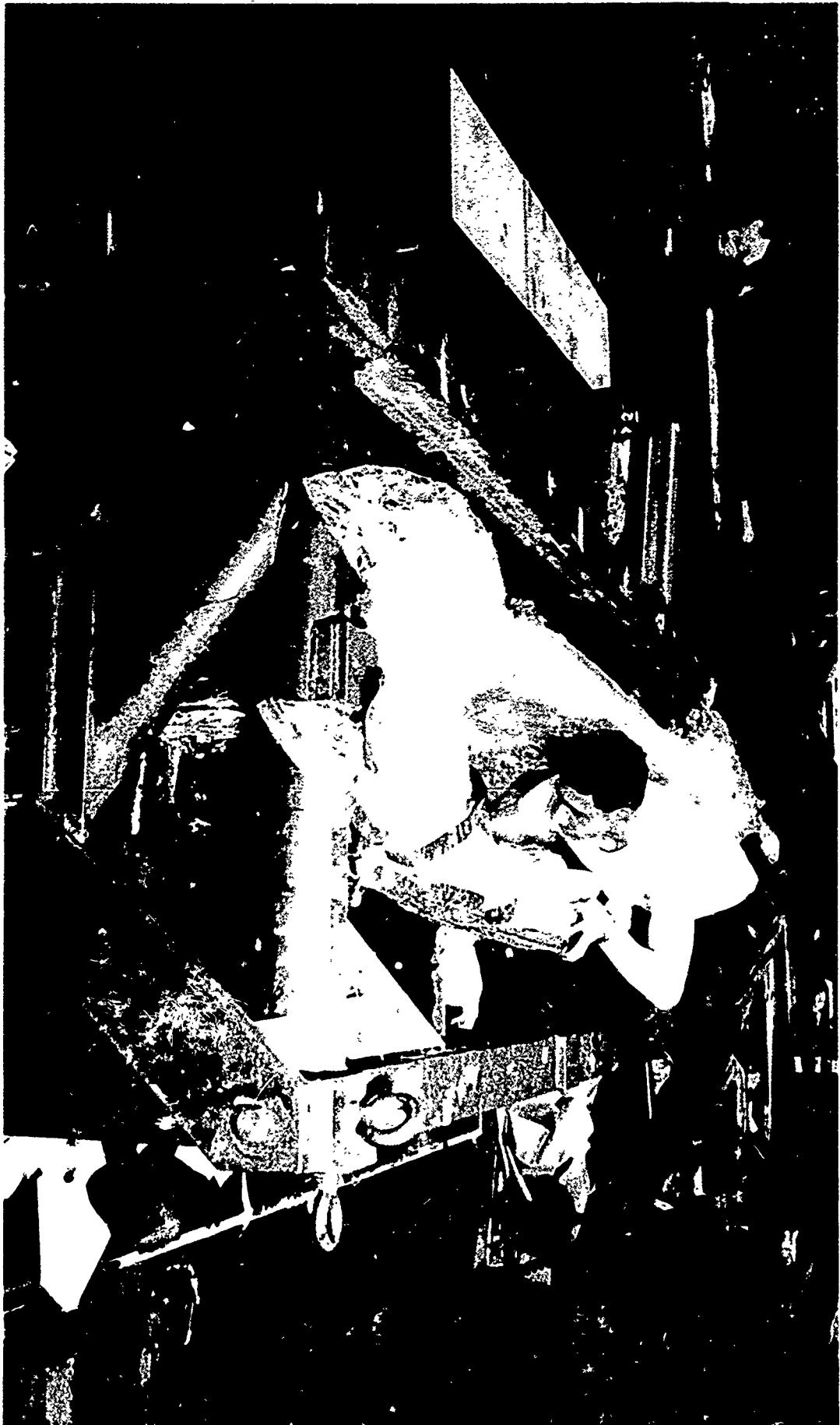


Figure 19. "Bagging" Operation Preparatory to the Autoclave Cure

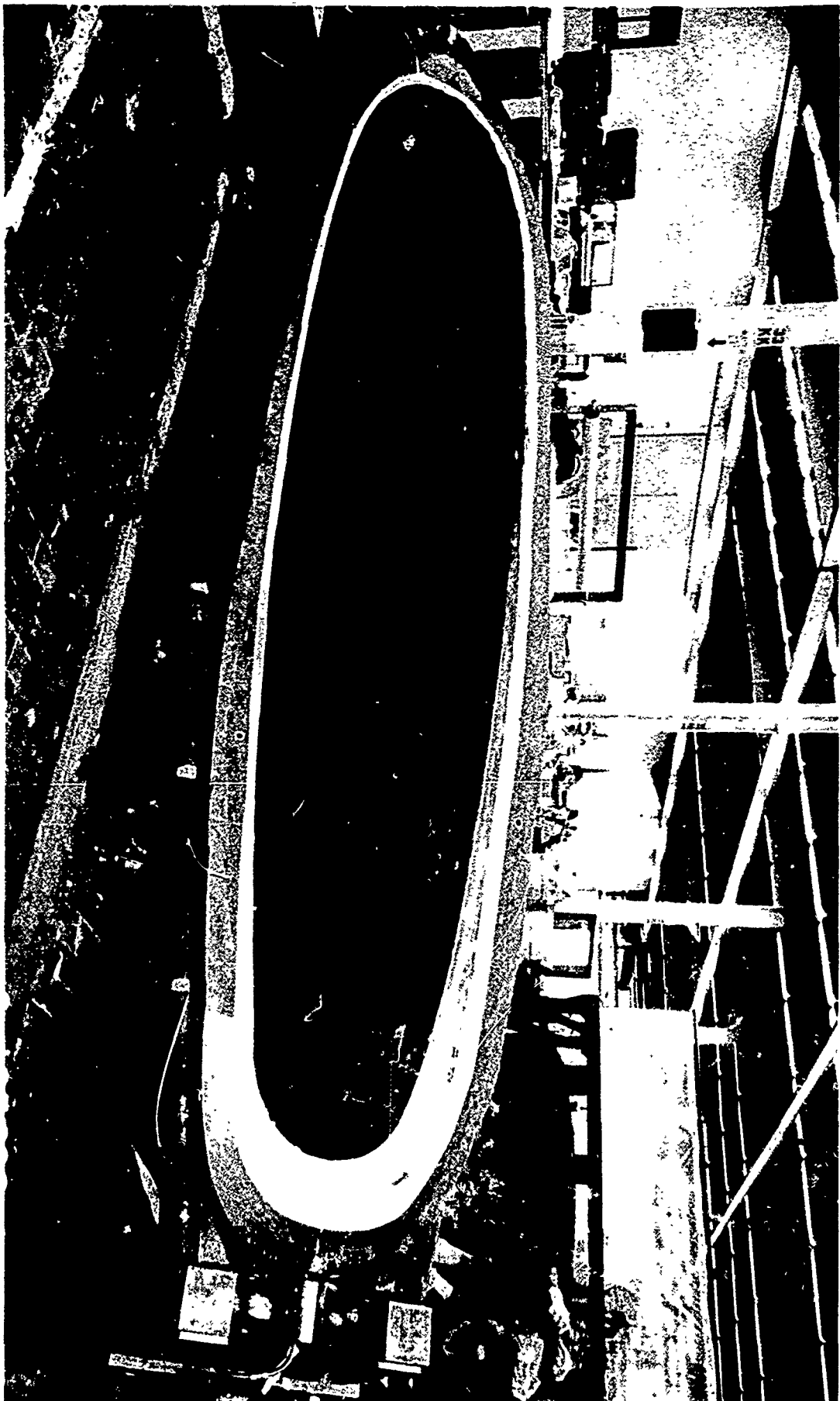


Figure 20 First Layer of Core Right Wing Pod Radome

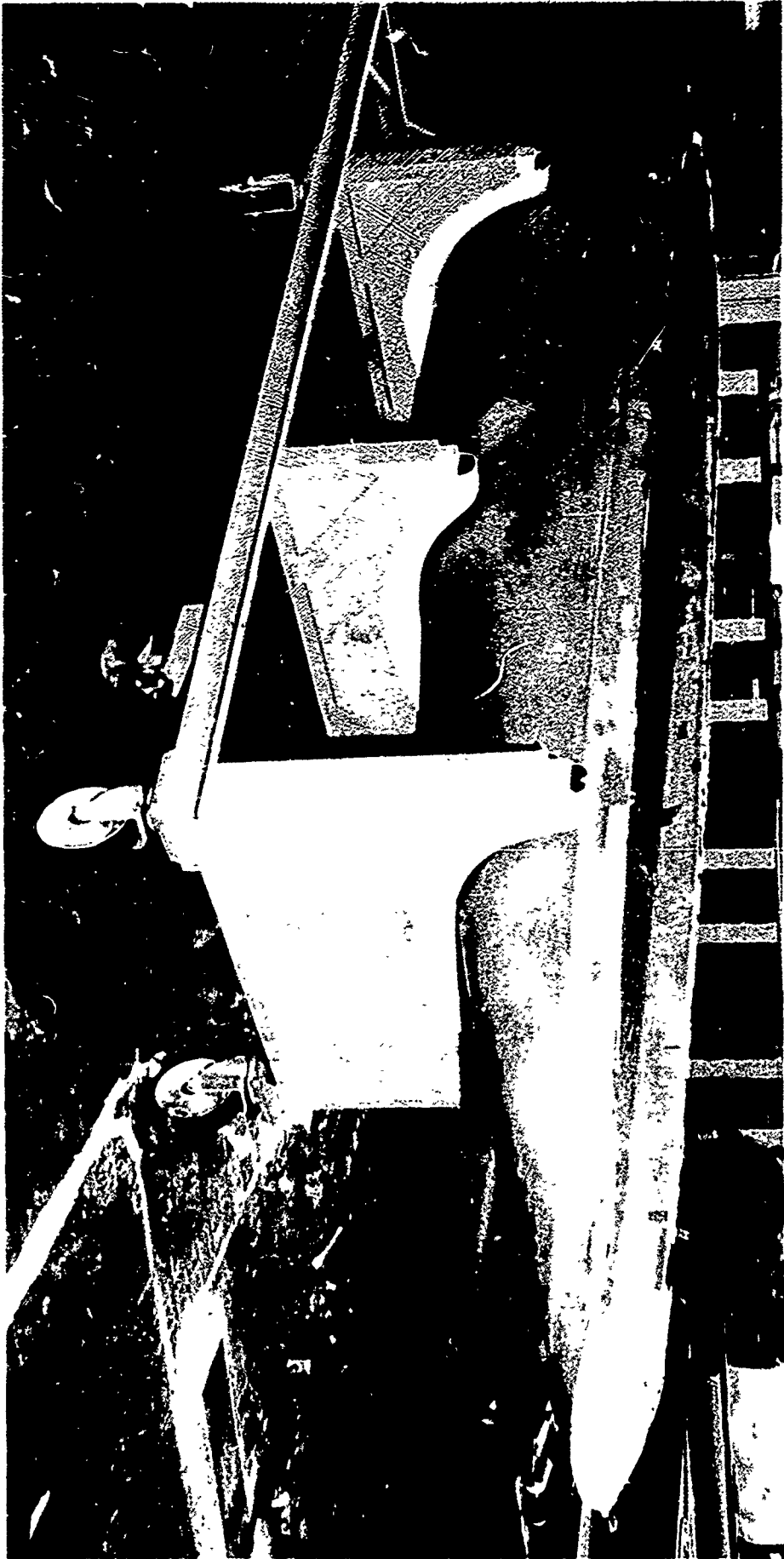


Figure 21. Completed Right Wing Pod Radome

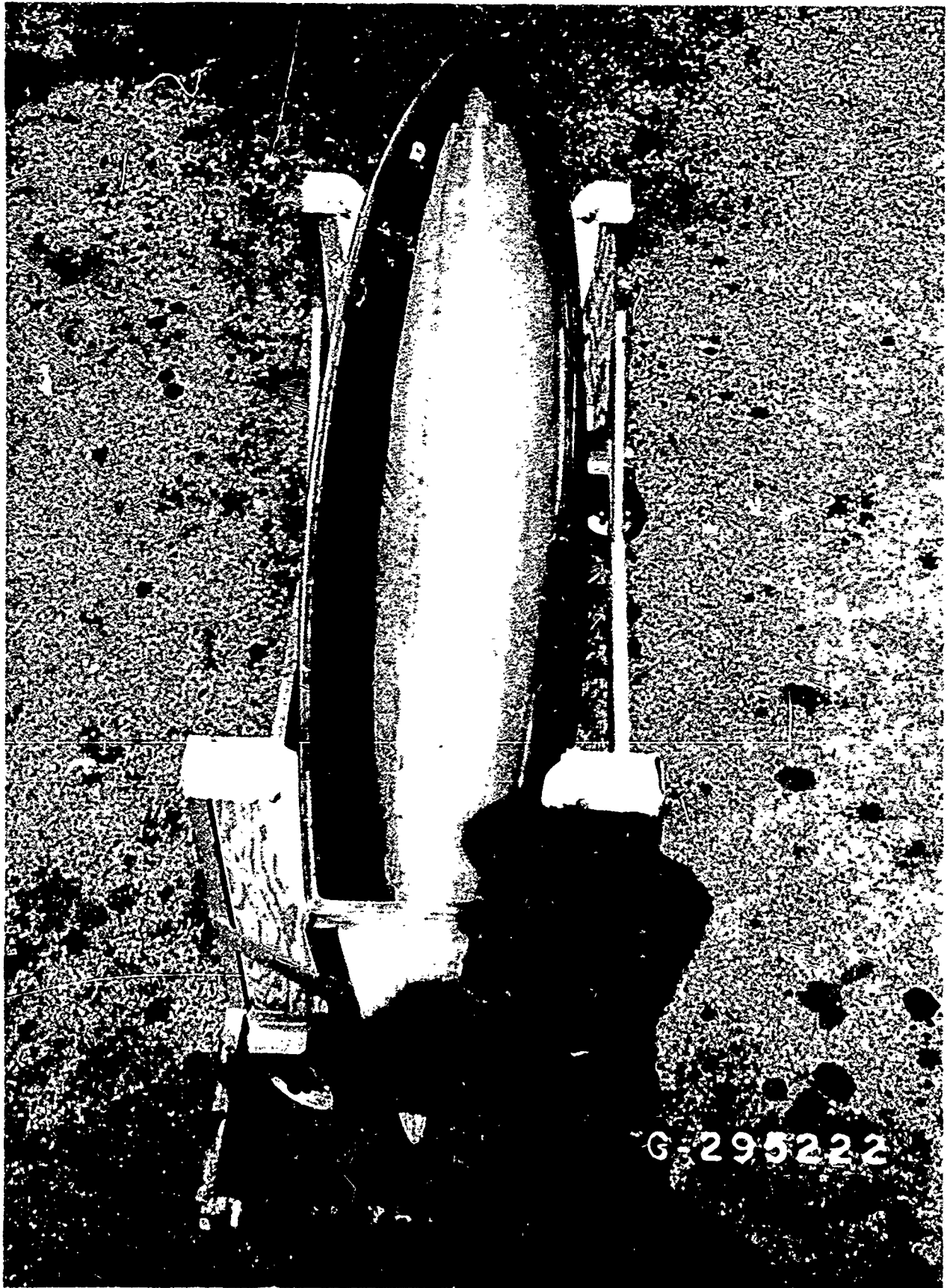


Figure 22. Completed Fin Pod - Note Discontinuity of Aft Sections

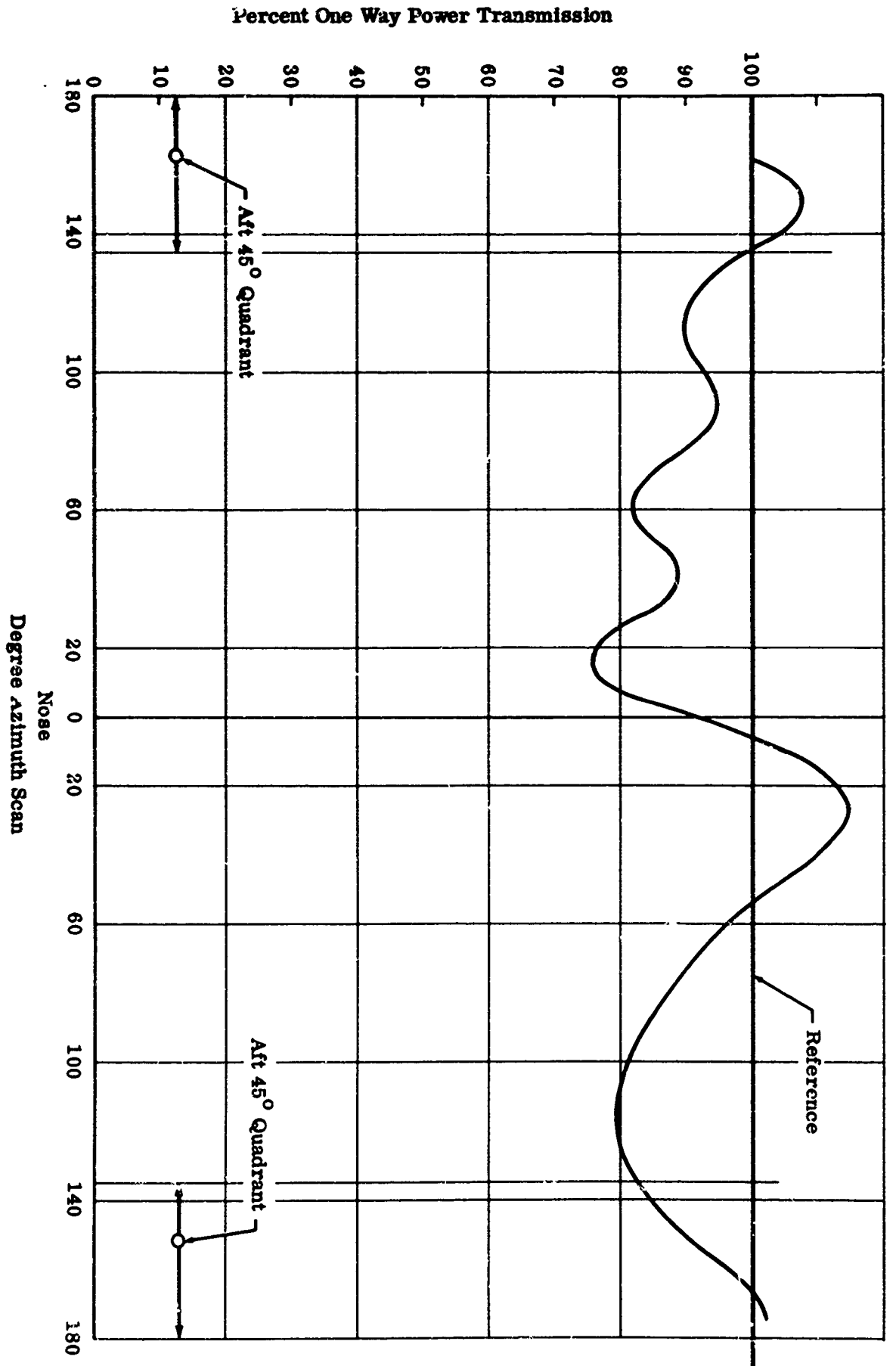


Figure 24. Transmission With System Antenna Vertical Fin
 Radome at Frequency 15
 Vertical Polarization

Proprietary Information

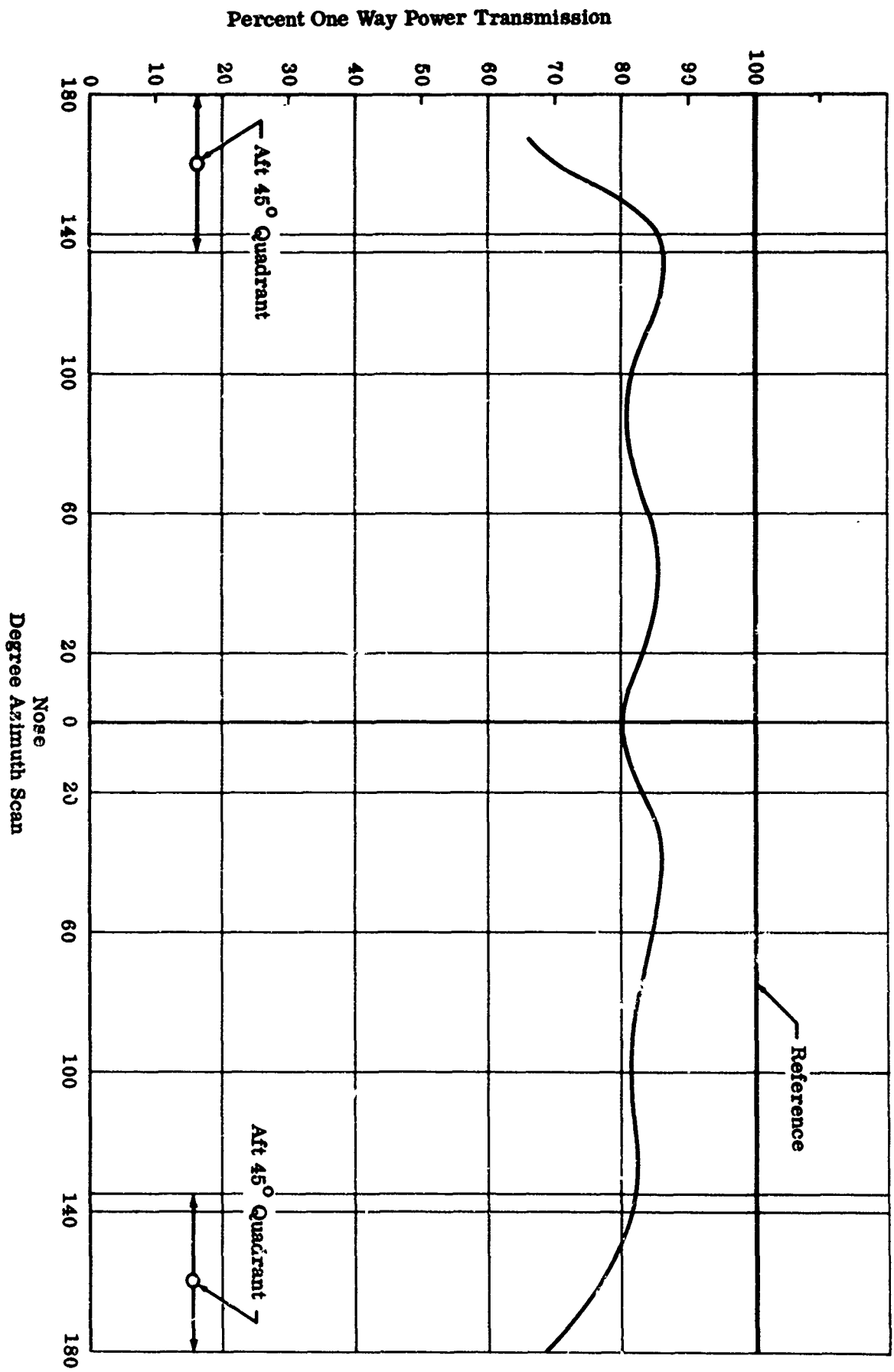


Figure 25. Transmission with Standard Gain Horn Vertical Fin
 Radome at Frequency f_5
 Vertical Polarization

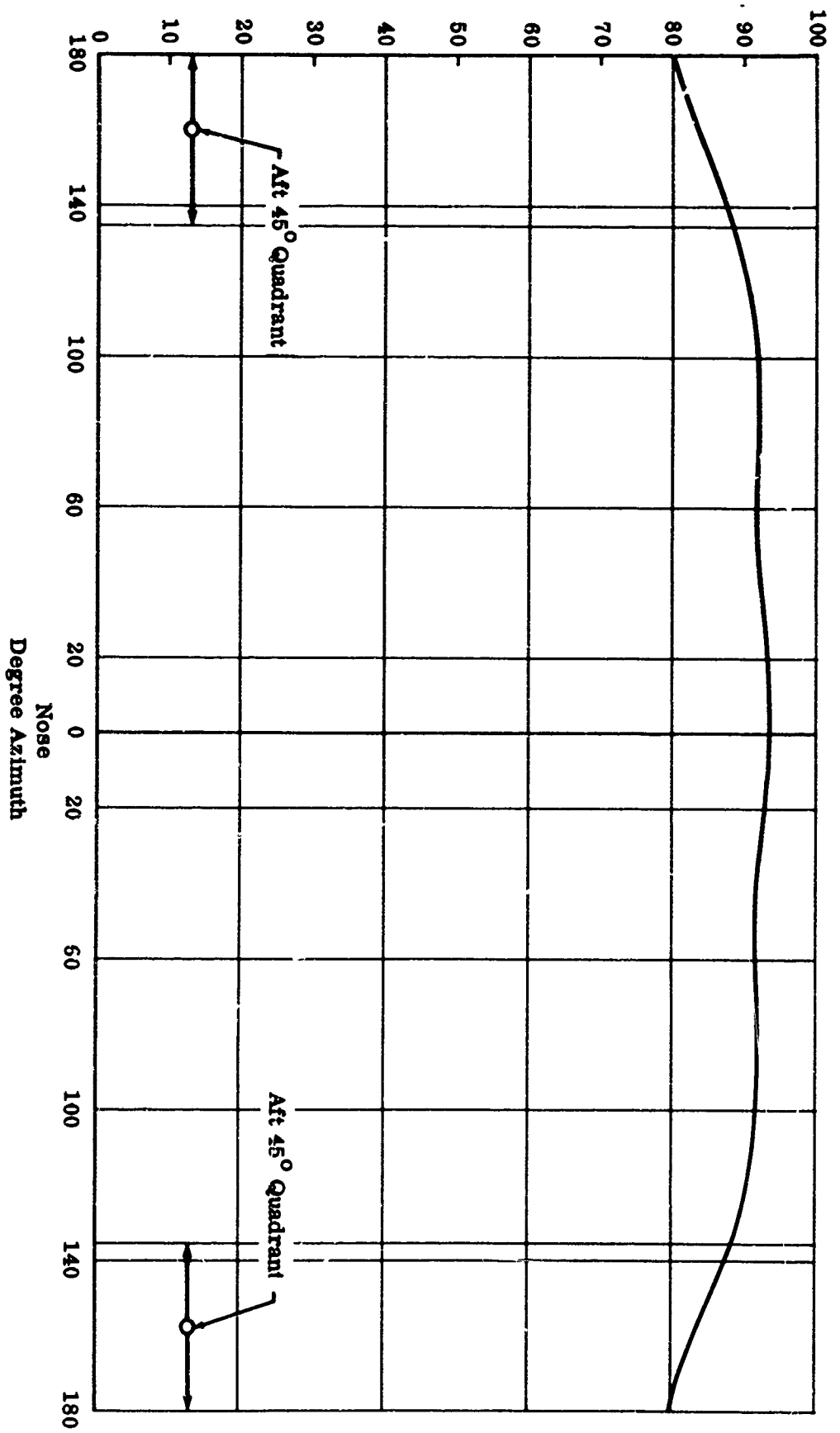


Figure 26. Total Transmission Computer Optimization Program Vertical Fin Radome at Frequency f_5 Vertical Polarization

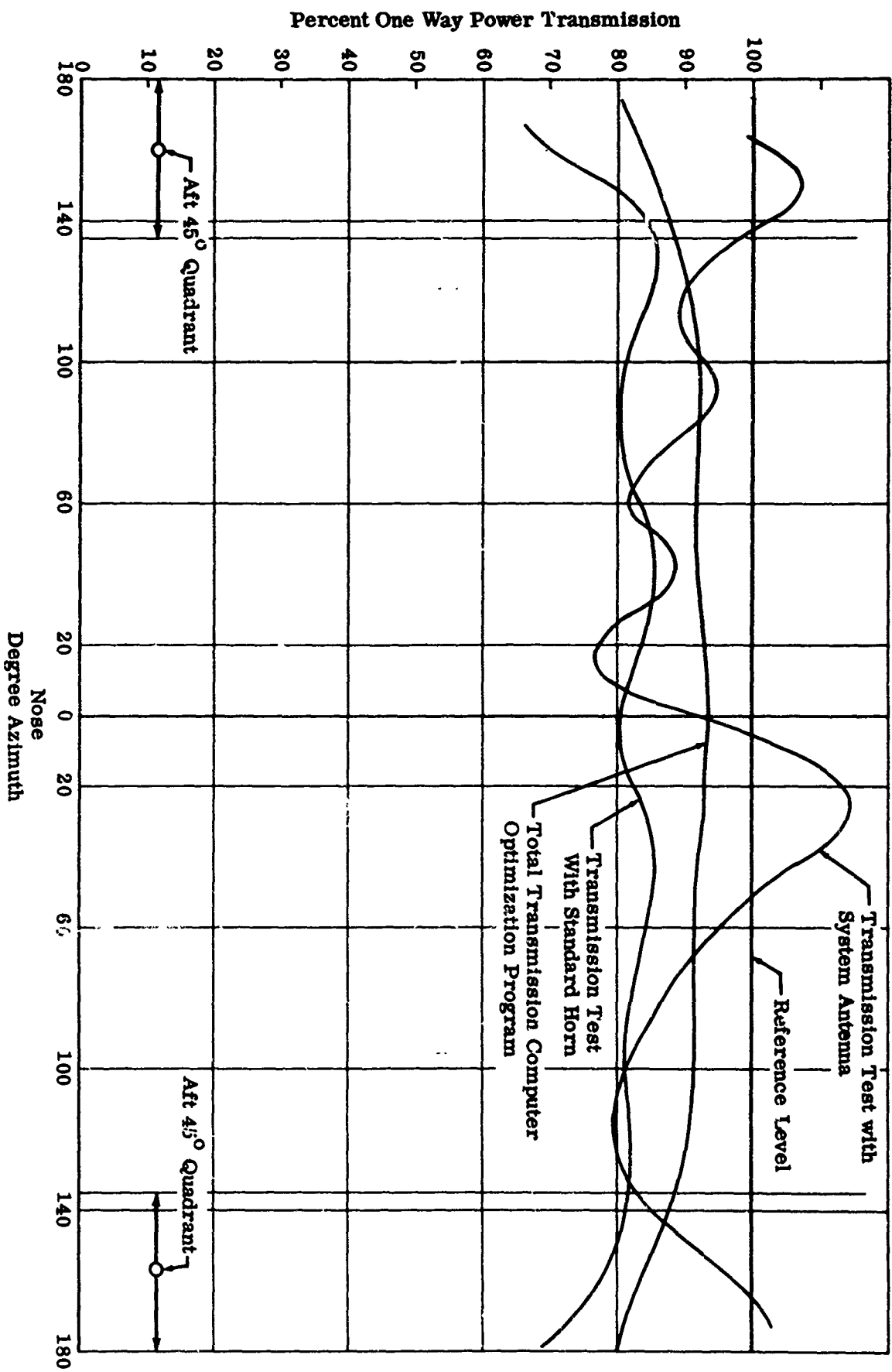


Figure 27. Transmission Comparison Vertical Fin Radome
At Frequency f_5
Vertical Polarization

THE SCANNABLE RAY-FED RADOME

Stephen J. Gotkis
Antenna Laboratory
Department of Electrical Engineering
The Ohio State University
Columbus, Ohio, 43210

Acknowledgments

The author is indebted to Dr. J.H. Richmond for many helpful suggestions. Credit is also due to Mr. E. Turner whose initial concepts led to the development of the prototype antenna.

The research reported in this paper was supported in part by Contract AF 33(615)-1081 between The Ohio State University Research Foundation and the Research and Technology Division, Air Force Systems Command, United States Air Force, Wright-Patterson Air Force Base, Ohio, 45433.

Introduction

A solid metal nose cone provides a missile or aircraft the greatest physical protection from the external elements. However such a shield totally obstructs the performance of a radar antenna or other radiating device enclosed by the protective "radome". The object of this paper is to discuss a novel radome technique for providing a maximum mechanical-strength structure and at the same time afford efficient energy transfer characteristics and good pattern fidelity.

To take advantage of the protective properties of the solid metallic surface, it was proposed¹ that an electromagnetic window be built consisting of a dipole array connected to an identical array on the opposing face of a metal sheet by a non-radiating transmission line. This technique permits a minimum structural weakening of the radome wall, necessitating only the passing of a minute transmission line through the wall.

In this paper methods of optimizing transmission through the integrated antenna-radome will be discussed. A condition has been derived for maximum power transfer and transmission efficiency calculations have been made applying this condition. A suitable Thevenin equivalent circuit for calculation of power transfer for any

element in the array has been derived. The effect of scanning in one plane on element driving point impedance and radome transmission efficiency have been shown.

A prototype model of this integrated antenna-radome was constructed. This model is shown in Fig. 1. It consists of a staggered fifteen by fifteen element array of closely spaced dipoles over a large flat "ground plane" representing the radome wall. An extension of the radiating wire serves as a connecting transmission line to the identical elements on the other side of the metal wall. Experimental results from the prototype model are shown.

Background

The device under consideration will be separated into two passive arrays for purposes of analysis. Each array consists of dipoles above a ground plane with the input terminals open circuited. This is shown in Fig. 2. For every pair of terminals in one array, there is a corresponding pair of terminals on the identical companion array.

In analyzing this array several simplifying assumptions are necessary. The arrays will be considered to be finite, but of such a great extent, that the input impedance at every pair of terminals is identical. Of course, this requires that edge effects of the exterior elements be neglected.

Sinusoidal currents of equal magnitude will be assumed to flow on the receiving elements when they are short circuited. This makes possible rapid calculation of mutual impedances between elements. These currents will, however, be a function of the incident radiation, assumed to be a plane wave at an arbitrary angle.

When the companion terminals of the second array are attached to the original array, every dipole in the mating array, for example that one connected to terminals $1'-1'$, will be treated as a passive load attached to the terminals $1-1$ of the original receiving dipole. With the above assumption of large array size every load will be considered equal. The receiving antennas with their equivalent loads are shown in Fig. 3.

The terminals $1-1$, $2-2$, $3-3$, etc., will be treated as the input terminals to the actual transmitting (or receiving) half-wave dipole and connecting transmission lines will be ignored.

When radiant energy is incident on the elements in the array, some of the energy will be absorbed in the equivalent loads 1'-1', 2'-2', 3'-3', etc., and some will be reradiated by the dipoles 1-1, 2-2. If the energy absorbed by the equivalent loads is considered to be the energy radiated by the companion array of dipoles, the actual power transmitted through the integrated antenna-radome can be found. A prerequisite to the design of such a device is finding the conditions for which the equivalent loads absorb maximum power, corresponding to maximum transmission.

The problem of optimizing the power absorbed by a center-loaded antenna has been treated for many cases of one and two elements with and without a ground plane.^{2, 3} Often scattering and absorbing cross-sections are found but there is confusion created by the definition of "forward scatter", (which in this case would also be energy transmitted). Direct computation of the power absorbed by the equivalent loads as a function of the available power to the receiving array appears to be the most direct approach to determining the transmission efficiency.

Analysis

Considering the array of Fig. 4, with the given coordinate system, it is possible to develop a Thevenin equivalent circuit for each dipole pair in the array. Symmetry conditions and the previous assumptions for a large array require that every equivalent circuit be identical.

By application of basic circuit theory, the current dipole in a representative load of any dipole is found to be:

$$(1) \quad I_l = \frac{V_{oc}}{Z_l + Z_{dp}}$$

where V_{oc} = open circuit voltage at 1-1 or any pair of terminals
 Z_{dp} = driving point impedance at terminals 1-1
 Z_l = equivalent load impedance 1'-1'.

$$(2) \quad V_{oc} = I_{sc} \cdot Z_{dp}$$

where I_{sc} is the short circuit current in any antenna in the presence of all other elements.

Several methods are available to evaluate the short circuit current in an element. One technique is to apply the appropriate boundary conditions to the incident and scattered fields or voltages.⁶ Along any given dipole this implies that

$$(3) \quad \int_{-\frac{\lambda}{4}}^{\frac{\lambda}{4}} E_i \cos \frac{2\pi}{\lambda} Z dZ = \sum_{n=0}^N \int_{-\frac{\lambda}{4}}^{\frac{\lambda}{4}} j30I \left(\frac{e^{-jk r_1 + \mu}}{r_1} + \frac{e^{-jk r_2 + \mu}}{r_2} \right) \cos \frac{2\pi}{\lambda} Z dZ \\ - \sum_{n=0}^N \int_{-\frac{\lambda}{4}}^{\frac{\lambda}{4}} j30I \left(\frac{e^{-jk \rho_1 + \mu}}{\rho_1} + \frac{e^{-jk \rho_2 + \mu}}{\rho_2} \right) \cos \frac{2\pi}{\lambda} Z dZ$$

where E_i is the total incident electric field and its tangential components are equal to zero on any dipole and on the ground plane. N is the total number of dipoles in the array.

$$r_1 = [(n_x d_x \sin \theta \sin \phi)^2 + (n_y d_y \cos \theta)^2]^{1/2}$$

$$r_2 = [(n_x d_x \sin \theta \sin \phi)^2 + (n_y d_y \cos \theta + \lambda/2)^2]^{1/2}$$

$$\rho_1 = [(n_x d_x \sin \theta \sin \phi)^2 + (n_y d_y \cos \theta)^2 + (2h \sin \theta \cos \phi)^2]^{1/2}$$

$$\rho_2 = [(n_x d_x \sin \theta \sin \phi)^2 + (n_y d_y \cos \theta + \lambda/2)^2 + (2h \sin \theta \cos \phi)^2]^{1/2}$$

$n_x = n^{\text{th}}$ dipole in the x direction

$n_y = n^{\text{th}}$ dipole in the y direction

h = height above the ground plane

μ = phase difference between dipoles due to oblique scanning

$k = 2\pi/\lambda$.

Solving Eq. (3) for the short-circuit current I_{sc} yields:

$$(4) \quad I_{sc} = \frac{\frac{2}{\pi} E_i \sin(kh \sin \theta \cos \phi) \lambda}{Z_{dp}}$$

where Z_{dp} is the driving point impedance at the terminals of any one dipole. By comparison with Eq. (2) it is seen that

$$(5) \quad V_{oc} = \left[\frac{2}{\pi} E_i \sin(kh \sin \theta \cos \phi) \lambda \right].$$

In determining the short circuit current it was necessary to evaluate the mutual impedance between the center of a dipole and all the elements and images in the array. By adding to this mutual impedance the input impedance of a dipole over a ground plane the resultant driving point impedance as a function of the coordinate angles ϕ and θ may be obtained.

A computer program was written to calculate and sum mutual impedances between a dipole in the array and every other element. The program was arranged to first calculate the mutual effect on a dipole in the center of a 3 by 3 array, then a 5 by 5 array, and for progressively larger arrays where the number of rows and columns are increased by two for each iterated computation. For all angles of scan and the various spacings tried, the mutual impedance between the center dipole and its surrounding elements was essentially constant for square arrays greater than 11 by 11 elements. This convergence of mutual impedance has been examined in the literature⁴ and has been observed experimentally.⁵ The following calculations for array efficiency were based on the driving point impedance data for elements in 11 by 11 arrays.

All the necessary calculations have now been performed for construction of the Thevenin equivalent circuit for a dipole and its equivalent load. The circuit is shown in Fig. 5. The dipole may be represented as a Thevenin voltage generator I_{sc} , Z_{dp} in series with the driving point impedance Z_{dp} . The load impedance Z_l connected across the terminals 1-1, represents the driving point impedance of the mating dipole in the companion array.

From this equivalent circuit the power dissipated in the load, Z_l , can be found. This power, as mentioned, is the same as the power that would be radiated by the mating dipole and is, in effect, the power transmitted by an element in the integrated antenna radome. The total power transmitted through the device is then equal to the power absorbed by an equivalent load times the number of elements in the entire array.

From inspection of the dipole equivalent circuit in Fig. 5, it is seen that maximum power is absorbed in the load Z_l when $Z_l = Z_{dp}^*$ (the complex conjugate of Z_{dp}). In the following calculations it will be assumed Z_l satisfies this condition for maximum power transfer.

Care must be taken not to attach any physical significance to power absorbed by Z_{dp} of the representative circuit.³ This impedance is useful in finding the power delivered to the equivalent load but is a part of the internal Thevenin circuit. In an array of n^2 dipoles the total power transmitted through the array will be $n^2 P_l$ where P_l is the power absorbed in any load.

With the aid of the Thevenin circuit it is now possible to calculate the efficiency of a large array. With every load adjusted for maximum power absorption the transmission efficiency may be expressed as:

$$(6) \quad \alpha = \frac{\text{power absorbed in equivalent loads}}{\text{power incident on the array area}} .$$

From the circuit parameters of Fig. 5

$$(7) \quad \alpha = \frac{\left[\frac{1}{2} \left(\frac{2}{\pi} E_i \sin(kh \sin \theta \cos \phi) \lambda \right)^2 n^2 \right] / [4R_L]}{\left[\frac{1}{2} \frac{E_i^2}{Z_0} A_{\text{norm}} \right]}$$

where Z_0 is the impedance of free space

A_{norm} is the aperture area normal to the direction of propagation of the incident radiation.

Alternately by application of reciprocity relations^{6,7} and from basic antenna definitions, the power absorbed in the load of a cylindrical antenna is $A_{em} \cdot S_i$ where:

A_{em} = maximum effective area

S_i = incident Poynting vector.

By equating effective area to gain,

$$(8) \quad A_{em} = \frac{\lambda^2}{4\pi} G(\theta, \phi)$$

where $G(\theta, \phi)$ is the directive gain. Making use of these identities another expression for efficiency is

$$(9) \quad \alpha = \frac{\lambda^2 G(\theta, \phi)}{4\pi A_{\text{norm}}}$$

Both Eqs. (7) and (9) reduce to

$$(10) \quad \alpha = \frac{n^2 Z_0 \sin^2 (kh \sin \theta \cos \phi)}{\pi^2 R_L A_{\text{norm}} (\lambda^2)} \quad \text{with } A_{\text{norm}} (\lambda^2) \text{ in square wavelengths.}$$

Results

Figure 6 shows driving point resistance for a very thin dipole in a large array for three different spacings as a function of scan angle. In Array 1 $d_x = \lambda$, in Array 2 $d_x = .5\lambda$ and in Array 3 $d_x = .3\lambda$. In all arrays $d_y = .6\lambda$. Resistance ranges $\pm 12\%$ from the medium value in Array 3 and $\pm 7\%$ from the mean in Array 1. Array 2, the most widely spaced shows a rapid variation in resistance.

Transmission efficiencies for these three arrays are shown in Fig. 7. Arrays 1 and 3 are above 90% efficient for ϕ ranging to 50° , with Array 3 being better than 96% for the angular range. Array 2 again shows somewhat more erratic behavior with transmission efficiencies falling rapidly.

In Fig. 8 the power loss due to mismatch of the dipoles during scanning is shown. The dipoles were conjugate matched by a passive quarter-wave transformer at 0° . The ratio of calculated power absorbed to maximum possible absorption is shown for Array 3. The calculations were made for infinitely thin dipoles and for dipoles of length to thickness ratio of 20. The curves indicate simple matching techniques might be used for one plane scanning over a reasonable range.

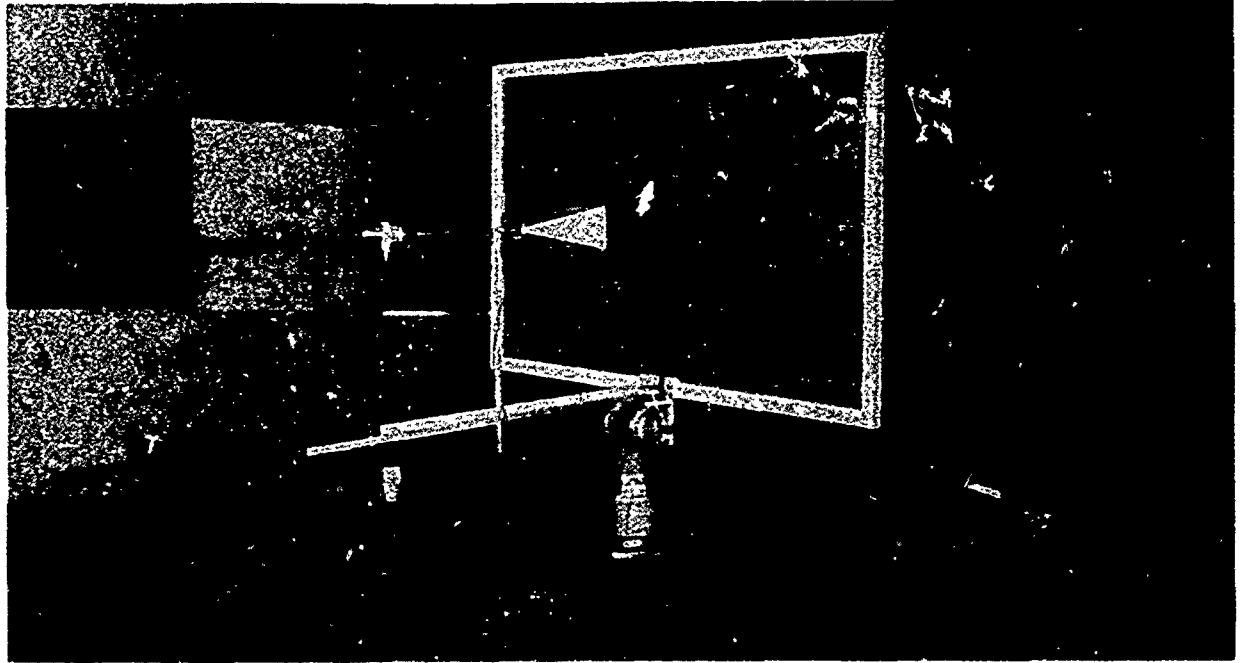
Patterns were taken on the prototype antenna and are shown in Fig. 9. The patterns show effects of the electromagnetic window on the radiation pattern for normal and 15 degree incidence. No attempt was made to match any elements in this array and the actual aperture was four wavelengths square.

Conclusions

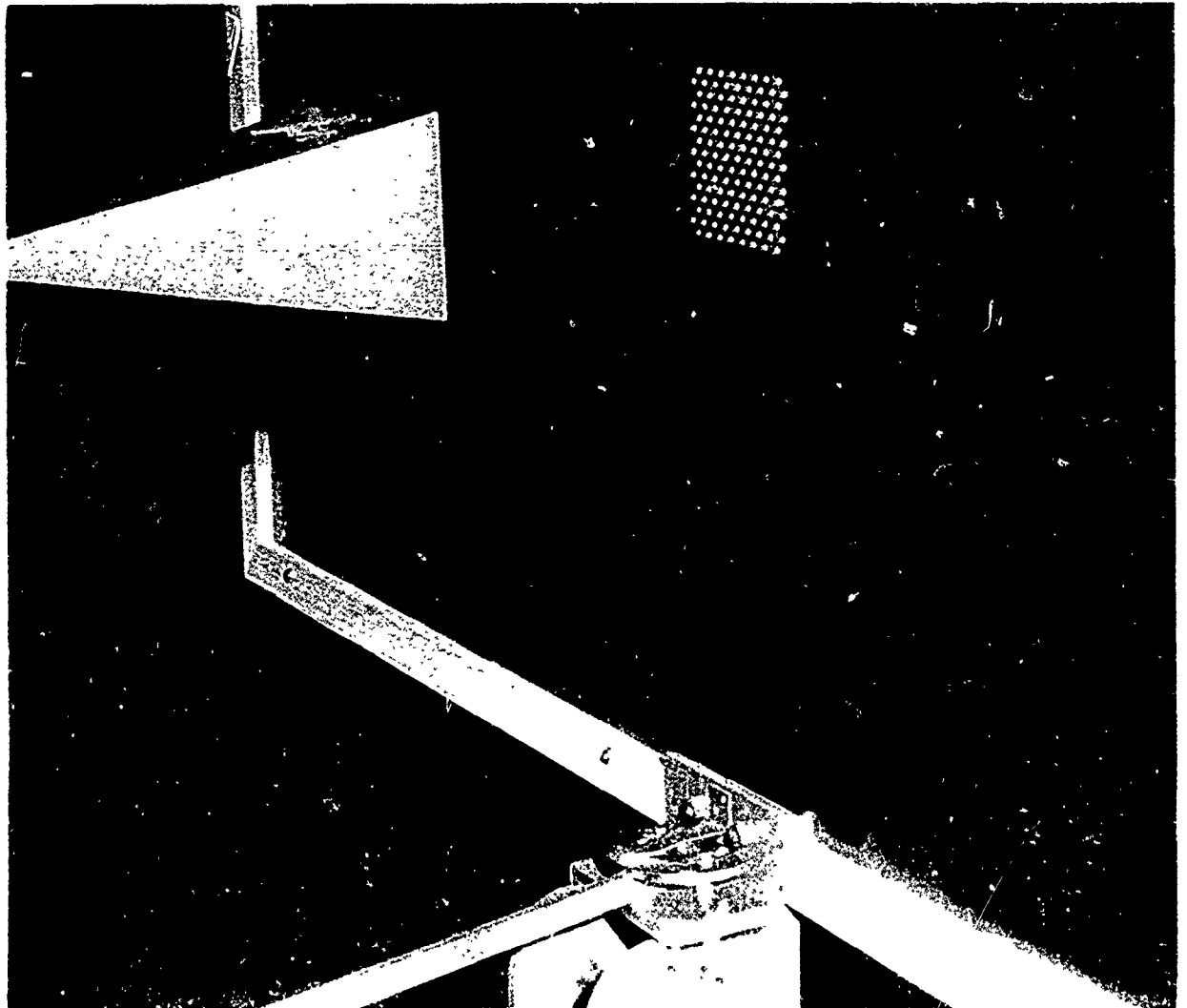
Calculations and results of tests on the prototype antenna indicate probable success for this type of electromagnetic window. Further calculations should be made to optimize efficiency and matching techniques must be examined. Experimental work is now being conducted on a parallel plate waveguide with probes, simulating a semi-infinite array of dipoles. It is hoped to obtain efficiency-vs-scan information from this model by simple measurements. Tuning can be effected by frequency variation.

References

1. Baechle, J.R., "Results of Some Preliminary Tests on the Prototype of a Concept in the Integration of the Design of an Antenna and Electromagnetic Window for Aerospace Vehicles," Report 1382-9, 30 April 1963, Antenna Laboratory, Department of Electrical Engineering, The Ohio State University, Columbus, Ohio.
2. King, R.W.P., Theory of Linear Antennas, Harvard University Press, Cambridge, Mass., 1956.
3. Green, R.B., "The General Theory of Antenna Scattering," Report 1223-17, 30 November 1963, Antenna Laboratory, Department of Electrical Engineering, The Ohio State University, Columbus, Ohio.
4. Allen, J.L., "Gain and Impedance Variation in Scanned Dipole Arrays," IRE Transactions on Antennas and Propagation, Vol. AP-10, September 1962.
5. Kurtz, L.A., et al., "Mutual-Coupling Effects in Scanning Dipole Arrays," IRE Transactions on Antennas and Propagation, Vol. AP-9, September 1961.
6. Richmond, J.H., unpublished notes on antenna theory, Antenna Laboratory, The Ohio State University, Columbus, Ohio.
7. Kraus, J.D., Antennas, McGraw-Hill Book, Co., Inc., New York, N.Y., 1950.



(a)



(b)

Fig. 1.

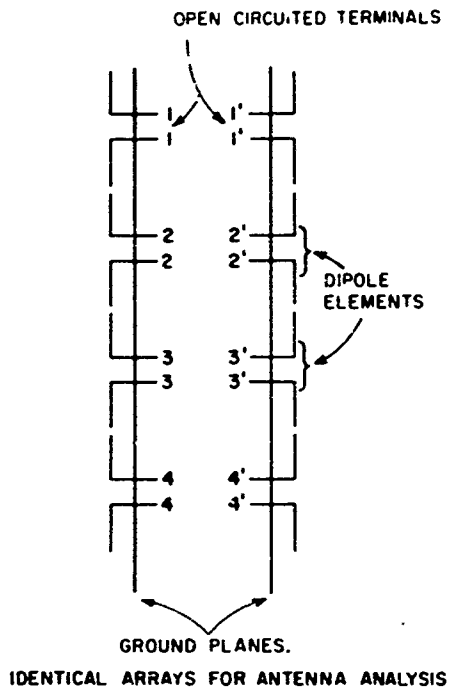


Fig. 2.

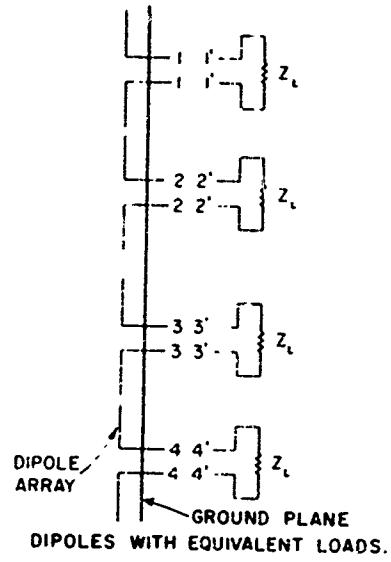


Fig. 3.

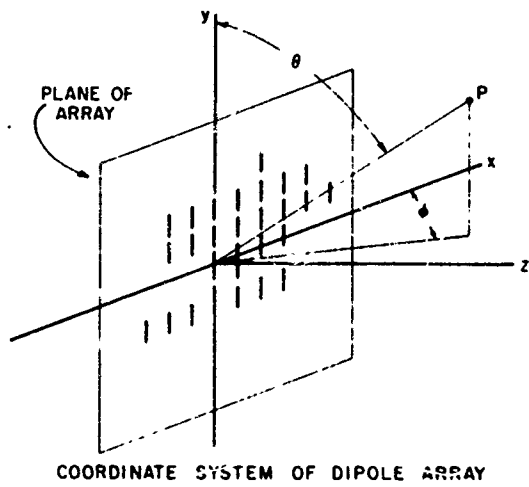


Fig. 4.

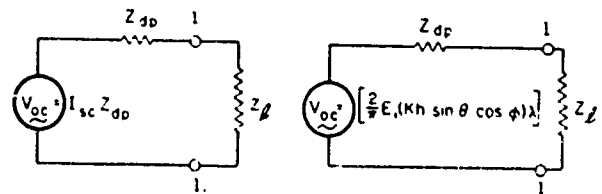


Fig. 5.

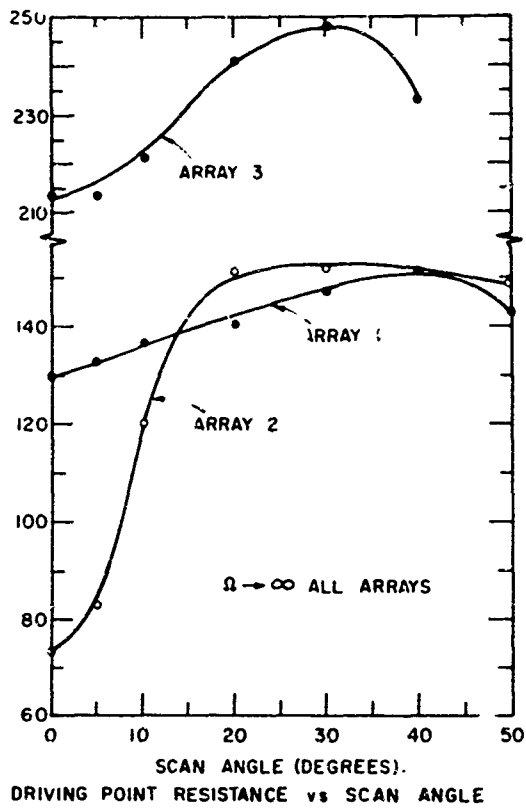


Fig. 6.

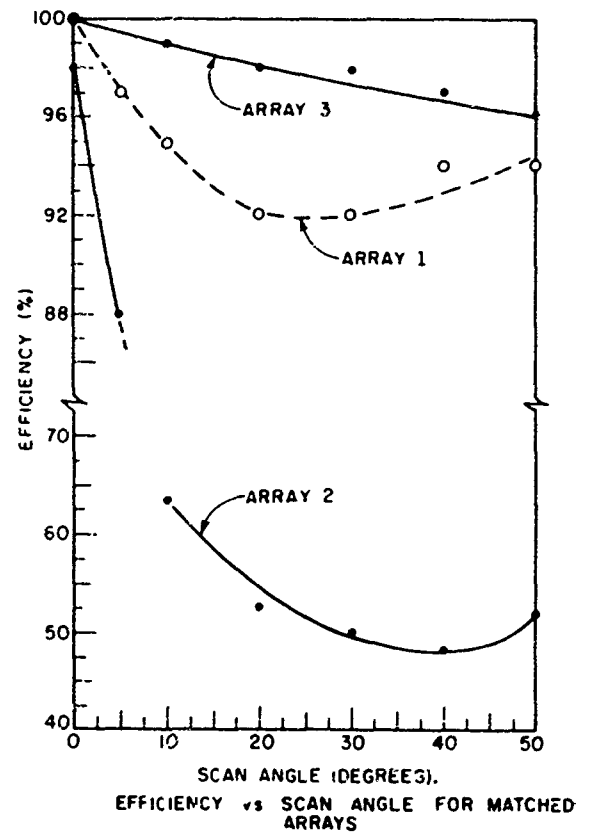


Fig. 7.

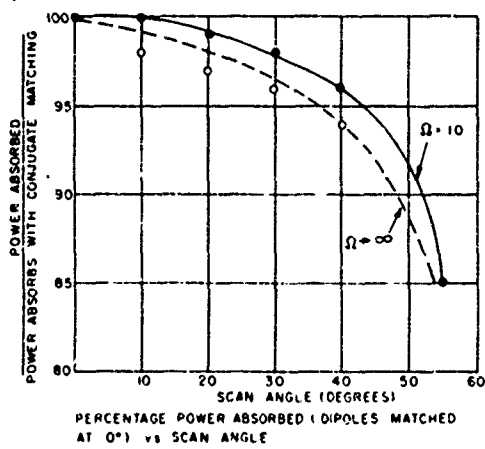


Fig. 8.

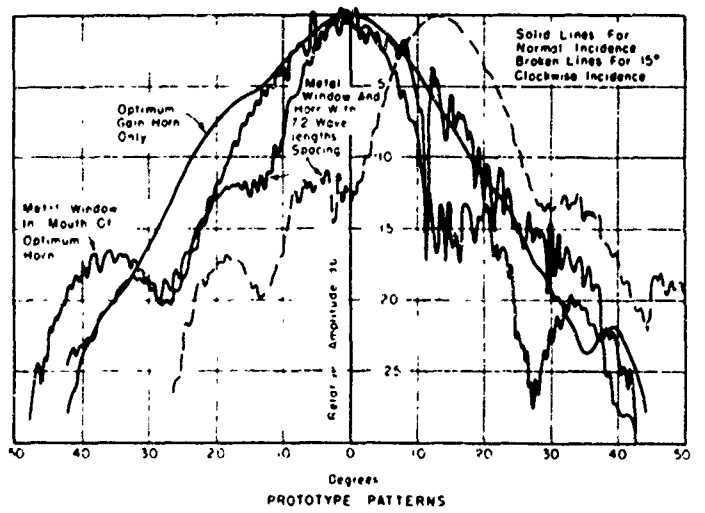


Fig. 9.

ESD 64-112R

AN APPLICATION OF RADOME
BROADBANDING

By

Peter Zuzolo
Chandler Hom
Stanley Jurczak

June 3, 1964

Prepared for

THE SEVENTH SYMPOSIUM ON
ELECTROMAGNETIC WINDOWS

Sponsored by

Research Technology Division
Wright - Patterson Air Force Base
and the Ohio State University
at Ohio State University
Columbus, Ohio
June 2nd to 4th, 1964

REPUBLIC AVIATION CORPORATION
ENGINEERING DIVISION
Farmingdale, L.I., New York

AN APPLICATION OF RADOME BROADBANDING

P. Zuzolo, C. Hom and S. Jurczak

Republic Aviation Corporation
Farmingdale, New York

A. Introduction

Multilayer sandwich configurations have been investigated extensively in recent years for broadband radome applications. This design approach is sound as far as theoretical calculations are concerned. However, the development and fabrication of such radomes, especially in complex shapes, are time consuming and costly.

This paper presents an application of radome broadbanding using a simple A-sandwich design.

B. A-Sandwich Design Techniques

The electrical properties of an A-sandwich radome will be examined by starting with an established transmission formula

$$|T|^2 = \frac{(1 - |P_2|^2)^2}{(1 - |P_1|^2) + 4|P_1|^2 \sin^2(\angle P_2 - \phi_c)} \quad (1)$$

where P_1 is the reflection coefficient at the outer skin and air interface given by the following equation

$$P_1 = \frac{r_1 + r_2 \text{EXP}(-2j\phi_s)}{1 + r_1 r_2 \text{EXP}(-2j\phi_s)} \quad (2)$$

and P_2 is the reflection coefficient at the skin and core interface given by the following equation

$$P_2 = \frac{r_2 + r_1 \text{EXP}(-2j\phi_s)}{1 + r_1 r_2 \text{EXP}(-2j\phi_s)} \quad (3)$$

In equations (2) and (3), r_1 and r_2 are the Fresnel interface reflection coefficients given by

$$r_1 = \frac{\sqrt{\alpha_e} - 1}{\sqrt{\alpha_e} + 1} \quad (4)$$

and

$$r_2 = \frac{\sqrt{\beta_e} - \sqrt{\alpha_e}}{\sqrt{\beta_e} + \sqrt{\alpha_e}} \quad (5)$$

The effective skin dielectric constant α_e is given by the following equations:

$$\text{For perpendicular polarization } \alpha_e = \frac{\alpha - \sin^2 \theta}{\cos^2 \theta} \quad (6)$$

$$\text{and for parallel polarization } \alpha_e = \frac{\alpha^2 \cos^2 \theta}{\alpha - \sin^2 \theta} \quad (7)$$

where α is the value of skin dielectric constant at a specific frequency

θ is the incidence angle

The effective core dielectric constant β_e is given by the following equations:

$$\text{For perpendicular polarization } \beta_e = \frac{\beta - \sin^2 \theta}{\cos^2 \theta} \quad (8)$$

$$\text{and for parallel polarization } \beta_e = \frac{\beta^2 \cos^2 \theta}{\beta - \sin^2 \theta} \quad (9)$$

where β is the value of core dielectric constant at a specific frequency

The angle ϕ_c is 2π times the electrical thickness of the core.

$$\phi_c = \frac{2\pi d_c}{\lambda_0} \sqrt{\beta - \sin^2 \theta} \quad (10)$$

where d_c is the physical core thickness.

The angle ϕ_s is 2π times the electrical thickness of the skin.

$$\phi_s = \frac{2\pi d_s}{\lambda_0} \sqrt{\alpha - \sin^2 \theta} \quad (11)$$

where d_s is the physical skin thickness.

Referring to equations (6) and (7), if the angle of incidence is small, the effective skin dielectric constant approaches to the actual dielectric constant of the material employed. The same condition will hold true for the core material used.

Furthermore, if the core material is chosen such that its dielectric constant is low relative to air, then the magnitudes of the Fresnel interface reflection coefficients r_1 and r_2 will be approximately equal to each other but opposite in sense, i.e.

$$r_1 \approx -r_2 \quad (12)$$

$$\text{or } |r_1| \approx |r_2|$$

If the above conditions are satisfied, it follows that

$$|\rho_1|^2 \approx |\rho_2|^2 \quad (13)$$

Substitute equation (13) into equation (1) to obtain the following relationship:

$$|T|^2 = \frac{(1 - |\rho_1|^2)^2}{(1 - |\rho_1|^2)^2 + 4|\rho_1|^2 \sin^2(\alpha \rho_2 - \phi_c)} \quad (14)$$

Equation (14) is a standard form of an efficiency equation. If we let

$$A = (1 - |\rho_1|^2)^2$$

$$B = 4|\rho_1|^2$$

$$C = \sin^2(\alpha \rho_2 - \phi_c)$$

the transmission efficiency equation assumes the form

$$|T|^2 = \frac{A}{A + BC} \quad (15)$$

Maximum power transmission can be obtained if the term BC in the denominator is zero. Zero condition can be achieved if either B is zero or C is zero. Also, high transmission can be realized if the product of B·C is small. This property of an A-sandwich dielectric sheets will be used to design a broad-band frequency radome.

The approach chosen is to minimize the value B by a proper choice of skin thickness and the value C by a proper choice of core thickness.

a. Skin thickness consideration

The term B is a function of ρ_1 . ρ_1 as given in equation (2) can be written in the following form:

$$\rho_1 = - \left[\frac{(r_1 + r_2 \cos 2\phi_s) - j(r_2 \sin 2\phi_s)}{(1 + r_1 r_2 \cos 2\phi_s) - j(r_1 r_2 \sin 2\phi_s)} \right] \quad (16)$$

To obtain optimum electrical characteristics, the skin thickness must be chosen so that the numerator of ρ_1 is approximately zero, i.e. the following conditions must be satisfied.

$$r_1 + r_2 \cos 2 \phi_s \approx 0 \quad (17)$$

$$r_2 \sin 2 \phi_s \approx 0 \quad (18)$$

Substitute equation (12) into equations (17) and (18); the above conditions can then be approximated by

$$r_1 - r_1 \cos 2 \phi_s \approx 0 \quad (19)$$

and

$$- r_1 \sin 2 \phi_s \approx 0 \quad (20)$$

Solving the above equations yield

$$\cos 2 \phi_s \approx 1 \quad \text{and} \quad \sin 2 \phi_s \approx 0$$

$$\text{or} \quad \phi_s = 0 \quad \text{and} \quad n \pi \text{ radians}$$

where n is any positive integer ($n = 1, 2, 3, 4, \dots$ etc.)

For these values of ϕ_s , it can be shown that the numerator of ρ_1 is approximately equal to zero. The value of skin thickness for optimum transmission characteristics at a given design angle and frequency can now be obtained from equation (11) with the above values of ϕ_s .

For the case when $\phi_s = n \pi$, the computed skin thickness will generally be too thick for practical application. For the case when $\phi_s = 0$, the theoretical skin thickness will also be zero. Since zero skin thickness is not physically realizable, it is suggested that a compromise solution would be to choose a thin skin. The acceptable value of this skin will be determined by structural and environmental considerations.

b. Core thickness consideration

The term C is a sine function which is determined by the core thickness once the skin thickness has been chosen. In order for the sine function to vanish, the angle ($4\rho_s - \phi_c$) must be zero or $n \pi$. The above condition will be met if the value of core thickness satisfies the following equation:

$$d_c = \frac{\lambda_0}{2\pi \sqrt{\beta - \sin^2 \theta}} \left\{ \pi \pi - \tan^{-1} \left[\frac{2(\alpha_e - 1) \sqrt{\beta_e \alpha_e} \sin 2\phi_s}{(\beta_e - \alpha_e)(1 + \alpha_e) + (\alpha_e - 1)(\beta_e + \alpha_e)(\cos 2\phi_s)} \right] \right\} \quad (21)$$

c. Transmission characteristics

In order to obtain broadband transmission characteristics the skin thickness will be chosen such that ϕ_s will be small throughout the frequency range. As can be expected, the value of core thickness that satisfies equation (21) will exhibit an oscillatory nature in the transmission curve with maxima occurring at frequencies satisfy equation (21). These maxima can be shifted within the frequency range by a differential variation of the core thickness.

The above properties of a three-layer dielectric sheets were carefully utilized to design a radome which has maxima occurring at the preferred frequency bands while maintaining broadband characteristics throughout the frequency range. The transmission requirement of a hypothetical application is shown in Figure 1. The broadband characteristics may be required up to 60 gigacycles with preferred frequency bands of operation as indicated.

The transmission curves were plotted from data obtained from IBM 7094 computer. The data presented are of approximate values since such effects as dielectric constants as a function of frequency, loss factor, etc., were neglected.

The minimum transmission efficiency for frequencies up to 60 gigacycles is 60 percent while at the preferred frequency bands it is greater than 80 percent.

The radome, as it is designed, is a structural support of another antenna system while it performs the primary function as a broadband radome.

C. Experimental and Fabrication Techniques

The development of this radome required close coordination between experimental data and fabrication changes. In order to meet the electrical requirement, the radome must have uniform transmission characteristics throughout most of the azimuth coverage except in a narrow region of waveguide runs. As a supporting structure, it must have the necessary structural integrity.

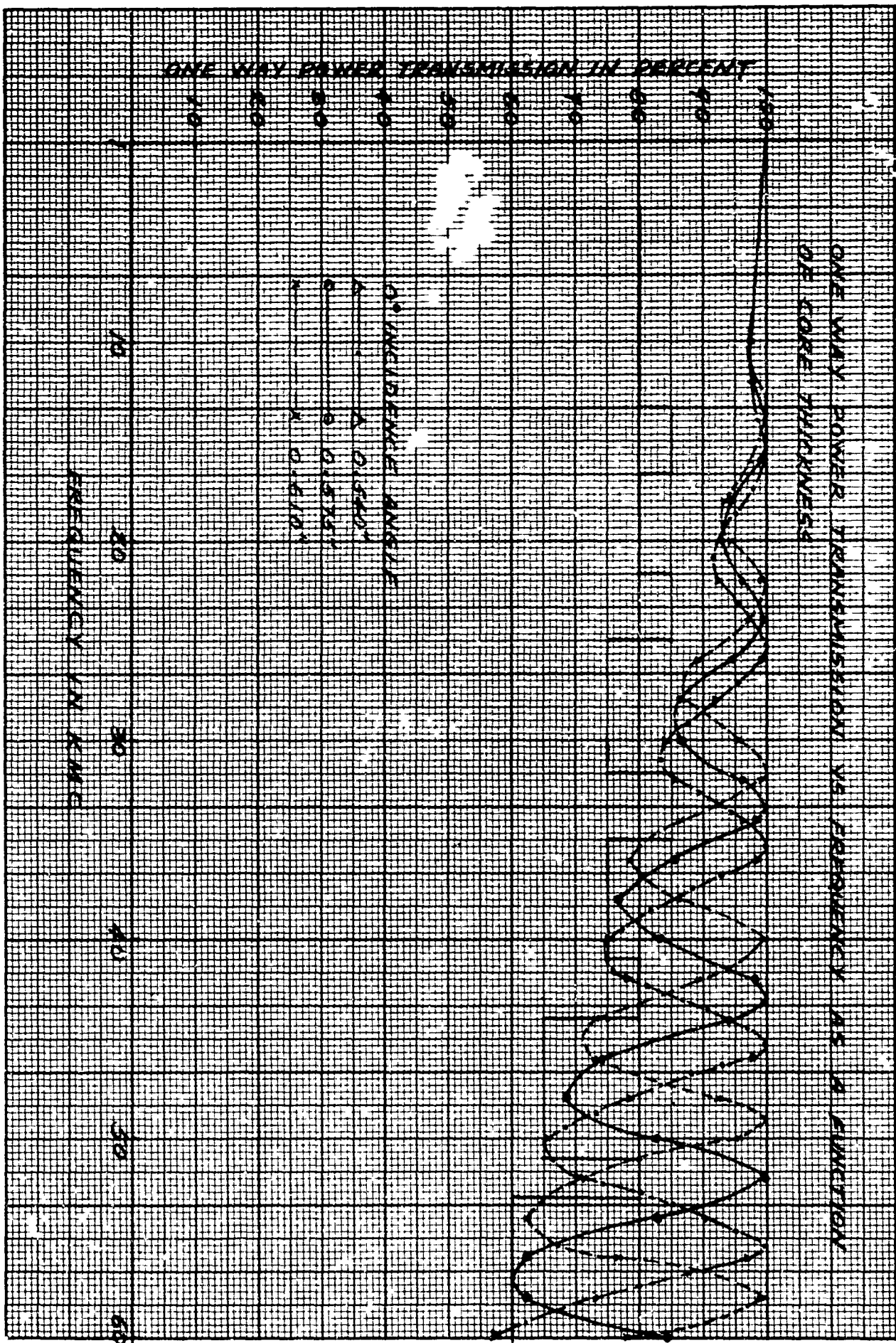


Figure 1 - COMPUTED TRANSMISSION CHARACTERISTICS AS A FUNCTION OF FREQUENCY

a. Electrical consideration

The core of the first prototype cone shaped radome consisted of two sections. Each section was hot foamed to shape from foamed polyurethane sheet. The skin and laminated flanges were made from type 181 fiberglass fabric impregnated with polyester resin. Figure 2 shows the die used for the fabrication of the cone shaped radome.

The first prototype was tested for transmission efficiency at the higher end of the operating frequency range. A representative set-up is shown in Figure 3 at Ka-band. The transmission curves is shown in Figure 4 for two frequencies covering a 360 degrees angular scan. It was noted that a 5 percent variation in transmission efficiency occurred at the butt joints of the core. This was due to the adhesive used for bonding the two sections together.

To eliminate this distortion, the core was made in one piece by machining a pre-cured block of "Lockfoam" with the skins overlap located at the RF blind spot. The improved transmission curves is shown in Figure 5. The slight variation was due to the geometry of the set-up and the rigidity of the supporting posts. This condition was subsequently improved and uniform transmission curves were obtained.

b. Structural consideration

Since the radome is a supporting structure for another antenna system, it must carry the entire weight of that system.

The prototype unit met all environmental and structural design requirements except lateral vibration test. The test set-up is shown in Figure 6. Various reinforcements were used at both the top and the bottom flanges (Figure 7). However, the approach did not prove completely satisfactory. It was found that the radome has a critical resonance that coincided with the dummy weight. Finally, the radome was modified to permit the installation of a rubber gasket on the flanges to isolate the radome structure from its associated hardware. The lateral vibration tests at 10 g's were conducted on the modified unit and there was no evidence of fracture or cracks in the radome.

D. Conclusion

A simple A-sandwich configuration has been successfully employed for a specific broadband application. (Figure 8). It is economical and time saving. This paper may encourage radome



Figure 3 - TRANSMISSION TEST SET-UP

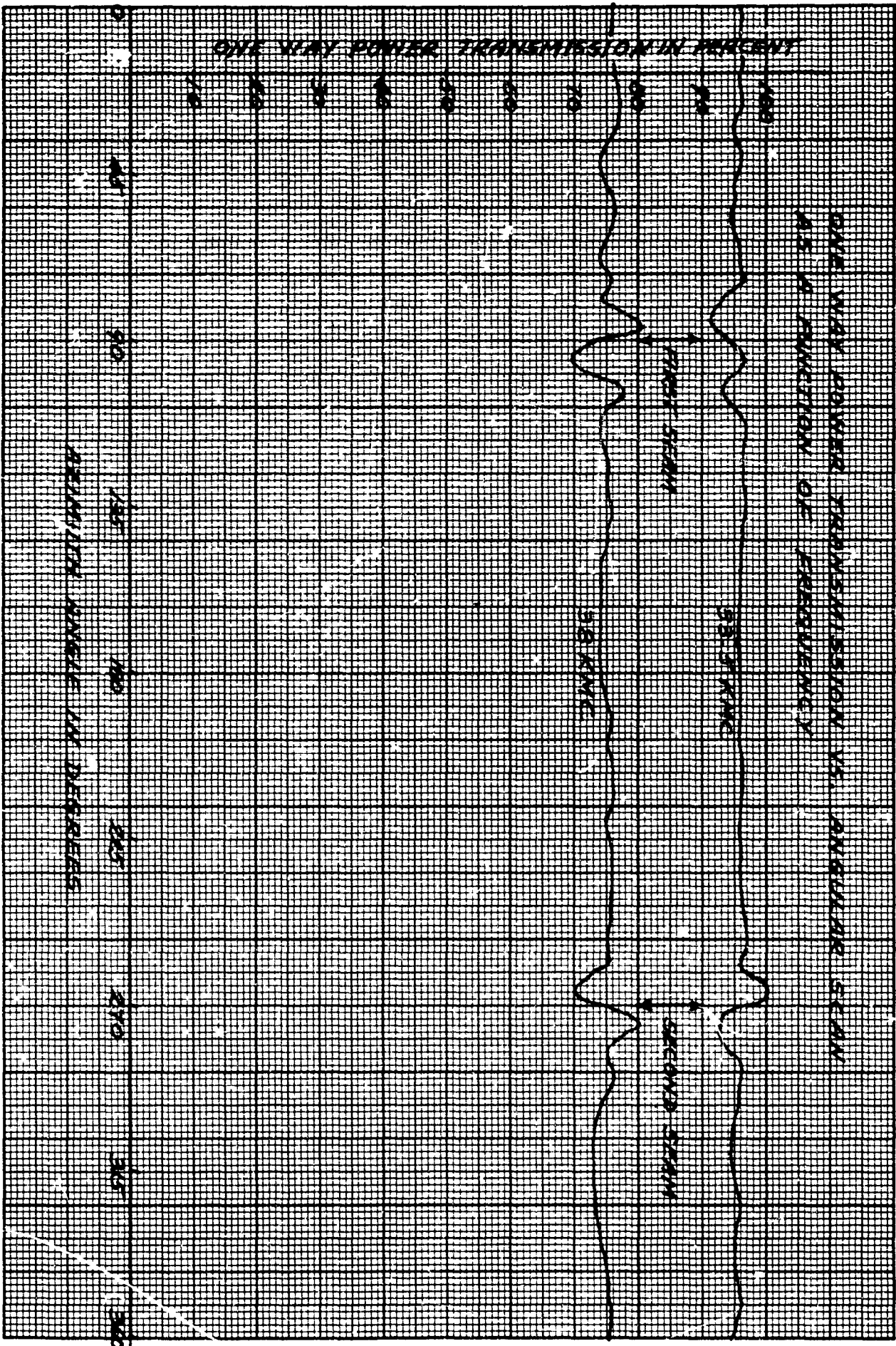


Figure 4 - EXPERIMENTAL TRANSMISSION CHARACTERISTICS OF PROTOTYPE AS A FUNCTION OF AZIMUTH ANGLE

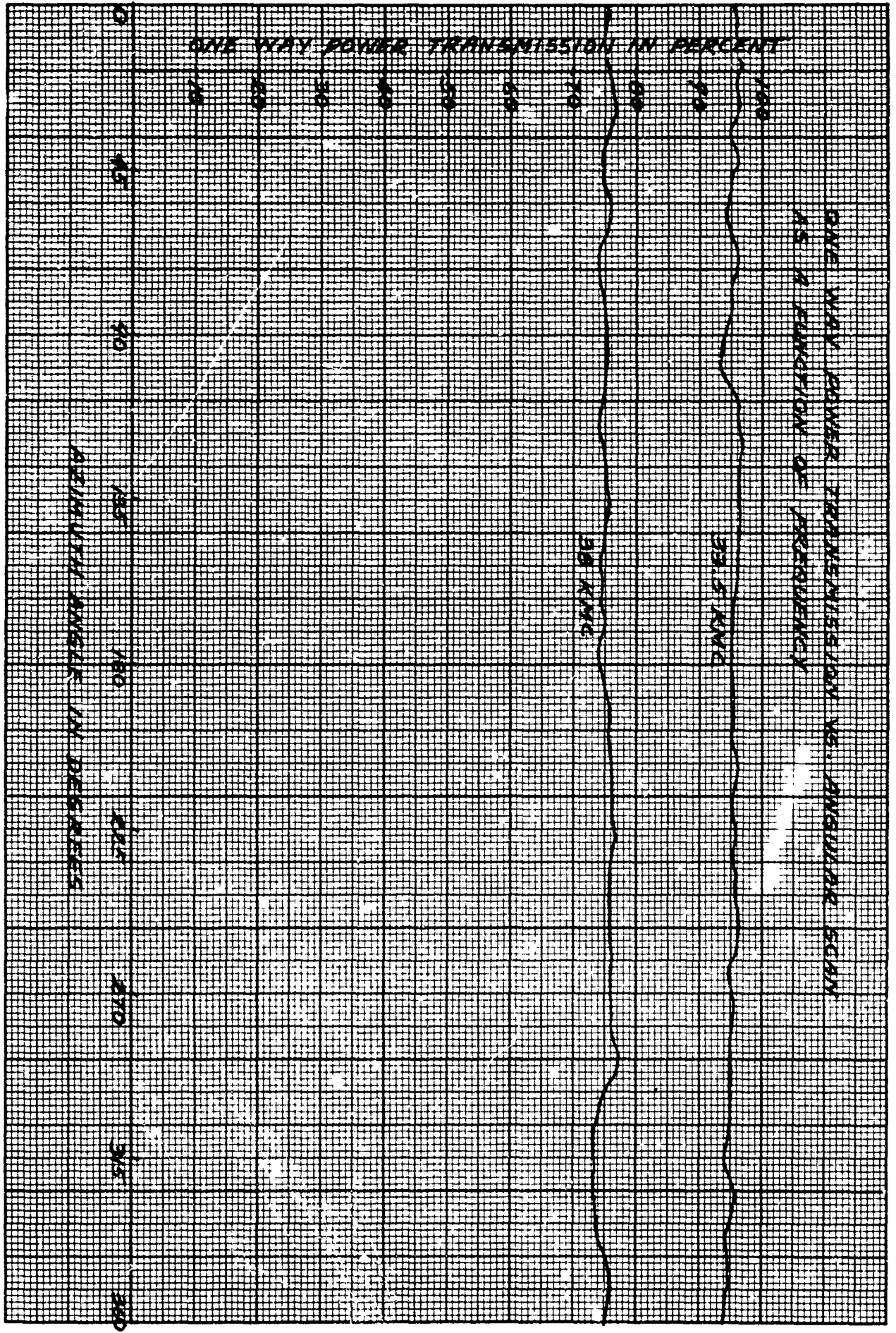


Figure 5 - EXPERIMENTAL TRANSMISSION CHARACTERISTICS OF FINAL UNIT AS A FUNCTION OF AZIMUTH ANGLE

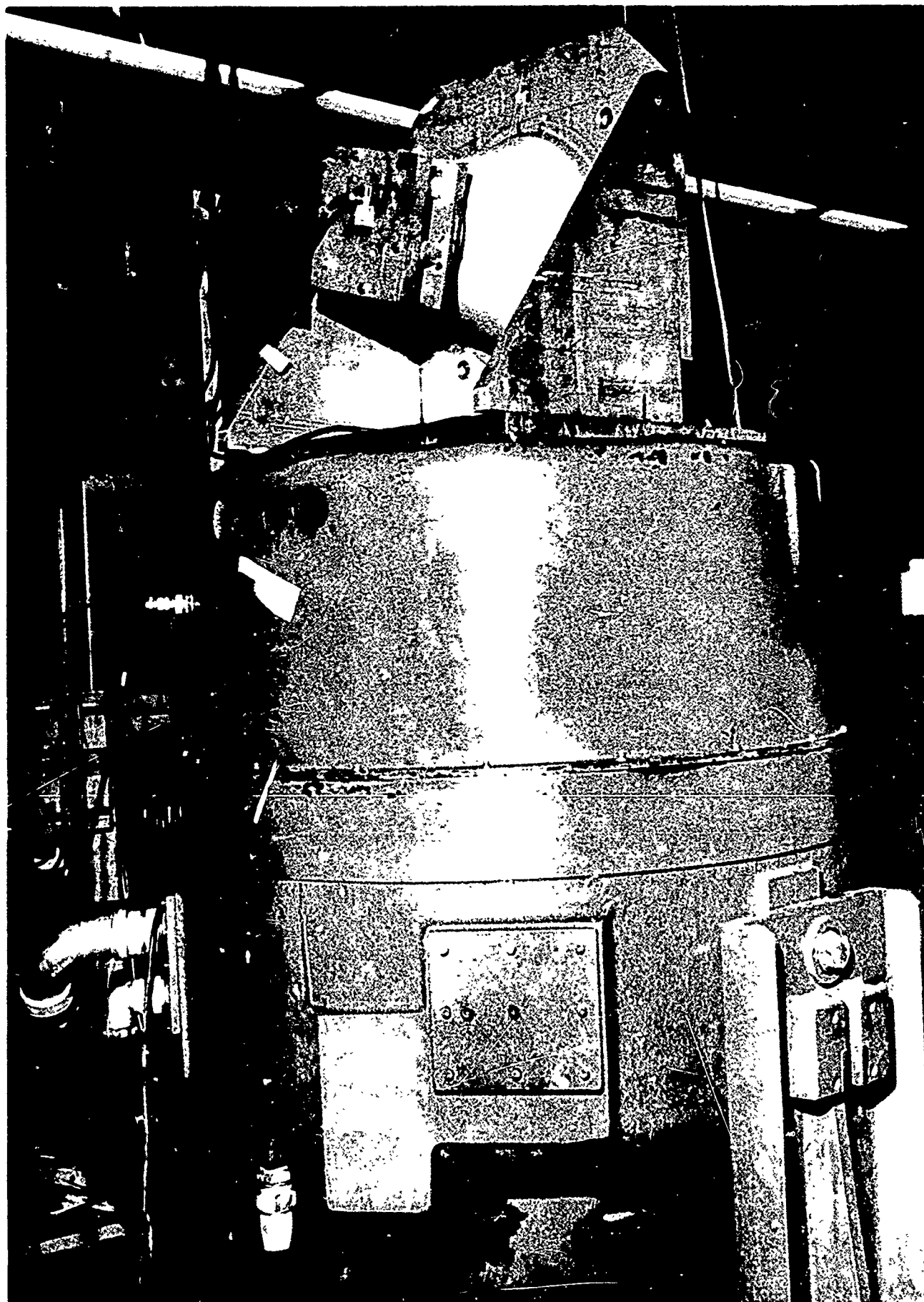


Figure 6 - LATERAL VIBRATION TEST SET-UP
12.



Figure 7 - REINFORCEMENT OF MOUNTING FLANGES

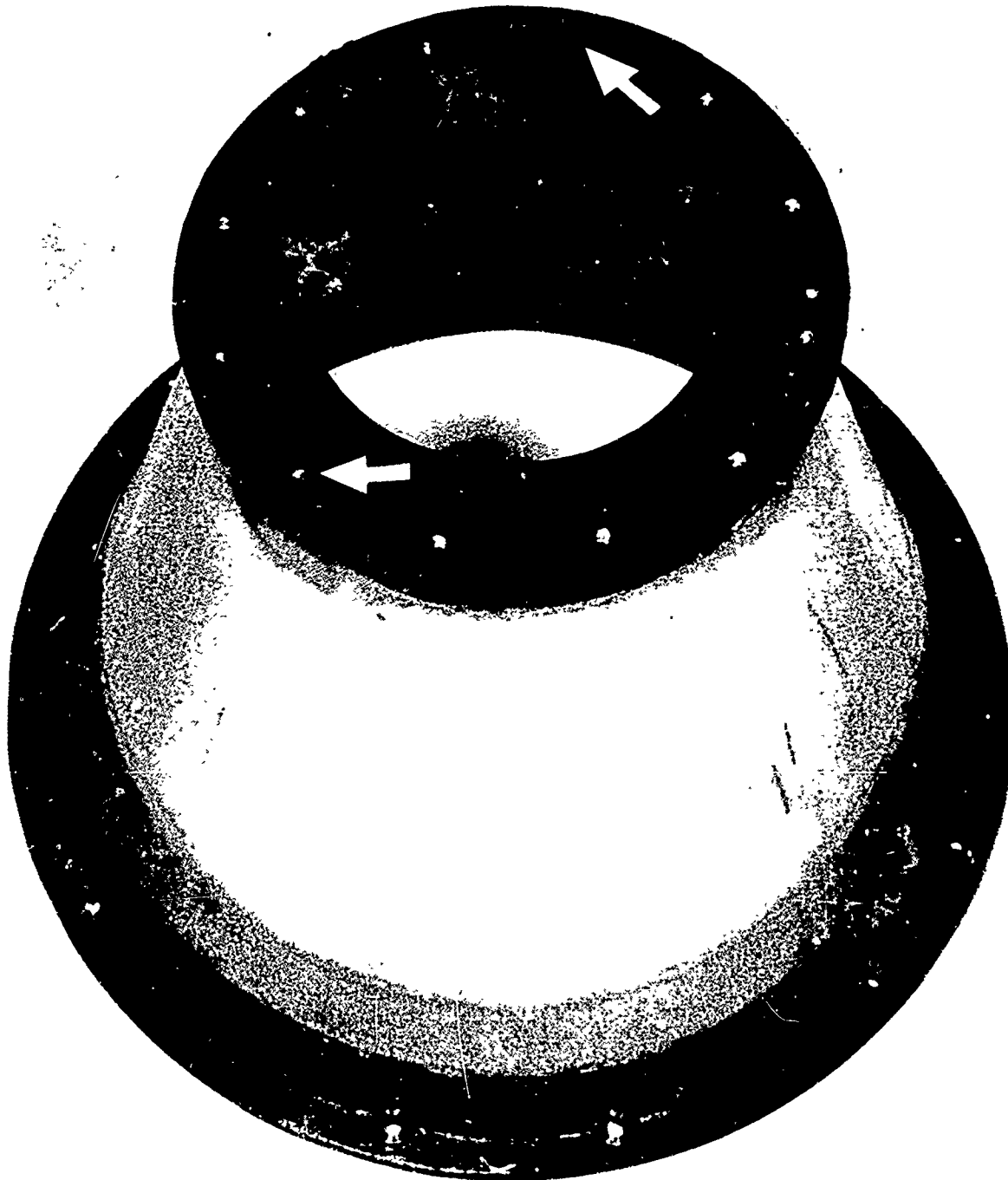


Figure 8 - FINAL MODEL OF RADOME
14.

designers to look for simpler solution for their special applications.

E. Acknowledgement

The authors wish to thank Dr. Henry Jasik for his permission to use the subject material. The radome was designed and developed under contract from his laboratory.

SESSION IV

BIAXIAL STRESS CONSIDERATIONS OF A BRITTLE DIELECTRIC MATERIAL

J. E. Burroughs and H. R. Thornton
General Dynamics/Fort Worth
Fort Worth, Texas

ABSTRACT

Design of a structural component utilizing brittle materials, namely ceramics, requires a rigid definition of the mechanical properties. Available mechanical property data are not adequate as critical design criteria. The fracture strength is a structure sensitive property and thus provides a basic parameter for study of the peculiar traits exhibited by brittle materials.

Most available information indicates that the bending strength of these brittle materials is, to some extent, dependent upon a size-shape factor. This treatise reports two methods of obtaining structural data; namely (1) behavior under a uniaxial stress caused by beam bending with variations in span length and thickness, and (2) behavior under a biaxial stress caused by concentrated transverse loading of a simply supported square plate. Theoretical considerations and test results are reported for Pyroceram 9606.

I. INTRODUCTION

The criteria utilized in the design of a dielectric window or radome specify material, electrical, structural, and aerodynamic requirements. The material requirements have been altered markedly with the advent of hypersonic regimes and reentry environments. In these elevated temperature regimes, the electrical, structural, and aerodynamic requirements are governed by the material requirement. Materials generally considered for radome applications are reinforced plastic and ceramic systems. The thermal integrity of current reinforced plastic systems diminish at approximately 550°F and thus would not be considered for application in reentry environments. As a result, ceramic materials are relied upon for application in radomes in this temperature regime.

The ceramic class of materials demonstrate inherent brittle tendencies. Design of a structural component utilizing these brittle materials requires a rigid definition of the mechanical properties. Available mechanical property data are not adequate as critical design criteria. The fracture strength is a structure sensitive property and thus provides a basic parameter for study of the peculiar traits exhibited by brittle materials.

Determination of the modulus of rupture is the method generally used as an indication of strength in a ceramic material. Most available information indicates that the modulus of rupture or bending strength of these brittle materials is, to some extent, dependent upon a size-shape factor. Should this be a positive statement, then design data generated from small beam specimens would not be valid criteria for large hardware components.

As has been stated, the strength characteristics of a brittle material are established through modulus of rupture determinations, i.e., uniaxial stress conditions. Under actual structural conditions, a material is rarely submitted to uniaxial stress conditions. The more realistic multiaxial stress conditions are difficult to simulate in a laboratory test procedure. However, the biaxial stress state more closely approximates realism than the uniaxial state.

This treatise reports two methods of obtaining structural data; namely, (1) behavior under a uniaxial stress caused by beam bending with variations in span length and thickness, and (2) behavior under a biaxial stress caused by concentrated transverse loading of a simply supported square plate.

II. DESCRIPTION OF MATERIALS

Ceramic materials currently receiving considerable attention for application in radomes are fused silica, alumina, and Pyroceram 9606. Incorporating immediate applicability as a criteria, Pyroceram 9606 is the only material that can be readily fabricated into large components utilizing existing processing techniques. Surface finishing, grinding, to the desired tolerances required for aerodynamic considerations is readily accomplished. Although Pyroceram 9606 is an intermediate temperature range material, useful to approximately 1500°F, the immediate application aspect intensified gathering of reliable design data. For this reason, Pyroceram 9606 was selected as the basis for this study.

III. PROCEDURES AND TEST CONDITIONS

1. Simple Beam Bending

Various span length beam specimens were fabricated from Pyroceram 9606. The specimens were 3 inches wide with 4, 6, 9, and 15 inch beam lengths. All specimens were 0.25 inches in thickness with the exception of the 15 inch beam length specimens where both 0.25 and 0.3125 inch thick specimens were incorporated. The beam specimens were ground smooth, with parallel faces, to ± 0.001 inch of the desired thickness.

Although contrary to some theorists, two different loading conditions were utilized in the determination of the modulus of rupture or flexural strength. Four-point loading, Figure 1, was used initially at room temperature. At temperature, it became necessary to change to three-point loading, Figure 2, as the four-point fixture oxidized too rapidly. The delay time in fabricating a new high temperature fixture was too great and the three-point, oxidation resistant, fixture was available to complete the testing. A 0.5 inch overhang was observed at each support for all beam specimens.

All testing was accomplished in an oxidizing atmosphere. The beam specimens were evaluated at room temperature, 1000° , and 1400° F. All testing at temperature was accomplished in moving air in an induction furnace. Figure 3 shows a typical beam specimen positioned on the test fixture for testing at elevated temperatures.

2. Plate Bending

A square specimen, five inches on a side, was chosen for testing under plate bending or biaxial stress conditions. The specimens were submitted to testing at temperatures of room temperature, 1000° , and 1500° F. Specimens 0.25 inches in thickness were utilized throughout with the exception of the room temperature testing. At room temperature both 0.25 and 0.3125 inch specimens were incorporated. The plate specimens were ground flat, with parallel faces, to ± 0.001 inch of the desired thickness.

In plate bending, a biaxial stress condition is realized by a concentrated transverse loading of a simply supported square plate. The flat plates were simply supported on all edges and were centrally loaded by a one half inch diameter rod. The periphery of the rod was chamfered slightly to maintain a

uniform loading on the plate in the deflected state. The test fixture is shown in Figure 4. The test fixture with a plate specimen in place ready for testing is shown in Figure 5. The elevated temperature test facility is shown in Figure 6. All testing was performed in an oxidizing atmosphere.

IV. PRESENTATION OF DATA

1. Simple Beam Bending

The modulus of rupture or flexural strength determinations of the various Pyroceram 9606 beam specimens are recorded in Table 1. The beam spans between supports ranged between three and fourteen inches. Each flexural strength value represents an average of at least five test specimens. There appears to be only a slight degradation in the strength characteristics over the temperature range, room temperature to 1400°F. This degradation appears to be more pronounced in the thicker beam specimens.

Stress-strain curves were obtained for Pyroceram 9606 under the various test conditions. In all cases the stress-strain curve was found to be fairly constant with temperature. A typical stress-strain curve is illustrated in Figure 7.

2. Plate Bending

The square plate was chosen for testing in plate bending because it produces the highest ratio between the two principal stresses at the center of the plate, the expected point of failure. Before any criteria can be established from the test data, the most applicable theory of failure has to be established. Most advanced strength texts advocate the use of the maximum normal stress theory since previous data indicates a "best fit" situation for brittle materials.

The maximum shear stress theory was also checked for punch cut shear around the periphery of the loading rod. As indicated later, this was not critical, despite the plate size.

TABLE I

SIMPLE BEAM BENDING TEST RESULTS

BEAM SPAN WIDTH (INCHES)	TEST TEMP °F	SPECIMEN THICKNESS (INCHES)	FLEXURAL STRENGTH (PSI)
Three (3)	RT	0.250	26,299
	1000	0.250	24,375
	1400	0.250	30,937
Five (5)	RT	0.250	26,299
	1000	0.250	21,200
	1400	0.250	22,400
Eight (8)	1400	0.250	21,120
Fourteen (14)	RT	0.250	25,130
	RT	0.3125	30,450
	1000	0.250	26,250
	1000	0.3125	23,000
	1400	0.250	28,195
	1400	0.3125	22,860

From Timoshenko (Ref. 1)

$$M_{x_{\xi}} = M_{y_{\xi}} = \frac{P}{4\pi} \left[(1 + \mu) \text{Log} (e) \frac{2a \text{Sin} \frac{\pi c}{a}}{\pi e} + 1 \right] + \frac{\gamma_1 P}{4\pi} \quad (1)$$

where:

P = load

μ = Poisson's ratio: Use 0.245

a = 4.0 in., c = 2.0 in.

e = radius of loading rod = 0.25 in.

$\gamma_1 = -0.565$ (a/b = 1.0)

$$M_{x_{\xi}} = \frac{P}{4\pi} \left[(1 + 0.245) \text{Log} (e) \frac{(2)(4) \text{Sin} \frac{\pi}{2}}{0.25\pi} + 1.000 - 0.565 \right]$$

$$M_{x_{\xi}} = M_{y_{\xi}} = \underline{\underline{0.275P}} \quad (2)$$

From the Maximum Normal Stress Theory:

$$\sigma_u = \sigma_x = \frac{6 M_x}{h^2} = \frac{6 (0.275P)}{h^2} = \frac{1.65P}{h^2} \quad (3)$$

For Maximum Shear Stress Theory Check of Punch-Out Shear

$$V = \text{shear/inch} = \frac{P}{2\pi e} \quad (4)$$

$$\tau = VQ/Ib \quad \text{Where: } Q = \frac{h^2}{8}, \quad I = \frac{bh^3}{12}, \quad b = 1$$

$$\tau = \frac{P}{2\pi e} \frac{h^2}{8} \frac{12}{h^3} = \frac{0.75P}{\pi(0.25)h} = 0.953 P/h \quad (5)$$

For this theory, $\tau_{\max} = \frac{\sigma_u}{2}$, then

$$\sigma_u = 2 (0.953) P/h = 1.906 P/h \quad (6)$$

Equating σ_u values to determine thickness at which shear becomes critical:

$$\frac{1.65P}{h^2} = \frac{1.906 P}{h} \quad (7)$$

$$h_{cr} \cong 1.65/1.906 = 0.866 \text{ in. (shear is critical above this thickness). Bending will be checked since specimens tested are less than this thickness.} \quad (8)$$

Timoshenko, in his analysis, refers to the simply supported plate with anticlastic deformation, while Seely and Smith (Ref. 2) have experimentally determined that the corners tend to curl up and that the critical section is approximately a diagonal section. In Seely and Smith's analysis of the square plate, the concentrated load at the center produces high stresses in the plate near the load. The distribution of the bending stress along this diagonal surface came from the theory of flexure of plates by Nadai and Westergaard (Ref. 3), which states that if the plate is a brittle material the significant stress in the plate may correspond more nearly to the maximum bending moment per unit of width, $0.44P$.

This analysis seems to fit the situation more so, but both theories are included to show the relative stress value obtained by calculation.

By Timoshenko, allowable bending stress

$$\sigma_u = \frac{1.65P}{h^2} \quad (9)$$

and by Seely and Smith

$$\sigma_u = \frac{2.64P}{h^2} \quad (10)$$

Where: σ_u = ultimate bending stress, psi
P = failing load, lbs.
h = thickness of plate, inches.

The results of the plate bending tests are outlined in Table II. The ultimate bending stresses are calculated for both the Timoshenko and the Seely and Smith theories. A comparison of the two approaches is illustrated in Figure 8. The Seely and Smith theory offers higher ultimate bending strengths over the entire temperature range than the Timoshenko approach. The plate bending results appear to prove out the theoretical analysis that failure should occur at the center of the plate and propagate toward the corners. Further evidence is obtained from the failure mode. Figure 9 illustrates a typical square plate failure showing the stress failure at the center of the plate and the ensuing propagation toward the corners.

Stress-strain curves were obtained for the flat plates under the various test conditions. A typical stress-strain curve of a 5 inch square plate is shown in Figure 10. The linear

relationship obtained with the beam bending does not hold true for the flat plate.

TABLE II

PLATE BENDING TEST DATA

TEST TEMP OF	PLATE THICKNESS (INCHES)	FAILING LOAD P_1 (LBS)	TIMOSHENKO u (PSI)	SEELY & SMITH u (PSI)
RT	0.3125	1580	26,800	67,000
RT	0.3125	1300	22,000	55,000
RT	0.250	900	23,700	38,000
RT	0.250	856	22,600	36,000
RT	0.250	778	20,500	32,700
1000	0.250	368	9,700	15,500
1000	0.250	346	9,200	14,600
1000	0.250	490	13,000	20,700
1500	0.250	575	15,200	24,300
1500	0.250	545	14,400	23,000
1500	0.250	585	15,500	24,700

3. Microstructure

In an effort to obtain a better understanding of the strength characteristics of Pyrocera 9606, an attempt to define the fracture mode was undertaken. The microstructure of the fracture surface was examined by electron microscopy. A typical section is shown in Figure 11. Evidence of both inter- and transgranular fracture are evident. This type of fracture is typical of a glass-ceramic system.

V. DISCUSSION OF RESULTS

The maximum stress theory for the flexure of beams assumes that a slab is loaded in a direction normal to its plane and that the slab is a homogenous, elastic, isotropic material of constant thickness. The maximum stress theory is not valid in the area of concentrated load. Timoshenko and Seely and Smith have offered theories to correct this situation. The validity of any theory would be a direct correlation between the modulus of rupture of the beam specimens and the ultimate bending stress of the plate under ideal conditions.

Pyroceram 9606 is a homogenous material and due to its production process also is isotropic. The beam specimens illustrate a linear stress-strain curve up to the point of failure. The plate specimens demonstrate a near linear stress-strain curve. The differential is related to the readjustment in the area of high stress concentration. This readjustment must be accounted for in any modified maximum stress theory.

A greater degree of correlation is observed between the flexural strength of the beam specimens and the ultimate bending stress calculated from Seely and Smith's equation than from the approach offered by Timoshenko. The degree of correlation may be observed in Figure 12. Due to the small number of specimens evaluated under this program, a true correlation cannot be expected.

The deviation from the maximum stress theory was substantiated by Newmark and Lepper (Ref. 4) utilizing plaster as the brittle material. The plaster specimens gave nearly straight stress-strain curves up to the point of failure. A special theory was proposed to account for the concentrated stress in a circular plate. The correlation between modulus of rupture of beam specimens and ultimate bending stress calculated from the special theory was good.

Beam specimens of various sizes and thicknesses were evaluated to determine whether a size factor does exist. There appears to be a minute size-shape factor for Pyroceram 9606. Neither an increase in thickness or an increase in span length affect the strength characteristics greatly. The effect of thickness is more significant under plate bending than beam bending. These conclusions can only be associated with one material, Pyroceram 9606, and cannot be firmly substantiated due to the limited number of specimens tested.

An analysis of the fracture surface of the beam and the plate specimens indicates a similar fracture mode for both types of failures. The electron micrographs show both inter- and transgranular fracture. The existence of a glassy phase in the grain boundaries often forms the plane of weakness in a glass-ceramic. It is anticipated that the initial crack occurs as intergranular and propagates as a combination fracture, mostly transgranular.

VI. CONCLUSIONS

The conclusions drawn from this study are not to be taken as absolute but rather indications of material behavior. This is due to the limited number of specimens involved in the study. As a result, a true statistical average cannot be established for the test results. However, generalized statements can be projected. These include:

1. A modified maximum stress theory must be utilized to describe plate bending under the application of a concentrated load.
2. The Seely and Smith approach to a modified theory offers best correlation between modulus of rupture and ultimate bending stress.
3. There appears to be a minute size-shape factor involved with Pyroceram 9606.
4. The mode of failure in Pyroceram 9606 appears to involve both inter- and transgranular fracture mechanisms.
5. Statistical analysis of fracture data is essential to determine structural reliability of brittle materials and, hence, will be useful in the selection of materials for design.

VII. REFERENCES

1. S. Timoshenko and S. Woinowsky-Krieger, Theory of Plates and Shells, p. 166, McGraw-Hill Book Company, Inc., New York, 1959. 580 pp.
2. F. B. Seely and J. O. Smith, Advanced Mechanics of Materials, p. 239, John Wiley & Sons, Inc., New York, 1952, 680 pp.
3. (a) A. Nadai, "Theories of Strength", J. Appl. Mech., 1 (3) 111-29 (1933).
(b) H. M. Westergaard, "Moments and Stresses in Slabs", Proc. Am. Concrete Inst., 17 (1921).
4. N. M. Newmark and H. A. Lepper, "Tests of Plaster-Model Slabs Subjected to Concentrated Loads," Bulletin 313, Engineering Experiment Station, University of Illinois, 1939.

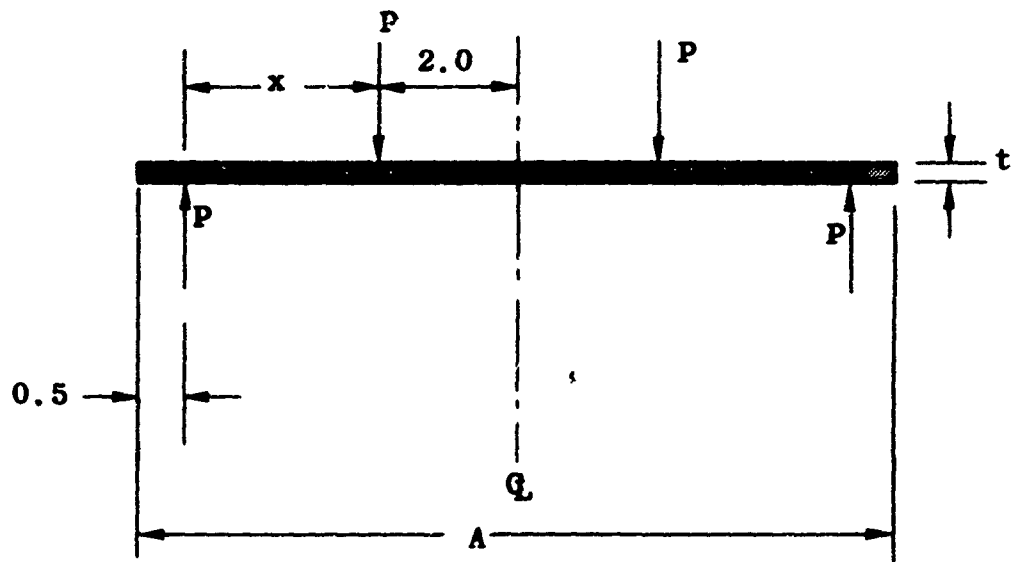


Figure 1. Rectangular Beam Cross-section, Four Point Loading

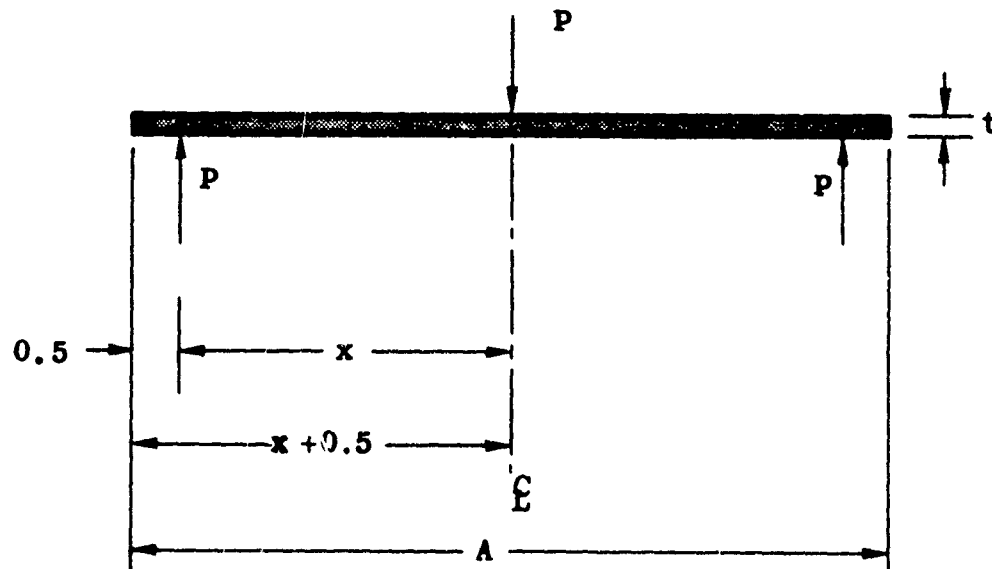


Figure 2. Rectangular Beam Cross-section, Three Point Loading

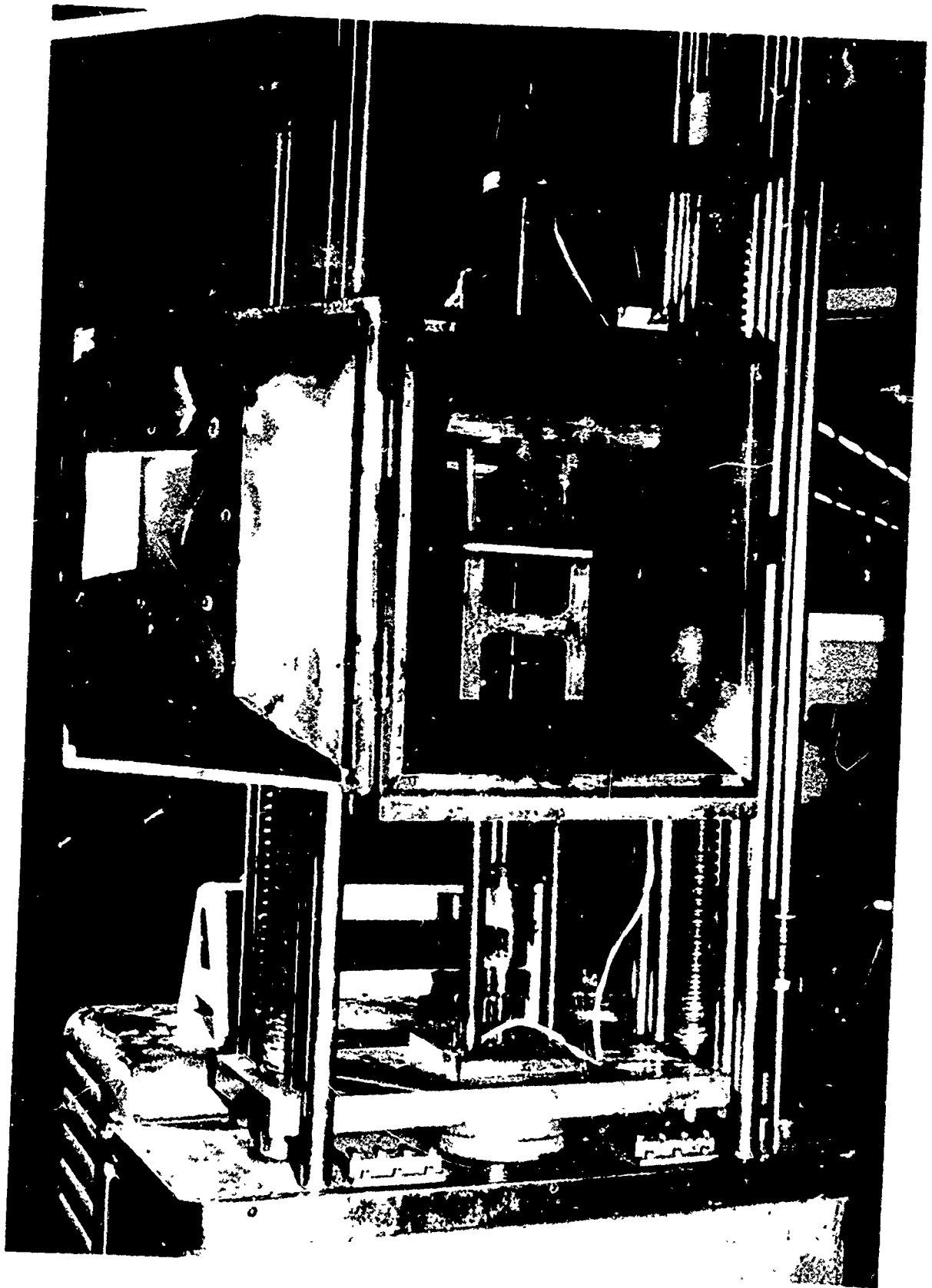


Figure 3. Typical Rectangular Beam Specimen in Test Furnace

FIG 64 171 P602
18 MAR 1964



Figure 4. Flat Plate Test Fixture

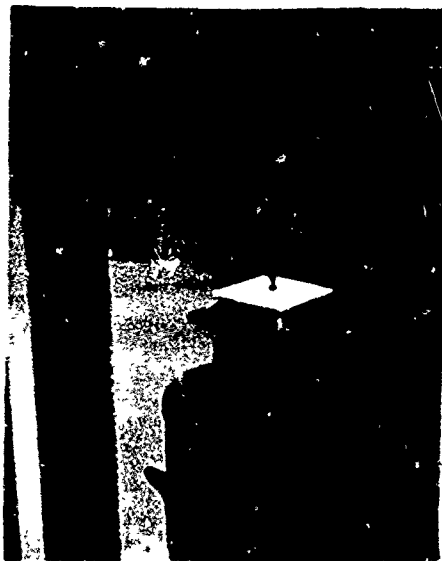


Figure 5. Flat Plate Test Fixture With Specimen in Place

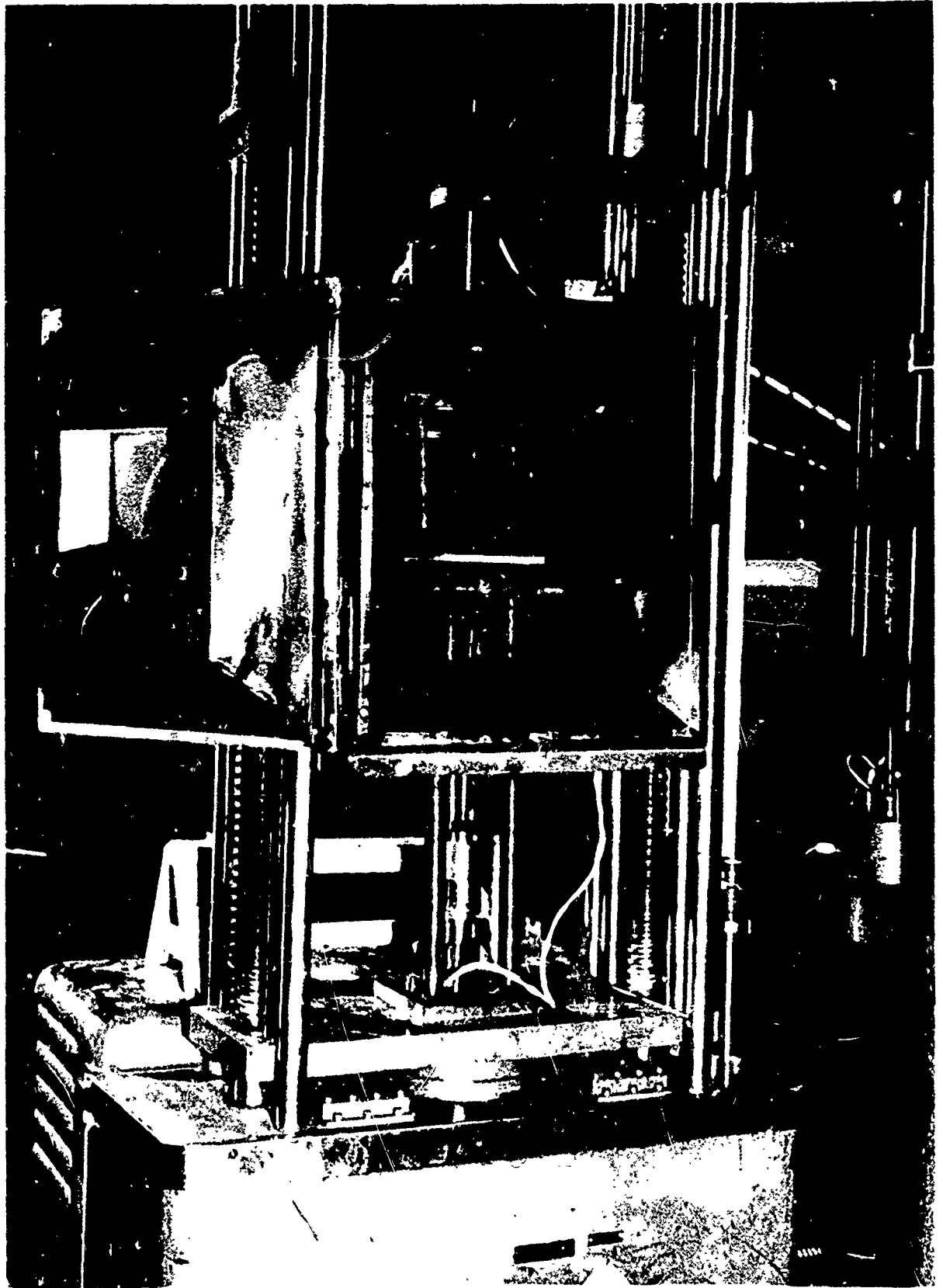


Figure 6. Flat Plate in Furnace, Elevated Temperature Test

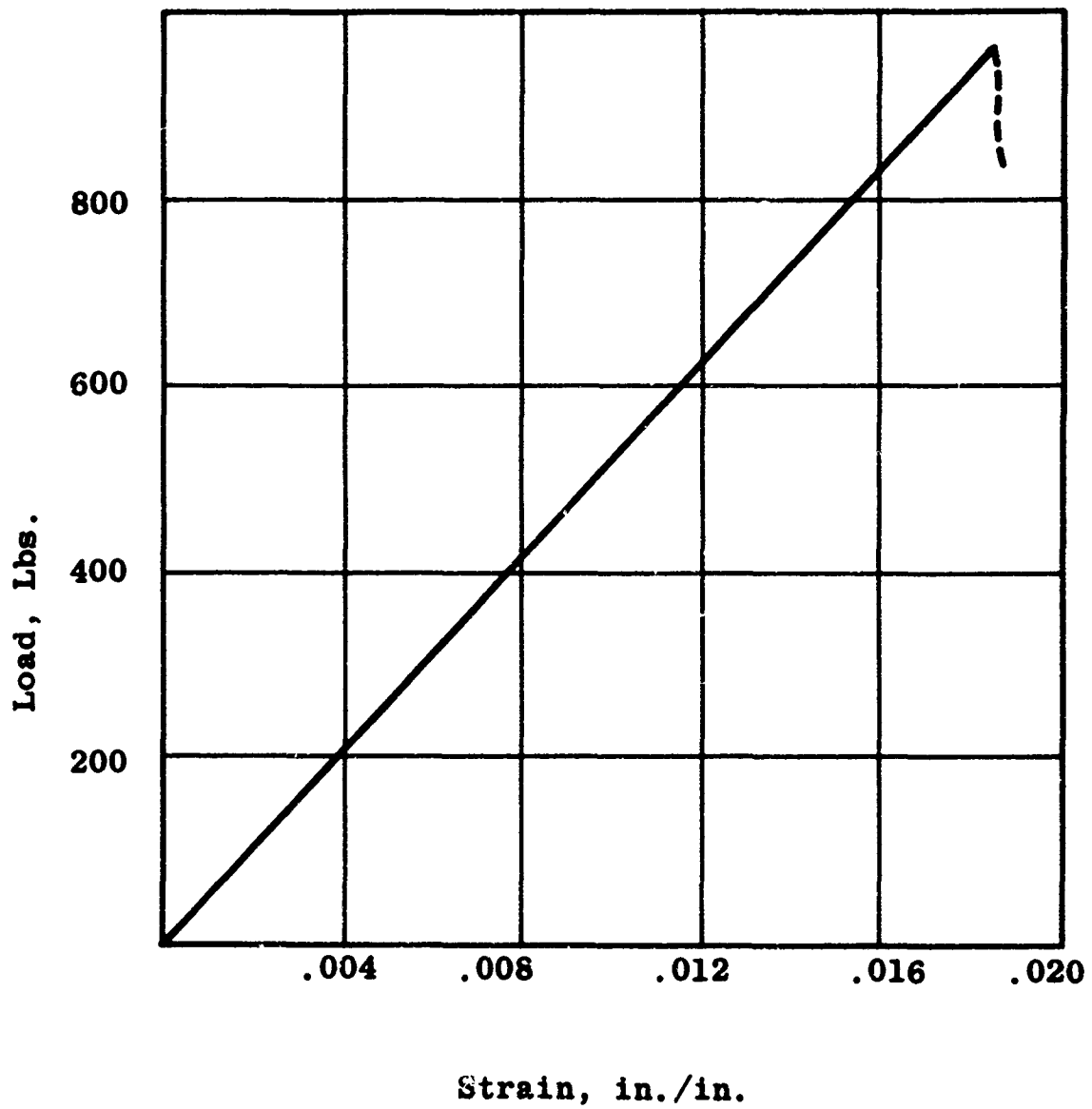


Figure 7. Typical Stress - Strain Curve for Beam Bending

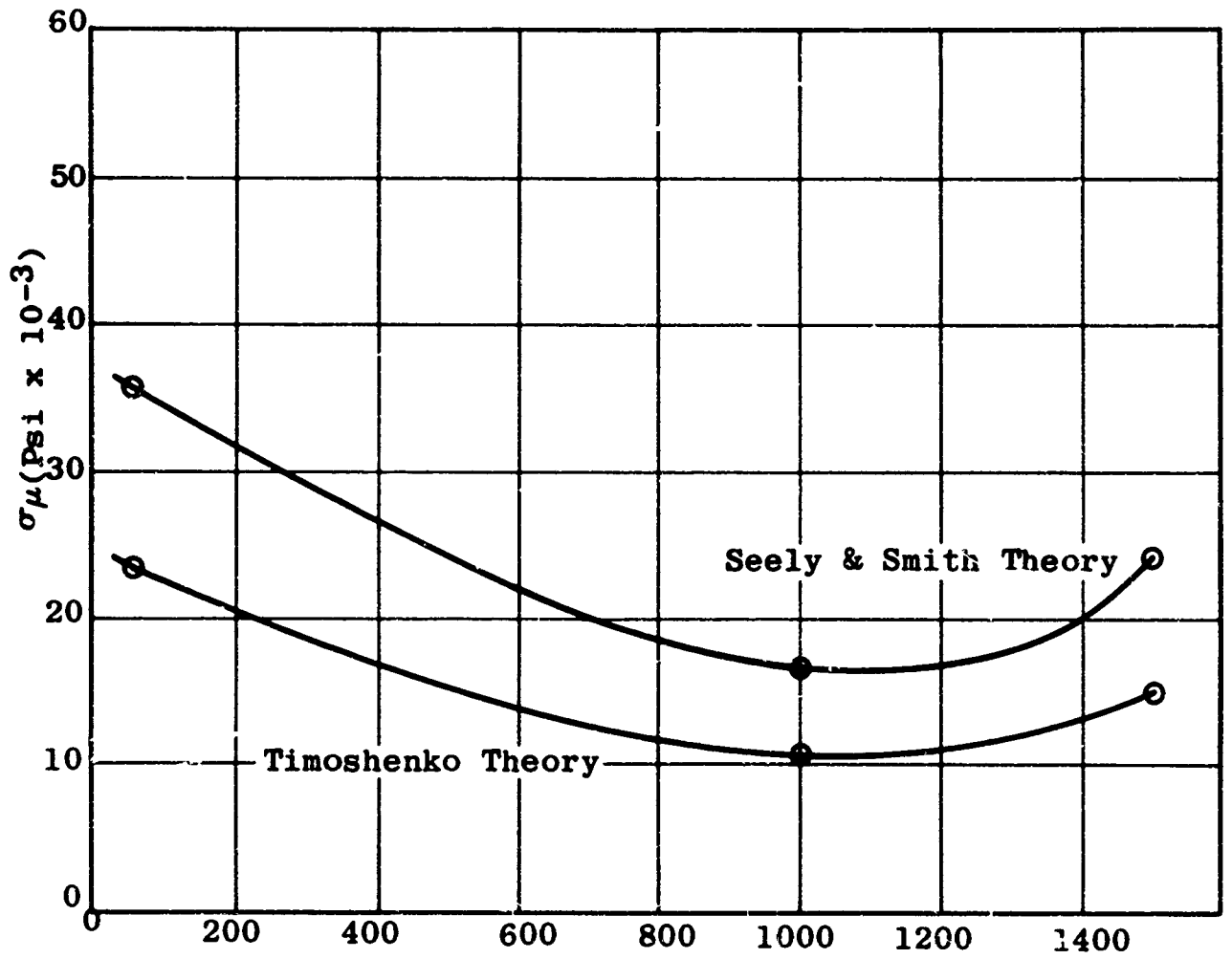


Figure 8. Comparison of Square Plate Results

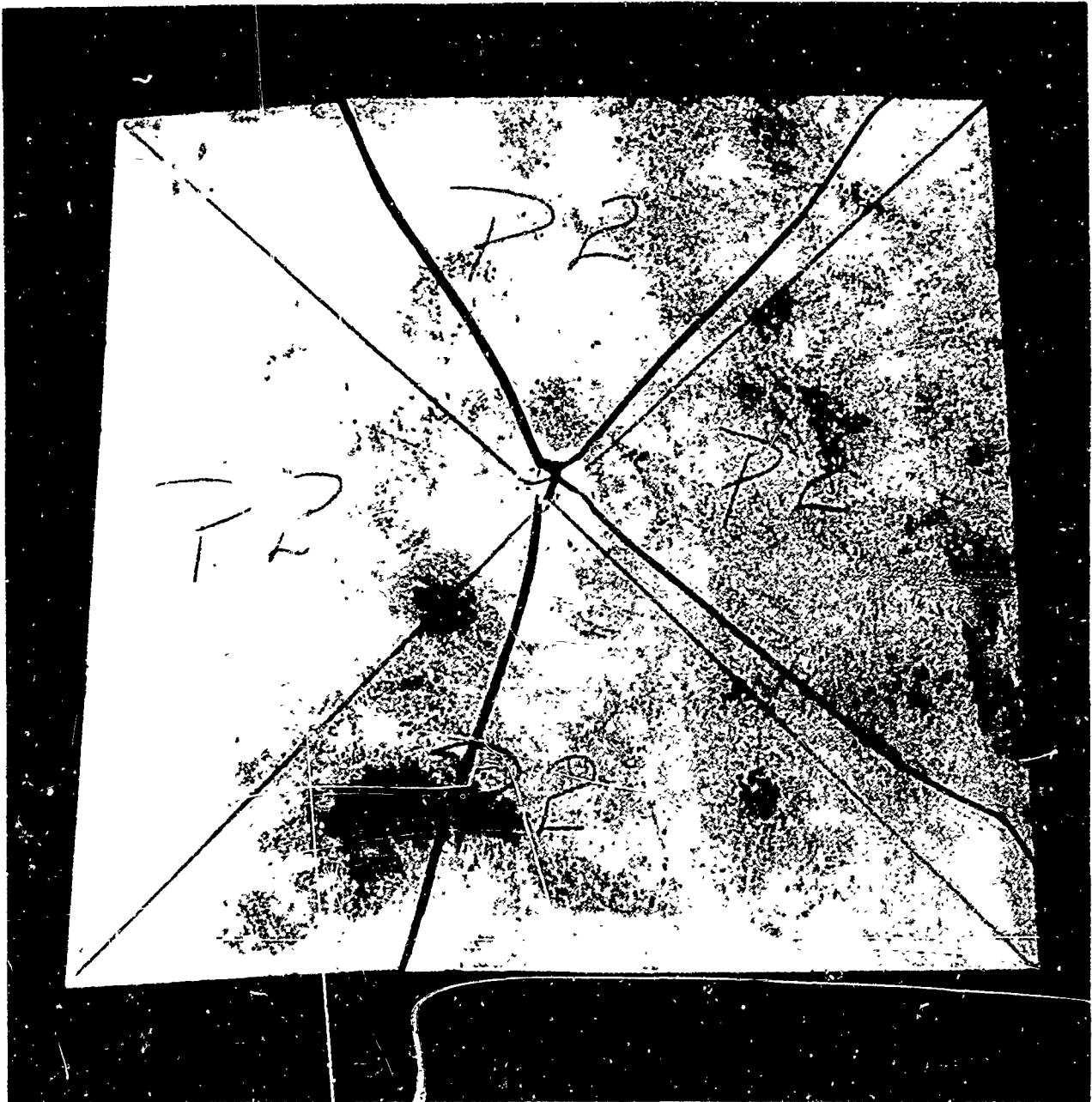


Figure 9. Typical Square Plate Bending Failure

FW/64/171/P607
18 MAY 1964

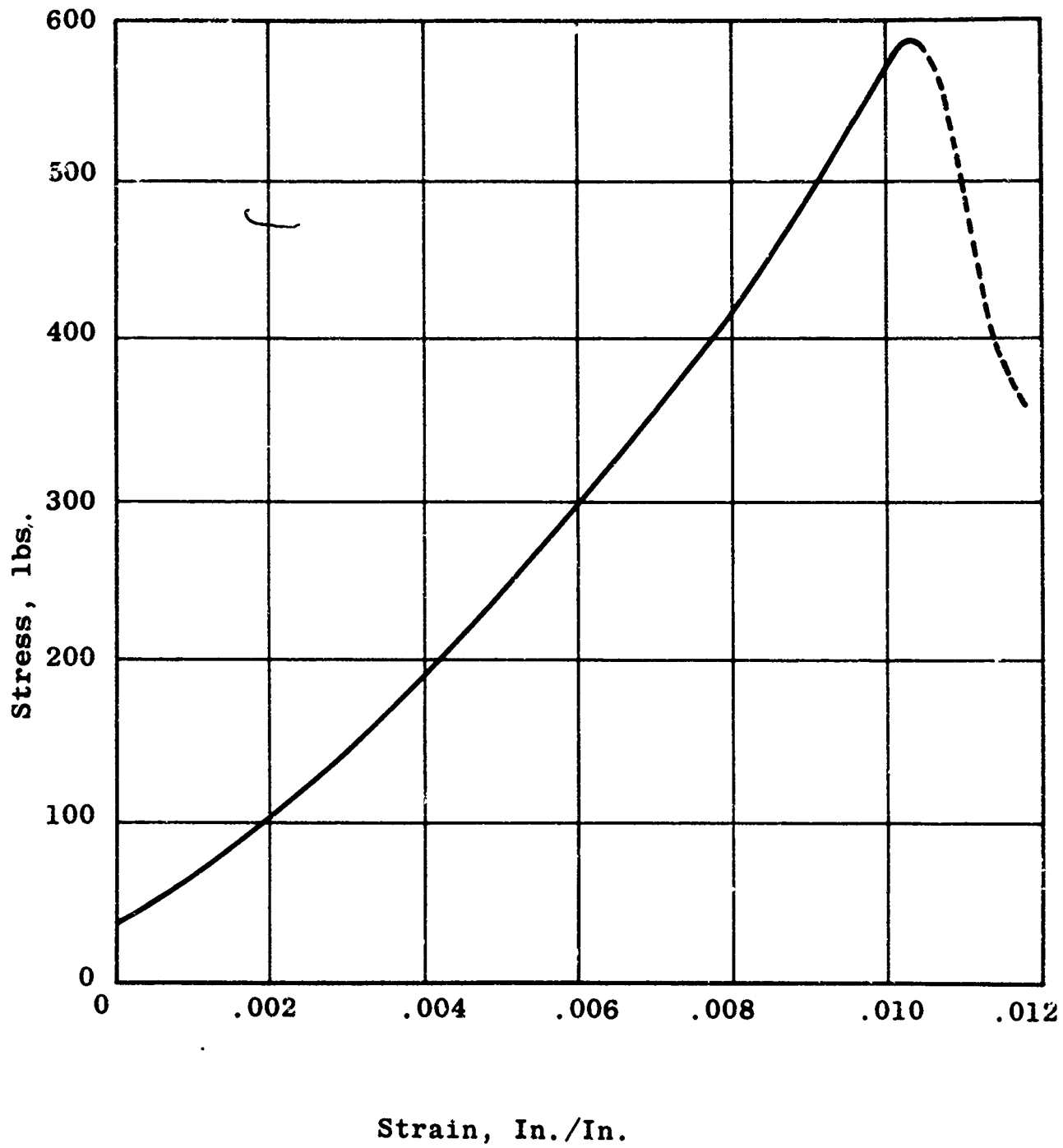


Figure 10. Typical Stress - Strain Curve for Plate Bending

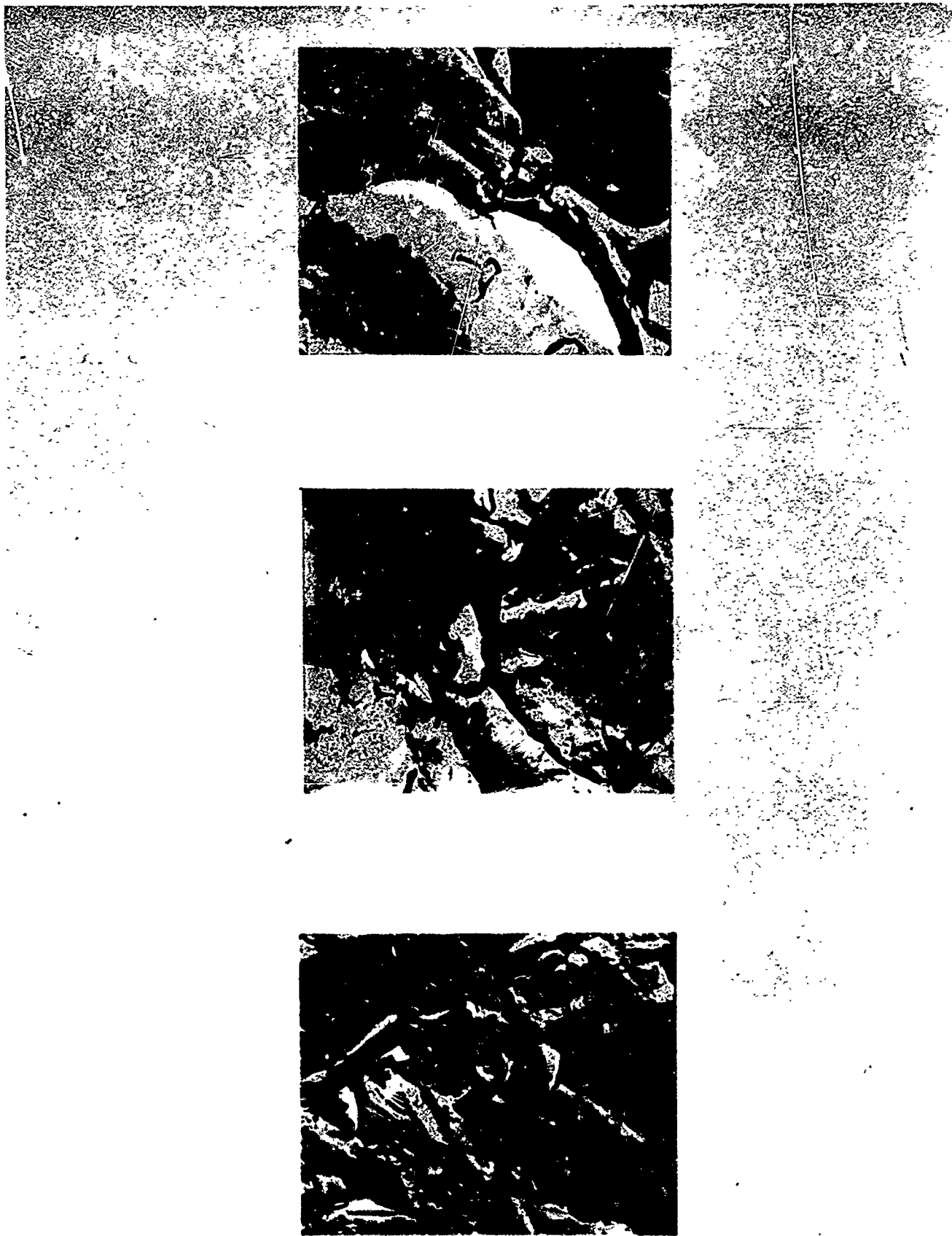


Figure 11. Electron Micrographs of Typical Fracture Surface (10,000X)

PW/64/171/P509
18 MAY 1964

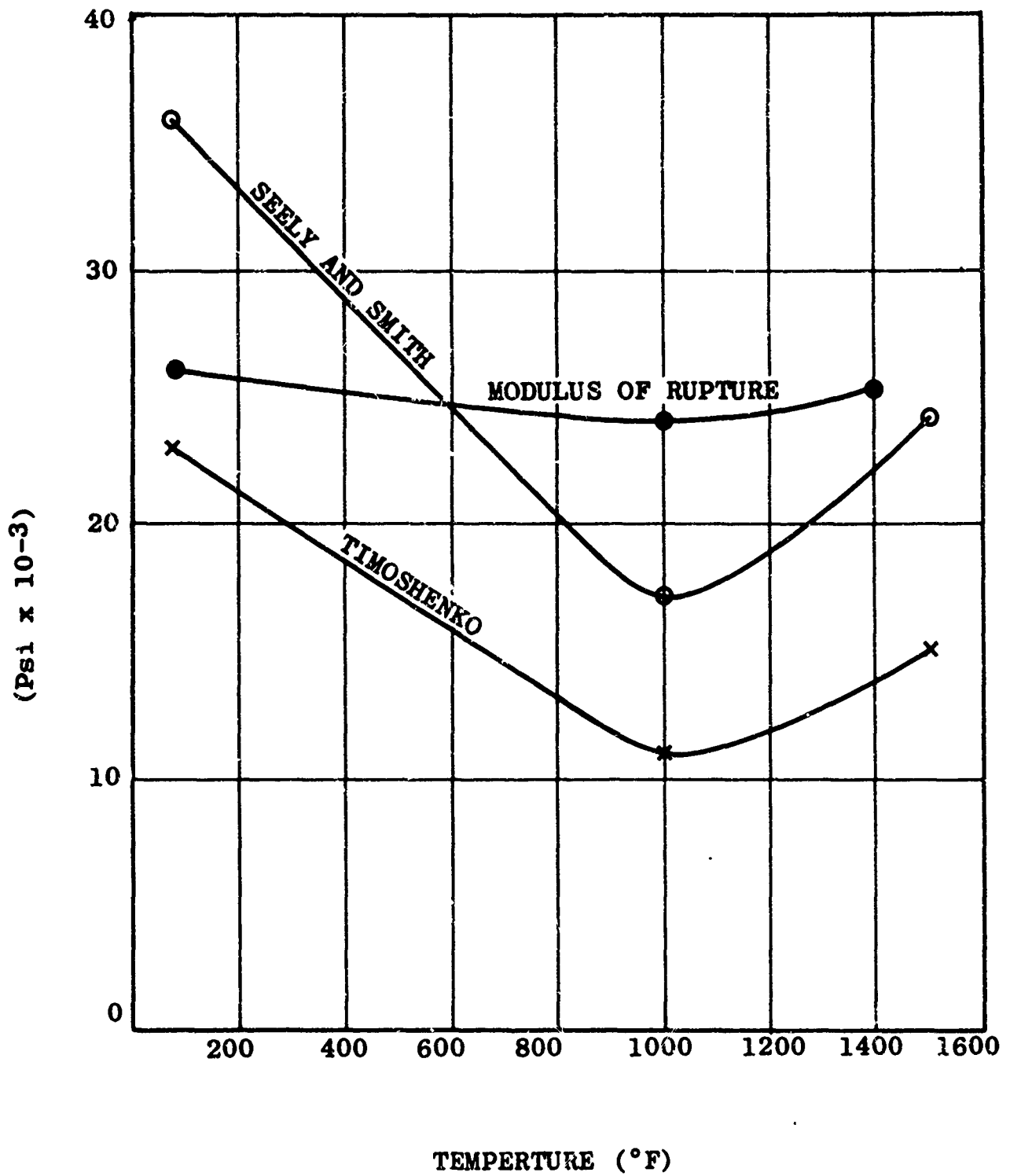


Figure 12. Comparison of Ultimate Stress Conditions in Beam and Plate Bending

**DESIGN TECHNIQUES FOR SECTIONALIZED,
STRUCTURALLY SUPPORTED AIRBORNE CERAMIC
RADOMES - A PROGRESS REPORT**

By

**Eino J. Luoma, Russell Stetson
of Emerson & Cuming, Inc.
Canton, Massachusetts**

and

**Professor Samuel J. Mason
of Massachusetts Institute of Technology
Consultant**

ACKNOWLEDGMENTS

The work reported herein was conducted under U. S. Air Force Contract AF33(615)-1376 with Mr. Richard Ireland of the Air Force Avionics Laboratory, Research and Technology Division as the Air Force Project Engineer. The digital computer facilities at Wright-Patterson Air Force Base are used in this program.

I. INTRODUCTION

Airborne radomes to date have used monocoque constructions. To avoid placing shadowing elements in the form of supporting ribs in front of the radar antenna, the airborne radome has consisted for the most part of a self-supporting shell of either Fiberglas plastic laminate or hard fired ceramic.

With the lower speed aircraft the Fiberglas plastic laminate was an ideal structural material for this application. Electrical properties, although not as excellent as those of hard fired ceramics, were good enough for most applications.

With the advent of supersonic and hypersonic aircraft and missiles aerodynamic requirements such as temperature and rain erosion resistance have forced a trend to ceramics. To date the use of ceramics as radome materials has been limited to small radomes on manned aircraft, and where it has been used in the larger sizes such as nose radomes, these have always been limited to unmanned missiles. Thus the shift to ceramic radome materials, while bringing about improved dielectric properties and rain erosion resistance, has complicated the structural problem,

These structural deficiencies of the best known ceramic radome materials in comparison with Fiberglas plastic laminates are:

1. Greater weights.

2. Lower flexural strength by a factor of 1/2 and less.
3. Higher elastic modulus resulting in brittleness, and susceptibility to fracture from thermal stresses.

The purpose of this radome development project is to overcome by suitable structural design these structural deficiencies inherent in ceramic materials. The design information resulting from this work should permit application of ceramic dielectric materials in large airborne radomes with minimum degradation in electrical performance.

The approach in general is to limit the size of individual sections of ceramic to small enough sections that structural integrity is maintained. These sections would have dimensions no larger than one foot by one foot. Further, the sections would be mounted into a metal supporting frame in such a way as to have the ceramic itself responsible for a minimum portion of the mechanical loads. The mounting is to be accomplished in a manner such as to keep thermal stresses to a minimum. Finally the entire arrangement must be such that electrical performance is compromised least by the presence of the metal supporting framework.

The use of dielectric sections in a metal framework is not without precedent. The large ground radomes have used such constructions successfully for many years. The secret of this success has been that the dimensions of the metal ribs were a very small part of the antenna aperture and the resulting windows were many wavelengths in dimension. Such radomes are practically invisible to the radar antenna much as a fine-strand open-mesh spider web or screen is nearly invisible to the eye.

At the other extreme, successful designs have been achieved by Stanford Research Institute, Boeing Airplane Company, and others on small resonant window arrays where the dielectric section dimensions are of the order of a half wavelength. These constructions permit the use of a greater metal area than the ground radome design, but would be subject to narrow-frequency-band performance due to the resonant principle applied.

This leaves largely unexplored the intermediate design area where the metal supporting sections occupy a substantial part of the antenna aperture and the ceramic windows are one to several wavelengths in size. It is in the design area where possibly may be found the best engineering compromises between structural and electrical performance for the large airborne ceramic radome. It is precisely this design area to which this program will devote its attention.

II. GENERAL PROCEDURE

The technical portions of the Statement of Work which is a part of the Contract AF33(615)-1376 are shown below. They are included here because they define specifically the work to be accomplished and form a logical basis for a general discussion of the approach to the problem.

EXHIBIT "A"

STATEMENT OF WORK

Design Techniques for Structurally Supported Radomes

1. Objective: To develop techniques for the design of metallic space frames for mechanically supporting large, sectionalized radome structures without appreciable degradation of the electrical performance.

2. Requirements:

a. The space frame shall consist of ribs and rings to mechanically support the dielectric sections comprising the radome.

b. The space frame shall provide adequate mechanical support to withstand the aerodynamic stresses and turbulence encountered for predetermined trajectories.

c. The structures shall provide facilities for attaching the sectionalized radome to the vehicle.

d. The structural members shall be designed for the frequency band from 1 gc to 25 gc with special consideration in the 3 and 10 gc bands.

e. Consideration shall be given to the attachment of the dielectric panels to the space frame.

f. The structure shall retain adequate mechanical strength at temperatures up to 2500°F, for a period of two (2) minutes. Adequate protection shall be provided to prevent oxidation at the maximum temperature requirements. The thermal expansion of the dielectric and the metallic materials shall be compatible.

g. Design techniques shall be provided for ogival radomes from 2 feet in diameter by 3-1/2 feet in length to 5 feet in diameter by 9 feet in length. Techniques for the design of chin domes up to 6 feet in diameter and 18 feet long, shall be included.

h. The final engineering report shall contain complete design criterion, (such as charts, graphs, or monograms) for space frames which will provide adequate structural and electrical properties at elevated temperatures, as a function of size, and frequency.

The work divides naturally into two areas, electrical and mechanical. In the following sections these are discussed separately. In both cases to compile the desired design data, the complexity of the problems are such as to dictate the use of digital computers. The computer facility for this program is provided by Wright-Patterson Air Force Base.

III. ELECTRICAL DESIGN DATA

A. Theoretical

Because of the complexity of the problem of computing theoretical electrical performance of a radome wall with metal supporting members, it is logical to follow the successful precedent of the all-dielectric radome wall design data computation. This procedure which has stood the test of time on the all-dielectric radome wall was to assume that the radome was locally flat even though a curved shape, and thus compute insertion loss and insertion phase for flat sheets.

For this flat sheet problem with metal members the parameters are:

1. dielectric constant of the ceramic
2. loss tangent of the ceramic
3. thickness of the ceramic
4. free space wavelength
5. shape of cross-section of metal members
6. dimensions of metal members
7. distances between adjacent metal members in two perpendicular planes
8. arrangement of metal members
9. incidence angle
10. polarization of electric field
11. insertion loss
12. insertion phase
13. reflection loss
14. reflection phase

The last four items of this list are of course functions of the first ten. Normalizing all dimensions in the first ten items of this list in terms of free space wavelength is a convenience and eliminates one item.

To establish the first Fortran computer program for the purpose of predicting transmission and reflection performance of this fenestrated flat sheet the procedure is as follows. Assume the two-layer dielectric wall, Figure A, is fenestrated by \bar{i} -beam supports. The structure has the same xy -plane section for any value of the third coordinate, z , which is normal to the plane of Figure A.

The structure is treated as a diffraction grating of spacial period x_1 . From the set of incident and reflected plane waves, traveling at angles θ_k and β_k corresponding to the various constructive diffraction angles of the grating, we compute the electric and magnetic fields on the plane $y=0$. (See Figure B)

It may be necessary to have I-beams which are thicker than the ceramic sections which are to be mounted into the I-beam structure. Thus, within the I-beam structure, there will be two dielectric regions (1) and (2) as shown in Figure A, one occupied by the ceramic and the other by air.

From the set of waveguide modes within these dielectric regions (1) and (2), we can compute the fields on the plane $y=0$. (We assume flange thicknesses a and b are very small and that the I-beams have infinite conductivity.) By matching boundary conditions at $y=0$, for a discrete set of points x_k , we can solve for a transmission matrix relating the incident wave set to the set of waveguide modes.

The same procedure applied to the boundary $y=y_1 + y_2$ leads, finally, to a transmission matrix relating the incident wave set to the transmitted wave set.

The accuracy of the approximation increases as the number of waves, modes, and match points x_k is increased. (Waveguide modes beyond cutoff and external waves beyond real propagation angles are, of course, included in the set.)

A Fortran program has been written and some parts of it have been compiled. Debug runs on the complete program are the next step.

B. Experimental

It is planned to gather enough experimental data to verify the results of the theoretical tabulation of insertion loss and insertion phase for the fenestrated flat sheet. To do this a microwave interferometer will be used. Figure 1 is a block diagram of the interferometer circuit which will be used.

Because of the need to have a rather large test sample, at least 6 feet by 6 feet to ensure a representative inspection zone without edge effects for the test sample, and because of the weight of the sample and need for mechanical stability during the measurement, a special sample holder was designed and built. Figure 8 is a photograph of this sample holder shown in place between the two interferometer antennas.

Since the time schedule permitted only the fabrication of this sample holder during the first quarter, no test data gained by its use can be reported at this time. It is expected that the next quarterly report will contain much of this type of experimental data.

On the other hand, during the first quarter, some preliminary testing on a microwave interferometer was accomplished. Figures 2 and 3 are sketches of test setups showing the horn arrangements and sample positions. Tests were performed at a frequency of 8.6 Gc. The purpose of the tests was to gain some preliminary information on minimum spacing that can be tolerated between adjacent metal members and on size of the inspection zone that would be representative of a given metal member arrangement. All tests were made

at 45° incidence, perpendicular polarization. One-inch steel I-beams (simulated by two channels back to back) were used for the metal members. The steel I-beams were not crossed but arrayed only in one direction as shown in Figure 2.

The measurements of insertion loss and insertion phase were made as the array of metal I-beams was moved in 1/4-inch increments across the line of transmission between the two horns. I-beam spacing was varied in one-inch increments from two inches to six inches. Horn aperture dimensions were 3" x 2 1/16" and the two apertures were 13 inches apart along the line of transmission.

Figures 4 and 5 are test results for perpendicular polarization, 45° incidence with the I-beams arrayed perpendicular to the electric field and the motion of the array in its own plane and in the direction of the electric field as in Figure 2.

Figures 6 and 7 are test results for perpendicular polarization, 45° incidence with the I-beams arrayed parallel to the electric field and with the motion of the array in its own plane and perpendicular to the electric field as in Figure 3. Only five-inch and six-inch spacings were included in this exercise because it was concluded from the previous exercise that smaller spacings were not practical.

It is concluded tentatively from this test data that at 8.6 Gc the minimum spacing between metal members in the sectionalized radome should be of the order of five inches. This spacing is required to keep the shadow area down to a reasonable value. The large phase variations shown in the results of Figure 4 would, of course, be expected to smooth out when tests are made with the horns farther apart and with a larger inspection zone.

IV. MECHANICAL ASPECTS

A. Test Equipment Design and Fabrication

We have completed design and fabrication of a test stand for electrical evaluation of basic metal grids, and later for possible use with partial or complete radome models. It will accommodate test grids with longitudinal members 6 feet long, with these members either parallel or perpendicular to electric field for either parallel or perpendicular polarization at any angle of incidence. The support frame may be tilted on a horizontal axis, to adjust angle of incidence in increments of 5° to a maximum approaching 90° either side of normal. The support frame may be moved for scanning in its own plane perpendicular to axis of tilt. The overall support assembly is freely movable on rigid-mounted locking casters. With the base fixed in location by locking the casters, the entire superstructure then may be moved for lateral scanning. Also provided is a means of scanning parallel to line of transmission. Several types of transmitting and receiving antennas may be interchangeably mounted at fixed elevation on supports which are movable along a fixed track, to maintain alignment but permit ready adjustment of antenna spacing.

This equipment has been set up in Eccosorb Anechoic Chamber No. 309 at our Plant 2 in Canton, to provide suitably reflection-free environment.

B. Definition of External Load Conditions

1. General Discussion

Developmental mechanical engineering to date has been aimed mainly at determining a sound basis for definition of aerodynamic load conditions bearing on the exterior of a radome. Of prime importance are normal pressure and heat, i. e. temperature and heat flux. Drag loads are expected to be of lower value and significance and probably can be evaluated as a ratio to the pressure. Inertial loads will be independent of environment. All these will be developed later.

The contract specification of external loading conditions is only the very brief statement "The structure shall retain adequate mechanical strength at temperatures up to 2500° F, for a period of two (2) minutes".

The temperature is stated clearly as a maximum, which we take to mean the highest temperature reached in any part of the structure. This immediately raises the question what temperatures may be reached in other parts and requires that we determine a reasonable pattern of temperature distribution to keep local design in step with local conditions.

The time specification of exposure to 2500° F for only two minutes appears to have no significance as related to pressure effects, which would be felt immediately throughout the structure. However it must be considered with relation to thermal effects, since this period of time probably is too short to even approach steady-state condition. Under the expected high heat flux the interior of the dielectric panels will lag appreciably below theoretical steady-state temperatures and thermal stresses thus will be accentuated. We expect interest will develop also in thermal history immediately prior to exposure to maximum design conditions, and will require establishing a typical mission profile.

To derive a pattern of distribution and to determine loading conditions other than temperature, we must assume a set of flight conditions which reasonably could induce such temperature. The prime variable in this respect is speed, expressed most usefully as Mach number. A temperature of 2500° F corresponds approximately to Mach 5.0, and we have set this as a target level, with the intent of including information for higher values to Mach 6.

Next, we assume that there is interest in flight conditions less severe than those for 2500° F. Therefore we are taking as our field of interest the range of Mach numbers from approximately 6, down to an arbitrary minimum of 2.0.

In addition to temperature we must know the values of heat flux into the wall at significant points. Obviously we must know also the magnitude and distribution of pressure. Since an ogive is a body of revolution whose orientation about its central axis cannot necessarily be predicted in flight, we must design for the maximum local load that reasonably can be expected at any point within each increment of length. Further, any departure from axisymmetric loading must be evaluated so we can determine bending loads, both locally and in the overall structure. Therefore we must determine, for each increment of length, the maximum and minimum simultaneous values of pressure and their relative orientation, for all reasonable conditions of flight.

Working toward such an evaluation for this project, we found several sources which gave values for the resultant pressure and temperature level on complete ogive shapes, but only one which spelled out a method for determining local pressures, temperatures and heat flux at all points. This source is WADD TR 59-22, from which we have built the method we propose using to define aerodynamic loads.

WADD TR 59-22, "Aerodynamic and Structural Analyses of Radome Shells" February, 1961, presents methods for computing values of local pressures and of temperature and heat flux at all parts of various shapes of radomes including tangent ogives in a range of fineness ratios, when subjected to a range of flight conditions which covers adequately the requirements of this project. Volume I, Chapter I, Part C is titled "Methods of Calculating the Pressure Distribution on Various Nose Shapes at Small Angle of Attack in the Range of Mach Numbers from 0.9 to 7.0" and Part D is titled "Calculation of Heat Transfer to Radome-Shaped Bodies".

Both of these parts are, in our opinion, sufficiently current and authoritative to warrant their combined use as a sole basis for definition of aerodynamic loads to the full extent of their applicability.

For the present we are restricting our attention to complete tangent ogives. Any subsequent interest in secant ogives can be satisfied by considering them as tangent ogives of the same nose angle but of less than full tangent-ogive length. Loads on the body portion immediately aft of the radome will differ markedly between tangent and secant noses, but are outside the scope of this project.

We are not presently recognizing chin radomes as distinct from complete tangent ogives, under the assumption that a chin radome will be shaped as a portion of a tangent ogive whose configuration is completed by adjacent supporting structure.

2. Aerodynamic Pressures

The basic equation for local pressure on tangent ogives as given of Page 91 of WADD TR 59-22 reads:

$$C_p = \frac{2}{\gamma M_0^2} \left\{ \left(\frac{P_s}{P_0} \right)_{\phi=0} \left[\frac{(M_s)_{\phi=0}}{M_N} - \frac{\gamma-1}{2} (M_s \delta_N)_{\phi=0} \left(1 - \frac{\delta}{\delta_N} \right) \right]^{\frac{2\gamma}{\gamma-1}} - 1 \right\}$$

where C_p = Pressure coefficient

γ = Ratio of specific heats

M_0 = Mach number, free stream conditions

M_s = Mach number immediately behind shock wave

M_N = Mach number at nose

P_s = Local normal pressure, psi

P_0 = Free stream atmospheric pressure, psi

δ = Local slope of body relative to axis

δ_N = Initial slope at nose, relative to axis

α = Angle of attack, radians

ϕ = Angular coordinate measured from extreme windward meridian

Values of $\left(\frac{P_s}{P_0} \right)_{\phi=0}$, $\frac{(M_s)_{\phi=0}}{M_N}$ and $M_s \delta_N$ are given in Table I, (Page 103 of WADD TR 59-22) in terms of $M_0 \delta_N$ and $\frac{\alpha}{\delta_N}$ for various values of ϕ . C_p can be defined by the conventional relation: $C_p = \frac{P_s - P_0}{\frac{\gamma}{2} M_0^2 P_0}$

Since the end use of this entire effort will be in determining dimensions of metal frame members and of dielectric panels, and structural computations for such are commonly based on inches rather than on feet, we prefer to use the inch basis from the start, e.g. expressing all pressures in psi rather than psf. This fits, too, the usual way of thinking of atmospheric pressure, for example as 14.7 psi for sea-level pressure.

Since we have no interest in Mach numbers above 7, we are concerned only in regions where WADD TR 59-22 shows that perfect gas relations are valid and γ , the ratio of specific heats, is constant at a value of 1.4. Using this value, and re-arranging

terms for easier computation, we re-write the equations thus:

$$\frac{\Delta P}{q} = \left\{ \left[\frac{(M_s)_{\phi=0}}{M_N} - 0.2(M_s \delta_N)_{\phi=0} \left(1 - \frac{\delta}{\delta_N}\right) \right]^7 \left(\frac{P_s}{P_0} \right)_{\phi=0} - 1 \right\} \frac{1.429}{M_0^2}$$

$$P_s = (0.7 M_0^2 \frac{\Delta P}{q} + 1) P_0$$

It is evident in the equation that pressure distribution, as related to radome configuration, is dependent only on nose angle and local slope, therefor only on Fineness Ratio or L/D, and thus is independent of relative size. This makes it practical to base pressure computations only on L/D, and to relate distribution to length normalized at a value of 1.0.

It is also evident that, since actual magnitude of ambient or free-stream pressure is introduced only as a multiplier in the final step of determining magnitude of local pressure, and in all prior work these two appear only as their ratio, it is practical to compute local pressures corresponding to only a single arbitrary free-stream pressure (e. g. for sea level), and to derive values for another free-stream pressure by direct ratio to the magnitude of that pressure.

We have set up a standard fill-in sheet to facilitate repeated manual computation, and used it to make a series of determinations of local normal pressures, first along a single meridian from nose to base at zero angle of attack for Mach 5.0 at sea level. This was done to determine the possible maximum loads we might conceivably be faced with in straight flight. We presume that there is very little probability of requiring design for Mach 5 flight at or near sea level, and in this respect our work with this speed results in unrealistically high loads. However it should be considered as basic data which can be readily adjusted for higher altitudes.

Then, to explore the effects of yaw, which would occur in maneuvering, we repeated the computation using a tabulated value from Table I (of WADD TR 59-22) corresponding to 14.3° angle of attack and determining normal pressure at radii in the plane of yaw and at 90° and 180° from it.

Results of these exploratory manual computations are plotted in Figure 9. Considering first the curve of zero yaw (straight flight) it is interesting to note the eye-opening value of over 200 psi for local pressure at the nose (this indicates the probability of formidable loads even after downward adjustment for altitude) and the extreme rapidity of decrease in pressure on moving aft, nearly to one-half this value at only 0.2 L, and to less than 7% of nose value at the base.

This indicates pronounced localization of peak pressures near the nose where configuration is small and of sharp curvature, thus is most able to resist pressure load. It indicates

increasingly lower pressure on moving aft where configuration is larger and tending to flatten locally. Considered within the concept of framing with rings and longitudinal spars, the trend in pressure distribution is to high values where skin area is small, and unsupported spans of dielectric and of frame are best made short and to low values where they are best made long. Compatibility thus seems to be excellent.

Looking now at the three curves for 14° yaw, we see that nose pressure on the windward side has increased only very slightly, but that nose pressures at 90° and 180° to direction of yaw have dropped drastically from straight flight value. We see further that on moving downstream, the pressure in the direction of yaw decreases substantially less than does that for the zero-yaw curve so, at the base of the ogive ($L = 1.0$), it stands at about 170% of the zero-yaw curve while the pressures for radial planes at 90° and 180° from plane of yaw show respective values of only 70% and 20% of the zero-yaw values. Thus there is very substantial difference in magnitude of local pressure among the planes of different orientation relative to direction of yaw.

The end result of this in an actual radome would be an unbalanced load of substantial magnitude acting on each increment of length and always in a single direction, which would develop into a large cumulative value of bending moment that must be resisted by the structural space frame. Obviously this must be recognized in the mechanical design.

3. Thermal Loads

WADD TR #9-22, Chapter I, Part E, titled "Charts and Equations for the Determination of Aerodynamic Heat Transfer to Radome-Shaped Bodies" includes a portion dealing with ogives. Section 3 A of Part E presents a step-by-step procedure, together with necessary charts, for deriving values for several intermediate functions which then are used in a first simple computation to come up with the local values of temperature and of heat flux under laminar flow and again in a second similar computation for heat flux under turbulent flow.

This procedure appears to be intractable for manual calculation except for spot values but to be readily adaptable to computerization. The major part is straightforward. With chart reference data programmed from punched cards or, where such may be available, introduced as an original mathematical equation, the computer is required only to perform a fairly complex series of very simple operations, all free of uncertainty except as we note below.

One source of uncertainty is the following. The referenced section of WADD TR #9-22 indicates that an area of uncertainty exists in this procedure in that one cannot predict readily whether actual flow over an ogive shape will be laminar or turbulent. The

values of heat flux derived for these two conditions differ widely. Since we see no immediate way to resolve this uncertainty, we will compute heat flux and other thermal functions for each of these modes of heat transfer, coming up with one set of values based on lower transfer rate for laminar flow and another set based on higher transfer for turbulent flow. The user of the data must weigh the degree of conservatism he wants to incorporate in his design and thus establish a suitable, probably intermediate value for each thermal function. Thus this uncertainty can be resolved through exercise of judgment by the designer.

There is another source of uncertainty. Part way through the procedure one is required to assume a skin temperature. The mathematics can be handled by selecting several values and completing the computation for each, thus deriving several combinations of wall temperature and associated "external" heat flux. The true values then would be identified through several separate computations of "internal" heat flux, all for a single proposed physical wall structure but assuming for each a skin temperature identical with one assumed for the "external" computation. The true values of temperature and heat flux then would be those which are identical in both "external" and "internal" computations. Thus we do not see the uncertainty as lying in the mathematics per se, but rather in the selection of specific values of temperature.

Where one prime objective of this computation is the determination of the very temperature we are now forced to assume, and it is likely to vary with location, it may not be practical to assume fixed values for use at all locations. Thus we should seek a basis for selecting several temperatures which will provide sufficient spread at a point, but for varying this selection from point to point so that suitable spread is provided at each.

The most promising approach now appears to exist in relating the assumed wall temperature, T_w , to the local adiabatic wall temperature, T_{aw} , which supposedly varies with location in a manner similar to that of the actual wall temperature. Thus the assumed values of T_w might be defined as $.95T_{aw}$, $.90T_{aw}$, $.85T_{aw}$ and $.80T_{aw}$ to suit several different characteristics of wall construction. Since the computed value of T_w depends on the assumed value of T_w , this concept of basing T_w on T_{aw} requires that the computer (human or digital) perform repeated trial-and-error computation, checked by feeding back revised values of T_{aw} until T_w does in fact come out at the assumed relation to T_{aw} . This somewhat complex procedure seems practical for the digital computer, though quite tedious for manual calculation.

Work to date has not produced results in sufficient volume to justify freezing on this method. We will continue this work into next quarter, and also will look for possible ways of relating temperature to local pressure or to some other function

so angle of attack may be recognized in the computation.

The possibility exists, of course, that knowledge may have been gained subsequent to publication of WADD TR 59-22 of which we are not aware and which will permit better definition within this area. We solicit comments.

4. Computerization

a. Pressure Tables

It is evident that computation such as described above for the many combinations of variables is impractical by manual methods. Therefore we have performed preliminary planning of a set of computerized tables to read out basic aerodynamic pressure load data for tangent ogive shapes.

Input related to flight will be free-stream Mach number and angle of attack, for 10 Mach numbers from 2.0 to 6.0 selected for roughly linear increments of M^2 , and for three angles of attack, e.g. 0° , 10° and 20° .

The tables will read out only for sea level, since mechanical data for other altitudes can be derived from the ratio of ambient pressures. Presentation will include properties of the ICAO standard atmosphere.

Input related to radome configuration will be only the fineness ratio, L/D. Length will be normalized as $L \approx 1.0$. We will tabulate for 10 values of L/D from 1.6 to 3.3, with increments of 0.1 at the low end increasing to 0.2 and to 0.3 maximum. This will cover the range of sizes mentioned in the Statement of Work, which correspond to L/D ratios from 1.75 to 3.0 assuming the specified maximum size of chin dome is a portion of an ogive.

The program will include data from WADD TR 59-22 either as tabular and plotted data transferred to punched cards, or as original mathematical expressions where they may be available.

Read-out data will be presented in 10 major sections, one for each of the indicated Mach numbers. Within each, there will be 10 sub-sections for the 10 indicated values of Fineness Ratio. Each such sub-section will start with a sub-routine identifying Mach number and L/D ratio, and showing (e.g.) computed radius of curvature for the specific Fineness Ratio.

Assuming 60-line pages, data under each sub-section will be printed in 8 or more lines for axial stations corresponding to decimal values of X/L from 0 (nose) to 1.0 (base) omitting 0.9 and possibly 0.7 and 0.5 as required to fit available page space. Organized in this manner, the tables will run to a total of 20 pages.

Columnar data will be presented for each of the functions listed below, probably as 4 digits with the intent of showing a minimum of 3 significant figures, using multiplying factors as powers of 10 in the column headings where necessary.

Each printed line will include a value in each of the following columns:

3 columns for basic geometry, e. g., local diameter in inches, local slope of the wall, and total area in square inches integrated from the nose to the local station.

3 columns for 0° angle of attack, e. g., local normal pressure as psi; local hoop compression as pounds force per inch of length; and total axial load in pounds integrated from the nose.

5 columns for, e. g., 10° angle of attack, including 3 values of local normal pressure in psi for radial planes at 0° , 90° and 180° respectively from the plane of yaw; one value of total axial load in pounds force, integrated from the nose; and local bending moment in inch-pounds, derived from algebraic summation of radial vectors parallel to plane of yaw, and integrated from nose to plane of local station.

5 similar columns for, e. g., 20° angle of attack.

It now seems practical to use values from the tables to come up with corresponding values for any specific radome configuration within the contemplated parameters, simply by multiplying tabulated values by suitable factors, each of which consists only of suitable powers of actual length, L , in inches.

b. Thermal Tables

As a companion to the pressure load tables described above, we have also planned a set of computerized tables to read out aerodynamic thermal data for tangent ogive shapes. Based on the method described above, it anticipates success in confirming validity of this method. We are confident the major concepts will hold with minor changes.

It now appears practical to program this set with parameters and physical arrangements identical with those of the pressure tables for Mach number, L/D ratio and station locations, X/L . Since the method of thermal computation in WADD TR 59-22 does not account for other than straight flight, all reference to non-zero angle of attack will be omitted but we expect to develop simple methods of estimating the effects of yaw and of adjusting the straight-flight values, probably through reference to pressure variations with yaw, which will be determined in the pressure tables.

Where the read-out values of the pressure tables can be easily adjusted for different altitudes and thus the parameter of altitude is omitted, altitude now must be recognized in the thermal tables since much of the basic data in WADD TR 59-22 assumes knowledge of its value. Thus we may be forced to expand the volume of the thermal tables over that of the pressure tables, probably in the ratio of the number of values of altitude that may ultimately be included.

Assuming 5 values of altitude may be of interest, this would lead to a total of 100 pages of data. This number might be reduced if it was decided that, for example, the highest Mach numbers could be omitted at low altitude, (quite possible) and that conversely the lowest Mach numbers could be omitted at high altitude (less likely). This we estimate might reduce the printed volume by not more than 1/3, or to approximately 70 pages minimum. The main justification for this reduction would be in saving computer time. Time to program would only be increased.

For best compatibility in use of this set of tables with the pressure tables, we will retain identical arrangement of pages and of main and sub-sections as related to Mach number and Fineness Ratio, L/D, and also with printed lines associated with identical station locations. This should result in maximum ease of cross referencing.

Each printed line will include a computed value in each of the following columns:

- 1 column showing distance from nose to local station, measured along the exterior surface of the wall.
- 6 columns related to $T_w = e.g. 0.95 T_{aw}$, consisting of 3 columns for laminar flow and 3 for turbulent flow. Each group of 3 will show values of T_w as local wall temperature, of q as local heat flux in BTU/sec - ft², and of total heat flux integrated from the nose to the local station, in BTU/sec.
- 6 similar columns for $T_w = e.g. 0.90 T_{aw}$.
- 6 similar columns for $T_w = e.g. 0.85 T_{aw}$.

As with the mechanical tables described previously, these tables will be based on normalized value of $L = 1.0$. Values of thermal properties read from the tables can be converted to those for any specific size of radome through use of simple factors each of which is composed of a suitable power of the actual radome length, L .

V. LOOKING AHEAD

A. Electrical Work

The theoretical work for the next quarter will consist of debugging the Fortran computer program for prediction of insertion loss and insertion phase. It is expected that this will progress to the stage of completion of theoretical work on the flat sectionalized sheets.

With the sample holder now completed, it is planned to conduct tests on a large number of variations of flat sheet design, including some with dielectric inserts, when time permits.

B. Mechanical Work

The work thus far has provided a sound basis for definition of external pressure loading on tangent ogive radomes. The tentative method for defining skin temperature and heat flux incident on the outer skin requires minor refinement. Both require programming and computerization.

Next phase will be to look at internal effects of these external conditions, starting with thermal and mechanical effects within the dielectric windows. Thermal stress looms as possibly the major consideration in their design. This work should define a maximum size of window and indicate a practical range of thickness for typical candidate materials. Concurrent electrical work can be expected to define minimum dimensions and acceptable thicknesses and properties.

Following phases then can develop dielectric window configurations and compositions optimized with parallel development of space frame configuration and materials.

REFERENCES:

1. "Aerodynamic and Structural Analyses of Radome Shells", General Applied Science Laboratories, February 1961. WADD TR 59-22

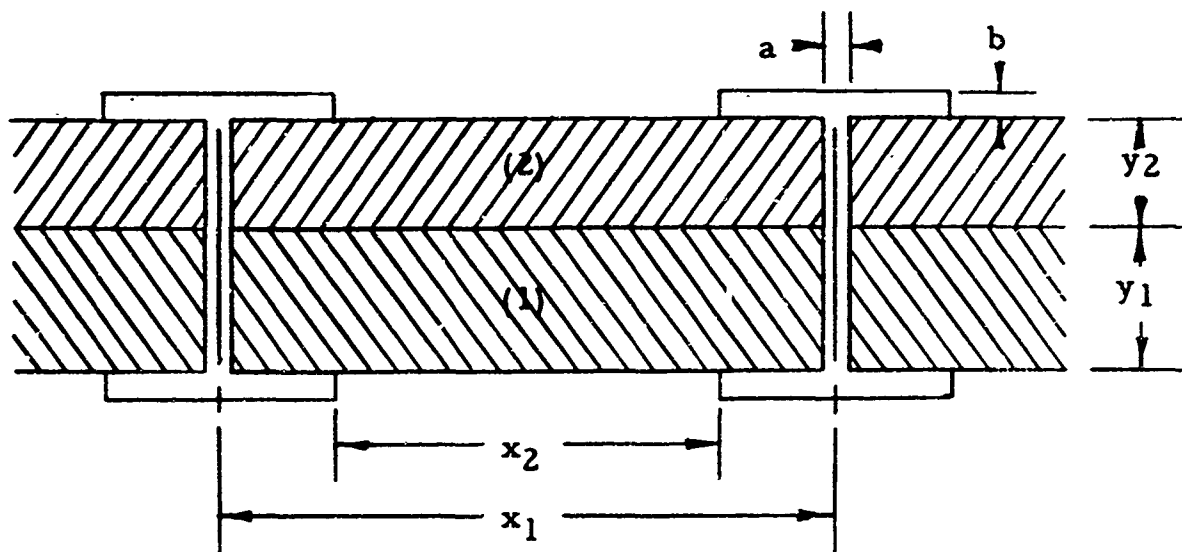


FIGURE A

DIELECTRIC WALL, FENESTRATED BY I-BEAM MEMBERS

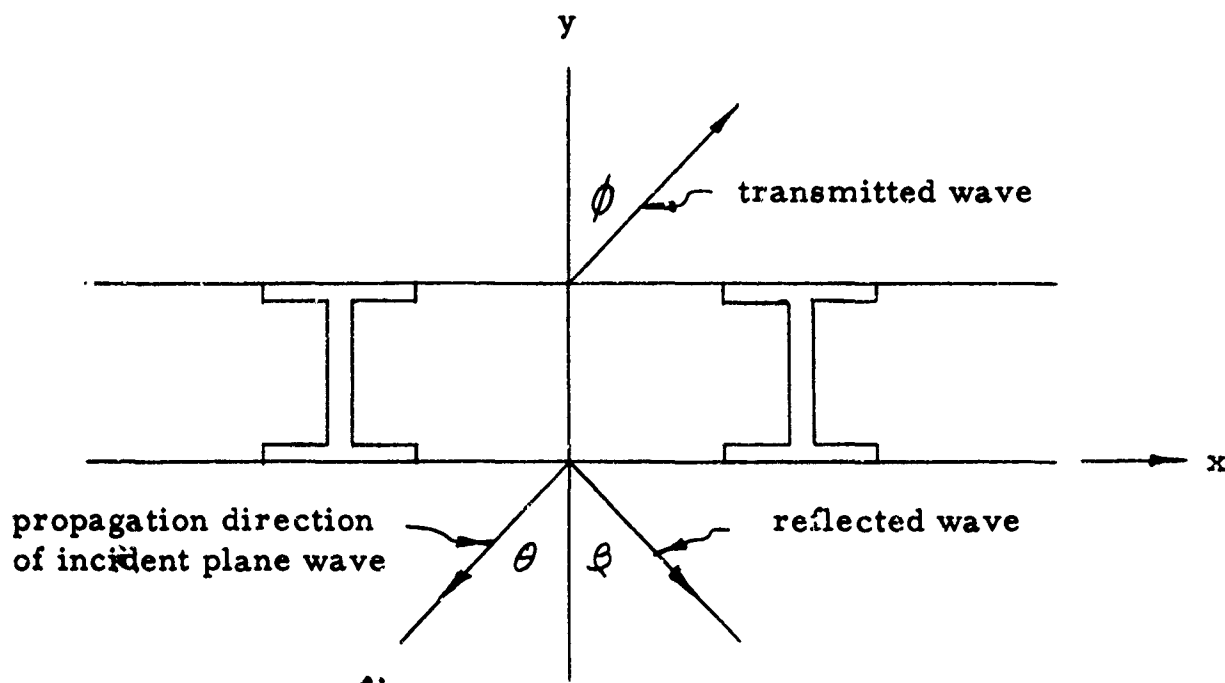


FIGURE B

ANGLES OF INCIDENCE, REFLECTION, AND TRANSMISSION

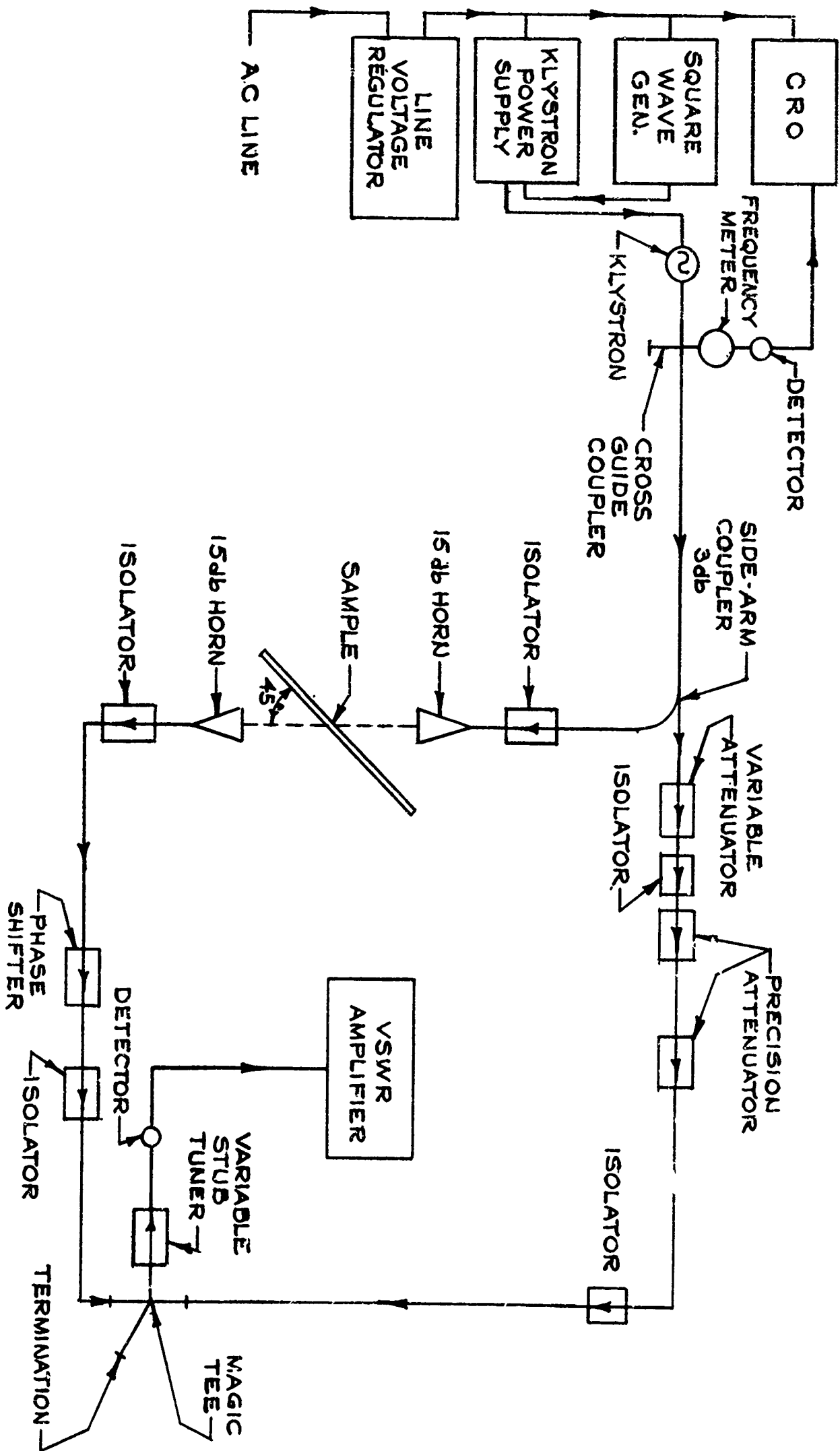


FIGURE 1

BLOCK DIAGRAM OF FREE-SPACE MICROWAVE INTERFEROMETER FOR MEASUREMENT OF DIELECTRIC PROPERTIES OF FLAT-SHEET MATERIALS

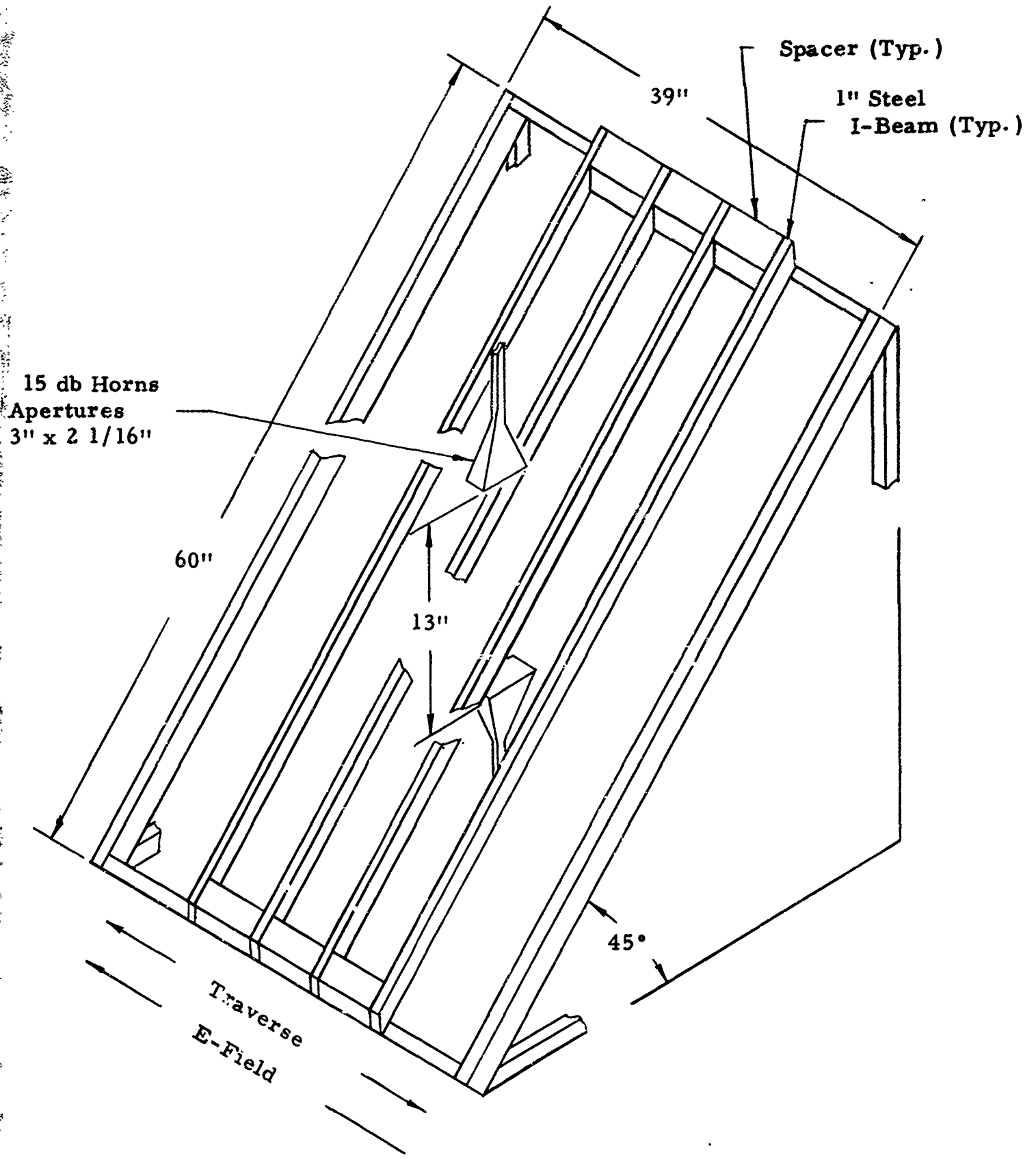


FIGURE 2

TEST SETUP FOR I-BEAM ARRAY
PERPENDICULAR TO E-FIELD

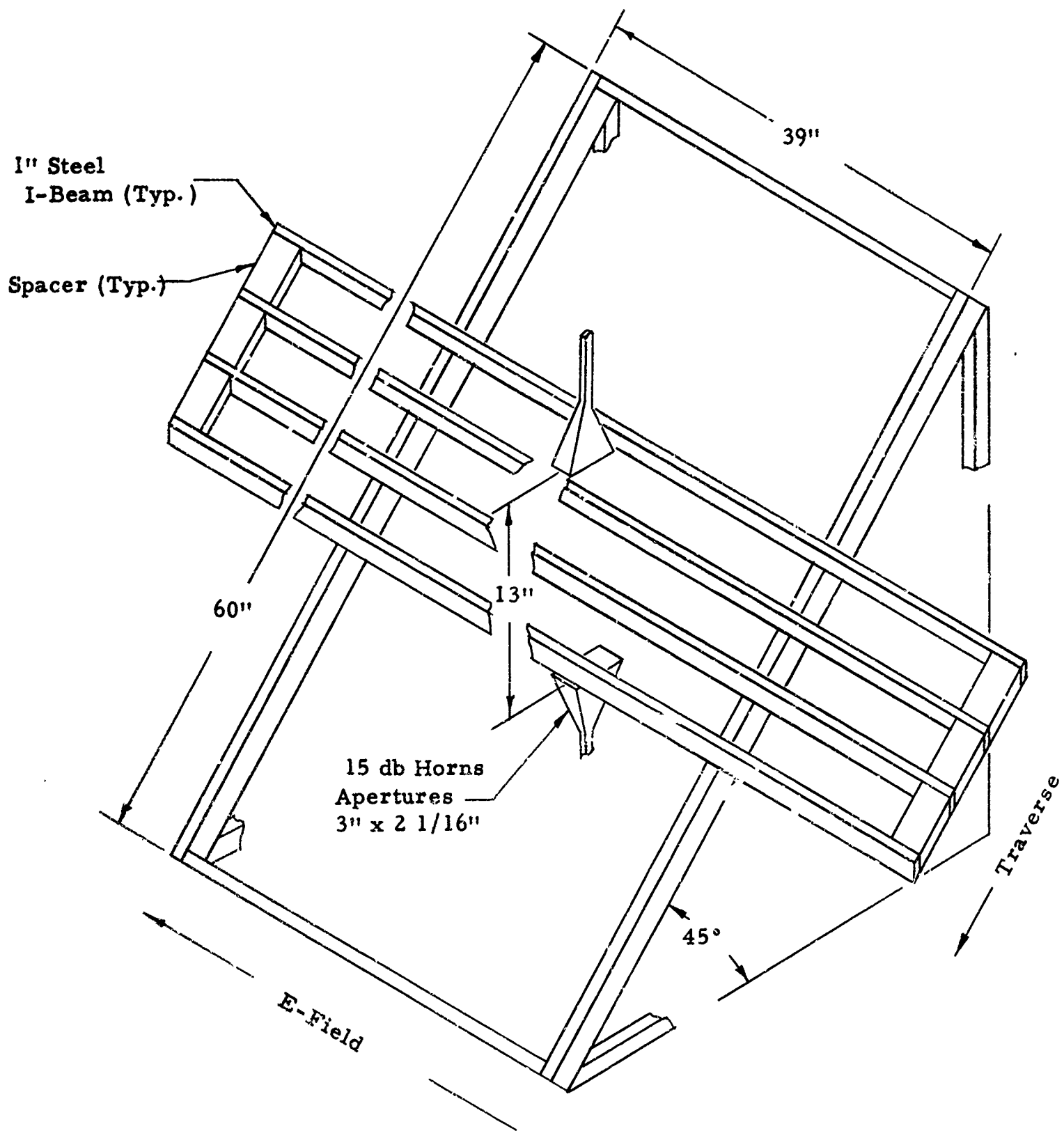
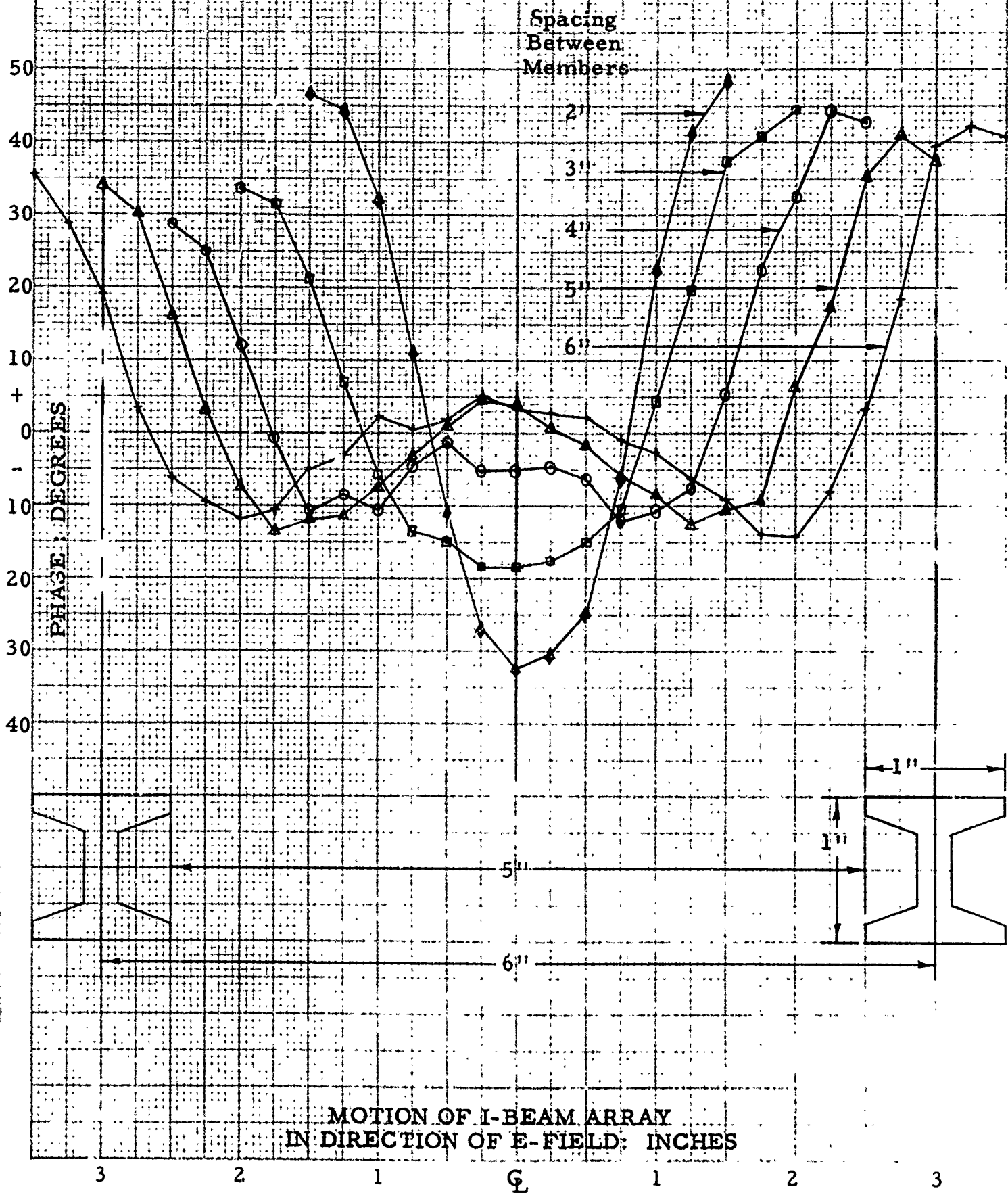


FIGURE 3

TEST SETUP FOR I-BEAM ARRAY
PARALLEL TO E-FIELD

FIGURE 4

INSERTION PHASE
PERPENDICULAR POLARIZATION AT 45° INCIDENCE
I-BEAMS PERPENDICULAR TO THE E-FIELD



MOTION OF I-BEAM ARRAY
IN DIRECTION OF E-FIELD: INCHES

FIGURE 5

INSERTION LOSS: DB
PERPENDICULAR POLARIZATION AT 45° INCIDENCE
I-BEAMS PERPENDIGULAR TO THE E-FIELD

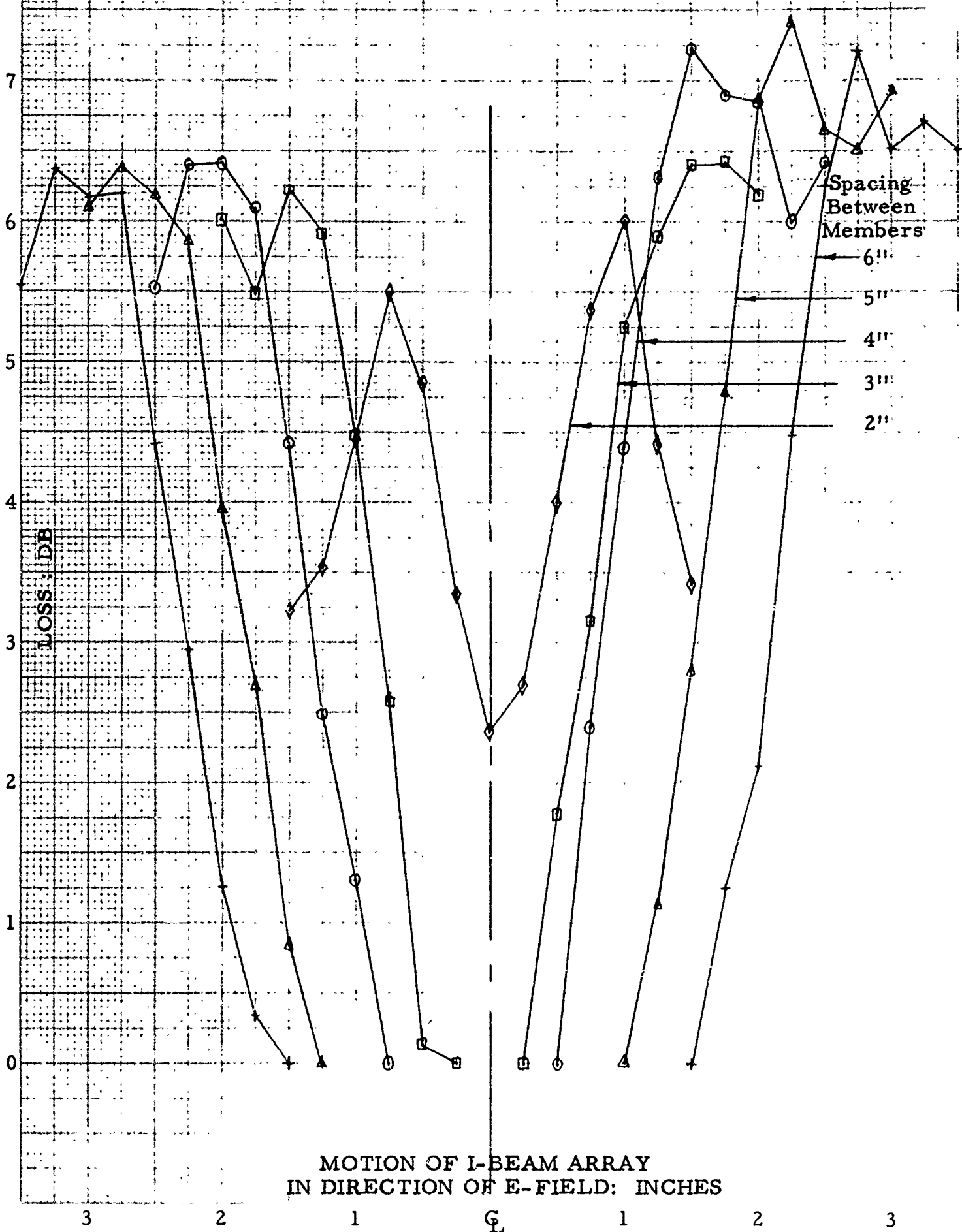


FIGURE 6

INSERTION PHASE
PERPENDICULAR POLARIZATION AT 45° INCIDENCE
I-BEAMS PARALLEL TO THE E-FIELD

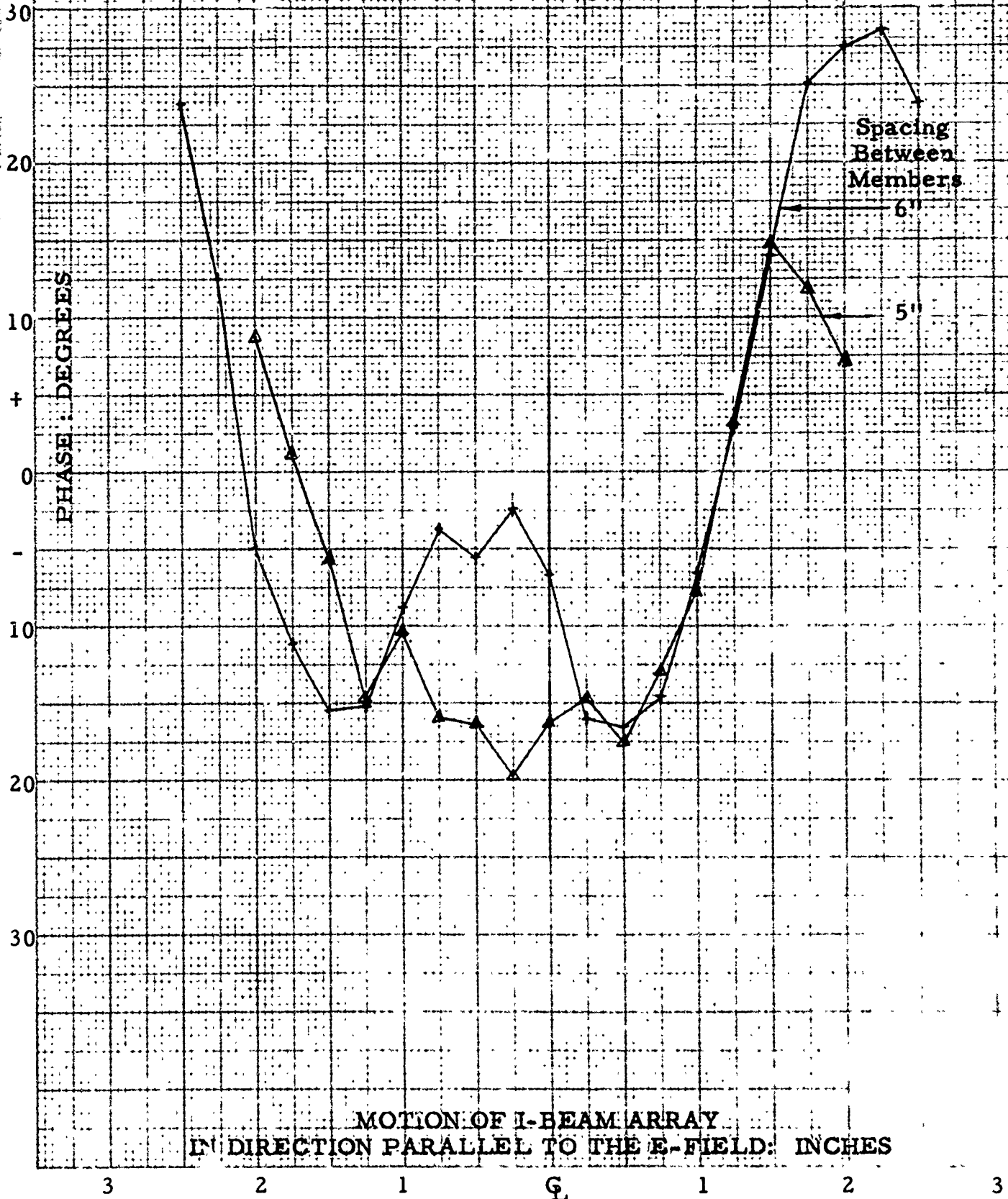


FIGURE 7

INSERTION LOSS: DB
PERPENDICULAR POLARIZATION AT 45° INCIDENCE
I-BEAMS PARALLEL TO THE E-FIELD

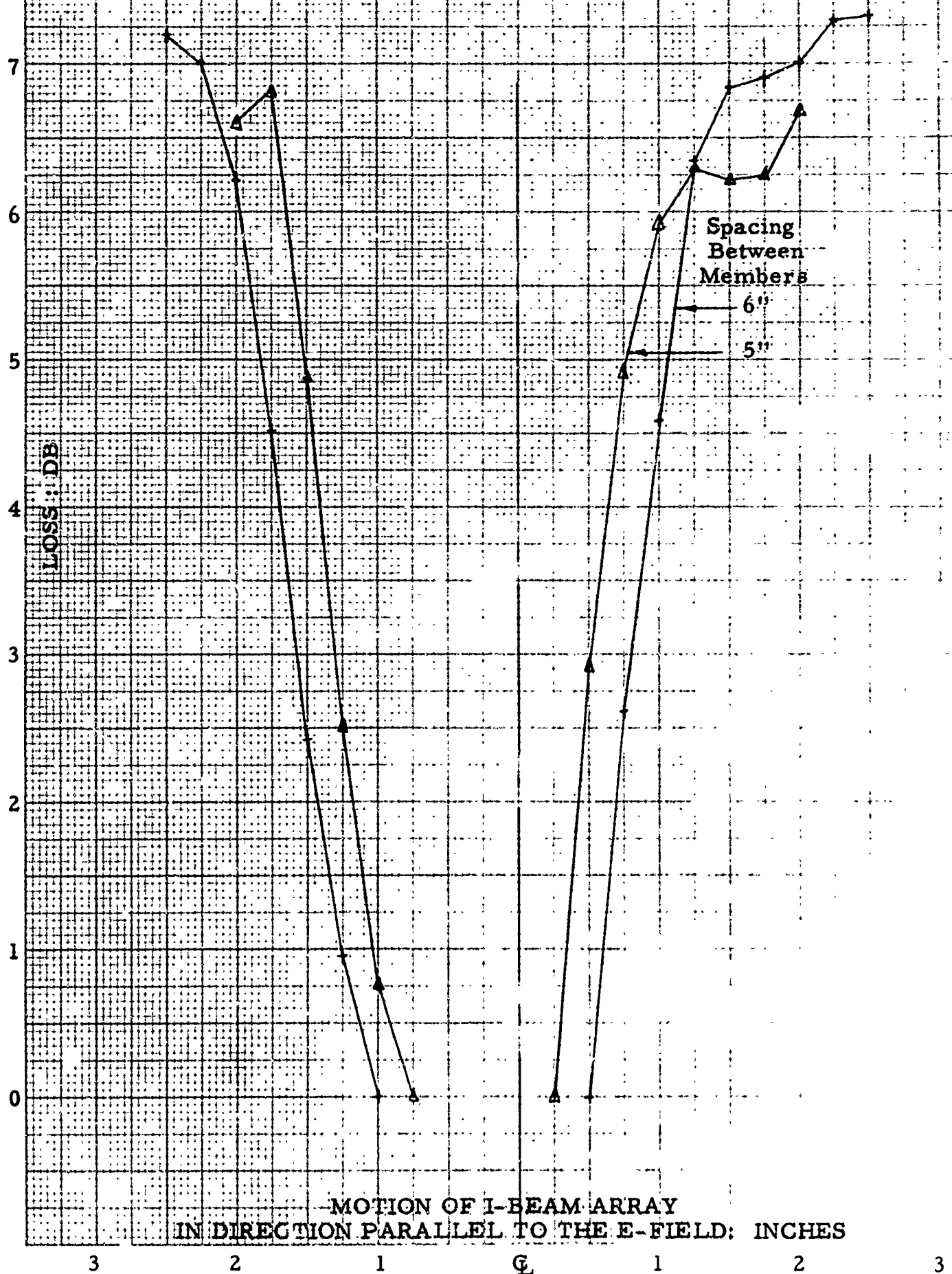




FIGURE 8

ARRANGEMENT OF SAMPLE HOLDER
WITH X-BAND INTERFEROMETER

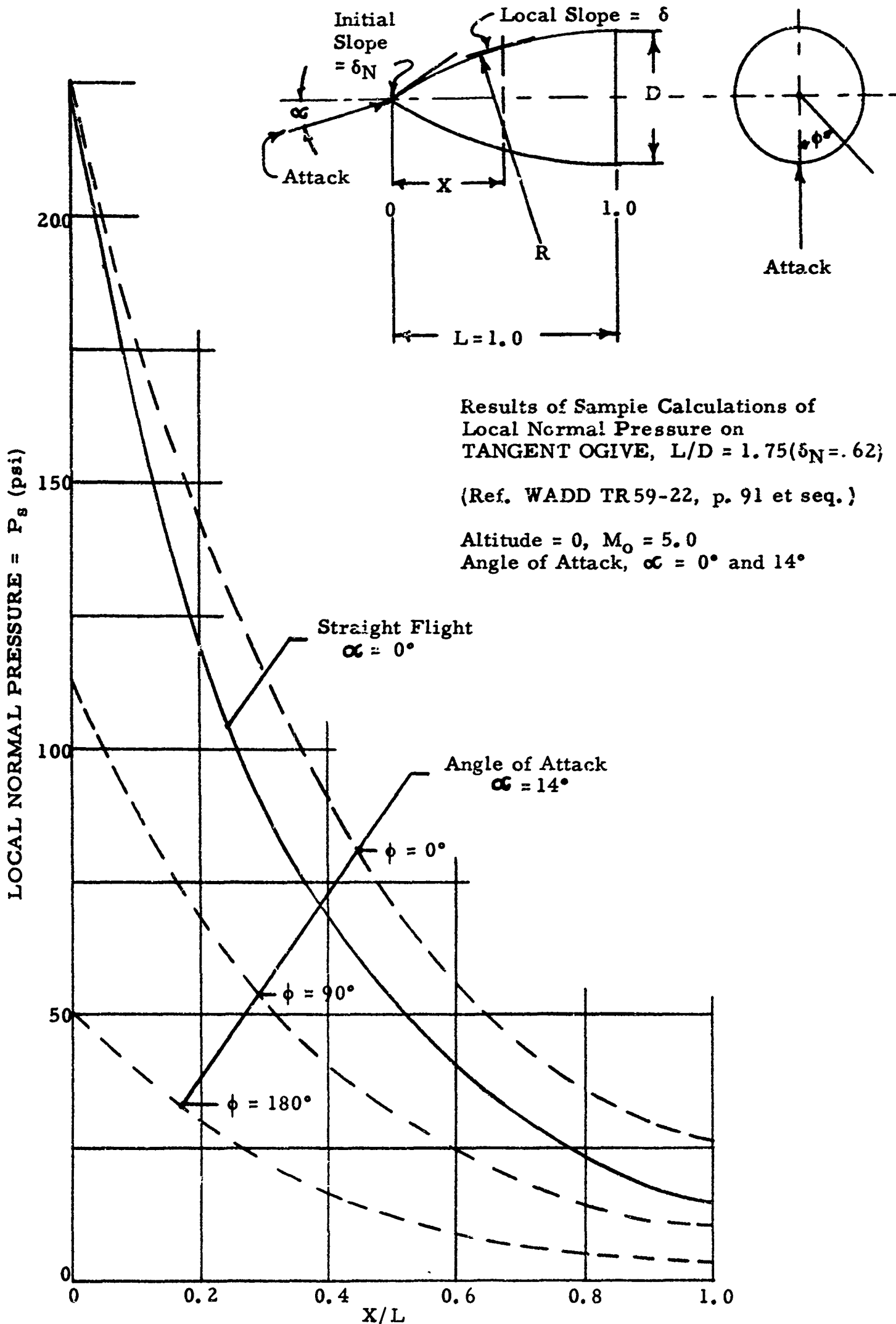


FIGURE 9
PRESSURE DISTRIBUTION ON TANGENT OGIVE

FEASIBILITY OF MONOLITHIC FOAM RADOMES

George C. Fretz, Jr.

Goodyear Aerospace Corporation

ACKNOWLEDGEMENTS

The author wishes to acknowledge the prior and parallel work of the National Research Council of Canada, Lincoln Laboratories of Massachusetts Institute of Technology, the U. S. Army Quartermaster Corps and the U. S. Air Force Rome Air Development Center in self-supported rigid foam radomes. Also acknowledged are the contributions of J. T. Dorsey, D. T. Stone, and C. J. Schmidt of Goodyear Aerospace to the electrical, structural, and design sections of this paper.

1. INTRODUCTION

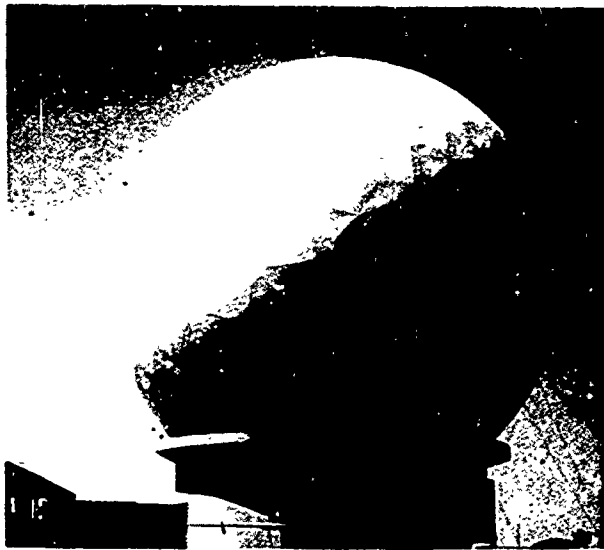
The experience gained and the excellent results obtained with smaller (17-ft and 26-1/2-ft) monolithic foam radomes warranted serious consideration of their feasibility for larger applications. This feasibility can now be assured, based on extensive environmental, structural, electrical, and fabrication technique investigations that have been made. The combined advantages of highest transmission efficiency over the entire frequency range and extremely low boresight error can now be offered in a 55-ft-diameter radome. This size will accommodate a variety of antenna systems, including FPS-3, 6, 7, 20, 26, and 27 and will enhance the performance of any of these radars.

Goodyear has produced radomes using five different basic types of construction (see Figure 1) in a wide range of sizes. These are

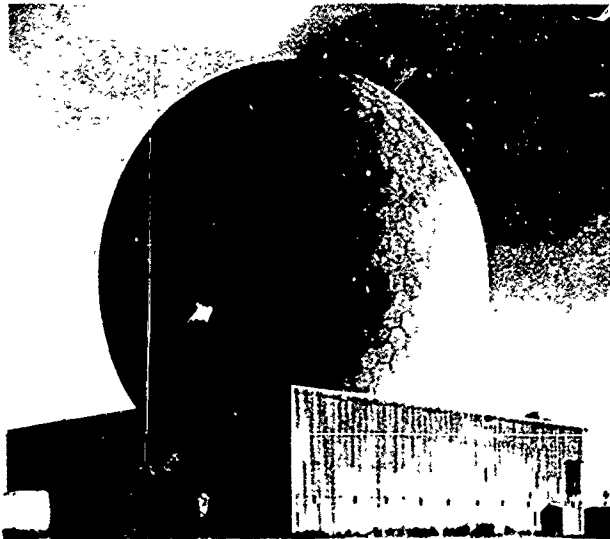
1. Metal space frame with thin skin
2. Honeycomb sandwich with channel joints
3. All-foam bonded joint
4. Bolted-flange solid laminate
5. Inflatable

This background provides performance data for all types that can be the basis for a valid performance estimate of a given type in some other size.

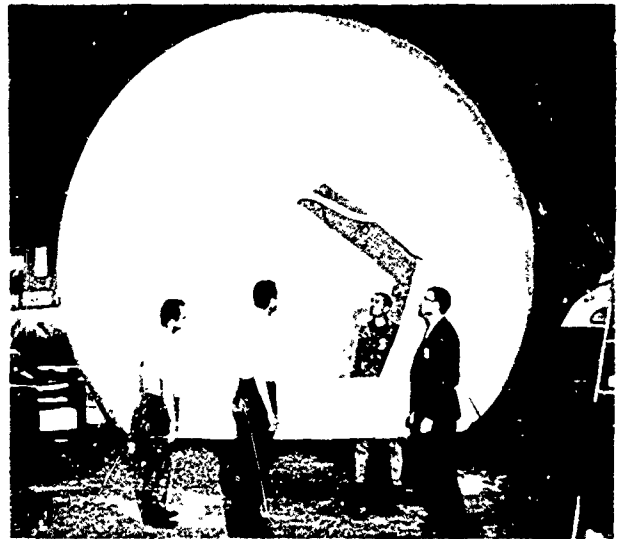
Figure 2 shows the transmission efficiency that is obtainable with a monolithic foam radome compared with that of four other types of construction that have been employed in larger sizes. Because it offers the best, rather than compromise performance, and because it does not require pressurization, air locks, and continuous monitoring, and is less subject to environmental hazards, a thorough investigation of the feasibility of a larger monolithic foam radome was made.



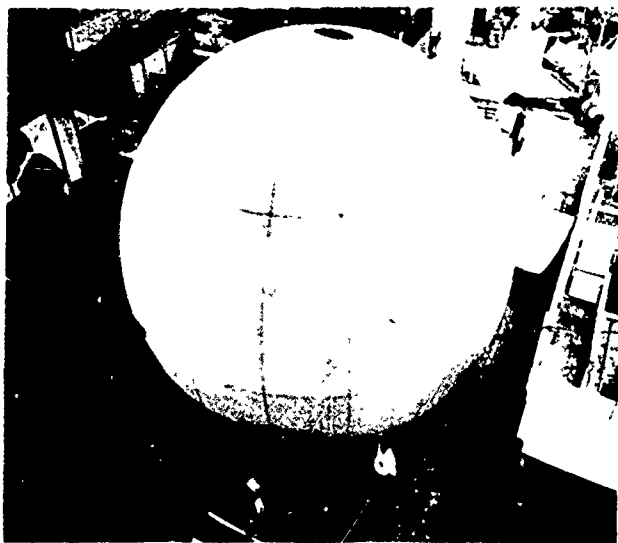
METAL SPACE FRAME



HONEYCOMB SANDWICH, BOLTED JOINT



ALL-FOAM, BONDED JOINT



SOLID LAMINATE, BOLTED FLANGE



TWO-PLY INFLATABLE

Figure 1 - Five Basic Radome Constructions

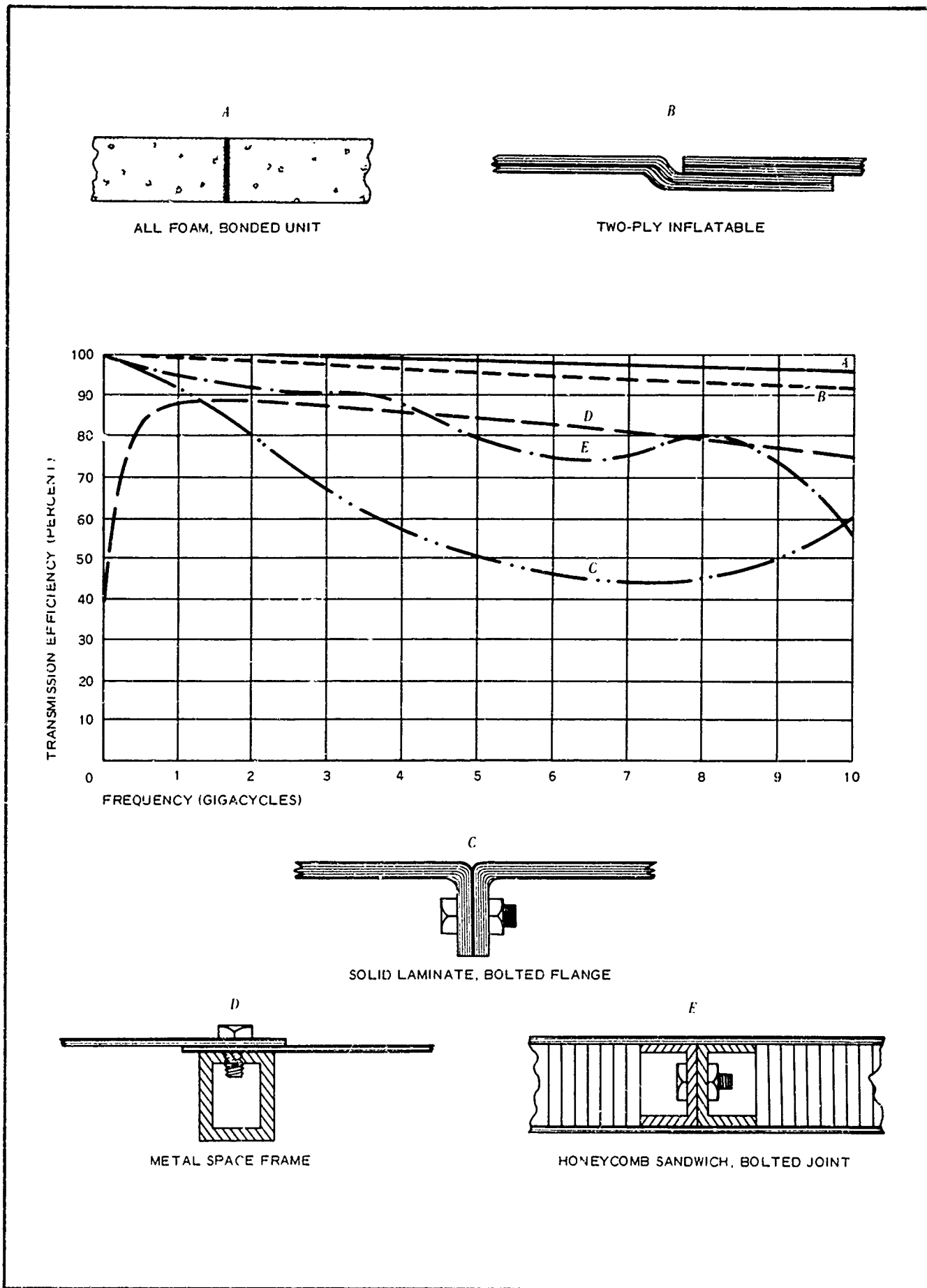


Figure 2 - Transmission Efficiency of Five Types of 55-Ft-Diameter Radomes

Based on world-wide environmental requirements, the structural aspects of the required radome were studied thoroughly to establish unit details for electrical evaluation. The study included structural analysis, a manufacturing design, and an extension to the 55-ft-diameter size of the component manufacturing, field erection, and protective techniques already established for the 17-ft-diameter radomes that are presently in service. The structural investigation, which is described later, resulted in the selection of 5.5-in.-thick, 6-pcf polyurethane wall sections to be the basis for the electrical properties study.

2. ELECTRICAL CONSIDERATIONS

a. General

The monolithic foam radome represents a definite advancement in the state of the art of large ground radomes. This radome offers the advantage of being extremely broad banded. It will provide average one-way power transmission of over 90 percent at frequencies from uhf through X-band. At many frequencies, the transmission efficiency will exceed 95 percent. Figure 3 shows flat-panel one-way power transmission characteristics at 1350 mc, 2400 mc, 2800 mc, 5400 mc, and 5900 mc. The radome also will provide low boresight error and error-rate properties over a broad range of frequencies. The boresight error for one antenna studied is expected to be ± 0.15 milliradian or lower, it being understood that the antenna pattern is symmetrical with respect to the radome and that the gimbal axes are on the spherical axis of the radome. Boresight errors of the order of ± 0.03 milliradian can be achieved, depending on the operating frequency, the particular antenna-radome combination, and the total magnitude of the fabrication tolerances that are maintained. The radome is expected to cause a less than 10-percent change from the free-space vswr of the system antenna.

The change in the half-power beam width of the main lobe and the gain in side-lobe levels is expected to be small. The actual changes that will occur will be dependent on the initial antenna characteristics without the radome and must be evaluated on an individual basis.

To ensure that uniformity of individual panels is maintained each panel should be tested in a two-horn interferometer similar to that shown in Figure 4.

b. Material Characteristics

The dielectric constant and loss-tangent properties of 5.5-in.-thick, 6-pcf polyurethane foam are shown in Figure 5. For a six-pound-density foam, the dielectric constant will be 1.095 and the loss tangent will be 0.00144. These low values of dielectric constant and loss tangent will cause only a small portion of the energy to be reflected or dissipated, thus allowing broad-band performance.

Panel density will have to be held to ± 0.3 pcf or less and even more stringent tolerances will be necessary for extremely low boresight radomes. Figure 6 shows the variation of transmission and insertion

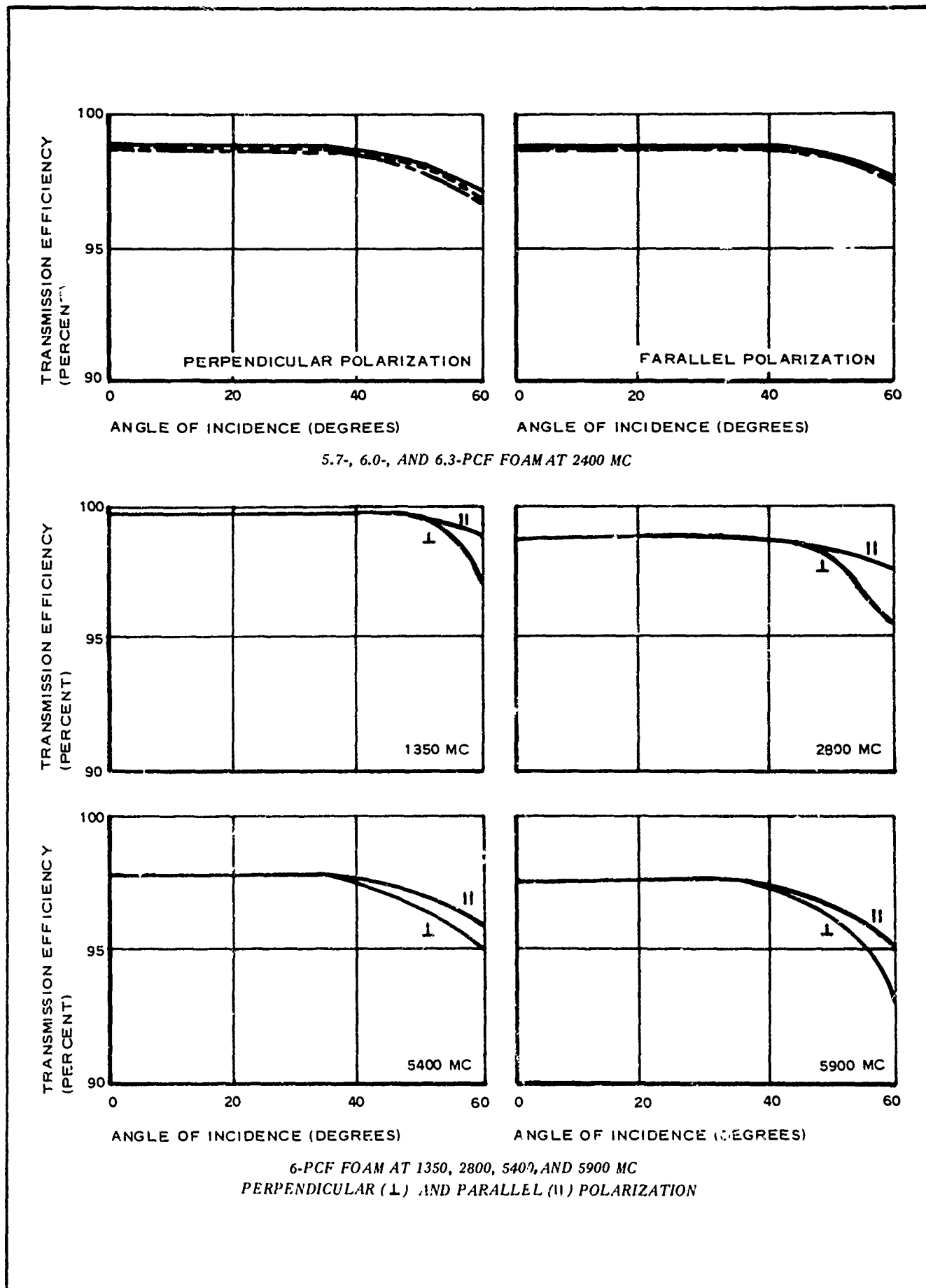
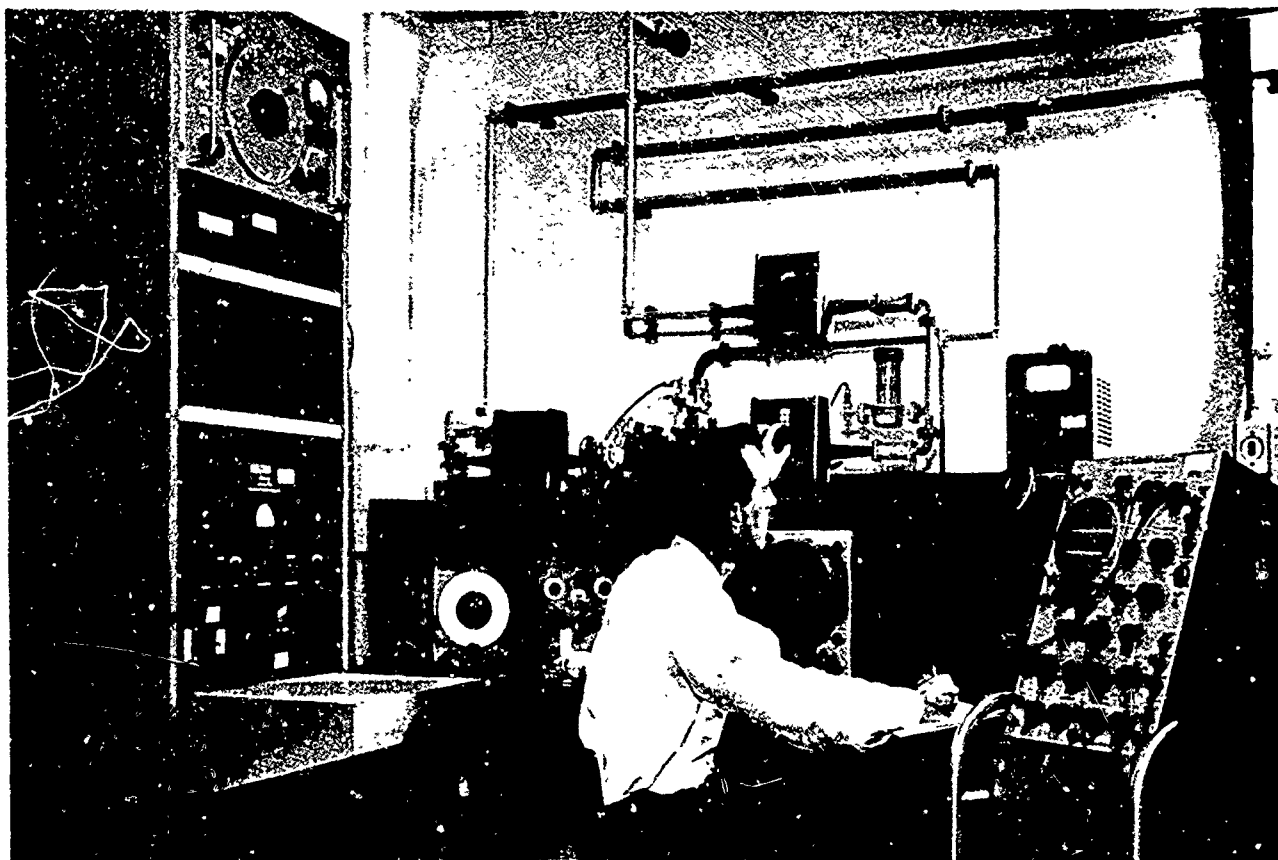


Figure 3 - Flat-Panel One-Way Power Transmission Characteristics of Polyurethane Foam at Various Frequencies and Densities



PANEL BETWEEN TEST HORNS



READING INSERTION PHASE DATA

Figure 4 - Two-Horn Interferometer

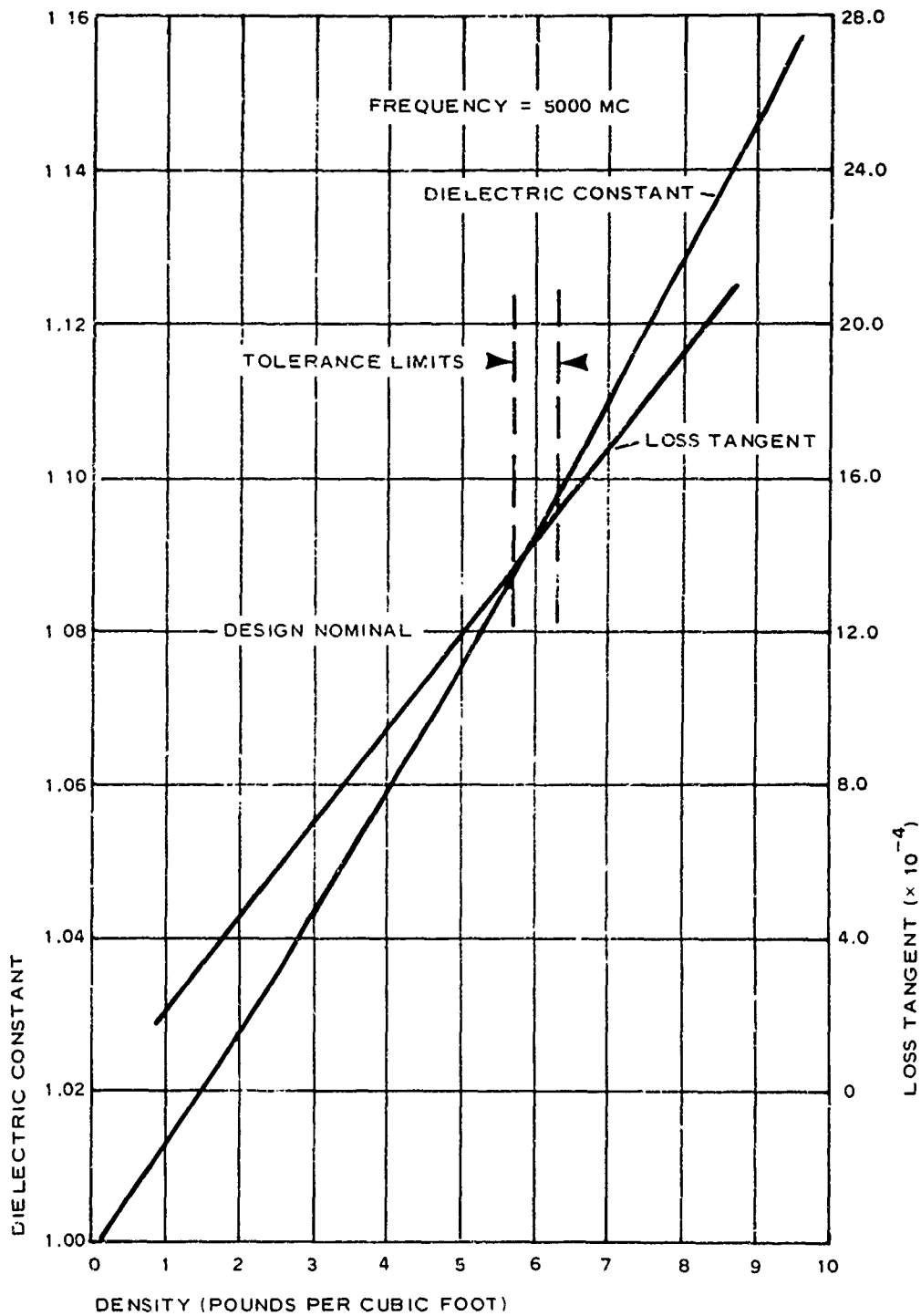


Figure 5 - Electrical Characteristics of Polyurethane Foam

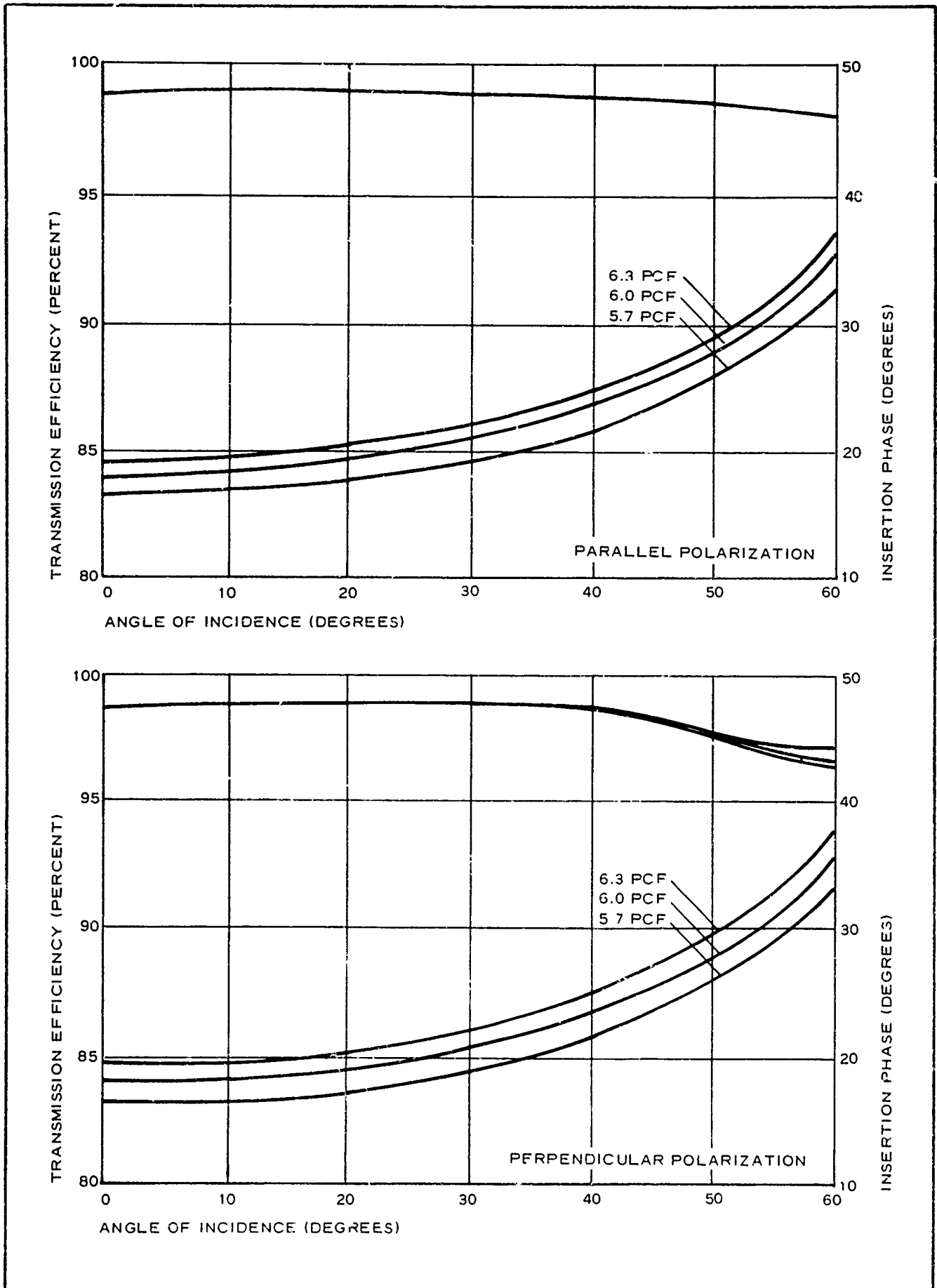


Figure 6 - Transmission and Insertion Phase versus Density of Polyurethane Foam

phase as a function of incidence angle for 6-pcf (± 0.3) density foam at S-band. The change in the transmission and insertion phase for the different densities is relatively small. Also, certain fabrication intolerances will be averaged out because a large number of panels will be seen by the antenna for any given look angle. This factor will help to obtain a very low boresight error.

c. Boresight Error

(1) Sources

(a) General

The boresight error of an all-dielectric large ground radome is a function of several interacting conditions. In general, radome boresight error, as picked up by an antenna, is caused by the following phenomena:

1. Antenna-signal interaction
2. Radome-antenna interaction
3. Radome fabrication anomalies

(b) Antenna-Signal Interaction

The antenna might not respond similarly to variations in signal polarization, strength, modulation, noise, etc. The boresight deviations resulting from these factors would occur without a radome, and their extent would be dependent entirely on the antenna system characteristics.

(c) Radome-Antenna Interaction

Radome-antenna interaction is manifested by variations in reflected energy caused by discontinuities in the radome or a varying distance between the radome and antenna, which results when the radar is slightly off center or the radome has a nonspherical area. Radome-antenna interaction is minimal in a foam radome in contrast to any other radome structure because of the very low reflection coefficient inherent with such a low-dielectric material (the dielectric constant is 1.095).

(d) Radome Fabrication Anomalies

Variations in thickness, density, presence of joints, etc. cause variations in the transmission and insertion phase of localized bundles of rays, causing a net beam bending. The effects of density and thickness variations are minimized in a foam radome due to the low dielectric-constant and loss-tangent values of the foam material and the small fabrication tolerances that can be maintained. A large portion of the effects of joint discontinuities is expected to be averaged

out due to the large number of radome panels seen by the antenna at any given look angle.

(2) Method of Analysis

Boresight error for large ground radomes is usually determined by ray-analysis techniques. A detailed study is not intended in this presentation. GAC has an IBM 650 digital computer already programmed for the rapid solution of boresight error calculations for problems of this type. Essentially, the programmed computer solves the following formula:

$$\theta_i = \frac{\lambda}{2\pi} \frac{(\sum E|T_i|) (\sum E|T_i|x\phi_i) - (\sum E|T_i|x) (\sum E|T_i|\phi_i)}{(\sum E|T_i|) (\sum E T_i x^2) - (\sum E|T_i|x)^2},$$

where

θ_i = boresight error (radians),

E = weighted ray voltage coefficient,

T_i = ray voltage transmission coefficient,

x = ray distance to central ray,

ϕ_i = insertion phase, and

λ = free-space wave length.

The allowable tolerances on local density and thickness values and their variations from panel to panel are determined with the aid of the computer. Calculations are made pertinent to a particular antenna over its operational r-f spectrum and for the anomalies expected in the full-size radome.

The anomalies in the radome panels can be checked by actual test in the interferometer shown in Figure 4.

3. STRUCTURAL CONSIDERATIONS

a. Service Conditions

Typical service conditions that have been considered for a 55-ft-diameter all-foam radome are as follows:

1. Ambient temperatures from -65 to +160 F
2. Maximum wind velocity, 130 knots (150 mph)
3. Ice load up to 8 in. of solid ice, or 15 in. of rime ice or snow, over the entire structure

4. Salt atmosphere as encountered in coastal regions
5. Service life of 10 years

b. Load Analysis

The load analysis is based on the most severe probable combination of service conditions. Examination of wind velocity versus temperature data collected by the USAF Climatic Center, Washington, D. C., for U. S. and world-wide geographical areas shows that, in general, maximum wind velocities are not associated with extreme temperatures. There are, of course, geographic exceptions to this generality that must be considered when designing for peculiar site locations. For this general investigation, it is assumed that the most severe wind conditions will occur at -10 F. Also, calculations have shown that ice loads produce stresses of opposite sign to those produced by wind loads and, because wind-load stresses will predominate, the most severe load condition will exist where wind loads are maximum and ice loads are zero. The wind load stresses in a ground radome are determined from the wind pressure distribution around the radome and the resultant lift drag and overturning moment on the radome. These quantities have been measured in wind tunnel tests of scale models with various truncation angles and support structure configurations. Figure 7 shows a measured pressure distribution along a great circle through the forward and rear stagnation points and the apex. A pressure distribution defined by a three-term trigonometric expression with coefficients selected to yield the same lift and drag as the measured pressure distribution is also shown. This expression, which closely resembles the actual pressure distribution, especially on the forward portion of the radome where the most critical stresses occur, is used to calculate the basic membrane stresses in the radome shell. The maximum shell loads expressed in pounds per inch for a 55-ft-diameter radome exposed to 130-knot winds at -10 F are estimated to be:

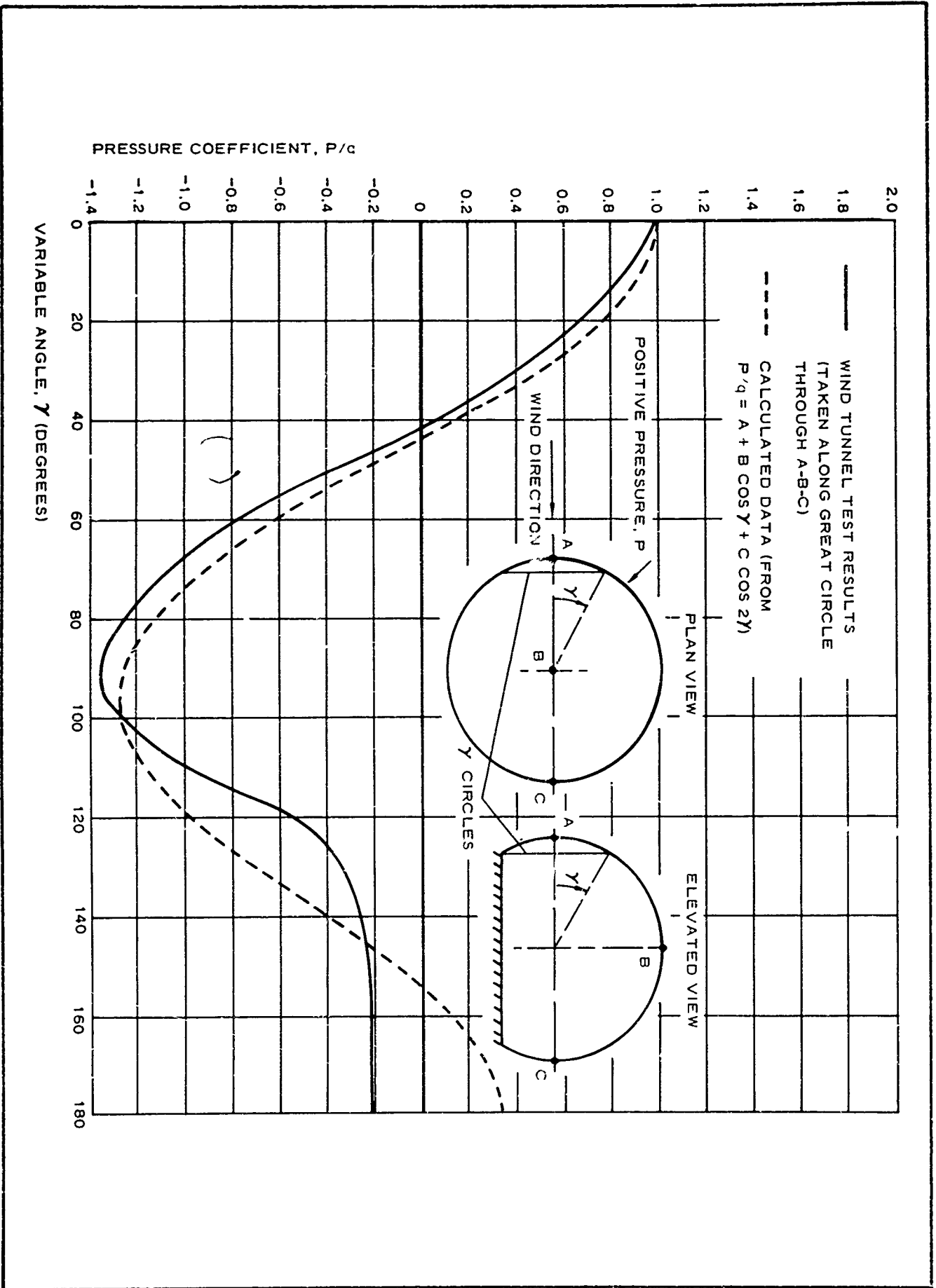
1. Tension = 300 lb per inch
2. Compression = 180 lb per inch
3. Shear = 170 lb per inch

and, for a 5.5-in. thick shell, the maximum unit stresses will be:

1. Tension = 54.6 psi
2. Compression = 32.8 psi
3. Shear = 31.0 psi

These values are approximate because undefined parameters such as stiffness, size, shape, and other characteristics of the base support structure will have an effect on radome stresses.

Figure 7 - Test and Calculated Pressure Distribution over 55-Ft-Diameter Radome



12

Typical minimum mechanical properties of 6 pcf polyurethane foam when molded to thickness are:

1. Tensile ultimate strength = 100 psi
2. Compressive ultimate strength = 120 psi
3. Shear ultimate strength = 50 psi
4. Modulus of elasticity = 6000 psi

The panel joints are expected to produce no significant loss of strength below that of the parent material. A 1.5 ultimate factor applied to the calculated stresses will give the following factors of safety for the radome strength:

1. Tension = $100/1.5 \times 54.6 = 1.22$
2. Compression = $120/1.5 \times 32.8 = 2.44$
3. Shear = $50/1.5 \times 31.0 = 1.07$

Detailed calculations of discontinuity stresses at the base of the radome might show a need for extra strength or special reinforcement near the base of the radome.

In addition to meeting the strength requirements, the radome shell must also must have sufficient elastic stability to preclude failure by elastic buckling. The critical buckling pressure is defined by the expression

$$p_{cr} = KE \frac{t^2}{R^2} ,$$

where

p_{cr} = critical buckling pressure,

K = dimensionless buckling constant,

E = modulus of elasticity,

t = shell thickness, and

R = spherical radius of the shell.

With the values

$$K = 0.30,$$

$$E = 6000 \text{ psi},$$

t = 5.5 in. and

R = 330 in. ,

$$P_{cr} = (0.30)(6000) \frac{5.5^2}{330}$$
$$= 0.500 \text{ psi .}$$

The stagnation point pressure for 130-knot winds at -10 F is 0.461 psi. Therefore, the factor of safety against buckling will be:

$$\frac{0.500}{0.461} = 1.07 .$$

c. Thermal Conditions

The effect of radar energy loss at the panel joints is calculated to produce a 40 F temperature rise at maximum power. Design specifications require withstanding 120 F ambients inside and out. At this temperature the 40 F rise to 160 F in the radome material would be acceptable. If other factors were to raise the interior temperature above 120 F, and the radar simultaneously be operated continuously at full power, auxiliary interior cooling would be desirable.

d. Weather Protection and Aging Effects

(1) General

Primarily, any radome containing plastic materials must be protected from two undesirable environmental conditions. These are (1) degradation of the surface due to ultraviolet radiation and (2) water absorption by the material. These two items are related inasmuch that water absorption by a material will increase as its surface decomposes.

Experience with urethane, which began in 1948 with its use in a sandwich radome, indicates that when properly treated, this material will remain stable indefinitely. Many of the early radomes containing urethane are still in service and have suffered no degradation, either physically or electrically.

(2) Weathering and Transmission Tests

GAC has been conducting weatherometer tests on both bonded and unbonded specimens that included control samples with no protection. These tests, which are run for a 1500-hr period, employ an Atlas weatherometer model STDTG^a with sunshine-carbon electrodes for ultraviolet exposure.

^aAtlas Electric Device Co., Chicago, Illinois.

On uncoated samples, weathering is indicated by surface chalking (loosening of the cells or beads on the surface); yellowing is also evident, particularly on uncoated urethane (see Figure 8). On the coated samples, acrylic paints provided adequate protection (see Figure 9). GAC currently considers these paints to be the most feasible from an economic and physical standpoint. However, other types of materials are being considered. No differences were observed between brush and spray coats. Double coats offered some protection over that afforded by single coats and are recommended for radomes.

The exterior surface of reinforced-plastic panels is as susceptible to ultraviolet weathering effects as the foam. During 1500-hr tests of uncoated fiberglass laminate panels, the resin covering the outer fibers decomposed and the surface assumed a fiber-like texture, that absorbed moisture readily (see Figure 10). Therefore, both foam and fiberglass-laminate surfaces require environmental protection.

GAC is now performing intensive r-f tests of weathered specimens to determine their electrical performance characteristics. The data obtained from these tests will reveal performance degradations of coated surfaces that might not be apparent by visual inspection.

GAC is also conducting transmission tests on various coatings and films during a simulated rainfall of approximately one inch per hour at a test frequency of 24,000 mc. The results of these tests indicate that the acrylic paints are among the better materials in regard to water-shedding properties.

A 10-year service life is readily obtainable with a bonded-foam radome if proper periodic maintenance is conducted. As with any properly designed and fabricated stationary structure, such maintenance is normal and will extend the life of the building indefinitely.

4. MANUFACTURE

a. Design

The bonded-foam 55-ft radome will have a 5.5-in. thick wall (± 0.06 in.) constructed of 261 prefabricated panels of polyurethane foam with a density of 6 pcf. The largest panel will weigh approximately 70 lb and have about 25 sq ft of area, the gross weight of the radome will be under 18,500 lb. The panels will have 5 basic shapes; 4 additional shapes will be obtained by cutting partial panels from the 5 basic patterns (see Figure 11). A special formulation of epoxy and adhesives will bond the panels. Weather protection will be provided by a suitable paint or a film of plastic.

b. Fabrication

Radome panels will be formed in jacketed molds that will permit hot

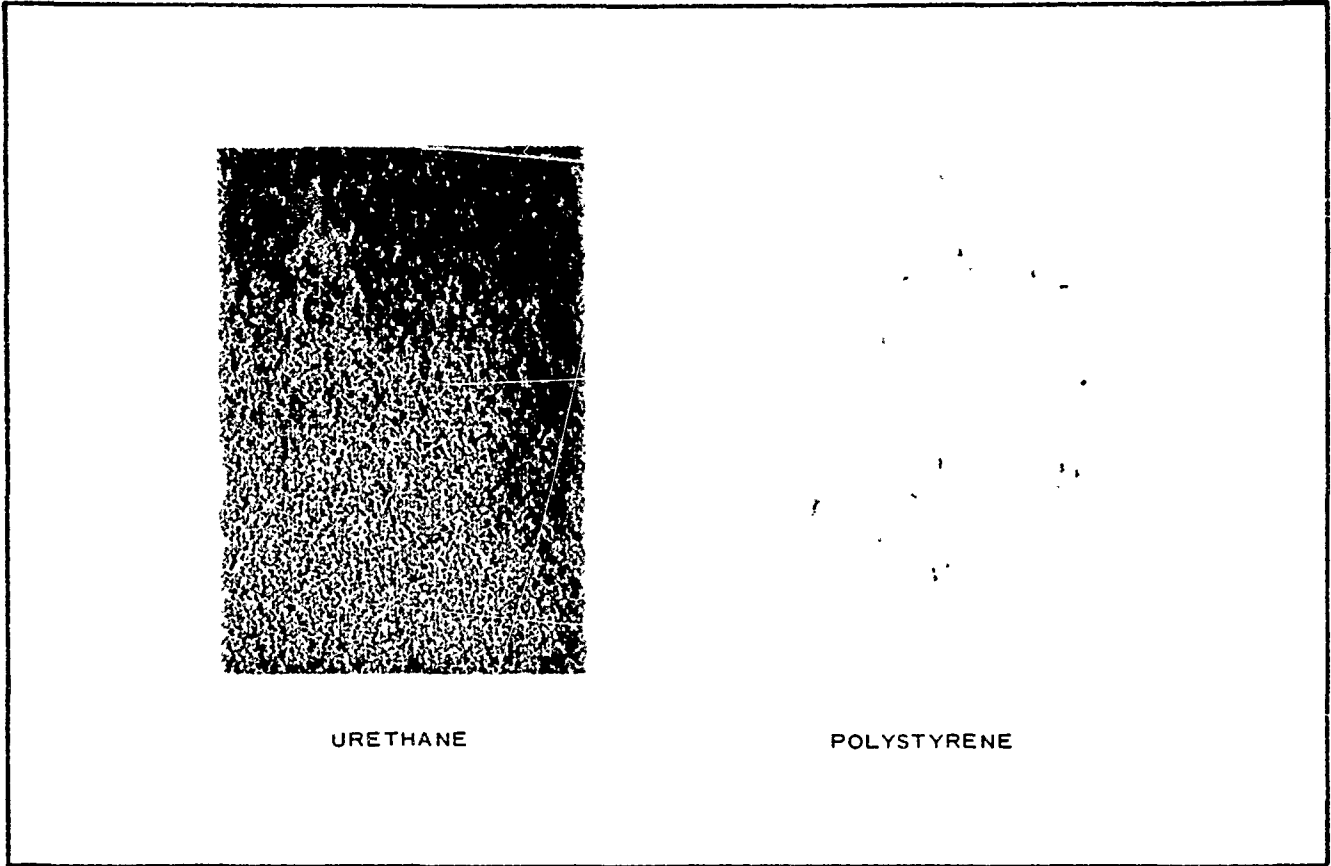


Figure 8 - Uncoated Test Samples after 1500 Hr

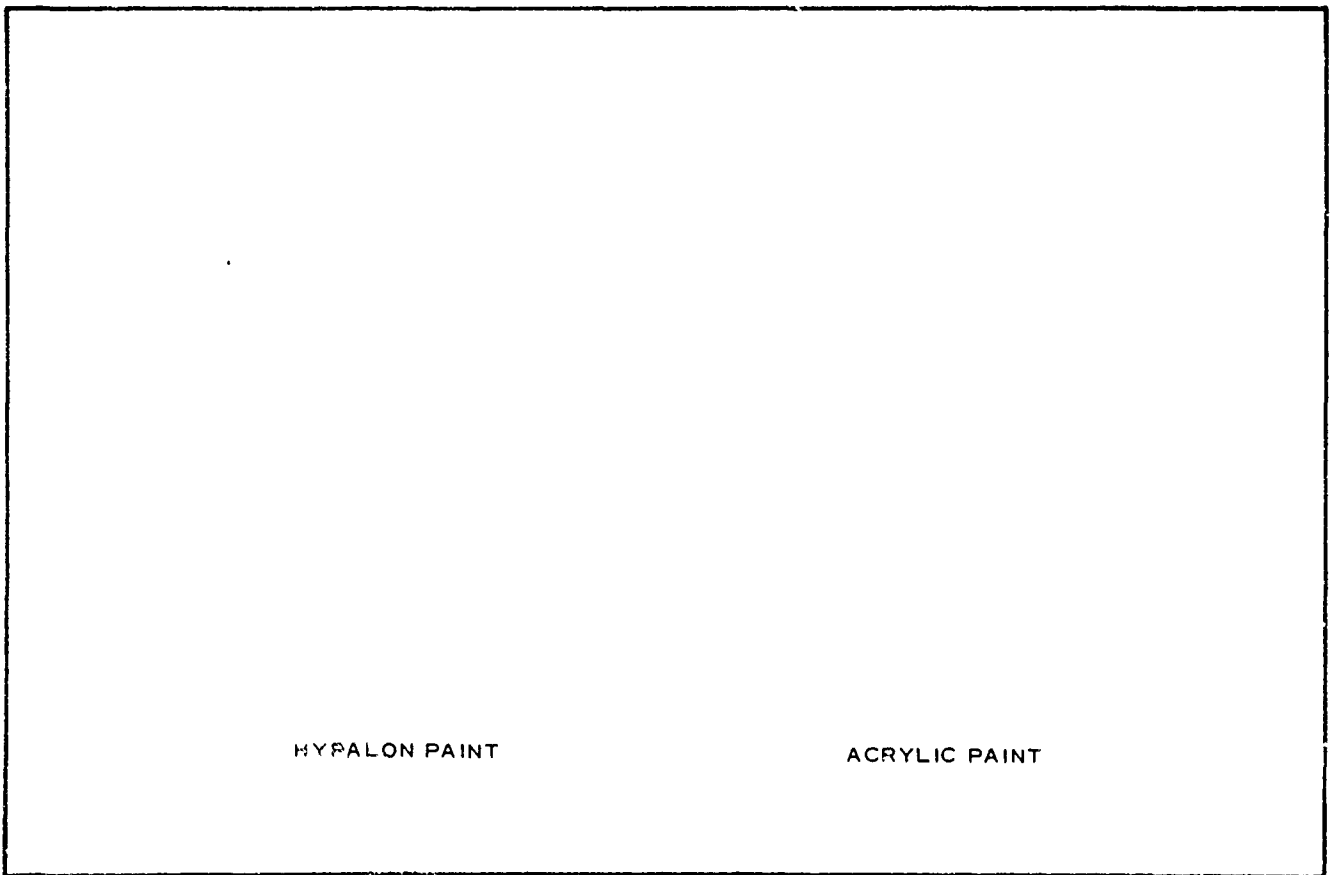


Figure 9 - Coated Test Samples after 1500 Hr

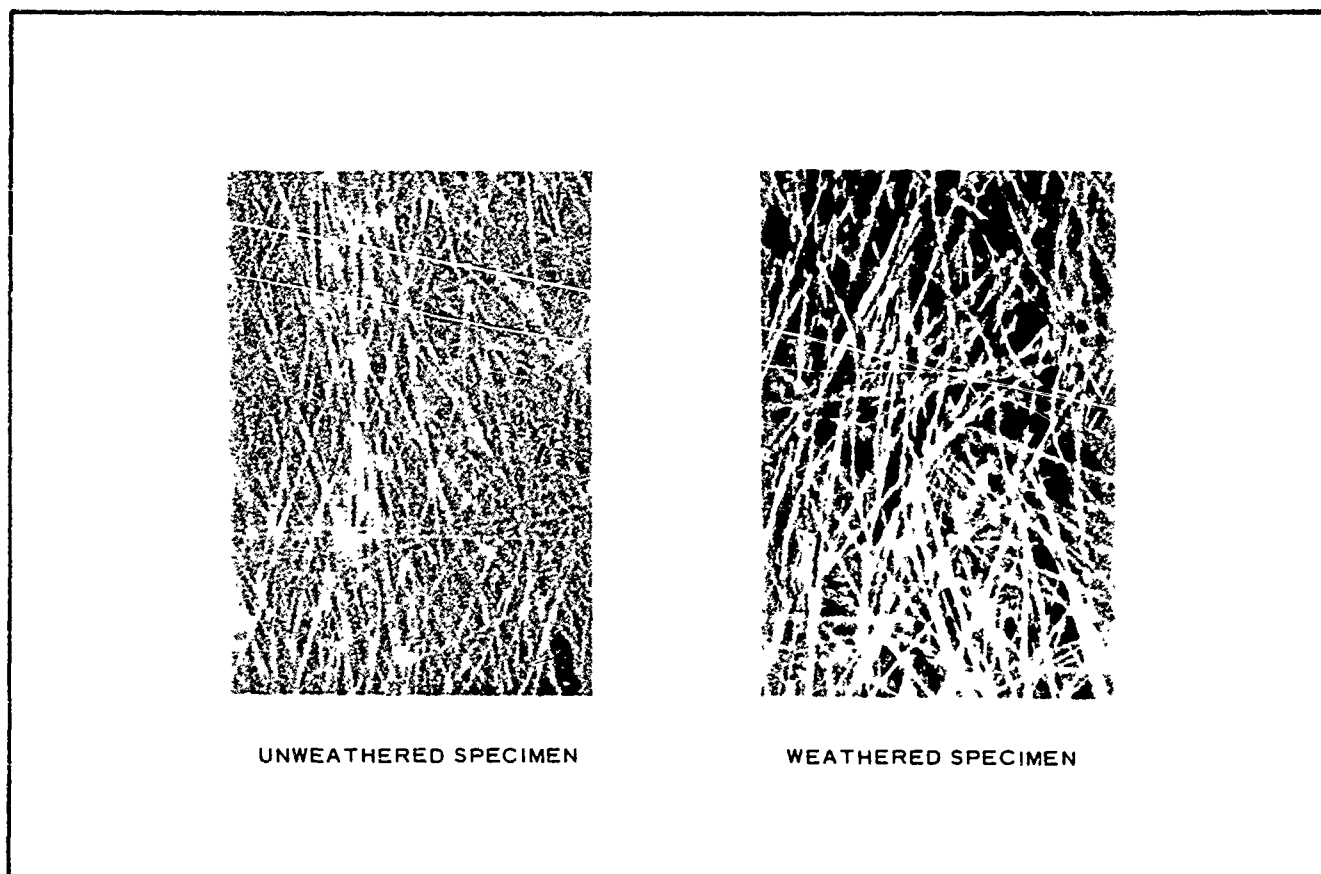


Figure 10 - Uncoated Fiberglass-Laminate Test Panels

water or steam circulation for initial heating of the mold to 140 F and curing of foamed panels at 180 F. The two principal molding surfaces will represent the outer and inner spherical surfaces of the radome and will be of sufficient size to produce the largest panels of the radome. Adjustable side rails or borders will be positioned to produce the various sizes of panels required. Liquid foam and reagent, automatically mixed, will be injected into the molds in the proper quantity for the panel size to be produced.

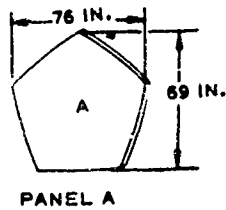
Cured and aged panels will be trim machined to size to within about $\pm 1/32$ in. for accurate fit of the erected sphere and to ensure minimum thickness bonding for best electrical and structural characteristics.

c. Erection

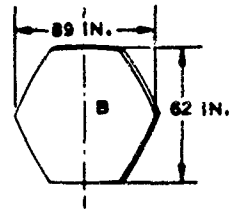
Some type of shelter will be desirable or necessary except when ideal weather conditions can be ensured. In most cases a simple space frame (scaffolding) covered by plastic sheeting will suffice. A dry-run assembly and disassembly prior to shipment of panels to the erection site should eliminate misfits and rework on location.

Radome erection will start with the fitting and bonding of the special base panels to the base ring of the foundation. Mating surfaces of the first and second tiers above the base tier panels will also be resin coated and the panels held in place with special clamps (see Figure 12) that fit into adjacent holes across the panel joint.

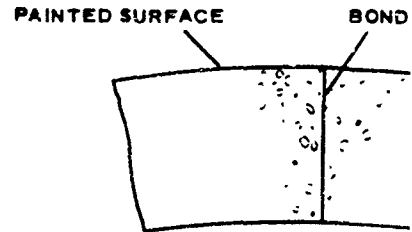
FRAMES



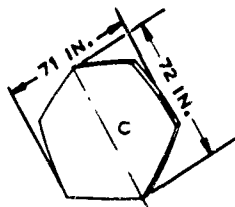
PANEL A



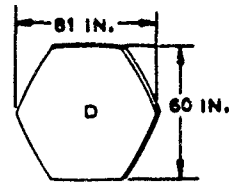
PANEL B



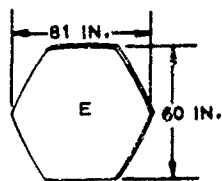
A-A
TYPICAL JOINT



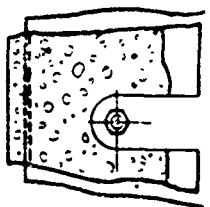
PANEL C



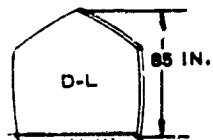
PANEL D



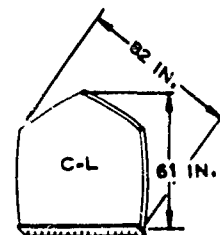
PANEL E



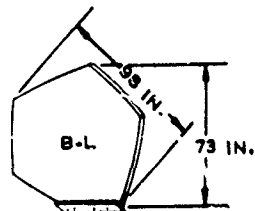
C-C
SCALE 1/2



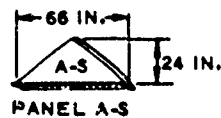
PANEL D-L, SHOWN
PANEL D-R, OPPOSITE



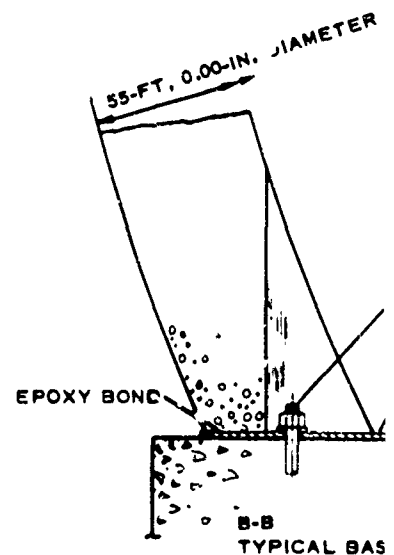
PANEL C-L, SHOWN
PANEL C-R, OPPOSITE



PANEL B-L, SHOWN
PANEL B-R, OPPOSITE

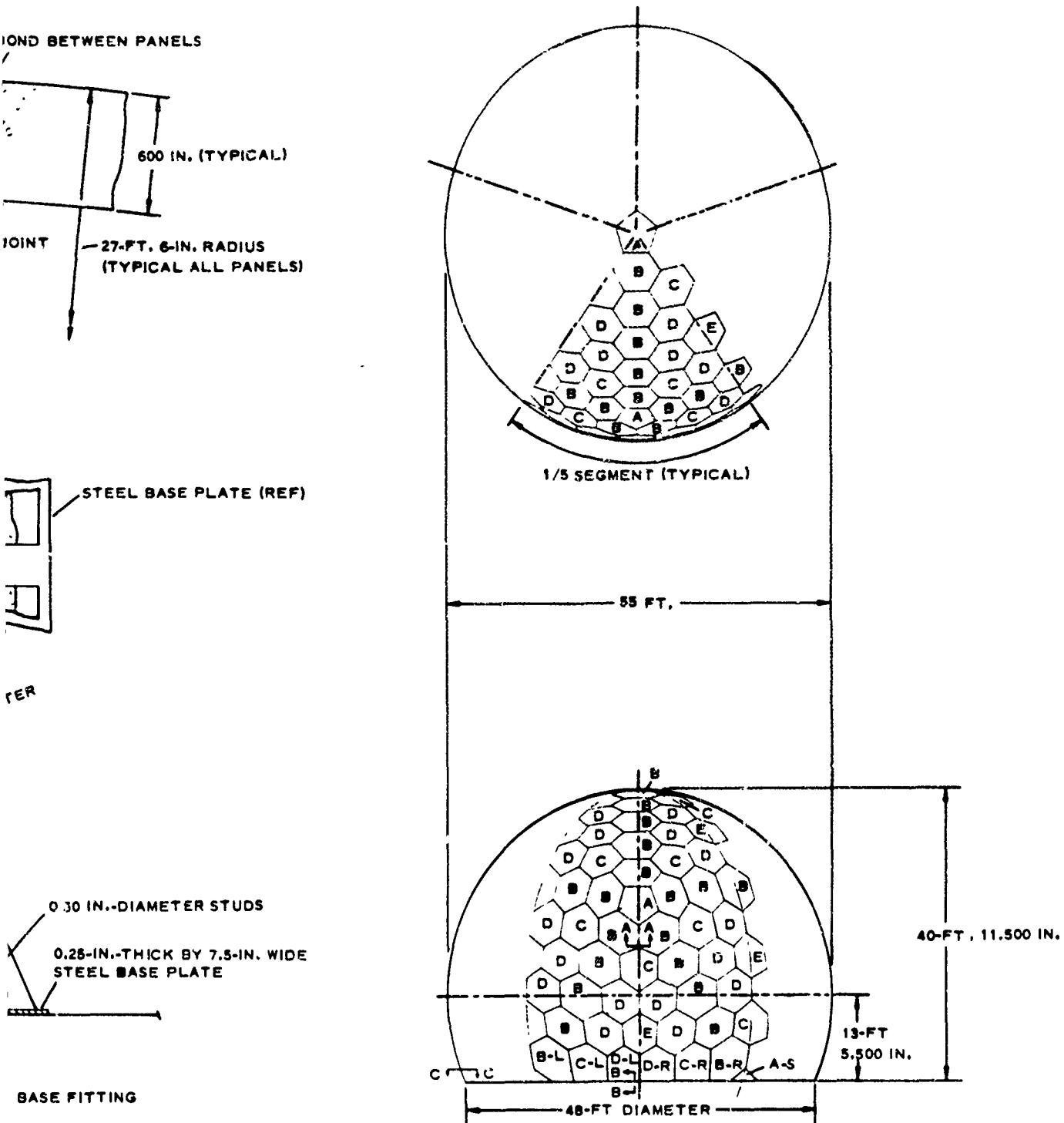


PANEL A-S



B-B
TYPICAL BASIN

ALL PANEL DIMENSIONS ARE APPROXIMATE



NOTES UNLESS OTHERWISE SPECIFIED:
 TOTAL RADOME AREA = 6,180 SQ FT
 AVERAGE HEXAGONAL PANEL AREA = 26.4 SQ FT

Figure 11 - Structural Details of Bonded Foam Radome



Figure 12 - Foam Panels Held by Clamps

Curing of the bond at the base by induction heating can be started as soon as the assembly and clamping of two tiers above has been accomplished. Assembly of the next tier can also be started so that the fit of two tiers ahead of final curing can continuously be ensured to completion of the sphere. Two hundred sixty panels in 10 tiers will be used in a 55-ft diameter topped by the top-center pentagonal panel.

5. CONCLUSIONS

A 55-ft diameter was chosen for the present all-foam radome study because it is a size that will contain and protect several models of currently existent radars. It also represents a logical upward step from the 17-1/2- and 26-ft diameter monolithic radomes that have been built and placed in operation.

Nothing in the feasibility analyses indicates that the 55-ft diameter reaches the limit of the state of the art. Because of this and because the physical and electrical properties of the basic foam materials are continually being improved, considerably larger monolithic foam radomes are a future possibility.

DESIGN AND PERFORMANCE OF 60 FOOT
C-BAND RIGID RADOME, CW-424/FPS-26

C. S. Beal

Rome Air Development Center

J. R. Gruber and D. J. Driscoll

AVCO Corporation/Electronics Division

The work described in this paper was performed by Avco under Contract AF 30(635)-19825 for Rome Air Development Center, Griffiss Air Force Base.

INTRODUCTION

The purpose of this radome development program was to design a rigid radome for use with radar set AN/FPS-26. The AN/FPS-26 is a high power, C-band radar which employs a high-gain nodding antenna to achieve precise elevation angle determination on distant targets.

The philosophy adopted for design guidance, was that of obtaining the maximum conservation of the radar's r-f power, pattern, and beam axis position and stability.

The primary problem revealed in the development of the radome was that of finding an optimum configuration for meeting the conflicting requirements of high r-f power transmission and mechanical strength within a restrictive weight limit.

Specific design and fabrication problems included dimensional control of the radome shell thickness, adequate strength of the panel joints and the acquiring of materials and facilities to produce large uniform seamless panels.

Figure 1 shows a general view of the radome. The more important dimensions and characteristics of the construction are as follows:

Major Diameter	60', 10.25"
Base Diameter	50', 1.75"
Number of Panels	161
Total Weight	14,000 pounds approximately
Wall Construction	Type 'A' sandwich 1 1/2" thick approximately Polyester fiberglass facings Paper polyethylene honeycomb core, 3/4" cell

DESIGN APPROACH

A spherical shell configuration for the radome was selected for the structural and electromagnetic advantages offered. Structurally, this shape is adapted to carrying distributed stresses throughout the shell and the double curvature provides stiffness.

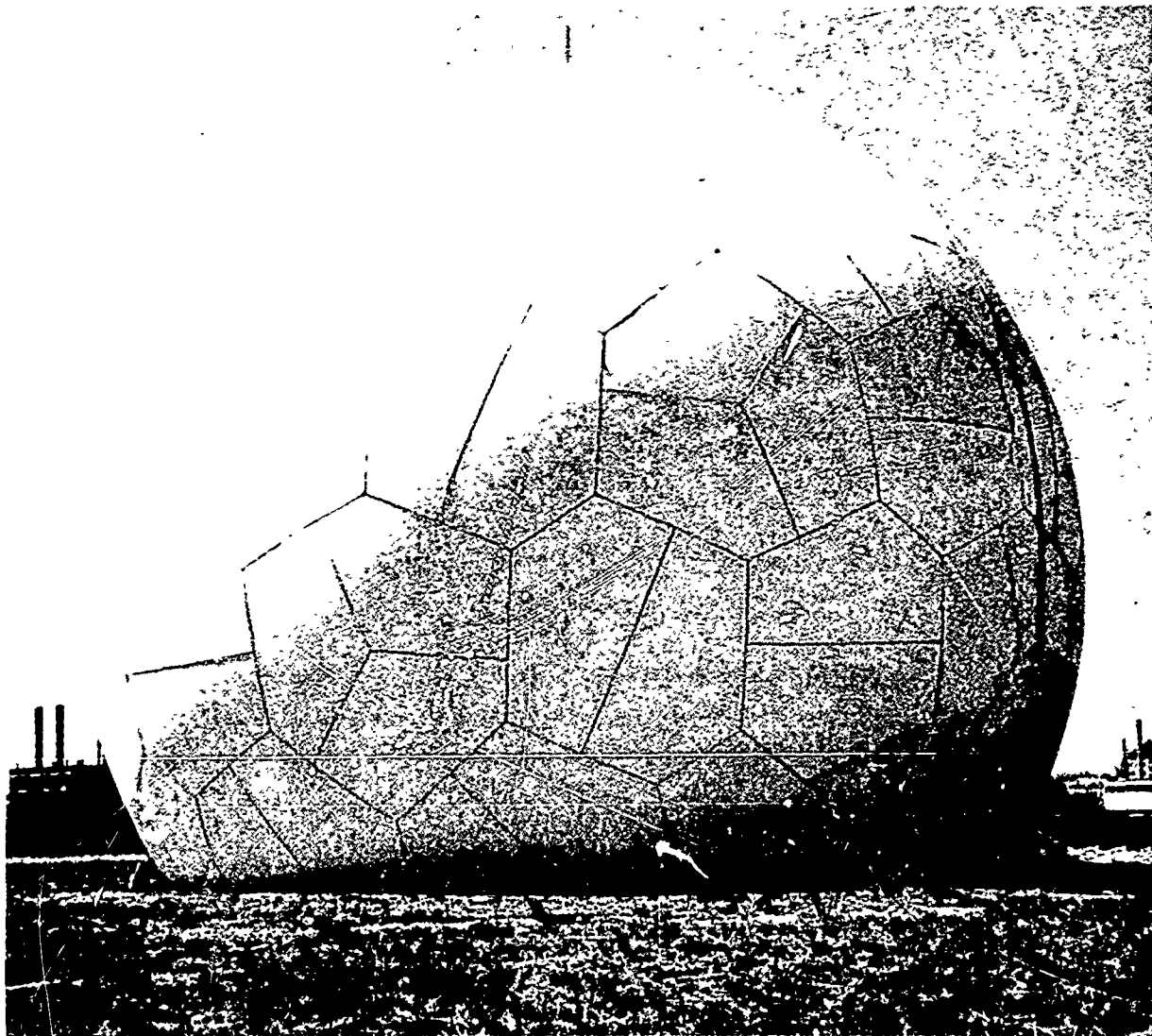


Figure 1. External View, Rigid Radome CW-424/FPS-26

From the electromagnetic viewpoint, the center of rotation of the antenna can be made to coincide with the geometric center of the sphere; thus allowing the radar beam to be always normal to the radome shell, which is the optimum situation for maximum beam axis stability and uniformity of beam pattern. The size and configuration were chosen to satisfy this condition which is illustrated in Figure 2. The antenna is shown in its maximum elevation position, +32°.

Following the establishment of the overall shell configuration and size, attention was given to the design of shell itself. A study was made of the possible design and fabrication approaches with major attention directed to the sandwich wall and metal space frame types of construction. A comparison of these two was made from the viewpoint of best satisfying the requirements of high r-f power transmission, high strength and low weight. The sandwich construction was chosen because it appeared to provide the best approach to achieving the more important objectives.

The materials used in the construction of the sandwich shell were selected for minimum power loss, minimum weight consistent with required strength and maximum performance over the life span.

The core material selected was a 3/4 inch cell honeycomb of 40P40 (18) craft paper and polyethylene. Electrically, because of the high percentage of open area in the 3/4 inch cell, the material has a very low dielectric constant and hence low power loss. Structurally, this material met the required compressive strength, core stress, and flexural strength.

The sandwich panel facing material selected was a laminate of fiberglass cloth #181 Volan A with 37% Hetron 92 polyester resin. Electrically, this polyester resin has the lowest dielectric constant of the structural resins. Structurally, the laminate met the required tensile and compressive strength requirements. In addition, the laminate is inherently flame retardant and the use of polyester resin provides a product of relatively low cost.

The resin selected to bond facings to core was Hetron 32A. The low dielectric constant of this resin was attractive. Structurally, tests showed a load failure of 12,000 lbs. per foot of panel versus a design requirement of 600 lbs. per foot.

The approach followed in selecting the sandwich dimensions consisted of developing a family of power transmission curves for first, second, and third order sandwich walls as a function of skin and core thickness. On the same chart a curve of structural strength was superposed. The intersections of these curves then gave a basis for selection of the sandwich wall dimensions which would give adequate strength with high power transmission. See Figure 3 and Appendix A and B.

An analysis of the data in Figure 3 leads to the selection of the second order ($N = 2$) sandwich for the radome. This choice was based on the need to control weight, which eliminated the first order sandwich, and to maintain good r-f power transmission, over the frequency range, which made the third order sandwich less desirable. Also the skins of

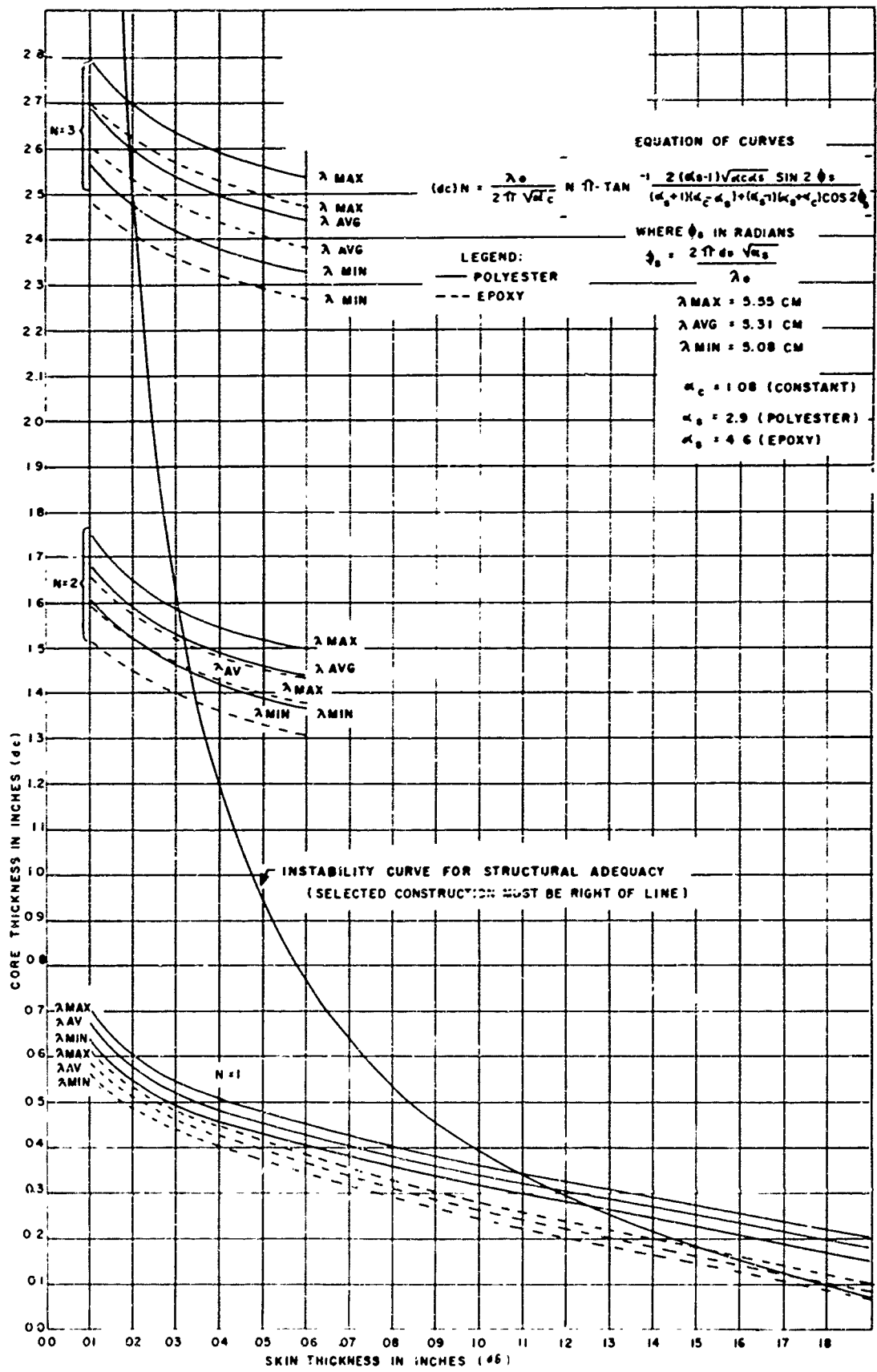


Figure 3. Optimum Core Thickness vs. Skin Thickness for Symmetrical Sandwich Radome

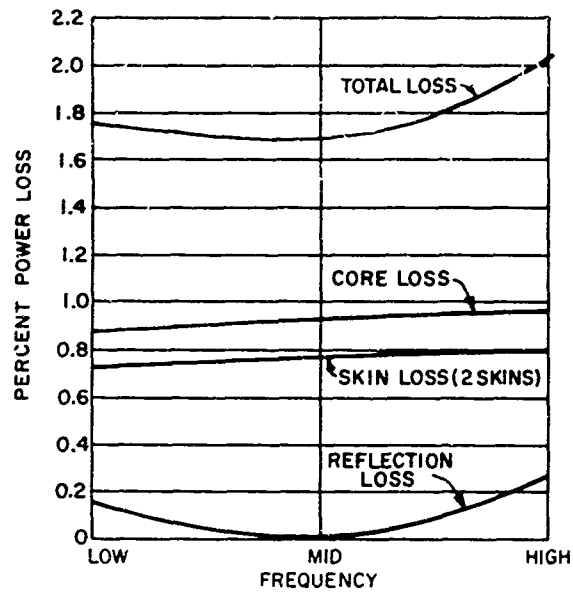


Figure 4. Radome Losses (.040" Polyester Skins)

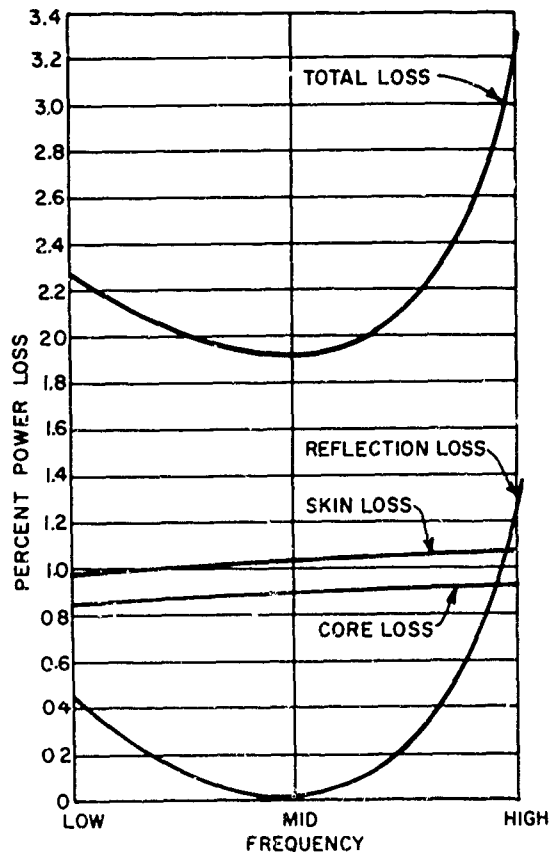


Figure 5. Radome Losses (.040" Epoxy Skins)

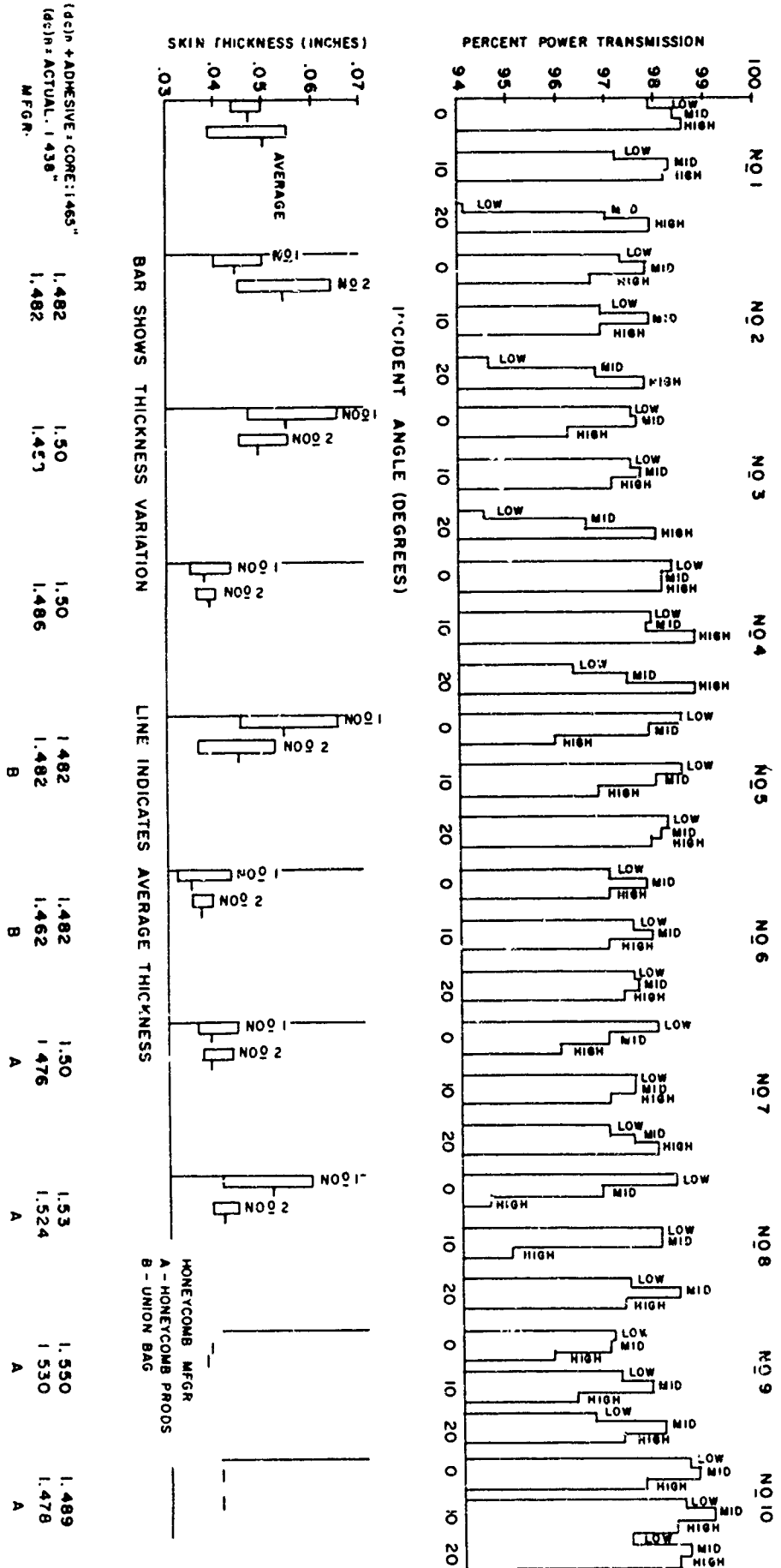


Figure 6. Flat Panel Test Data

TABLE I
ELECTRICAL & PHYSICAL DESCRIPTION

PANEL	#9		#10		REMARKS
	#1	#2	#1	#2	
SKIN					2 1/2 Ft Sq
Matl (Cloth)	181 Volan A	181 Volan A	181 Volan A	181 Volan A	3 Layers
Resin Formula					
Hetron 92	92%	92%	92%	92%	
Styrene	6%	6%	6%	6%	Benzoyl-Peroxide 50%
Catalyst	2%	2%	2%	2%	TCP - 50%
(3) Curing Pressure	9 PSIG	9 PSIG	3 PSIG	3 PSIG	9 PSIG Was Applied
Curing Temp.	165°F for 1/2 hr. & 200°F to 220° for 1-1/2 hr.				To Panel #10, How-
Thickness	.0285 to .0295	.029 to .030	.030 to .034	.031 to .034	ever Due to Excessive
Percent Resin	37% (Approx)	37% (Approx)	39% (Approx)	39% (Approx)	Leakage into the mold,
Specific Gravity	1.95 (Approx)	1.95 (Approx)	1.86 (Approx)	1.86 (Approx)	only 3 PSIG (Approx)
(1) Dielectric Cont.	3.35	3.35	3.25	3.25	was actually realized
(2) Dielectric Const.	3.2	3.2	3.2	3.2	
SANDWICH					
Core	40 P 40(18)3/4 (1.550 ± .005) TK (1.489 ± .005) TK-40 P 40(18)3/4				
Bonding Resin	Hetron 92	Hetron 92	Hetron 32	Hetron 32	Vendor: Honey-Comb Products Co.
Hetron	91.7%	91.9%	91.9%	91.9%	
Catalyst	2%	2%	2%	2%	Benzoyl-Peroxide 50%
styrene	6%	6%	6%	6%	TCP - 50%
D.M.A.	.3%	.1%	.1%	.1%	
Cure Time	1/4 Hr.	2/3 Hr.	2/3 Hr.	2/3 Hr.	Room Temperature
Thickness	.010	.010	.008	.008	
Bending Pres.	1 PSI	1 PSI	1 PSI	1 PSI	
Transmission (%)					
With Paint	.978 (Mid Band 10° Incident <)		.991 (Mid Band 10° Incident <)		1 Coat Primer
Without Paint	.982 (Mid Band 10° Incident <)				Adweld 3880

- Values Based on Equivalent Samples

- (1) Skin only
- (2) Skin Plus Adhesive
- (3) Autoclave Utilized

- 1 Coat Primer
- Adweld 3880
- 2 Coats Finish Goodyear Radolon

the third order sandwich were so thin that they would likely be damaged in manufacturing, shipping, and erection operations.

Calculated power losses for the second order sandwich design selected, are shown in Figures 4 and 5 for both polyester and epoxy panel facings.

Experimental Test Panels

Tests for power transmission were conducted on ten flat panels of this type, produced by the manufacturing facility and in the laboratory. Figure 6 shows the percent power transmitted at low, medium, and high frequency bands and at the same time shows the variation of the actual thickness of each skin. The panel numbers 1 thru 10 are arranged in the order in which they were made. The final closing up of the skin tolerance at the nominal thickness sought (.040) is evident in panel ten. The effective skin thickness in a finished panel, as well as the effective core thickness, is a function of the amount of free bonding resin left on the inner surface of the facing laminates after cure of the panel. See Figure 7.

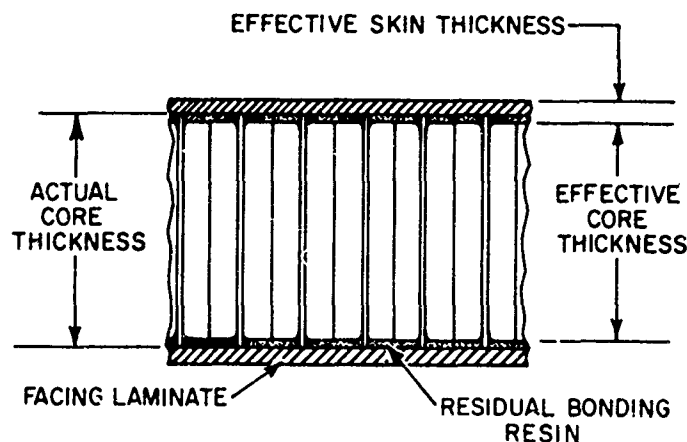


Figure 7. Cross Section Through Sandwich

Depending on the composition of the bonding resin, the porosity of the core, the surface condition of the facing laminates, the cure cycle, the thickness of the residual bonding resin can vary widely. This is, in part, responsible for the broad skin tolerances shown for panels 2, 3, and 5. Panel 10 was selected as the standard for construction of the curved shell of the radome. The electrical and physical description of this panel along with panel 9 is given in Table I.

Radome Panel Detail Design

To facilitate erection of the radome in the field, panelized construction was necessary. Reinforcement of the panel edges to insure adequate joint strength is required and has the adverse effect of blockage of r-f power transmission. In order to achieve an optimum design for this condition, a geometric partition of the spherical radome surface was

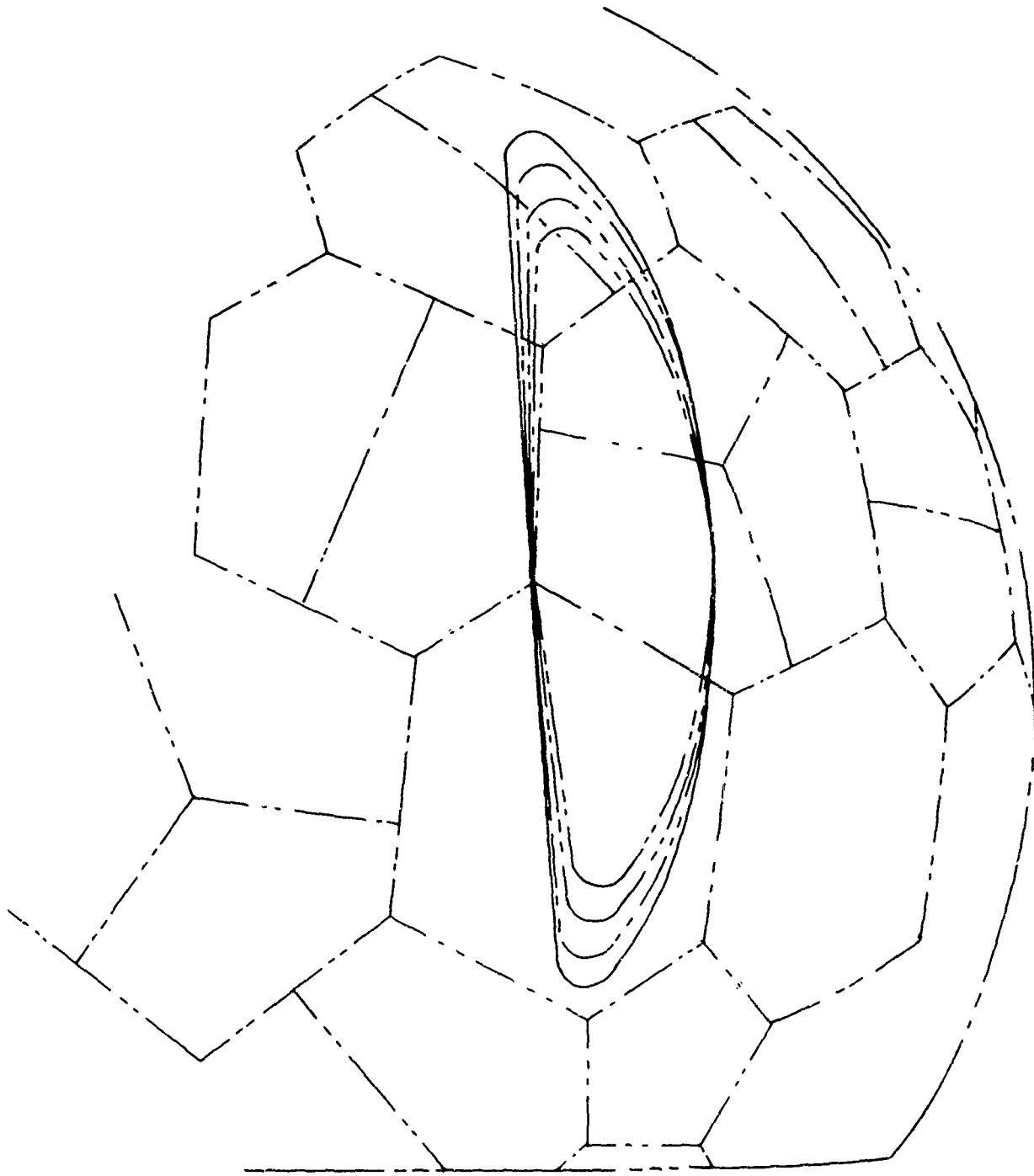


Figure 8. Antenna Aperture Projected on Radome Shell with Antenna in Four Different Polesite Test Positions

sought that would provide minimum total length of panel joint and at the same time a randomness of joint direction in the aperture projection of the antenna. See Figure 8.

Reduction of the total joint length has the effect of increasing the size of the individual panels which are limited in turn, in the case of seamless construction, by the available widths of core material and fiberglass cloth. In order to achieve the desired minimum blockage of $2\frac{1}{4}\%$, it was necessary to develop sources for weaving cloth up to 90" wide for panel facing laminates. The availability of the wider material not only achieved the desired total joint length, but also eliminated splices which were shown by experiment to produce inadmissible distortion and attenuation of the radar beam as well as a significant reduction in the tensile strength of the panel.

The acceptable total joint length was based on a joint width of 1" which necessitated a panel edge treatment of not over $\frac{1}{2}$ " in width. The narrowness of this edging presented a problem from the standpoint of bonding the panel facings as well as a problem of obtaining enough rigidity in the edging to prevent deflection between the bolt fastening points when the joint was under transverse tensile loading. The design finally adopted consisted of a shallow fiberglass channel, an aluminum channel and a flat stainless steel strip bonded together as shown in Figure 9.

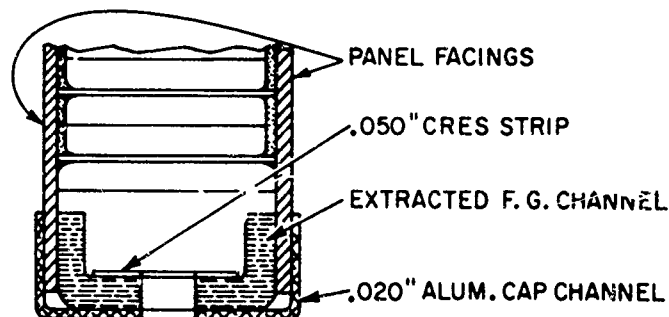


Figure 9. Panel Edge Design

The two nested channels provided bond attachment to both sides of the panel facings, thus doubling the bond area in shear and providing a stable joint. The sandwiching of the fiberglass channel between the stainless steel strip and the aluminum channel gave sufficient beam stiffness to allow a 9.6" center spacing of the panel joining bolts under the design load of 5000 lbs. per foot of joint. The steel strip also served to prevent punching shear effects in the vicinity of the bolt heads.

Access for installation of the bolts was provided by cutting circular holes about 4 inches in diameter in the inner panel facings at the bolt locations and clearing this area of core. This treatment proved troublesome in joint tensile tests due to the stress concentrations

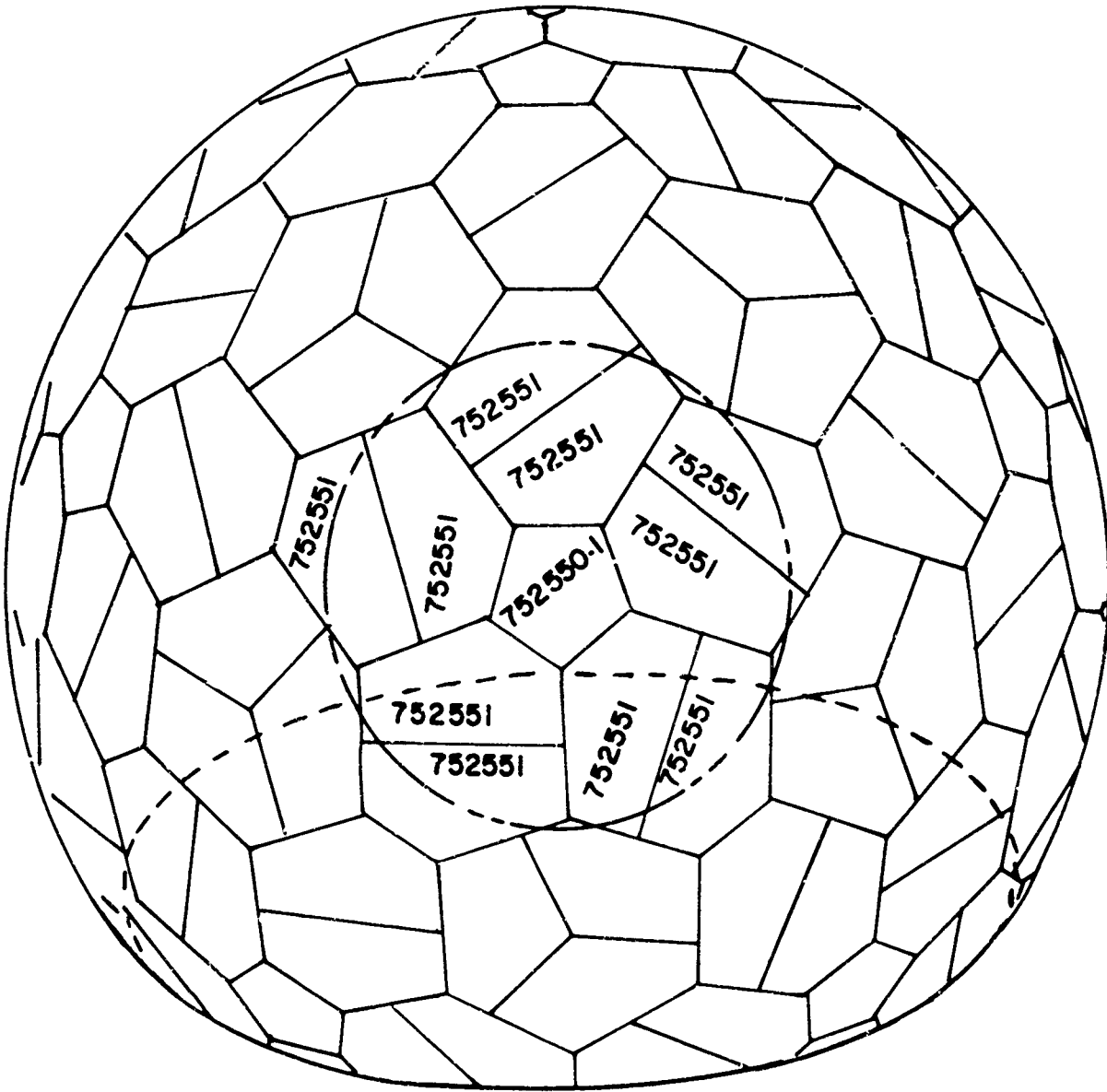


Figure 10. Location of 25 Foot Segment Used for Test
(Panel Part Numbers Shown)

it caused at the hole edges. Moulded foam "horseshoes" were then inserted and bonded between the panel facings and around the holes to redistribute the stresses. Electrical transmission tests on this joint design showed no appreciable change over the results obtained for the joint without the bolt access holes.

With the size, configuration, and edge treatment of the panels established, the final details for the fabrication tools and fixtures and the manufacturing processes were worked out.

Major tools consisted of: (1) A cast iron mold of positive spherical contour and 12 foot diameter (this mold was used as the master to produce the other molds), (2) a mold of negative spherical contour made of fiberglass, (3) two positive and two negative skin molds, and (4) drill and trim fixtures for panel edging.

STRUCTURAL PERFORMANCE TEST

From these tools a group of eleven panels was made to produce a circular segment 25 feet in diameter representative of the radome wall outlined in Figure 10. This representative group of panels was subjected to positive and negative loads equivalent of those produced by a 130 knot wind. A segment test was used since it was impractical to conduct a full scale test of this type. Figure 11 shows the test set-up.

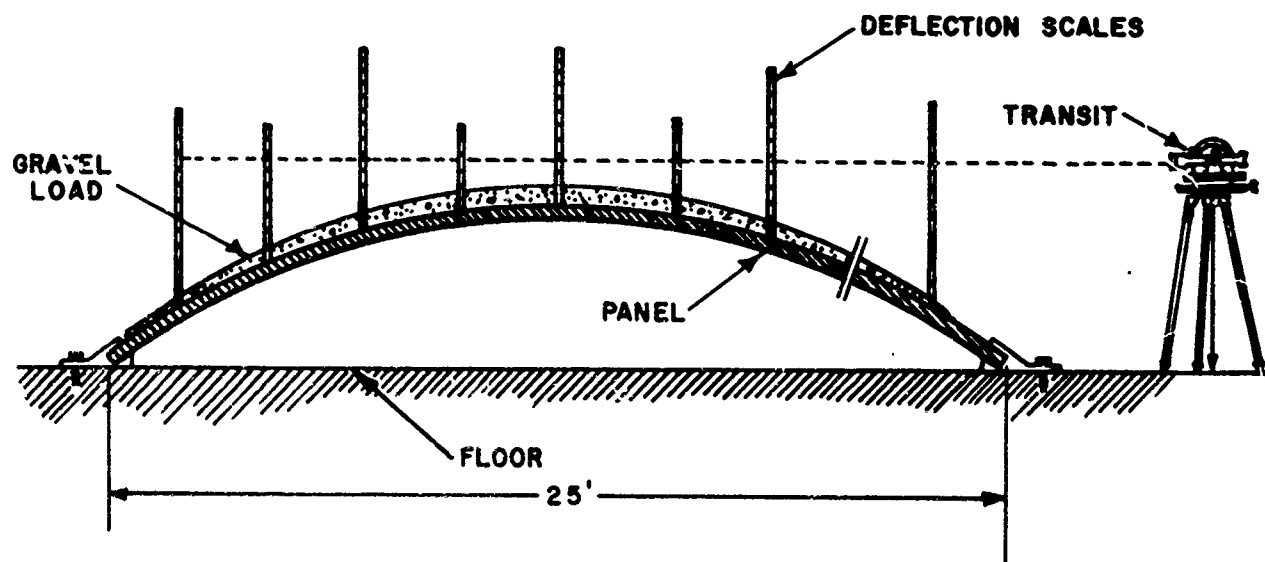


Figure 11 Arrangement for Representative Panel Tests

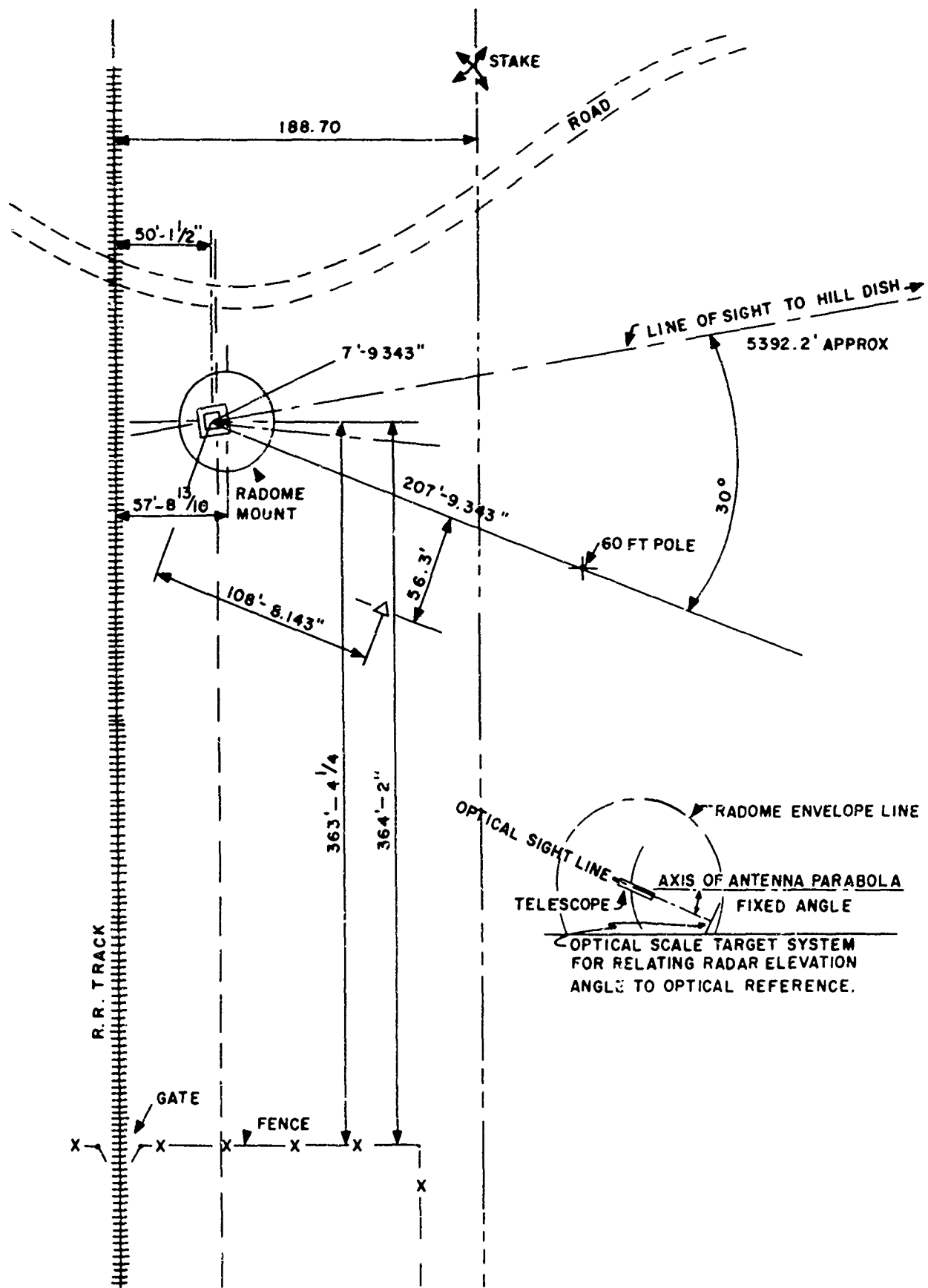


Figure 12. Plot Plan Test Facilities, Rigid Radome

ERRATA *

Table II on page 16 should be Table IV.
Table III on page 16 should be Table V.

Table IV on page 18 should be Table VI.
Table V on page 18 should be Table VII.

TABLE II

PRINCIPAL PLANE PATTERNS

LEVELS IN DB BELOW PEAK OF MAIN BEAM

	Low Freq. 5.4 GC		Mid Freq. 5.65 GC		High Freq. 5.9 GC	
	W/ Radome	W/O Radome	W/ Radome	W/O Radome	W/ Radome	W/O Radome
Elevation	27.0	29.7	27.5	29.4	26.0	28.0
Azimuth	25.5	24.8	29.3	30.0	29.2	27.9

TABLE III

BEAMWIDTH CHANGE

AVERAGE BEAMWIDTH, DEGREES

	W/ Radome	W/O Radome	Change, %
	Elevation	0.597	0.60
Azimuth	2.22	2.23	0.5

* "Design and Performance of 60-Foot C-Band Rigid Radome, CW-424/ FPS-26".
C.S. Beal, D. J. Driscoll, J R. Gruber

The positive load was applied with air at a pressure of 20 inches of water, under the dome segment. The negative load was applied by a distributed dead load of 9000 lbs. of gravel plus a vacuum under the dome to produce a negative pressure of 7.13 inches of water. Vertical scales on the dome surface were observed with an optical level to read deflections. The positive load caused a maximum scale deflection of .75 inches. The negative load caused a maximum deflection of .40 inches.

Several failures at the joints around the edges of the center panel occurred during the initial load test, requiring minor modifications of the joint design to achieve the required strength.

ELECTRICAL PERFORMANCE TESTS

After the structural test of a group of jointed panels, a complete set of panels for a radome was produced. The radome was then erected on a test site on which the radar height finder antenna had previously been installed and tested to verify performance without a radome. Figure 12 shows the site arrangement. This facility was located in an open field with no obstructions of any type within a distance of 500 feet. The foreground of the line of sight to the r-f transmitter was level and clear for 1000 feet. The test transmitter for most of the performance measurements was located 5400 feet east of the radome and on top of a 200 foot hill. All electrical measurements were made, both with and without a radome in place, to evaluate the effects of the radome on the antenna performance.

A complete set of principal plane patterns were taken for three test frequencies. Elevation plane patterns showed some increase in side lobes due to the radome, while azimuth plane patterns showed some side lobe improvement due to the radome. Table II shows the highest side lobe levels as taken from the antenna pattern charts. Table III reveals that the radome produced no significant change in antenna beamwidth.

An extensive set of spurious lobe patterns was made with the antenna under the radome to determine whether the radome might give rise to excessive ground clutter effects, especially on the range-height indicator. Patterns were recorded through an angle of ± 60 degrees in azimuth at fourteen elevation angles -3 through $+30$ degrees inclusive. These patterns were measured at low, mid, and high frequencies. No side lobes higher than -33.9 db below the main lobe were recorded, excluding those parts of the main beam and principal plane side lobes which extend into other space planes. It was concluded from the data that no significant degradation of the system performance would result from the very low side lobe levels found.

The axis shift test was performed on two ranges, namely, the "hill site" range and the "pole site" range. A six foot parabolic transmitting antenna was mounted at the "hill site". The power transmitted was 1 watt. Four pyramidal horns were mounted at the "pole site" at 0, 2, 5 and 8 degrees in elevation relative to the radar antenna. A signal generator was used to energize the horns. The AN/FPS-26 reflector was equipped with

TABLE II

ELEVATION AXIS SHIFT MEASUREMENT TO HILLSITE

Frequency	Antenna Erect Degree Shift	Antenna Plunged Degree Shift
Low	+ 9. 0034	+ 0. 0092
Mid	+ 0. 0068	+ 0. 0092
High	0. 0000	+ 0. 0045

ELEVATION AXIS SHIFT MEASUREMENT TO POLESITE

Frequency	Nom. El. Angles Degrees	Horn No.	Antenna Erect Degrees Shift	Antenna Plunged Degrees Shift
Low	0	1	+ 0. 0045	+ 0. 0136
	2	2	+ 0. 0034	
	5	3	+ 0. 0186	+ 0. 0045
	8	4	+ 0. 0170	- 0. 0045
Mid	0	1	+ 0. 0073	+ 0. 0136
	2	2	+ 0. 0073	
	5	3	+ 0. 0057	+ 0. 0090
	8	4	- 0. 0045	+ 0. 0073
High	0	1	+ 0. 0073	+ 0. 0118
	2	2	+ 0. 0090	
	5	3	0. 0000	+ 0. 0045
	8	4	+ 0. 0045	+ 0. 0090

TABLE III

AZIMUTH AXIS SHIFT TO HILLSITE

Frequency	Degree Shift Due to Radome
Low	+0. 023
Mid	-0. 020
High	+0. 011

+ CW Shift
-CCW Shift

a two horn monopulse feed to achieve high angular precision for axis shift measurements. The null depth from the difference arm of this feed when the antenna was aimed directly at the signal source was about 25 db.

Repeated measurements indicated an elevation positioning accuracy (boresight) of ± 0.0025 degrees. This accuracy was determined by means of an optical system mounted on the elevation pivot axis of the antenna. The optical system consisted of a telescope with a reticle which could be trained to read a fixed reference scale within the radome mounting circle and 33 feet from the telescope. This angular reference could be used after the radome was in place and visual access to the test antenna and horns was obscured. The system permitted accurate reading of engraved scales graduated in 1/32 inch increments. Any angular change in antenna elevation was thus indicated as a change in scale reading. By calculation 4.4 divisions on the scale were equal to an angular change of 0.02 degrees and the scale could be read to one half division.

Measurements of axis shift were made on both ranges with and without radome. The data is shown in Table IV. Differences in axis shift to the several pole-mounted horns is attributed to the different panel geometry seen by the radar antenna at each elevation angle. See Table IV.

Azimuth plane axis shift measurements were made using the AN/FPS-26 standard feed horn with the antenna. Measurement method was similar to that used for elevation axis shift except that the beam center (boresight axis) was located at one half the distance between the -3 db beam positions. The data taken is shown in Table V.

Power transmission through the radome was measured using the "hill site" (5400 feet) range. A six foot diameter reference antenna was mounted outside the radome and adjacent to it. The test signal modulated at 1000 cps from the "hill site" antenna was received and detected by both the reference antenna and the antenna under the radome. These detected signals were alternately connected to a common standing wave amplifier to compare the relative output levels of the two antennas. To compensate for the difference in gain between the reference antenna and the test antenna a precision variable attenuator was used ahead of the detector in the test antenna. The attenuator was fixed at a setting which gave approximately the same detected output level at the standing wave amplifier. This eliminated the need for switching ranges on the standing wave amplifier and all readings were made on the same range setting using the expanded db scale position for greatest accuracy.

Reference readings were measured prior to radome erection by "aiming in" both the reference antenna and the test antenna for maximum detected power from each. The precision attenuator on the test antenna was adjusted for the same level indication on the standing wave amplifier as given by the reference antenna. Different attenuator settings were required at each of the three test frequencies.

TABLE IV
MEASURED POWER TRANSMISSION
(Vertical Polarization)

Frequency	DB Loss Due to Radome	Percent Power Transmission
Low	0.20	95.5
Mid	0.13	97.0
High	0.21	95.3

TABLE V
VSWR MEASUREMENTS

Frequency	Without Radome		With Radome	
	Vertical	Horizontal	Vertical	Horizontal
Low	1.13	1.50	1.12	1.50
Low + 100 mc	1.10	1.07	1.11	1.07
Low + 200 mc	1.07	1.27	1.05	1.25
Mid	1.03	1.28	1.01	1.32
Mid + 50 mc	1.01	1.31	1.02	1.29
Mid +150 mc	1.12	1.04	1.15	1.09
High	1.24	1.05	1.07	1.15

After radome erection the outputs of the two antennas were again compared at each test frequency using the previously established attenuator settings. The power transmission loss due to the radome was determined from the difference in readings on the standing wave amplifier.

Table VI contains the results of the power transmission measurements. A thorough investigation of all possible sources of measurement error revealed that the accuracy sought (about $\pm .05$ db) is "pushing the art". This is particularly true when considering the effects of one mile of intervening terrain, antenna pointing accuracy, signal frequency stability, aging of detectors and calibration of the standing wave amplifier. For example, the received power from the transmitting antenna depends somewhat upon the ground reflection coefficient which is a function of the moisture in the ground and the growth of ground cover over the signal path.

Table VII compares the VSWR of the test antenna measured with and without radome. It is seen that the radome has only a slight effect upon the antenna VSWR.

SUMMARY

The performance of this rigid radome indicates that adequate strength can be developed in a sandwich wall type structure to resist the effects of a 130 knot wind and at the same time permit operation at C-band with high r-f power transmission (greater than 95%) and very small beam axis shift. These characteristics were achieved by holding reflective and dissipative losses to a minimum through (1) precise control of core and skin thickness, (2) a uniform distribution of a controlled amount of bonding agent, (3) a minimum amount of material in the radome wall consistent with strength, and (4) a minimum width and accumulated length of panel joint consistent with strength and panel size limitations.

ACKNOWLEDGMENTS

We would like to acknowledge the contributions of Geometrics Incorporated, and Universal Moulded Fiber Glass Corporation during the design, fabrication, and testing of this program.

APPENDIX A

ELECTRICAL DESIGN STANDARDS

Electrical design of the radome sandwich has been based upon material from a number of references, the most pertinent of which are listed in references 1 and 2. No publication on rigid radomes is generally accepted as a design standard. However, the first two references are widely used for radome design.

All important design formulae and much useful information concerning material properties and measuring techniques are contained in Reference 1, Radiation Laboratories Series, Volume 26.

The two most important electrical design calculations are:

- (1) calculation of the core thickness which gives maximum power transmission at midband, and
- (2) calculation of power reflected from a given sandwich as a function of frequency.

The formula for calculation of optimum core thickness for normal incidence is,

$$(d_c)_N = \frac{\lambda_o}{2\pi\sqrt{a_c}} \left[N\pi - \tan^{-1} \frac{2(a_s - 1)\sqrt{a_s a_c} \sin 2\phi_s}{(a_s + 1)(a_c - a_s) + (a_s - 1)(a_s + a_c) \cos 2\phi_s} \right] \quad (1)$$

where N is the integer, the order of the sandwich,

$(d_c)_N$ is the thickness of the core of sandwich of order N ,

λ_o is the free-space wavelength,

a_c is the specific dielectric constant of core,

a_s is the specific dielectric constant of skin, and

ϕ_s is the 2π x electrical thickness of the skin.

The formula for calculation of power reflected from a sandwich at normal incidence is,

$$/R/2 = \frac{4/\rho/2 \sin^2(\Delta \phi_c)}{(1 - / \rho/2)^2 + 4/\rho/2 \sin^2(\Delta \phi_c)},$$

in which

$$\Delta \phi_c = \frac{2\pi\sqrt{a_c} \Delta d_c}{\lambda_o} \quad (2)$$

and

$$/\rho/2 = \frac{a_s (\sqrt{a_c} - 1)^2 - (a_s - 1)(a_c - a_s) \sin^2 \phi_s}{a_s (\sqrt{a_c} + 1)^2 - (a_s - 1)(a_c - a_s) \sin^2 \phi_s}$$

$|\rho|$ is the absolute value of the amplitude reflection coefficient for a wave incident as the skin from the core, or on the core from the skin.

Equation (1) has been used to calculate the data presented in Figure 3 and equation (2) has been used to calculate the reflection losses in Figures 4 and 5.

APPENDIX B

STRUCTURAL DESIGN STANDARDS

Determination of the loads, induced by the environmental conditions, dictated that the radome sandwich panels be designed to be structurally adequate to prevent buckling. Buckling is the design criteria for the spherical shell radome except in the area of the base attachment ring. To determine the necessary face and core dimensions, the following approach was used.

The formula for the critical pressure that will produce buckling is:

$$P_{cr} = KE \frac{t^2}{R^2} \quad (3)$$

where P_{cr} is the critical pressure, E is the modulus of elasticity, t is the thickness of shell, and R is the major radius of radome.

The classical value of K is given by Timoshenko (References 8, 9) as 0.6. Experimental work by Von Karman (Reference 10) and Hsue-Shen Tsien (References 10, 11) show the value of K , based on uniform loading of hemispheres, to be a function of t/R , with a value of $K = 0.27$ for the region of t/R for the radome. Because of the unequal stresses existing at the stagnation point, resulting from the wind loading seen by the radome, the value of K used was 0.22.

Another item that must be accounted for is the fact that the above formula is derived for a homogeneous shell, differing from the honeycomb sandwich construction actually used. Modification of the formula for use with sandwich construction is shown below, together with the margin of safety resulting from its application to the radome for 150 mph winds.

For sandwich construction,

$$P_{cr} = KE_e \frac{t_e^2}{R^2} \quad (4)$$

where E_e is the effective modulus of elasticity, and t_e is the effective thickness of sandwich.

Letting $(EI)_{solid} = (EI)_{sandwich}$,

$$\frac{E_e t_e^3}{12} = \frac{t}{2} (c+t)^2 E,$$

$$E_e = \frac{6 t E (c+t)^2}{t_e^3} \quad (5)$$

where c is the core thickness of sandwich, and t is the skin thickness of sandwich.

Letting $(EA)_{\text{solid}} = (EA)_{\text{sandwich}}$,

$$E_e t_e = 2 t E$$

$$E_e = \frac{2 t E}{t_e} \quad (6)$$

Setting equation (5) equal to equation (6), we obtain

$$\frac{2 t E}{t_e} = \frac{6 t E (c+t)^2}{t_e^3}$$

$$t_e = \sqrt{3} (c+t)^2 \quad (7)$$

Using equation (4) and solving for t_e , and using equation (6) substituting for E_e ,

$$t_e^2 = \frac{P_{cr} R^2}{K E_e}$$

$$t_e^2 = \frac{P_{cr} R^2}{K \times 2 t E / t_e}$$

$$t_e = \frac{P_{cr} R^2}{2 K E t} \quad (8)$$

Setting equation (7) equal to equation (8),

$$\sqrt{3} (c+t)^2 = \frac{P_{cr} R^2}{2 K E t}$$

$$\sqrt{3} (c+t) = \frac{P_{cr} R^2}{2 t E t}$$

$$t (c+t) = \frac{P_{cr} R^2}{2 \sqrt{3} K E}$$

Using $P_{cr} = .5781$ PSI*; $R = 360''$; $E = 2.0 \times 10^6$; $K = .22$ and substituting in the above equation.

$$t(c+t) = \frac{.5781 \times (360)^2}{2\sqrt{3} \times .22 \times 2 \times 10^6}$$
$$t \times c + t^2 = .04915.$$

Assuming values of "t" ranging from 0.01 to 0.15 inches the respective values of core thickness is determined, and the curve plotted. Selection of the core and face thickness, for proper transmission characteristics, must be to the right of the curve, see Figure 3.

* This value for P_{cr} was obtained as follows:

Pressure coefficients were obtained from wind tunnel tests as reported by Bezbatchenko. Figure 13 shows the pressure distribution over a radome from these tests.

In the area of the equator, presented to the wind, buckling is critical. The pressure coefficient in this area is 1.0.

-20° F air at sea level pressure and at a velocity of 130 knots will produce a dynamic pressure of .4625 lbs per square inch. Using the pressure coefficient of 1.0 for the critical area and a factor of 1.25 to provide a structural margin for non-uniformity due to hand fabrication we have:

$$1.0 \times 1.25 \times .4625 \text{ psi} = .5781 \text{ psi}$$

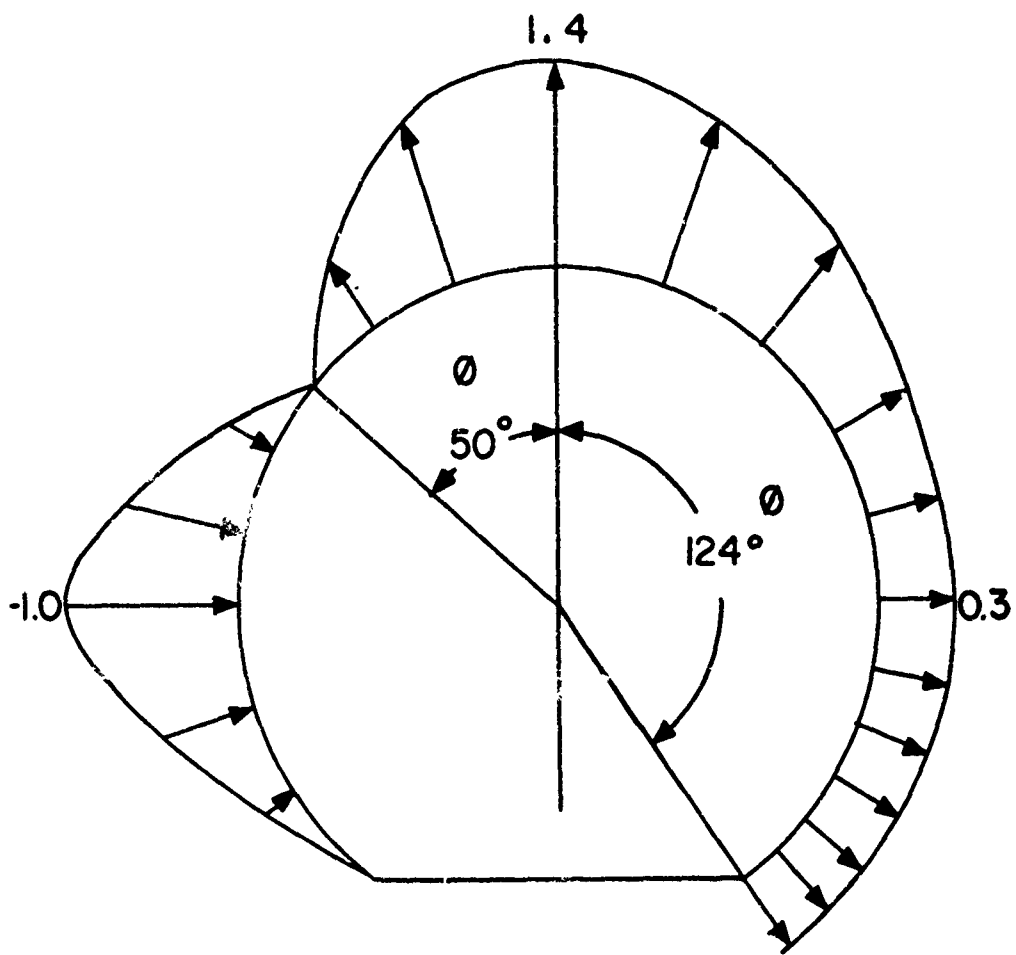


Figure 13. Pressure Distribution over the Radome

REFERENCES

1. Radar Scanners and Radomes - Volume 26 of Radiation Laboratory Series: McGraw-Hill Book Company, 1948.
2. Techniques of Airborne Radome Design - WADC Technical Report 57-67, September 1957; Astia No. AD 142001.
3. Supplementary Graphs of Transmission and Phase Delay of Plane Dielectric Sheets and Sandwich Construction for Radome Design - AD 45543, U. S. Naval Air Development Center Report No. NADC-EL-5313, 16 January 1954.
4. Graphs of Transmission and Phase Data of Plane Dielectric Sheets for Radome Design - AD 45316, U. S. Naval Air Development Center Report No. NADC-EL-5313, 1 July 1953.
5. Von Hippel, A. R. , Dielectric Materials and Applications - John Wiley & Sons, 1954.
6. Proceedings of the WADC-OSU Radome Symposia at Ohio State University; June 1957 and June 1958.

Lavrench, W. , Electrical Performance of Rigid Ground Radomes, - IRE Transactions on Antennas and Propagation, November 1960.
8. Timoshenko, "Theory of Plates and Shells. "
9. Timoshenko, "Theory of Elastic Stability. "
10. Von Karman, T. , and Tsien, Hsue-Shen, "Buckling of Spherical Shells," Journal of Aeronautical Science, Vol 7, Dec. , 1939.
11. Tsien, Hsue-Shen, "Theory of the Buckling of Thin Shells," Journal of Aeronautical Science, Vol. 9, August 1942.
12. Erzbatchesko, J. W. , "A Study of Aerodynamic Loads on Large Spherical Radomes for Ground Installation. "

HARDENED GROUND RADOMES FOR SYSTEM SURVIVAL

G. J. Cook
North American Aviation, Inc.
Columbus Division
Columbus 16, Ohio

ACKNOWLEDGMENT

The work reported herein was performed under Contract AF30(602)-2923. The Air Force project engineer for this contract was Mr. R. B. Curtis of the Development Engineering Laboratory, Research Technology Division, Rome Air Development Center, Griffiss Air Force Base, New York.

ABSTRACT

This investigation consists of determining the dynamic response of a thin, uniform-thickness, truncated spherical shell to air-blast induced shock loads. The response analysis includes a failure criterion for determining the vulnerability of this type of structure to nuclear blasts.

The structural dynamic characteristics of the radome were represented by the normal mode approach. The mathematical representation of the blast-induced pressure loading was based on published experimental data. A failure criterion developed from strain energy considerations is suggested, which, when applied to the dynamic response is indicative of structural failure. Solutions to this mathematical model were obtained from an operational analog computer. The results of this study are promising; however, further investigations considering radomes of various height-to-diameter ratios are required to substantiate the generality of this approach.

LIST OF ILLUSTRATIONS

<u>FIGURE</u>		<u>PAGE NO.</u>
1	Radome Mode Shapes Used in Dynamic Analysis	21
2	Nuclear Blast Shock Wave in Relation to Radome	22
3	Schematic Loading Diagram for Front-Half of Radome	22
4	Variation of τ_2 and τ_3 with Free-Field Overpressure	23
5	Pressure Magnitude Attenuation Function	24
6	Distortion of Radome Polar Axis in First Mode Shape	25
7	Dimensionless Strain Energy versus Overpressure for Aluminum Shell Radomes	26
8	Critical Free-Field Overpressure versus Radius-to-thickness Ratio for Aluminum Shell Radomes	27
9	Dimensionless Strain Energy versus Overpressure, Glass-Reinforced Laminated Plastic Radomes	28
10	Critical Free-Field Overpressure versus Radius-to-thickness Ratio, Glass-Reinforced Laminated Plastic Radomes	29

LIST OF SYMBOLS

A	Area of complete sphere.
ΔA_m	Area associated with the m <u>th</u> control point.
D	Radome diameter.
E	Modulus of elasticity.
F_i, G_i	Indefinite integrals in the i <u>th</u> generalized force expressions.
M_j	Generalized mass in the j <u>th</u> mode.
P	Pressure.
P_{cr}	Critical free-field overpressure.
P_1, P_2, P_3	Pressures describing schematic loading diagram.
P_o	Ambient pressure.
P_{ro}	Peak reflected overpressure at $x = -R$.
P_{so}	Peak free-field overpressure.
Q_i	Generalized force in the i <u>th</u> mode.
R	Spherical radius.
U	Propagation velocity of shock front; strain energy.
\bar{U}	Dimensionless strain energy.
\bar{U}_{cr}	Dimensionless strain energy at failure.
\bar{U}^*	Modified dimensionless strain energy.
a	Constant defined by P_2/P_1 .
b	Constant defined by P_3/P_1 .
C_o	Ambient speed of sound.
f_i	Natural frequency of the i <u>th</u> mode, c.p.s.

LIST OF SYMBOLS (Cont'd)

$f(x/D)$	Pressure magnitude attenuation function.
ξ_i	Structural damping coefficient for the i <u>th</u> mode.
h	Height of truncated sphere.
p	Pressure.
q_i	Generalized coordinate of the i <u>th</u> mode.
\bar{q}_i	Generalized coordinate of the i <u>th</u> mode, q_i/t .
t	Time, shell thickness.
x, y, z	Radome coordinates.
\bar{x}	Coordinate for describing pressure loading, $\bar{x} = x + R$.
θ, ϕ	Spherical coordinates.
δ	Deflection.
ν	Poisson's ratio.
ρ	Mass density of radome material.
τ_0	Time duration of positive overpressure.
τ_1, τ_2, τ_3	Times corresponding to P_1, P_2, P_3
ϕ_i	i <u>th</u> mode shape.
ϕ_{x_1}, y_1, z_1	$x, y, \text{ or } z$ deflection component of the i <u>th</u> mode.
$\bar{\phi}_{x_1}$	Modified x -deflection component in the fundamental mode.
ϕ_{xcg_1}	Modified x -deflection component in the fundamental mode.
ω_i	Natural frequency of the i <u>th</u> mode, radians/sec.
$(\dot{\quad})$	First derivative with respect to time.
$(\ddot{\quad})$	Second derivative with respect to time.

INTRODUCTION

The reliability of our missile defense system requires that each system be designed and constructed to perform its designated function in the environment associated with national defense. The environment for national defense includes the possibility of nuclear attack against major national targets. Thus, it is necessary for the elements of the defense system to survive, to the maximum practical extent, the effects of the nuclear blast and be able to perform their designated functions. Hardening of the missile system proper is accomplished by placing the interceptor missiles underground in hard silos. The associated antenna system, however, must be above ground. The protection of antenna systems may possibly be provided by properly hardened radomes which have been designed to withstand the environment imposed by nuclear weapons. Therefore, in order to determine the feasibility of radome hardening a method of analysis is required for determining the vulnerability of such a structure to nuclear blasts.

This investigation is concerned with determining the vulnerability of a large ground-based radome to dynamic overpressures generated by a nuclear blast. For this investigation, vulnerability is defined as that level of free-field overpressure which will just cause structural failure of the shell-like radome. The radome of interest is a single-material, spherical shell of uniform thickness which is truncated such that $h/D = 0.71$.

When exposed to a blast loading of sufficiently low intensity, the shell will respond elastically without experiencing any permanent deformation. As the load intensity is increased the response will eventually become inelastic resulting in a permanent deformation or even complete destruction. Experiments¹ have shown that the difference between blast overpressures which just initiate dynamic buckling and overpressures which cause complete failure is quite small. From a design consideration, therefore, it is sufficient to consider the onset of inelastic response as complete failure rather than attempting to define the inelastic or postbuckling response.

Because of shock reflection effects the blast loading on a radome is a complex function of space and time. If the nature of the loading is known, however, and available analytical techniques can be used to determine the structural resistance of the shell, then the equations of motion which describe the dynamic response in the elastic range can readily be formulated. The solutions to these equations then yield time histories of either deflections or internal loads. This is the usual mathematical model which is generated for any general dynamics problem. If a failure criterion were available, the dynamic response obtained from this model can be used to determine the vulnerability of the ground-based radome to nuclear blasts.

EQUATIONS OF MOTION

A common method of approximating a continuous structure is that of a semi-rigid representation. According to this method the structure is treated as having only a finite number of degrees of freedom which are specified by displacement functions, or modes. Obviously, the representation cannot be perfect, but provided that the displacement functions are well chosen and adequate in number, it is sufficiently good for practical purposes. Two kinds of displacement functions have been used for the semi-rigid representation of structures; viz., assumed modes and resonant modes. The use of assumed modes has the advantage that ingenuity, rather than labor, is involved in choosing the modes. Normal modes have the theoretical advantage that the resulting generalized equations of motion are inertially and elastically uncoupled. Also, a fewer number of resonant modes is usually required to represent the structure. The use of normal modes has the disadvantage, however, that considerable labor is involved in determining the mode shapes.

For this investigation the structural dynamic characteristics of the radome were represented by the resonant mode approach. This method of dynamic analysis expresses the deformation of the structure in terms of normal vibration modes through the series:

$$\delta(x, y, z, t) = \sum_{i=1}^n \phi_i(x, y, z) q_i(t) \quad (1)$$

where the generalized coordinates (q_i) are determined from the familiar generalized equations of motion ---

$$M_i \ddot{q}_i(t) + \omega_i^2 M_i q_i(t) = Q_i(t) \quad , \quad j = 1, \dots, n \quad (2)$$

The generalized masses (M_j) and generalized forces (Q_j) are defined as,

$$M_i \delta_{ij} = \int_S \rho t \phi_i(x, y, z) \phi_j(x, y, z) dA \quad (3)$$

$$Q_i = \int_S \rho(x, y, z, t) \phi_i(x, y, z) dA \quad (4)$$

where δ_{ij} is Kronecker's delta.

If desired, a viscous damping term of the form $g_j \omega_j M_j q_j$ may be included in Equation 2. Having presented the generalized equations of motion in terms of a continuous system, it is noted that the same equations apply to a lumped-parameter system. The only difference occurs in the numerical evaluation of the generalized mass and generalized force.

VIBRATION ANALYSIS

Before the generalized equations of motion can be completely defined the natural frequencies and mode shapes are required. Hrennikoff's lattice analogy² of continuous structures was considered to be the most practical approach for determining the normal modes of a spherical shell. It was observed, however, that the lattice analogy per se could be by-passed by taking advantage of the known membrane solution for the "breathing" mode frequency of a spherical shell.

The well-known direct stiffness method was used to determine a flexibility influence coefficient matrix for a lattice-type radome. A conventional vibration analysis yielded the normal mode shapes and natural frequencies for the space-frame radome. The resulting mode shapes were considered directly applicable to a shell-type radome, but some method for relating the frequencies of the framework to the frequencies of a shell was required. The natural frequencies of the framework were normalized by dividing each frequency by the frequency of the "breathing" mode, i.e., the membrane shell mode whereby the shell expands and contracts in a spherically symmetric fashion. Asserting that these frequency ratios are applicable to a spherical shell and using the membrane solution for the frequency of the "breathing" mode,³

$$\omega = \sqrt{\frac{2}{1-\nu}} \sqrt{\frac{E}{\rho R^2}} \quad (5)$$

the frequencies of a radome shell are established.

Of the eigenvectors which were obtained, only three modes could be visualized as contributing to the dynamic response of the radome. The remaining modes were complex in shape such that the generalized forces in these modes would be quite small. The three mode shapes which were retained for the dynamic response analysis are shown pictorially in Figure 1. The first mode is frequently referred to as a "rocking" mode although Figure 1 shows that most of the motion involves lateral translation. The second mode involves the top portion of the radome deflecting downward with the sides deflecting outward, and the third mode of interest is the breathing mode. Hereafter, these modes will be referred to as modes one, two and three, although the breathing mode is not necessarily the third normal mode of the structure. The experimental results of Reference (4) indicate that the rocking mode and the breathing mode are predominant in the blast-response of a radome for which $h/D = 0.71$.

The frequency ratios of these modes were obtained by dividing each frequency by the frequency of the breathing mode giving:

$$f_1/f_3 = 0.269$$

$$f_2/f_3 = 0.310$$

$$f_3/f_3 = 1.0$$

and using Equation 5 the frequencies associated with the three modes of interest are given by:

$$\begin{aligned} \omega_1 &= (f_1/f_3) \omega_3 = \sqrt{\frac{.1447}{1-\nu}} \sqrt{\frac{E}{\rho R^2}} \\ \omega_2 &= (f_2/f_3) \omega_3 = \sqrt{\frac{.1924}{1-\nu}} \sqrt{\frac{E}{\rho R^2}} \\ \omega_3 &= (f_3/f_3) \omega_3 = \sqrt{\frac{2}{1-\nu}} \sqrt{\frac{E}{\rho R^2}} \end{aligned} \quad (6)$$

NUCLEAR BLAST REPRESENTATION

Immediately after the occurrence of a low-altitude explosion a high-pressure wave, known as the incident blast wave, develops and moves spherically outward from the fireball. When the incident blast wave strikes the earth a reflected blast wave is formed. The reflected shock wave travels through the atmosphere at a higher velocity than the incident shock and the two eventually merge to form a single shock front called the Mach stem, as shown in Figure 2. The significance of the Mach stem is that the destructive shock wave of concern is normal to and travels parallel to the earth's surface. Considering the Mach stem as an ideal shock wave relations involving shock velocity, wind velocity, free-field overpressure, dynamic pressure, and the density of air behind the shock front can be formulated from the Rankine-Hugoniot relations and the equation of state for air.⁵

When the Mach stem strikes an object, the resulting flow field is quite complex because of interactions between the free-field flow and shock waves which are reflected from the surface of the obstacle. As a result of reflection the overpressure on the surface of a structure rapidly increases to a peak value which is several times larger than the free-field overpressure. As the blast wave moves on, the reflected overpressure at a point on the structure decreases quite rapidly to the free-field overpressure plus a

dynamic pressure. The reflected overpressure, or "diffraction loading", is dependent on the peak free-field overpressure and the local angle of incidence between the shock wave and the structure. After reflection effects have subsided the dynamic pressure is the significant consideration in determining the "drag loading".

Because of the complexity of the interrupted flow field model or full-scale tests appear to be the best source of pressure data. Full-scale tests⁵ have determined that the characteristics of the shock wave are governed by the Rankine-Hugoniot relations and since the flow generated within a laboratory shock tube satisfies these same relations, the shock tube serves as a practical analog of the Mach stem. The pressure expressions developed below are based primarily on the results of shock tube tests which were conducted by Armour Research Foundation in 1958 to determine the blast loading on arches and domes.⁶

Assuming that the pressure inside the radome remains ambient, the pressure-time history for a point on the upstream half of the radome is as shown in Figure 3, where τ represents time referenced from the time of shock wave arrival at that point. Test data indicate that the reflected overpressure quickly attains its peak value, such that for practical purposes $\tau_1 = 0$. Thus, the pressure at a particular point on the front half of the radome can be described by:

$$p(\tau) = 0 \quad \text{---} \quad \tau \leq 0$$

$$p(\tau) = P_1 + \left(\frac{P_2 - P_1}{\tau_2} \right) \tau \quad \text{---} \quad 0 \leq \tau \leq \tau_2$$

$$p(\tau) = P_2 + \left(\frac{P_3 - P_2}{\tau_3 - \tau_2} \right) (\tau - \tau_2) \quad \text{---} \quad \tau_2 \leq \tau \leq \tau_3$$

$$p(\tau) = P_3 \left[1 - \left(\frac{\tau - \tau_3}{\tau_0 - \tau_3} \right) \right] \exp \left[- \left(\frac{\tau - \tau_3}{\tau_0 - \tau_3} \right) \right] \quad \text{---} \quad \tau_3 \leq \tau \leq \tau_0$$

(7)

At the lower overpressures of interest shock reflection effects on the rear half of the radome are small such that:

$$p(\tau) = 0 \quad \text{---} \quad \tau \leq 0$$

$$p(\tau) = P_1 (1 - \tau/\tau_0) \exp(-\tau/\tau_0) \quad \text{---} \quad 0 \leq \tau \leq \tau_0$$

(8)

Examination of the experimental data indicates that P_2 and P_3 can be approximated by:

$$P_2 = a P_1, \quad P_3 = b P_1$$

where $a = .71$ and $b = .50$ regardless of overpressure or location. This suggests that the pressure on the front half of the radome can be expressed in terms of the pressure at $\bar{x} = 0$ (See Figure 2 for coordinate system). Letting t represent time referenced to the time of shock arrival at $\bar{x} = 0$, then $\tau = t - \bar{x}/U$ and,

$$p(\bar{x}, t) = p(0, t - \bar{x}/U) \cdot f(\bar{x}) \quad (9)$$

which expresses the pressure at any point in terms of the pressure at $\bar{x} = 0$, a time delay, and a magnitude attenuation function. The magnitude attenuation function can be determined from experimental data^o by the relation

$$f(\bar{x}) = P_1(\bar{x}) / P_1(0) \quad (10)$$

Notice that the pressure is a spatial function of the x-coordinate only. This is attributed to the dependence of the reflected overpressure upon the incident angle between the shock wave and the radome surface. This angle is constant over any circle whose plane is parallel to the shock wave.

The final pressure equations can now be written by transforming to the radome coordinate system using $\bar{x} = x + R$. The time intervals applicable to each pressure equation are also converted to spatial intervals on the x-coordinate. These spatial intervals define the limits of integration in the generalized force equations.

For $-1/2 \leq x/D \leq 0$:

$$p(x/D, t) = P_0 f(x/D) \left\{ 1 - \left[\frac{1-a}{(U/D)\tau_2} \right] \left[(U/D)t - \frac{1}{2} \right] + \left[\frac{1-a}{(U/D)\tau_2} \right] (x/D) \right\} \quad \text{-----} \quad (11)$$

$$\text{----- } (U/D)(t - \tau_2) - \frac{1}{2} \leq x/D \leq (U/D)t - \frac{1}{2}$$

$$p(x/D, t) = P_{r0} f(x/D) \left\{ a - \left[\frac{a-b}{u_D(\tau_3-\tau_2)} \right] \left[u_D(t-\tau_2) - 1/2 \right] + \left[\frac{a-b}{u_D(\tau_3-\tau_2)} \right] (x/D) \right\} \quad \text{---} \quad (12)$$

$$\text{---} \quad u_D(t-\tau_3) - 1/2 \leq x/D \leq u_D(t-\tau_2) - 1/2$$

$$p(x/D, t) = P_{r0} f(x/D) b \left\{ 1 - \left[\frac{u_D(t-\tau_3) - 1}{u_D(\tau_0-\tau_3)} \right] + \frac{2(x/D)}{u_D(\tau_0-\tau_3)} \right\} \exp \left[- \left(\frac{t-\tau_3}{\tau_0-\tau_3} \right) \right] \quad \text{---} \quad (13)$$

$$\text{---} \quad u_D(t-\tau_0) - 1/2 \leq x/D \leq u_D(t-\tau_3) - 1/2$$

For $0 \leq x/D \leq 1/2$:

$$p(x/D, t) = P_{r0} f(x/D) \left\{ 1 - \left[\frac{(u_D)t - 1}{(u_D)\tau_0} \right] + \frac{2(x/D)}{(u_D)\tau_0} \right\} \exp(-t/\tau_0) \quad \text{---} \quad (14)$$

$$\text{---} \quad u_D(t-\tau_0) - 1/2 \leq x/D \leq (u_D)t - 1/2$$

Note that the definition $P_1(0) = P_{r0}$ has been used and that the last two equations have been linearized with respect to the spatial coordinate.

The shock wave velocity is related to free-field overpressure by the Rankine-Hugoniot equations, which give:

$$U = c_0 \sqrt{1 + \frac{6P_{s0}}{7P_0}} \quad (15)$$

The peak reflected overpressure at $x = -R$ is assumed to be given by:

$$P_{r0} = 2P_{s0} \left(\frac{7P_0 + 4P_{s0}}{7P_0 + P_{s0}} \right) \quad (16)$$

which is the equation for the peak reflected overpressure on a flat plate at normal incidence with the shock wave.⁵

Equations 11 through 14, together with 15 and 16, now express the pressure loading on the radome as a function of space, time and free-field overpressure. The period of the positive phase duration, τ_0 , as a function of overpressure can be found in References (5) or (7). Variations of τ_2 and τ_3 with overpressure, as shown in Figure 4, were taken from Reference (6). The function $f(x/D)$, also based on the data of Reference (6), is shown in Figure 5.

Having developed expressions for the pressure loading on the radome as a function of space and time, relations can now be written for the modal generalized forces. Since four expressions were necessary to describe the pressure, the generalized force in the i^{th} mode can be written as:

$$Q_i(t) = \sum_{j=1}^4 Q_i^{(j)}(t) \quad (17)$$

where "j" designates that portion of the generalized force associated with a particular pressure equation. From the definition of generalized force,

$$Q_i^{(j)}(t) = \int_{L.L.}^{U.L.} p^{(j)}(x,t) \phi_i^r(x,y,z) dA, \quad (18)$$

where $\phi_i^r(x,y,z)$ is the radial deflection component of the i^{th} mode and the upper and lower limits (U.L. and L.L.) of integration are functions of time which are specified by the applicable range of x/D associated with each pressure equation. Substituting Equation 11 into Equation 13 gives:

$$\ddot{Q}_i(t) = P_{r_0} \left\{ \left[1 - \frac{1-a}{\left(\frac{U_0}{D}\right)\tau_2} \right] \left[\left(\frac{U_0}{D}\right)t - \frac{1}{2} \right] \int_{L.L.}^{U.L.} f \phi_i^r dA + \frac{1-a}{\left(\frac{U_0}{D}\right)\tau_2} \int_{L.L.}^{U.L.} f \phi_i^r \left(\frac{x}{D}\right) dA \right\} \quad (19)$$

Now define,

$$F_i \left(\frac{x}{D}\right) \equiv \int f \phi_i^r dA \approx D^2 \sum_m f_m \phi_{i_m}^r \left(\frac{\Delta A_m}{D^2}\right) \quad (20)$$

$$G_i \left(\frac{x}{D}\right) \equiv \int f \phi_i^r \left(\frac{x}{D}\right) dA \approx D^2 \sum_m f_m \phi_{i_m}^r \left(\frac{x_m}{D}\right) \left(\frac{\Delta A_m}{D^2}\right)$$

where the indefinite integrals can be approximated by the summations, as shown, with the summations of "m" being carried out for control points whose x/D - coordinates lie between $x/D = -1/2$ and x/D . Since ...

$$\int_{L.L.}^{U.L.} f \phi_i^r dA = F_i \left(\frac{x}{D} = U.L.\right) - F_i \left(\frac{x}{D} = L.L.\right)$$

Equation 19 can then be written as:

$$\ddot{Q}_i(t) = D^2 P_{r_0} \left\{ \left[1 - \frac{1-a}{\left(\frac{U_0}{D}\right)\tau_2} \right] \left[\left(\frac{U_0}{D}\right)t - \frac{1}{2} \right] \left\{ F_i \left[\frac{x}{D} = \left(\frac{U_0}{D}\right)t - \frac{1}{2}\right] - F_i \left[\frac{x}{D} = \frac{U_0}{D}(t - \tau_2) - \frac{1}{2}\right] \right\} + \frac{1-a}{\left(\frac{U_0}{D}\right)\tau_2} \left\{ G_i \left[\frac{x}{D} = \left(\frac{U_0}{D}\right)t - \frac{1}{2}\right] - G_i \left[\frac{x}{D} = \frac{U_0}{D}(t - \tau_2) - \frac{1}{2}\right] \right\} \right\} \quad (21)$$

Similarly,

$$\begin{aligned} \dot{Q}_i^{(2)}(t) = D^2 P_o \left\{ a - \left[\frac{a-b}{u_D(\tau_2-\tau_1)} \right] \left[u_D(t-\tau_2) - \frac{1}{2} \right] \right\} & \left\{ F_i \left[x_D = \frac{u_D}{D}(t-\tau_2) - \frac{1}{2} \right] - F_i \left[x_D = \frac{u_D}{D}(t-\tau_1) - \frac{1}{2} \right] \right\} \\ + \left[\frac{a-b}{u_D(\tau_2-\tau_1)} \right] & \left\{ G_i \left[x_D = \frac{u_D}{D}(t-\tau_2) - \frac{1}{2} \right] - G_i \left[x_D = \frac{u_D}{D}(t-\tau_1) - \frac{1}{2} \right] \right\} \end{aligned} \quad (22)$$

$$\begin{aligned} \dot{Q}_i^{(3)}(t) = D^2 P_o b \left\{ 1 - \left[\frac{u_D(t-\tau_3) - 1}{u_D(\tau_3-\tau_2)} \right] \right\} & \left\{ F_i \left[x_D = \frac{u_D}{D}(t-\tau_3) - \frac{1}{2} \right] - F_i \left[x_D = \frac{u_D}{D}(t-\tau_2) - \frac{1}{2} \right] \right\} \\ + \left[\frac{2}{u_D(\tau_3-\tau_2)} \right] & \left\{ G_i \left[x_D = \frac{u_D}{D}(t-\tau_3) - \frac{1}{2} \right] - G_i \left[x_D = \frac{u_D}{D}(t-\tau_2) - \frac{1}{2} \right] \right\} \exp \left[- \left(\frac{t-\tau_3}{\tau_3-\tau_2} \right) \right] \end{aligned} \quad (23)$$

$$\begin{aligned} \dot{Q}_i^{(4)}(t) = D^2 P_o \left\{ 1 - \left[\frac{(u_D/D)t - 1}{(u_D/D)\tau_0} \right] \right\} & \left\{ F_i \left[x_D = \frac{u_D}{D}t - \frac{1}{2} \right] - F_i \left[x_D = \frac{u_D}{D}(t-\tau_0) - \frac{1}{2} \right] \right\} \\ + \left[\frac{2}{(u_D/D)\tau_0} \right] & \left\{ G_i \left[x_D = \frac{u_D}{D}t - \frac{1}{2} \right] - G_i \left[x_D = \frac{u_D}{D}(t-\tau_0) - \frac{1}{2} \right] \right\} \exp \left(- \frac{t}{\tau_0} \right) \end{aligned} \quad (24)$$

Since Equations 11, 12 and 13 were applicable only for the front half of the radome, Equations 21, 22 and 23 are restricted to $-1/2 \leq x/D \leq 0$. Similarly, Equation 24 is restricted to $0 \leq x/D \leq 1/2$.

FAILURE CRITERION

A spherical shell subjected to hydrostatic pressure contracts uniformly and the strain energy increases as the applied pressure is increased. According to the works of Von Karman and Tsien,⁸ at some critical pressure the spherical equilibrium configuration becomes unstable and the shell "jumps" from the spherical configuration to a different stable configuration. Tsien⁹ indicates that the shell fails as a result of this sudden change from one energy level to a lower energy level.

The failure criterion used in this investigation was developed by noting that there may be a similarity in the buckling mechanisms of spherical shells under hydrostatic loading and under the transient dynamic loading of a blast. It was reasoned that as the peak free-field overpressure is increased, the maximum strain energy increases until, at a critical free-field overpressure, failure occurs. It was hypothesized that the static failure and the dynamic

failure of a shell occur at the same critical strain energy level. Thus, the critical value of strain energy at which the radome fails when subjected to a blast loading can perhaps be determined from knowledge of the strain energy at which hydrostatic buckling occurs.

Consider a uniform thickness, single material, spherical shell under a uniform static pressure loading. As long as the deflection is in the elastic range the radial deflection is uniform and equal to:

$$\delta = \frac{PR^2(1-\nu)}{2Et} \quad (25)$$

Thus, the strain energy is given by:

$$U = \frac{1}{2} P A \delta = \frac{P^2 A R^2 (1-\nu)}{4Et} \quad (26)$$

In the case of a truncated sphere with a fixed base, the strain energy can be approximated by ...

$$U = \frac{P^2 A R^2 (1-\nu)(h/D)}{4Et} \quad (27)$$

if the additional strain energy introduced near the restrained base is ignored.

If an acceptable theory were available for predicting the hydrostatic buckling pressures of spherical shells, Equation 27 could be used to determine the critical strain energy. Several investigators^{10,11,12} have determined the theoretical buckling pressure based upon Love's thin shell theory:

$$P_{cr} = \frac{2}{\sqrt{3(1-\nu^2)}} E \left(\frac{t}{R}\right)^2 \quad (28)$$

Although experimental data are widely scattered¹³ it is generally concluded that Equation 28 gives results which are conservative by a factor of three or four.⁸ Experimental buckling pressures have been determined⁴ for three 4-inch diameter aluminum shells having radius-to-thickness ratios of approximately 370, 246 and 183. The results show that

$$P_{cr} = 0.35 E \left(\frac{t}{R}\right)^2 \quad (29)$$

Using Equation 29 to modify Equation 28 gives

$$P_{cr} = K \frac{2}{\sqrt{3(1-\nu^2)}} E (t/R)^2 \quad (30)$$

where $K = .286$. This relation is then in general agreement with experimental data.

Substituting Equation 30 into Equation 27 and nondimensionalizing by

$$(R/t)^3 (1+\nu) / \pi R^3 E$$

results in a critical, dimensionless strain energy expression which is dependent only upon the height-to-diameter ratio:

$$\bar{U}_{cr} = .109 (h/D) \quad (31)$$

Since $h/D = 0.71$ in this investigation, $\bar{U}_{cr} = .0774$ defines the level of strain energy at which buckling occurs.

The dynamic strain energy in a system can be expressed in terms of the generalized coordinates by¹⁴

$$U(t) = \frac{1}{2} \sum_{i=1}^3 \omega_i^2 M_i q_i^2(t) \quad (32)$$

The results of this study indicate that the maximum strain energy is due almost entirely to the response in the first mode. A study of the first mode shape (Figure 1) shows that a considerable amount of the motion is a lateral translation of the radome with respect to the base. Intuitively, it appears as though failure in this mode should occur near the base at the rear of the shell where a high state of compression exists. On occasion this type of failure has been observed experimentally.¹⁵ The more common mode of failure, however, is a "snap" or "dimple" buckling on the upstream side of the radome. In the attempt to explain the occurrence of these two types of failure due to response in the first mode, let the x-deflection components of the first mode be given by the superposition of two other shapes,

$$\varphi_x(x, y, z) = \bar{\varphi}_x(x, y, z) + \varphi_{xcg}(z) \quad (33)$$

where $\phi_{xcg_1}(z)$ can be considered as a curving or distortion of the polar axis ($z = \text{axis}$) of the radome in the first mode. In terms of spherical coordinates,

$$\phi_{xcg_1}(z) = \frac{\rho t \int_0^{2\pi} R(\sin \theta) \phi_x(\phi, \theta) d\phi}{\rho t \int_0^{2\pi} R \sin \theta d\phi} \quad (34)$$

which is seen to be the lateral translation of the center of gravity of a horizontal, circular section of the radome at any z -location. Equation 34 was evaluated and the results are shown in Figure 6. This portion of the modal deformation appears to result from local shearing or bending in the vicinity of the truncation plane.

Using the definition of generalized mass, Equation 3, the strain energy in the first mode can be written as

$$U_1 = \frac{1}{2} \omega_1^2 q_1^2 \rho t \int_S (\phi_x^2 + \phi_y^2 + \phi_z^2) dA. \quad (35)$$

Substituting Equation 33 into Equation 35 gives

$$\begin{aligned} U_1 &= \frac{1}{2} \omega_1^2 q_1^2 \rho t \int_S [(\bar{\phi}_x + \phi_{xcg_1})^2 + \phi_y^2 + \phi_z^2] dA \\ &= \frac{1}{2} \omega_1^2 q_1^2 \rho t \left[\int_S (\bar{\phi}_x^2 + \phi_y^2 + \phi_z^2) dA + \int_S \phi_{xcg_1}^2 dA + \int_S 2\bar{\phi}_x \phi_{xcg_1} dA \right]. \end{aligned} \quad (36)$$

Equation 36 splits the strain energy in the first mode into three parts. It can be shown that, by definition of $\bar{\phi}_x$ and ϕ_{xcg_1} , the third integral in Equation 36 is identically zero. The second integral describes that portion of the strain energy resulting from the translatory-type of motion (ϕ_{xcg_1}) in the first mode. It can be seen from Figure 6 that the strain due to this deformation is concentrated near the base of the radome and could possibly result in failure at the base.

The strain energy failure criterion will be applied to the remaining portion of the strain energy in the first mode, as given by

$$U_1^* = \frac{1}{2} \omega_1^2 q_1^2 \rho t \int_S (\bar{\phi}_x^2 + \phi_y^2 + \phi_z^2) dA, \quad (37)$$

together with the strain energies of the second and third modes.

Defining a modified generalized mass in the first mode as

$$M_1^* = \int_s \rho t (\bar{\phi}_x^2 + \phi_y^2 + \phi_z^2) dA, \quad (38)$$

the modified strain energy due to the response in all three modes is obtained by rewriting Equation 32 as

$$U^*(t) = \frac{1}{2} [\omega_1^2 M_1^* q_1^2(t) + \omega_2^2 M_2 q_2^2(t) + \omega_3^2 M_3 q_3^2(t)]. \quad (39)$$

Finally, the failure criterion asserts that when the blast overpressure is large enough such that the dynamic response of the radome gives

$$\bar{U}^*(t) = U^*(t) \left[\frac{(R/t)^3 (1+\nu)}{\pi R^3 E} \right] = 0.0774, \quad (40)$$

some degree of structural failure has occurred.

RESULTS

Solutions to the mathematical model just described were obtained from an operational analog computer. Since the simulation technique is not the subject of this paper the computer mechanization will not be discussed.

The method of analysis which has been presented was verified by analyzing three radome models for which experimental data were available. These radome models consisted of four-inch diameter aluminum spheres, truncated such that $h/D = 0.71$. The three aluminum shells had radius-to-thickness ratios of approximately 370, 246 and 183. The critical blast overpressures for these models were determined from shock-tube tests which were conducted by MIT/Lincoln Laboratory.⁴

Each of these three shells was simulated on the analog computer to determine the variation of peak strain energy with free-field overpressure. These results are shown in Figure 7 for the three different radius-to-thickness ratios. The intersections of the horizontal line at $\bar{U}_{cr} = .0774$ with the strain energy curves give the theoretical, critical overpressures. A comparison of theoretical and experimental results is shown in Figure 8. It should be noted that the experimental pressures represent mean values of the experimental data. The correlation shows a maximum deviation of 16.8% and an average deviation of 6.8% for the three check cases.

Variations in the radome diameter, while maintaining a constant R/t, resulted in the same dimensionless strain energy curves, indicating that the critical overpressures shown in Figure 8 are applicable to any diameter. This result was not unexpected since the same conclusion can be made from an examination of the equation of motion of a simple second order system. This same result is discussed in detail by Muldoon¹⁵ with the conclusion that a full-scale radome will exhibit the same dynamic behavior as a model provided that all dimensions are scaled as a linear function of the diameter.

Having established the applicability of this method for predicting critical overpressures, radomes constructed of glass-reinforced plastic laminates were then analyzed. The following typical material properties were used to represent a practical radome material:

$$E = 2.0 \times 10^6 \text{ psi}$$

$$\rho = 0.06 \text{ lbs./in.}^3$$

$$\nu = 1/6$$

No consideration was given to any non-orthotropic properties of the material. The variation of maximum strain energy with free-field overpressure is shown in Figure 9 for various radius-to-thickness ratios and Figure 10 gives the critical free-field overpressure versus R/t for the laminated plastic radomes.

CONCLUDING REMARKS

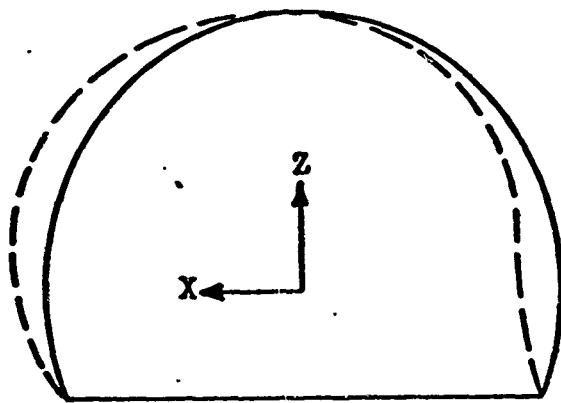
A method has been presented for determining the vulnerability of shell-like radomes to the transient pressure loading induced by a nuclear blast and the accuracy of the method has been demonstrated. It should be noted that this investigation considered only one height-to-diameter ratio such that the generality of the approach used here has not been established.

Data were presented showing critical blast overpressures for radomes constructed of glass-reinforced laminated plastic. The critical overpressures shown are applicable for any diameter, however, the data are restricted to radomes having a height-to-diameter ratio of approximately 0.71. Intentionally, no conclusions are made regarding the feasibility of protecting antenna installations by means of hardened radomes. Conclusions of this nature would involve such considerations as cost of construction, electromagnetic transmissibility and the probability of exceeding a prescribed overpressure in the event of an attack.

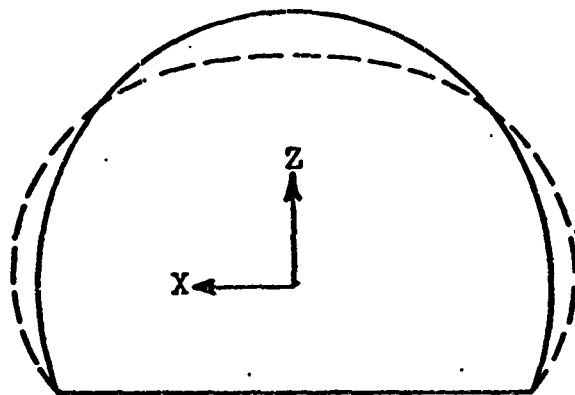
REFERENCES

1. Witwer, E. A., Herrman, W., Leech, J. W. and Pian, T. H. H., "Responses of Plates and Shells to Intense External Loads of Short Duration," Massachusetts Institute of Technology, WADD Technical Report TR60-433, April, 1960.
2. Brennikoff, A., "Solution of Problems of Elasticity by the Framework Method," Journal of Applied Mechanics, December, 1941.
3. DuBerg, J. E., et al, "Analysis and Design of Domes, Arches and Shells," Volume I, "Elastic Analysis of Spherical Domes," University of Illinois, AFSWC-TR-59-9.
4. MIT/Lincoln Laboratory, "TTR 2-psi Hardened Radome," Division 7, Final Report Volume I, September, 1961.
5. U. S. Department of Defense, "Effects of Nuclear Weapons," U. S. Atomic Energy Commission, April, 1962.
6. Gallagher, E. V., "Air Blast Loading on Arches and Domes," Armour Research Foundation, Final Test Report No. 13, AFSWC-TN-58-26-AFSWP-1108, September, 1958.
7. Norris, C. H., et al, "Structural Design for Dynamic Loads," McGraw-Hill Book Co., Inc., New York, 1959.
8. Von Karman, T. and Tsien, H. S., "The Buckling of Spherical Shells by External Pressure," Journal of Aeronautical Sciences, Vol. 7, No. 2, December, 1939.
9. Tsien, Hsue-Shen, "A Theory for the Buckling of Thin Shells," Journal of Aeronautical Sciences, Vol. 9, No. 10, August, 1942.
10. Zoelly, R., "Uber ein Knickungsproblem der Kugelschalen," Dissertation, Zurich, Techn. Hochschule, 1915.
11. Schwerin, E., "Zur Stabilitat Der Dunnwandigen Hohlkugel Unter Gleichmessigem Aussendruck," Z. A. M. M., Vol. 2, No. w, 1922.
12. Van der Neut, A., "De Elastische Stabiliteit van den Dunwendigen Bol," Dissertation, Delft, 1932.
13. Stocker, J. E., "The Buckling of Spherical Shells Under Uniformly Distributed Static Pressures," North American Aviation, Inc., Report No. NA62H-503, May, 1962.

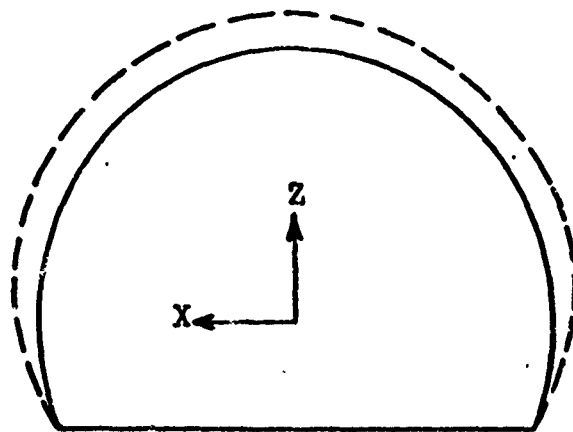
14. Bisplinghoff, R. L., Ashley, H. and Halfman, R. L., "Aeroelasticity," Addison-Wesley Publishing Co., Inc., Cambridge, Massachusetts, 1955.
15. Muldoon, R. A., "Dynamic Buckling of Space Frame Radome Models," MIT/Lincoln Laboratory, Group Report No. 71G-3, February, 1962.



Mode 1



Mode 2



Mode 3

FIGURE 1

RADOME MODE SHAPES USED IN DYNAMIC ANALYSIS

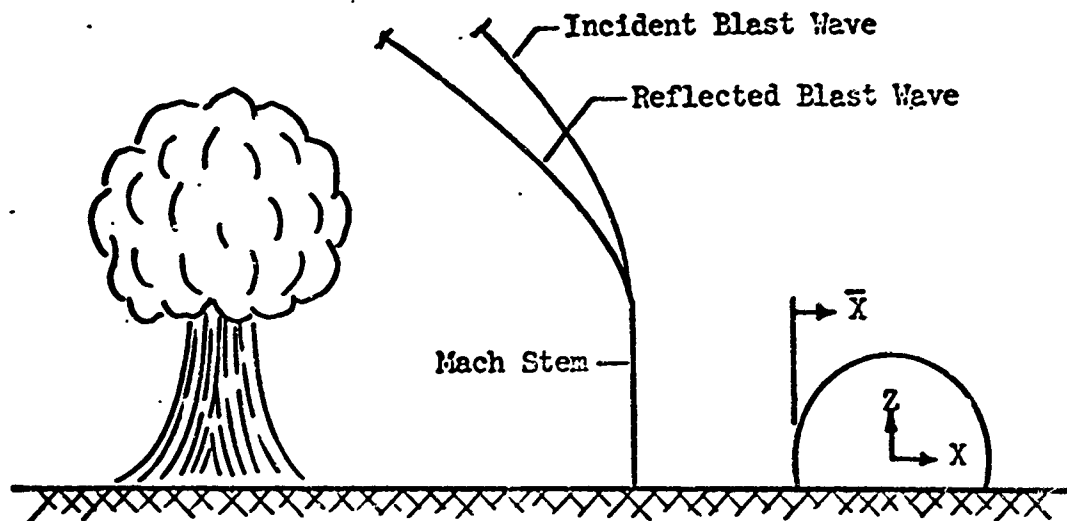


FIGURE 2

NUCLEAR BLAST SHOCK WAVE IN RELATION TO RADOME

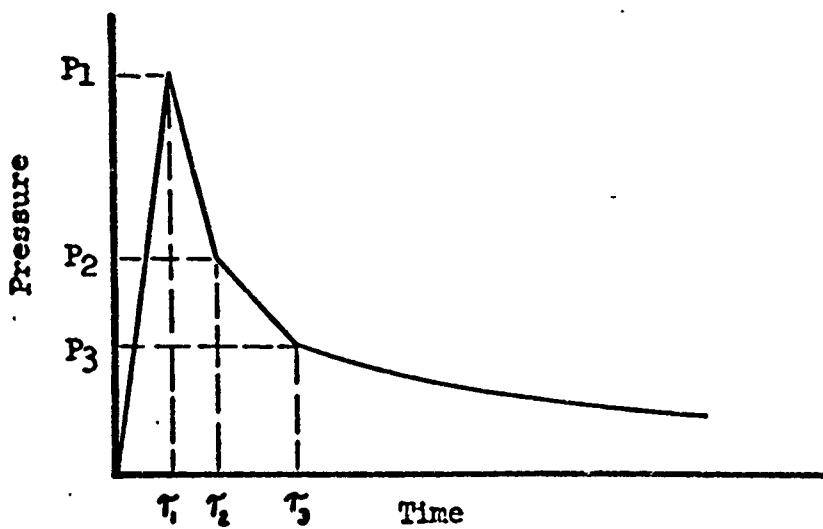
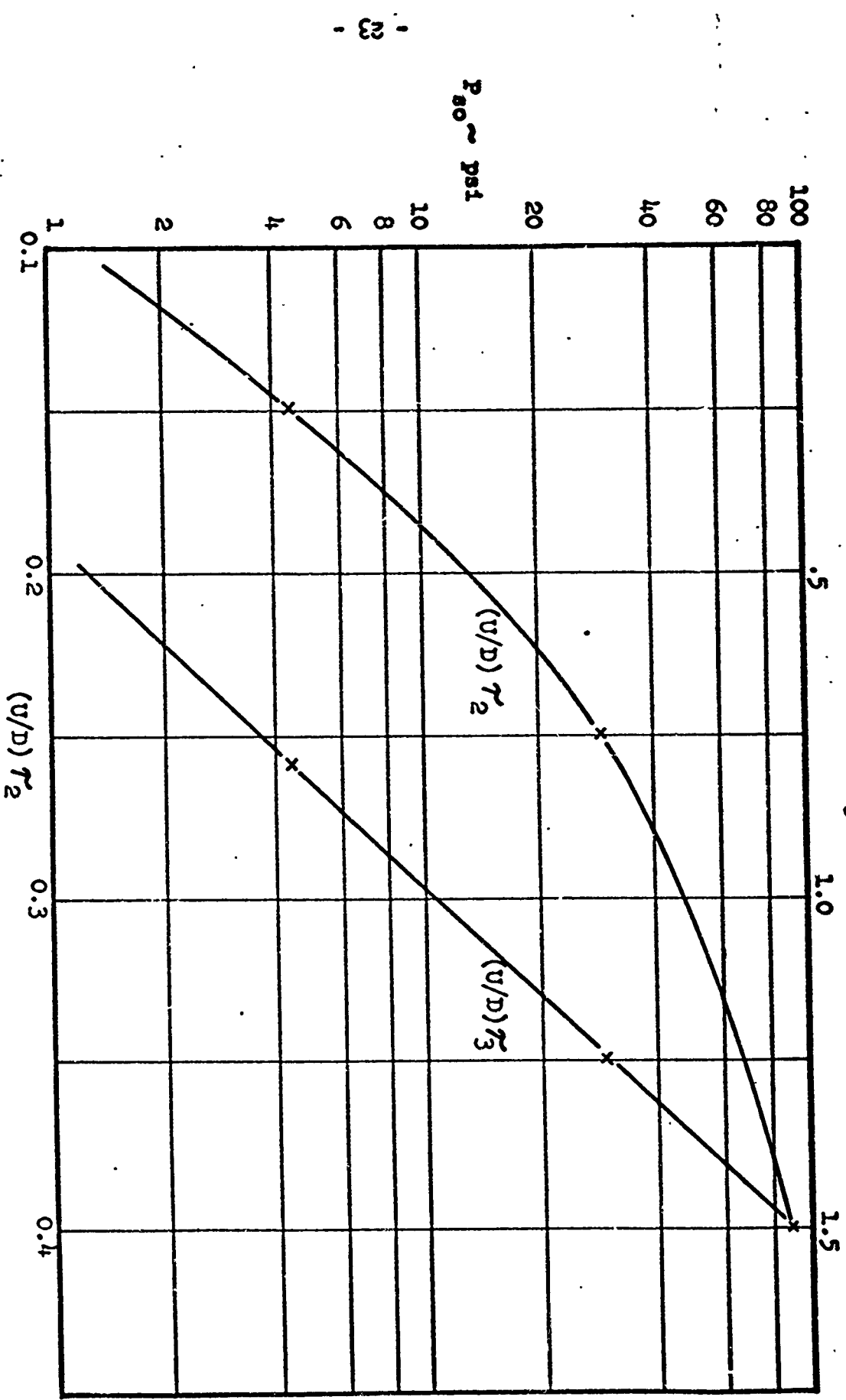


FIGURE 3

SCHEMATIC LOADING DIAGRAM FOR FRONT-HALF OF RADOME



VARIATION OF τ_2 AND τ_3 WITH FREE-FIELD OVERPRESSURE

FIGURE 4

13

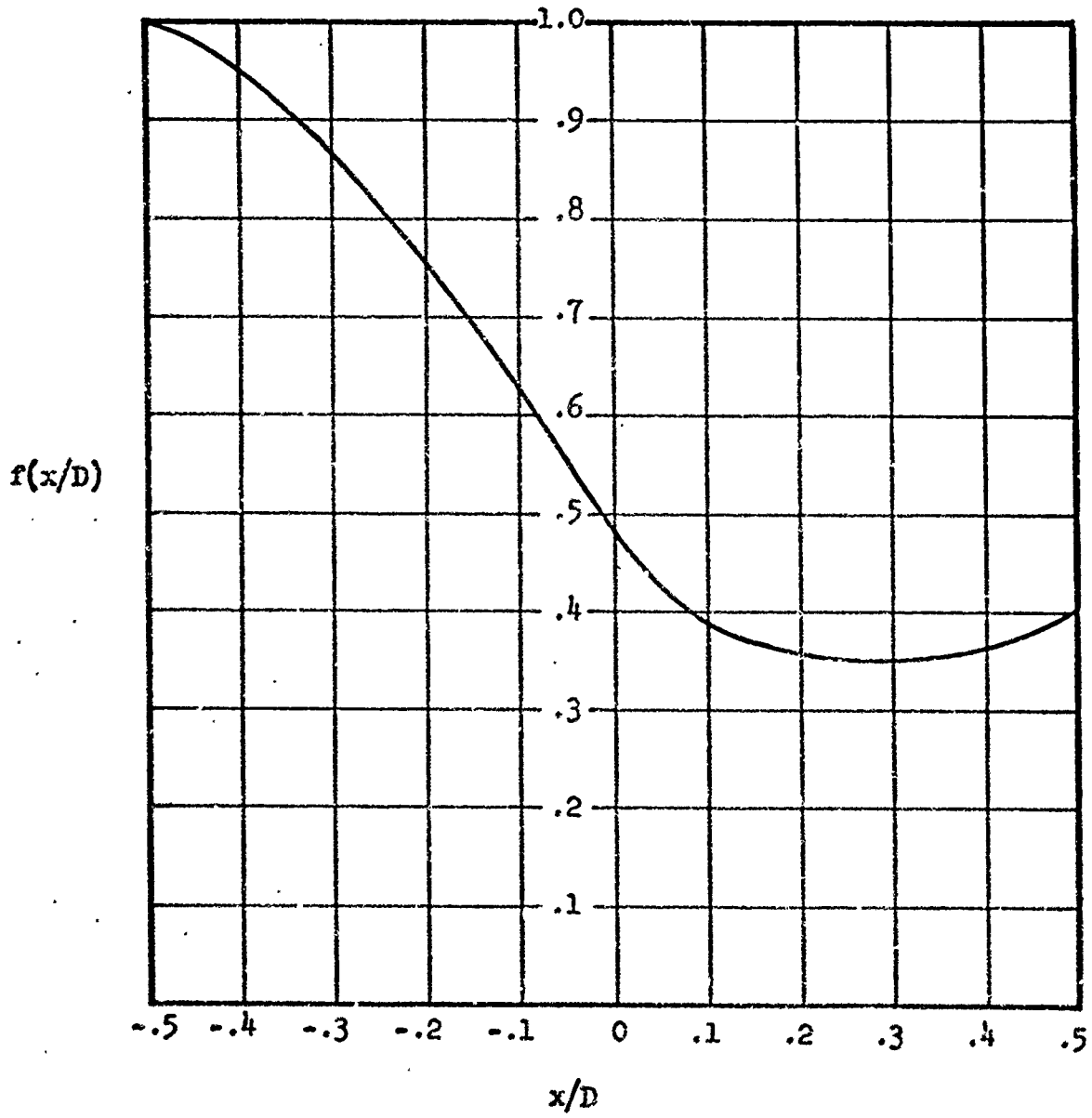


FIGURE 5

PRESSURE MAGNITUDE ATTENUATION FUNCTION

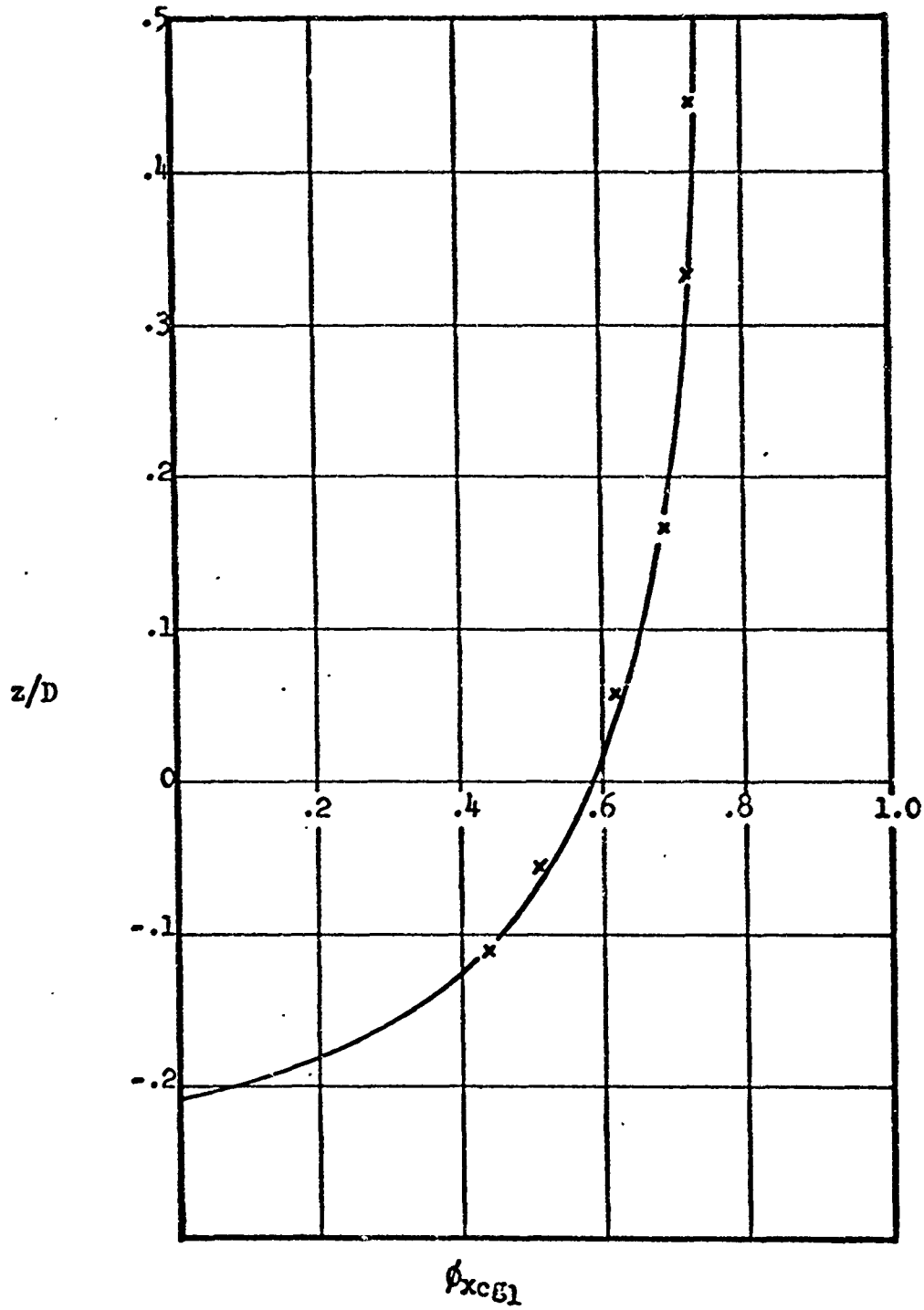


FIGURE 6

DISTORTION OF RADIAL POLAR AXIS IN THE FIRST MODE SHAPE

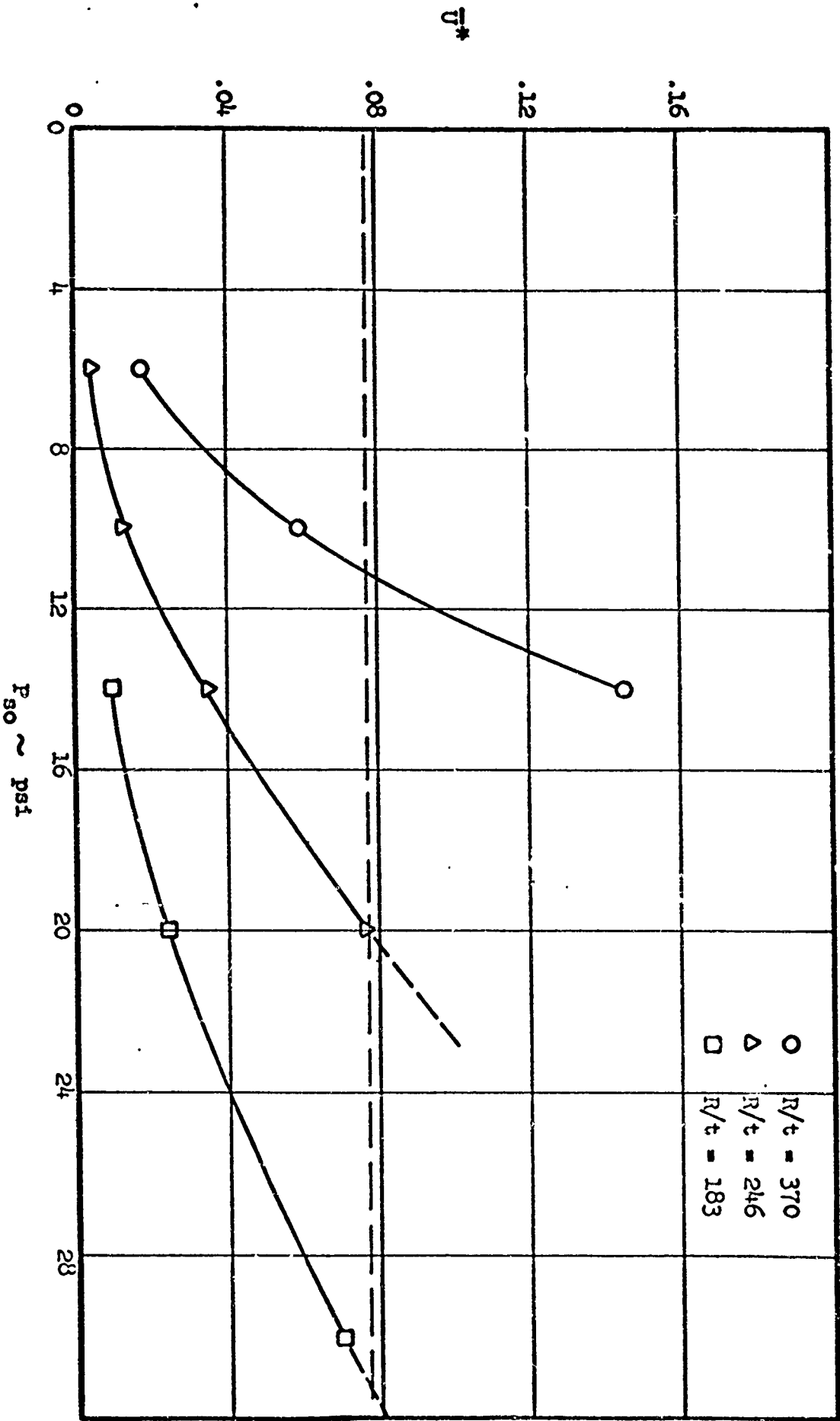


FIGURE 7

DIMENSIONLESS STRAIN ENERGY VS. OVERPRESSURE FOR ALUMINUM SHELL RADOMES

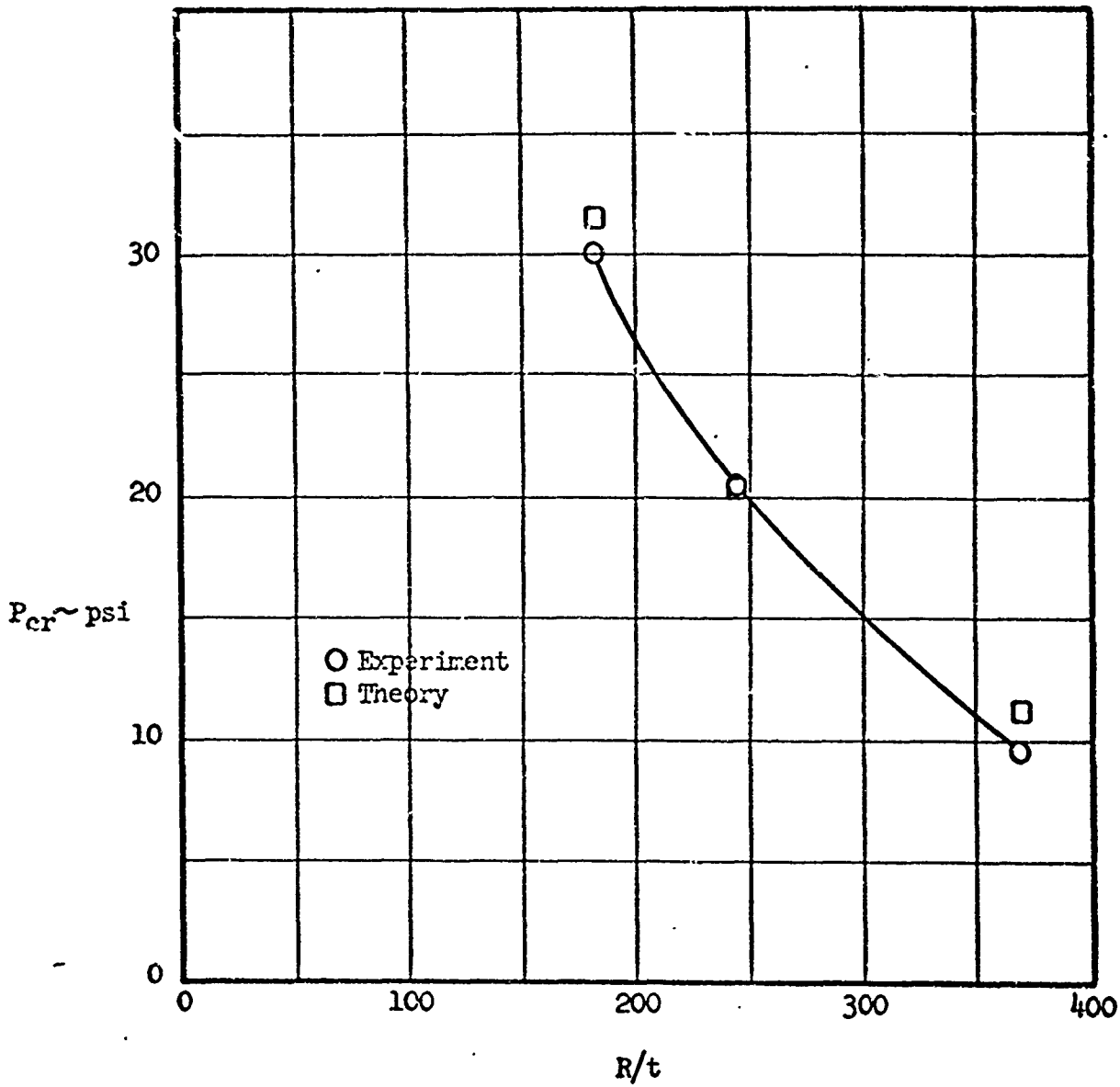


FIGURE 8

CRITICAL FREE-FIELD OVERPRESSURE VS. RADIUS-TO-THICKNESS RATIO FOR ALUMINUM SHELL RADOMES

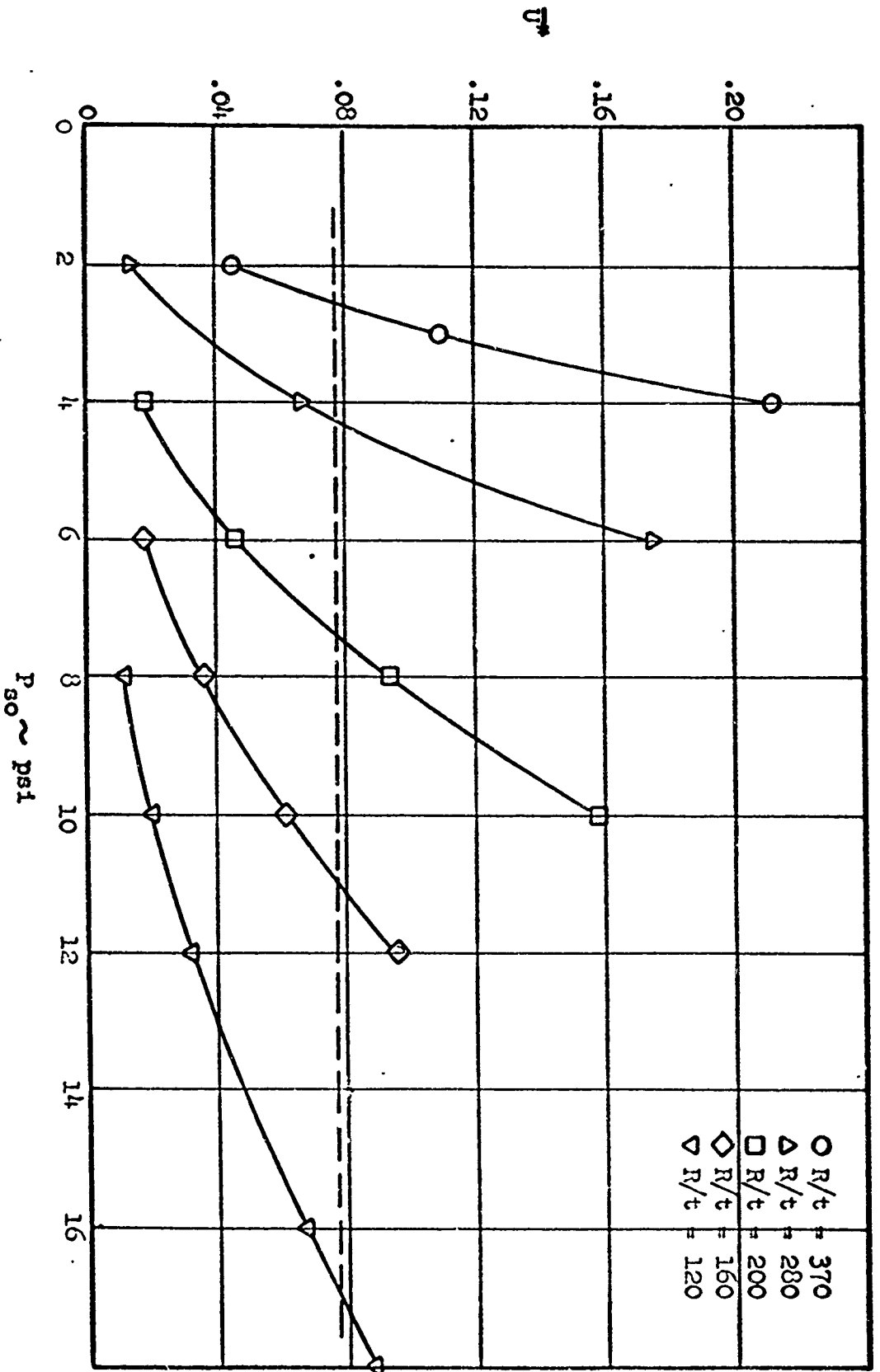


FIGURE 9

DIMENSIONLESS STRAIN ENERGY VS. OVERPRESSURE, GLASS-REINFORCED LAMINATED PLASTIC RADOMES

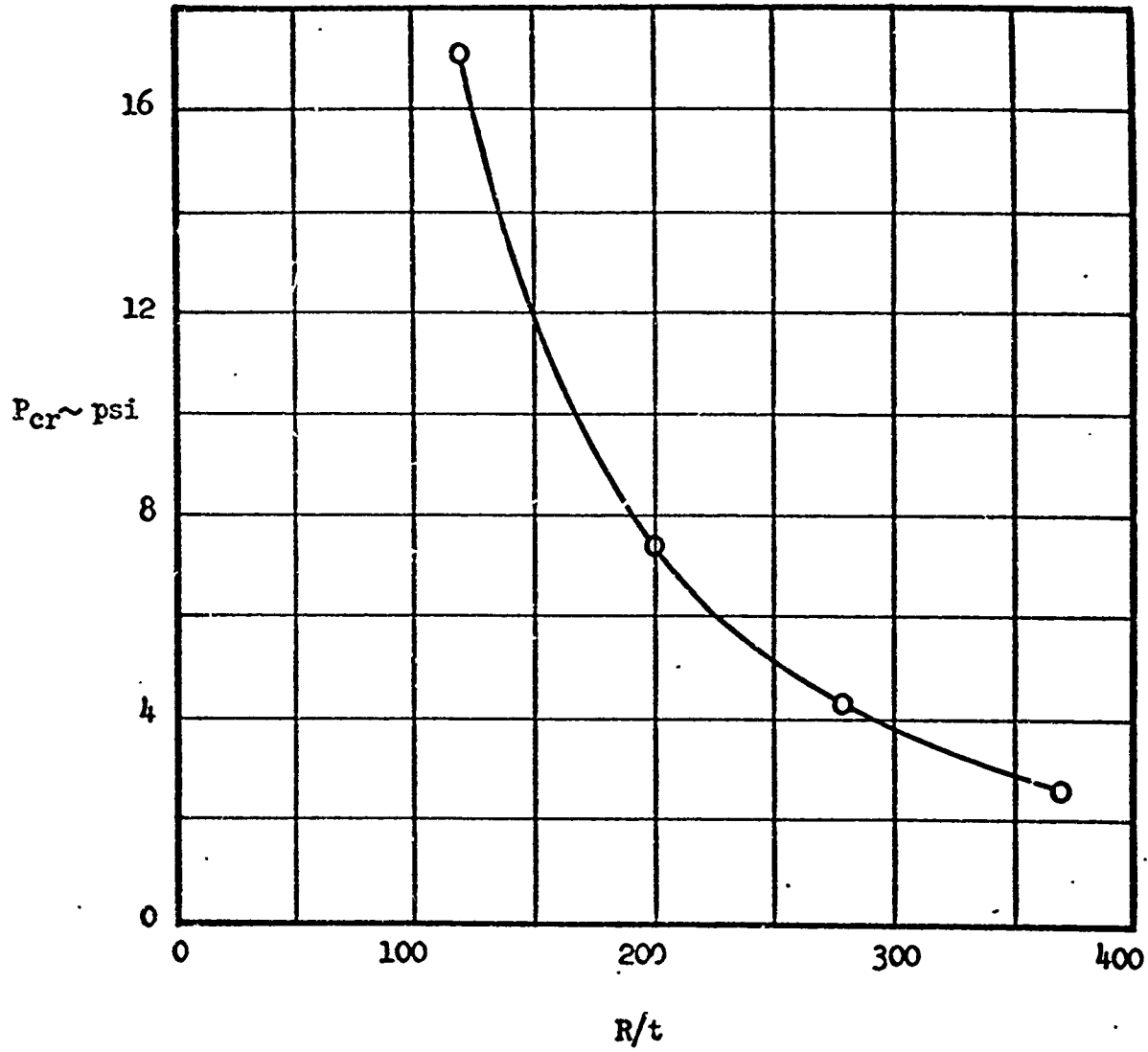


FIGURE 10

CRITICAL FREE-FIELD OVERPRESSURE VS. RADIUS-TO-THICKNESS RATIO,
GLASS-REINFORCED LAMINATED PLASTIC RADOMES